

DOTTORATO DI RICERCA IN FISICA
UNIVERSITÁ DEGLI STUDI DELL' INSUBRIA – DIPARTIMENTO DI SCIENCE
CHIMICHE FISICHE E MATEMATICHE

Chaos and Localisation: Quantum Transport in Periodically Driven Atomic Systems

Binationale Dissertation
der Fakultät für Physik
der Ludwig-Maximilians-Universität München

DISSERTAZIONE IN COTUTELA



vorgelegt von Sandro Marcel Wimberger
aus Passau

München, den 17. Oktober 2003

DOTTORATO DI RICERCA IN FISICA
UNIVERSITÁ DEGLI STUDI DELL' INSUBRIA – DIPARTIMENTO DI SCIENZE
CHIMICHE FISICHE E MATEMATICHE

Chaos and Localisation: Quantum Transport in Periodically Driven Atomic Systems

Binationale Dissertation
der Fakultät für Physik
der Ludwig-Maximilians-Universität München

DISSERTAZIONE IN COTUTELA

vorgelegt von Sandro Marcel Wimberger
aus Passau

1. Gutachter/Tutore: PD DR. ANDREAS BUCHLEITNER
2. Gutachter/Tutore: PROF. ITALO GUARNERI

Tag der mündlichen Prüfung: 14. Januar 2004

München, den 17. Oktober 2003

Meinem Lehrer, Herrn Manfred Wenniger.

O how much more doth beauty beauteous seem
By that sweet ornament which truth doth give!
The rose looks fair, but fairer we it deem
For that sweet odour which doth in it live;
The canker blooms have full as deep a dye
As the perfumed tincture of the roses,
Hang on such thorns, and play as wantonly,
When summer's breath their masked buds discloses;
But for their virtue only is their show
They live unwooded, and unrespected fade,
Die to themselves. Sweet roses do not so;
Of their sweet deaths the sweetest odours made;
And so of you, beauteous and lovely youth;
When that shall vade, by verse distils your truth.

W. Shakespeare

Zusammenfassung

In dieser Arbeit untersuchen wir quantalen Transport im Energierraum anhand zweier Paradebeispiele der Quantenchaostheorie: hoch angeregte Wasserstoffatome im Mikrowellenfeld, und gekickte Atome, die das Modellsystem des δ -gekickten Rotors simulieren. Beide Systeme unterliegen aufgrund des äußeren, zeitlich periodischen Antriebs einer komplexen Zeitentwicklung. Insbesondere werden zwei Quantenphänomäne untersucht, die kein klassisches Analogon besitzen: die Unterdrückung klassischer Diffusion, bekannt unter dem Schlagwort dynamischer Lokalisierung, und die Quantenresonanzen als dynamisches Regime, das sich durch beschleunigten Transport im δ -gekickten Rotor auszeichnet.

Der erste Teil der Arbeit belegt auf neue Weise die quantitative Analogie zwischen dem Energietransport in stark getriebenen, hoch angeregten Atomen und dem Teilchentransport im Anderson-lokaliserten Festkörper. Eine umfassende numerische Analyse der atomaren Ionisationsraten zeigt in Übereinstimmung mit der Lokalisierungstheorie nach Anderson, dass die Ratenverteilungen einem universellen Potenzgesetz unterliegen. Dies wird sowohl für ein eindimensionales Modell als auch für das reale dreidimensionale Atom demonstriert. Außerdem werden die Konsequenzen aus der universellen Verteilung der Ionisationsraten für die asymptotische Zeitabhängigkeit der Überlebenswahrscheinlichkeit der Atome diskutiert.

Der zweite Teil der Arbeit klärt den Einfluss von Dekohärenz – induziert durch Spontanemission – auf die kürzlich im Experiment mit δ -gekickten Atomen beobachteten Quantenresonanzen. Wir leiten Skalierungsgesetze ab, die auf einer quasiklassischen Näherung der Quantendynamik beruhen und die Form von Resonanzpeaks beschreiben, welche in der mittleren Energie eines atomaren Ensembles im Experiment beobachtet wurden. Unsere analytischen Resultate stimmen mit numerischen Rechnungen ausgezeichnet überein und erklären die zunächst überraschenden experimentellen Befunde. Darüberhinaus weisen sie den Weg zur Untersuchung des wechselseitig konkurrierenden Einflusses von Dekohärenz und Chaos auf die Stabilität der quantenmechanischen Zeitentwicklung gekickter Atome. Die Stabilität lässt sich mittels des Überlapps zweier anfänglich gleicher, aber unterschiedlich propagierter Zustände charakterisieren. Dieser Überlapp, bekannt als „Fidelity“, wird hier für eine experimentell realisierbare Situation untersucht.

Riassunto

In questa tesi viene studiato il trasporto quantistico nello spazio dell'energia di due sistemi modello della teoria del caos quantistico: atomi di idrogeno altamente eccitati sottoposti ad un campo di micro-onde ed atomi calciati che simulano il modello “ δ -kicked rotor”. Entrambi questi sistemi presentano una evoluzione dinamica complessa, derivante dall'interazione con una forza periodica esterna. In particolare vengono studiati due fenomeni quantistici che non hanno una controparte classica: la soppressione della diffusione classica, conosciuta come localizzazione dinamica, e le risonanze quantistiche come regime dinamico del trasporto amplificato.

La prima parte della tesi fornisce un nuovo supporto all'analogia quantitativa fra il trasporto di energia in idrogeno altamente eccitato sottoposto a un campo elettromagnetico intenso, ed il trasporto di particelle in solidi con localizzazione di Anderson. Un'analisi numerica completa dei rate di ionizzazione atomica mostra che questi obbediscono ad una distribuzione universale conforme ad una legge algebrica, in accordo con la teoria della localizzazione di Anderson. Questo risultato viene dimostrato sia per il modello unidimensionale che per l'atomo reale in tre dimensioni. Vengono inoltre discusse le ripercussioni della distribuzione universale dei rate di ionizzazione sul decadimento della probabilità di sopravvivenza asintotica degli atomi.

La seconda parte della tesi chiarisce l'effetto della decoerenza – causata dall'emissione spontanea – nelle risonanze quantistiche che sono state osservate in un esperimento recente con atomi calciati. Vengono derivate due leggi di scala basate sull'approssimazione quasi classica dell'evoluzione quantistica. Queste leggi descrivono la forma dei picchi di risonanza nell'energia di un insieme sperimentale di atomi calciati. I risultati analitici ottenuti sono in perfetto accordo con simulazioni numeriche e motivano osservazioni sperimentali inizialmente inspiegati. Aprono inoltre possibilità di studio sull'effetto competitivo della decoerenza e del caos sulla stabilità dell'evoluzione quantistica degli atomi calciati. La stabilità si può caratterizzare tramite la sovrapposizione di due stati inizialmente uguali, però soggetti ad evoluzioni temporali differenti. Questa sovrapposizione, detta fidelity, viene studiata per una situazione sperimentale realizzabile.

Abstract

This thesis investigates quantum transport in the energy space of two paradigm systems of quantum chaos theory. These are highly excited hydrogen atoms subject to a microwave field, and kicked atoms which mimic the δ -kicked rotor model. Both of these systems show a complex dynamical evolution arising from the interaction with an external time-periodic driving force. In particular two quantum phenomena, which have no counterpart on the classical level, are studied: the suppression of classical diffusion, known as dynamical localisation, and quantum resonances as a regime of enhanced transport for the δ -kicked rotor.

The first part of the thesis provides new support for the quantitative analogy between energy transport in strongly driven highly excited atoms and particle transport in Anderson-localised solids. A comprehensive numerical analysis of the atomic ionisation rates shows that they obey a universal power-law distribution, in agreement with Anderson localisation theory. This is demonstrated for a one-dimensional model as well as for the real three-dimensional atom. We also discuss the implications of the universal decay-rate distributions for the asymptotic time-decay of the survival probability of the atoms.

The second part of the thesis clarifies the effect of decoherence, induced by spontaneous emission, on the quantum resonances which have been observed in a recent experiment with δ -kicked atoms. Scaling laws are derived, based on a quasi-classical approximation of the quantum evolution. These laws describe the shape of the resonance peaks in the mean energy of an experimental ensemble of kicked atoms. Our analytical results match perfectly numerical computations and explain the initially surprising experimental observations. Furthermore, they open the door to the study of the competing effects of decoherence and chaos on the stability of the time evolution of kicked atoms. This stability may be characterised by the overlap of two identical initial states which are subject to different time evolutions. This overlap, called fidelity, is investigated in an experimentally accessible situation.

Resumen

En este trabajo se investiga el fenómeno de transporte cuántico en el espacio de energía de dos sistemas paradigmáticos de la teoría del caos cuántico: por un lado, estados altamente excitados de átomos de hidrógeno en un campo de microondas, y por otro lado átomos golpeados que simulan el modelo “ δ -kicked rotor”. Los dos sistemas presentan una dinámica compleja proveniente de la interacción con una fuerza externa periódica en el tiempo. En particular son estudiados dos fenómenos cuánticos sin contraparte clásica: la supresión de difusión clásica, conocido como localización dinámica, y resonancias cuánticas como un régimen dinámico de transporte amplificado.

La primera parte de esta tesis proporciona una nueva demostración de la analogía entre el transporte de energía en átomos altamente excitados sometidos a campos electromagnéticos intensos y el transporte de partículas en sólidos localizados de Anderson. Un análisis numérico detallado de las tasas de ionización atómica muestra que éstas obedecen una distribución universal conforme a una ley algebraica, lo cual está de acuerdo con la teoría de localización de Anderson. Esto es demostrado tanto para un modelo unidimensional como para átomos reales tridimensionales. Se discuten también las implicaciones de las distribuciones universales de las tasas de ionización para el decaimiento asintótico en el tiempo de las probabilidades de sobrevivencia de los átomos. La segunda parte de la tesis clarifica el efecto de decoherencia por emisión espontánea en las resonancias cuánticas observadas en un experimento reciente con átomos golpeados. Leyes de escalamiento son deducidas, basadas en una aproximación cuasiclásica de la evolución cuántica, las cuales describen la forma de los picos resonantes en la energía media de un ensamble experimental de átomos golpeados. Nuestros resultados analíticos encajan perfectamente con sendos cálculos numéricos y explican observaciones experimentales que inicialmente fueron sorprendentes. Mas aún, abren las puertas para el estudio de los efectos competentes de decoherencia y caos en la estabilidad de la evolución temporal de átomos golpeados. Esta estabilidad puede ser caracterizada por el solapamiento de dos estados iniciales idénticos, pero a la vez con distintas evoluciones en el tiempo. Este solapamiento es llamado fidelidad y es investigado para una situación accesible experimentalmente.

Contents

1	Introduction	1
1.1	Quantum chaos and experiments	1
1.2	Quantum transport in periodically driven atomic systems	2
1.2.1	Anderson localisation and decay-rate statistics	4
1.2.2	Quantum resonances with δ -kicked atoms	8
1.3	Outline of the thesis	10
2	Theoretical and experimental preliminaries	13
2.1	Periodicity in time, position, and momentum	13
2.1.1	Floquet theory	13
2.1.2	Bloch theory in position space	14
2.2	The δ -kicked rotor	15
2.2.1	The model	15
2.2.2	Quantum resonances	17
2.2.3	Particle vs. rotor: Bloch theory for kicked atoms	19
2.3	Experimental realisation of the kicked rotor model	20
2.3.1	Experimental setup	20
2.3.2	Derivation of the effective Hamiltonian	22

2.3.3	Experimental imperfections	25
2.4	Quantum chaos and microwave-driven Rydberg states	27
2.4.1	Atomic hydrogen in a microwave field	27
2.4.2	Quantum-classical correspondence	30
Part I	Signatures of Anderson localisation in the multiphoton ionization of hydrogen Rydberg atoms	32
3	Driven Rydberg atoms as an open quantum system	35
3.1	Universal statistics of decay rates	37
3.1.1	Numerical results	37
3.1.2	Discussion of decay-rate distributions	42
3.1.3	Algebraic decay of survival probability	48
3.2	Experimental tests	55
3.2.1	Status quo	55
3.2.2	Floquet spectroscopy	55
3.2.3	Atomic conductance fluctuations	57
Part II	Quantum resonances and the effect of decoherence in the dynamics of kicked atoms	63
4	Kicked-atom dynamics at quantum resonance	65
4.1	Quantum resonances in experiments	65
4.2	Noise-free quantum resonant behaviour	68
4.2.1	Momentum distributions	70
4.2.2	Average kinetic energy	75
4.3	Destruction of quantum resonances by decoherence	75

4.3.1	Stochastic gauge	76
4.3.2	Theoretical model for randomised dynamics	78
4.3.3	Average kinetic energy	82
4.3.4	Asymptotic momentum distribution	86
4.3.5	Theoretical model vs. numerical results	89
4.3.6	Reconciliation with experimental observations	93
5	Dynamics near to quantum resonance	101
5.1	ϵ -quasi-classical approximation	102
5.2	Classical scaling theory for quantum resonances	106
5.2.1	ϵ -quasi-classical analysis of the resonance peaks	106
5.2.2	Validity of the ϵ -quasi-classical approximation	113
5.3	Classical scaling in presence of decoherence	114
6	Decay of fidelity for δ-kicked atoms	121
6.1	Stability of quantum dynamics and experimental proposal	121
6.2	Fidelity at quantum resonance	124
6.2.1	Dynamical stability in absence of noise	124
6.2.2	Fidelity in presence of decoherence	129
6.3	Fidelity near to quantum resonance	133
6.4	Fidelity with quantum accelerator modes	134

7	Résumé	141
7.1	Summary of results	141
7.2	Future perspectives	143
	Appendix	147
A	Analysis of the Steady State Distribution (4.15)	147
A.1	Proof of estimate (4.16)	147
A.2	Proof of inequality (A.2)	148
A.3	Proof of the asymptotic formula (4.17)	148
B	Statistics of the process Z_m	150
B.1	Independence of the variables z_j	150
B.2	Central Limit property	151
C	Asymptotic distribution of the process W_t	152
D	Derivation of equation (5.26)	154
E	Extraction of fidelity from Ramsey fringes	155
F	Some formulas used in Part II	157
G	Publications	159
	Bibliography	161

Chapter 1

Introduction

1.1 Quantum chaos and experiments

Continuous development of knowledge unavoidably leads to specialisation and differentiation. This process in science tends to separate the specialties, and often pushes them so far apart that researchers working in one branch have a hard time in keeping their interest in the main questions of even related fields. A methodological integration is desirable to overcome language problems between different communities, and inter-disciplinarity between various branches in science (not only physics) in turn may foster new development. P. W. Anderson [1] noticed about 30 years ago that the study of complex systems – where at each level of complexity new and interesting phenomena emerge – offers a variety of connections between different branches of physics, chemistry, biology, and increasingly also economics and computer science [2, 3].

The field of “quantum chaos” which sprouted a few years later [4–6] is an excellent example of a fruitful merger of ideas originating from many branches of physics. For the investigation of complex dynamical systems, classical and quantum physics were brought together. In particular, concepts from nuclear, atomic, molecular physics, nonlinear systems theory and statistics serve in the inter-disciplinary study of quantum systems which show signatures of classical chaos. Although a vast amount of effort has been undertaken in theoretical and numerical investigations on the quantum mechanical analogues of classically chaotic systems [7–10], clean experimental studies of quantum manifestations of classical chaos had been rather restricted up to the mid 1980ies [11–18].

The only early experimental contribution, which in turn motivated the development of quantum chaos, came from nuclear physics, supplying a huge database of nuclear energy spectra [19]. Their statistical characterisation, without knowledge of exact solutions of the quantum many body scattering problem in heavy nuclei, is possible through the meanwhile well-established Random Matrix Theory [9, 17, 20, 21], which nowadays is used in many other branches of

physics [22, 23].

Several time-independent systems with (Hamiltonian) classically chaotic analogues were studied afterwards. The spectral properties of highly-excited Rydberg atoms subject to a strong magnetic field [24, 25] have been extensively investigated providing insight into the influence of classical dynamics on the corresponding quantum problem. This conservative system of perturbed Rydberg atoms with a large density of states, whose classical dynamics is highly chaotic, is a real complex system for which the experimentally measured spectra were found to match perfectly with quantum mechanical *ab initio* calculations [12, 24–29]. More recently, also Rydberg states in crossed electric and magnetic (static) fields have been studied [14, 30–34]. Rydberg atoms in crossed fields may eventually provide an atomic realisation (with dominantly chaotic dynamics) of cross sections exhibiting Ericson fluctuations [30]. The latter are well-known in nuclear (chaotic) scattering [35–37].

A fashionable and direct way to illustrate wave functions as well as to study plenty of energy levels (up to very high energies) is offered by billiard systems [17, 18], where either particles (e.g. electrons) or light rays scatter off hard walls. Light-ray billiards, which are relevant, for instance, to the development of small micro-laser cavities [38, 39], are toy models for the study of wave chaos [17, 40–42]. There one resorts to the analogy between the two-dimensional Helmholtz equation for the electric field modes and the stationary Schrödinger equation [17].

All the above mentioned systems are governed by a time-independent Hamiltonian. In this thesis deceptively simple quantum systems are investigated which show a variety of complex transport phenomena induced by an external time-dependent driving force. The driving pumps energy into the unperturbed system and may turn even one-dimensional systems chaotic on the classical level, while for time-independent, autonomous problems at least two degrees of freedom are necessary for the occurrence of chaos [43–45]. If one is able to control well the external forces and to isolate the composite systems from additional noise sources, such time-dependent, low-dimensional systems are good candidates for the experimental and theoretical study of quantum chaos.

1.2 Quantum transport in periodically driven atomic systems

The interest in simple Hamiltonian systems with periodic time dependence was boosted by the ionisation experiments performed by Bayfield and Koch in 1974 [4]. An efficient multi-photon (the ionisation potential of the atomic initial state exceeded 70 times the photon energy) ionisation of atomic hydrogen Rydberg states subject to microwave fields was observed, and the highly non-perturbative nature of the process could be successfully explained by a classical diffusion process in energy space [46–49]. A great experimental breakthrough for the study of quantum transport in momentum or energy space was

then the demonstration of “dynamical localisation” in microwave-driven Rydberg atoms [13, 50–53], and later also in cold atoms subject to pulsed standing waves [54, 55]. This phenomenon had been predicted theoretically [6, 56–60], and its explanation flourished by summoning concepts of nonlinear dynamics and of solid state physics [61, 62] in an inter-disciplinary manner.

Modern day experiments are able to control essentially isolated atoms with high precision. In this thesis we focus on two periodically driven atomic systems which are accessible to state-of-the-art experiments under large control of parameters, and thus of the underlying classical dynamical regimes. While the first part of the thesis is devoted to the above mentioned ionisation of highly excited hydrogen Rydberg atoms, the second part concentrates on a model system which has found a reliable experimental realisation in the last decade, namely the δ -kicked rotor – a standard model in quantum chaology [6, 9, 17, 63, 64]. Both of these Hamiltonian systems are conceptually rather simple at first glance. The kicked rotor is a free pendulum which is subject to time periodic kicks. Hydrogen is the simplest existing atom. However, the external driving force induces a complicated, yet deterministic dynamical evolution on the classical as well as on the quantum level. The experimental realisations of these two systems can to a great deal be viewed as isolated from possible noise sources which makes them experimentally “clean”, and permits a direct comparison between theoretical and experimental results. Thus, there is no need for further assumptions or simplifications, which may be necessary, for instance, when models of mesoscopic chaotic systems are studied [18, 65–70]. In particular, Rydberg states are experimentally controllable up to very high quantum numbers [11, 16, 71–74]. This provides a large density of states and, hence, may allow for an approximate description by semiclassical methods (see, e.g. [75–77] and references therein).

Transport is by definition the change of location, i.e. the time evolution within a given system in an appropriate parameter space. In physical problems one may have in mind the phase space flow of classical densities [78] or temperature equilibration in configuration space. In our systems of interest, transport occurs classically also in phase space [78], but the essential coordinate is energy. While mesoscopic transport typically occurs as a flow of charge carriers in real (configuration) space, driven systems can exchange energy with the external field and the natural view of transport must focus on momentum or energy space. The reader should keep in mind the ionisation of atoms where the initial bound state is coupled to the atomic continuum through the energy absorption from the external microwave field. This is a real-life example of an open quantum system. The δ -kicked rotor has no continuum, yet its energy is unbounded from above (apart from unavoidable cutoffs in experiments or numerical computations). Therefore, we investigate transport in energy space, induced by the periodic driving force, on a microscopic scale of single atoms – both in external (centre-of-mass motion of kicked cold atoms) and internal (electronic excitation in Rydberg atoms) degrees of freedom.

Although this thesis focuses on quantum effects which do *not* have classical analogues, the knowledge of the classical evolution (obeying *mixed* regular-chaotic dynamics) and the use of semiclassical methods provide a deeper insight into

the physical mechanisms, which are otherwise difficult to extract from purely quantum data (e.g. the quantum spectrum). In the first part of the thesis, well-developed concepts of nonlinear systems theory help us to understand effects lying beyond the analogy between the Anderson [9, 17, 79, 80] and the driven hydrogen problem. (Semi-)classical tools are extensively used in the second part of the thesis when the quantum resonances for δ -kicked atoms are studied. Our detailed mathematical and numerical analysis of the quantum resonances occurring with δ -kicked atoms is motivated by recent, equally puzzling and inspiring experimental results [81–83].

1.2.1 Anderson localisation and decay-rate statistics

The initially surprising observation of efficient multi-photon ionisation in periodically driven hydrogen atoms [4] had been explained by the classical analysis of the dynamics of the periodically driven Kepler problem [46]. Such analysis was supported later by quantum calculations [84–87]. However, for driving frequencies larger than the ones used in the early experiments [4, 5], the quantum evolution starts to deviate substantially from the classical prediction [50, 51]. The classical diffusive motion is then suppressed by quantum interference effects. They set in at frequencies at which the driving field is able to resonantly couple – by a one-photon transition – unperturbed eigenstates of the atom in the vicinity of the initial state. This effect was qualitatively predicted by an appropriate one-dimensional description of the microwave-driven hydrogen problem using an approach very analogous to the δ -kicked rotor. To emphasise its dynamical origin as well as its affinity to the problem of Anderson localisation [79, 88, 89] the corresponding formalism was baptised dynamical localisation theory [59, 60].

Anderson localisation occurs, for instance, in disordered solids and implies an exponential localisation of the charge carriers' wave functions in configuration space [79, 80, 88, 89]. As illustrated in figure 1.1, the quantity of interest is the transmission of a (quasi-)particle across a random potential, at a given injection energy. At the potential humps, the particle can be either reflected or transmitted with randomly distributed amplitudes, and a quantitative analysis – formalising the transmission problem by a transfer matrix approach [9, 80] – shows the existence of exponentially localised eigenfunctions along the solid-state lattice. The characteristic length scale, over which the eigenfunctions spread, is given by the localisation length ξ . The measured conductance across the sample depends critically on the ratio of ξ/L , L being the length of the sample. This ratio determines the population of the last lattice site at the edge of the sample, and hence the probability flux to the lead.

The sketched scenario can be exported to the problem of energy absorption in periodically driven systems. While a formal mapping to the Anderson model is readily possible for the δ -kicked rotor, its application to the excitation and ionisation dynamics of atomic Rydberg states under microwave driving is not straightforward. However, both periodically driven problems can be formu-

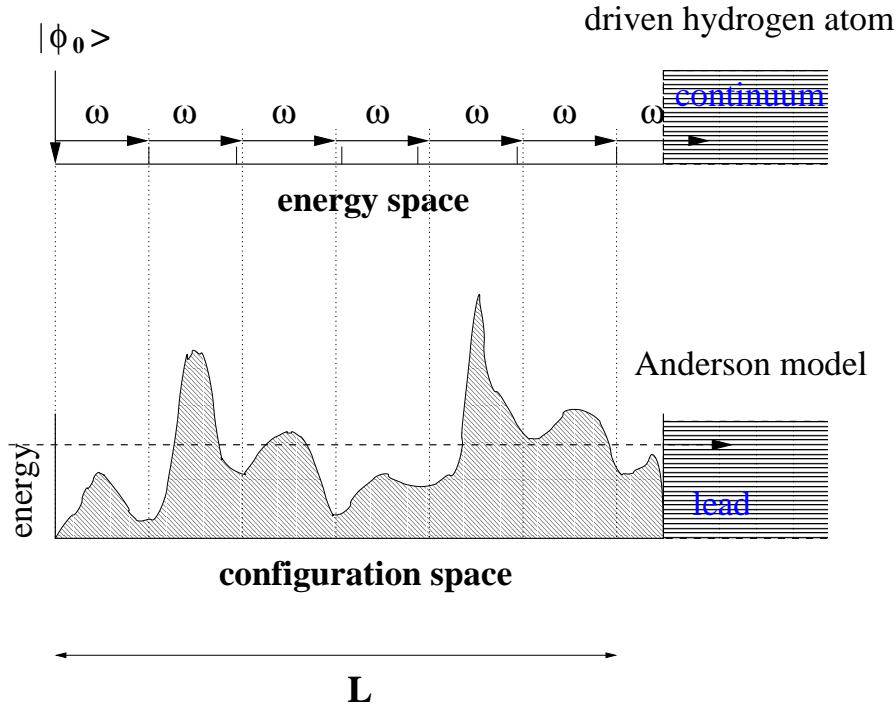


Fig. 1.1: The Anderson scenario imported into the atomic realm: an initial population of the bound state $|\phi_0\rangle$ is transported to the atomic continuum in energy space, much in the same way as a particle is transmitted across a disordered potential in one-dimensional configuration space (dashed horizontal line). While the particle can be either reflected or transmitted at each potential hump, with random probability amplitudes, in the atomic problem, absorptions/emissions of photons from/into the microwave field of frequency ω lead to transmission into the atomic continuum (indicated by a chain of arrows). The “atomic sample length” L corresponds to the ionisation potential of $|\phi_0\rangle$, measured in multiples of the photon energy ω . The one-photon transitions are slightly detuned from the unperturbed hydrogen levels. The resulting fluctuations in the coupling matrix elements mimic the intrinsic disorder present in the Anderson model.

lated within the Floquet description (see chapter 2.4). In this way, the more complicated Rydberg system may be mapped onto the δ -kicked rotor locally in energy space [59, 60]. Doing so, the effect of dynamical localisation was predicted. The random features of disordered transport manifest on the atomic scale in the complex dynamical phase evolution of a large number of states, which constitute the time-dependent electronic wave packet.

In the Rydberg regime, a *high density of states* is guaranteed since the energy splittings lie in the microwave frequency domain. Consequently, many states will be efficiently coupled by the external driving through subsequent, near-resonant one photon absorption and emission processes. The anharmonic hydrogen spectrum necessarily leads to detunings of the one-photon transitions sketched in figure 1.1. Therefore, the coupling matrix elements fluctuate in a (pseudo-)random manner [9, 87, 90] what mimics the intrinsic disorder of

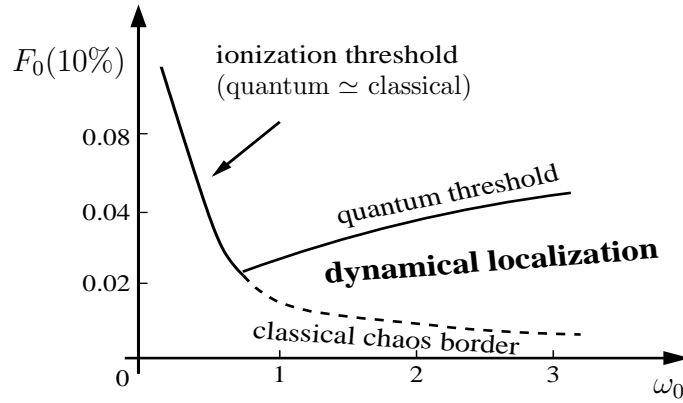


Fig. 1.2: Sketch of the scaled classical and quantum ionisation threshold $F_0(10\%) \equiv F(10\%)n_0^4$ vs. scaled frequency $\omega_0 \equiv \omega n_0^3$ for microwave driven hydrogen Rydberg atoms, from theoretical predictions [50, 59, 60, 94] and experiments [11, 50, 51]. Above $\omega_0 \simeq 1$ the quantum threshold (full line) is considerably higher than the corresponding classical one (dashed): this is the regime of dynamical localisation. For $\omega_0 < 1$, classical and quantum predictions approximately agree. The measured quantum thresholds are the central experimental evidence for Anderson localisation affecting the ionisation dynamics of driven Rydberg states (for alkali atoms the situation is very similar, with proper account for the locally reduced level spacing induced by non-vanishing quantum defects [95–99]).

the Anderson model [87, 91]. The atomic ionisation scenario is then a perfect analogue of particle transport in the Anderson problem. It consists of the transport of electronic population, initially prepared in a well-defined bound state $|\phi_0\rangle$, towards the atomic continuum.

Anderson localisation manifests itself via the exponential decay of wave functions – in the configuration space of disordered solids, and in the energy space of periodically driven systems – and the experimentally accessible signature of localisation is the leakage (decay or ionisation) out of the sample. The characterisation of the latter is the main topic of the first part of this thesis. The measurable quantity in the experiments with Rydberg atoms is the ionisation probability, for given field amplitude F , frequency ω , and interaction time t . The microscopic transport problem can, therefore, be studied by measuring the macroscopic probability of ionisation, whereby signatures of complex nonlinear dynamics show up in the local structures of the ionisation signal [11, 92, 93]. While dynamical localisation has been directly measurable only in kicked-atom experiments (where it manifests itself through exponentially decreasing momentum distributions), the central experimental result for driven Rydberg states is the increase of the ionisation threshold with the scaled frequency $\omega_0 = \omega n_0^3$ [13, 50, 51]. ω_0 corresponds to the microwave frequency ω expressed in units of the Kepler frequency of the unperturbed electron $1/n_0^3$. More precisely, the quantity extracted in the experiments is the field amplitude $F_0(10\%) \equiv F(10\%)n_0^4$, rescaled to the strength of the Coulomb

potential, at which 10% of the atoms ionise when launched from the initial state with principal quantum number n_0 . The increase of $F_0(10\%)$ with n_0 , at fixed F , ω , and interaction time t , contradicts classical asymptotic (i.e. $t \rightarrow \infty$) estimates, which predict ionisation thresholds systematically lower than those measured in experiments [60, 72, 87, 100–102].

The field threshold $F_0(10\%)$ behaviour as a function of ω_0 is sketched in figure 1.2. The quantum suppression of classically chaotic diffusion in the regime $\omega_0 > 1$ is explained by dynamical localisation theory. Yet, the fundamental dependence of $F_0(10\%)$ on ω_0 provides only a rather indirect proof of Anderson/dynamical localisation in the atomic ionisation process. One may imagine other mechanisms which stabilise the atom against ionisation, such as semiclassical stabilisation effects [87, 103, 104]. These may be caused, for instance, by barriers in classical phase space, which hinder the quantum transport. Remnants of broken tori or even chains of nonlinear resonance islands are possible candidates for such processes [72, 77, 105–107]. Moreover, also purely classical calculations predict a raise of $F_0(10\%)$ with increasing ω_0 , for finite interaction times t [50, 72].

An accurate theoretical treatment of microwave driven one-electron Rydberg states has become available in the last decade, along with the necessary computer power for the numerical diagonalisation of the exact problem [95, 108]. Clear support for the hypothesis that Anderson localisation is indeed responsible for the $F_0(10\%)$ threshold behaviour comes from the fact that the amplitudes $F_0(10\%)$ show a universal scaling, for many atomic species investigated. This has been shown by heavy numerical calculations [95–98] which are very helpful to correctly interpret experiment data [13, 99].

In this thesis, however, we pursue a different course, which goes beyond the threshold scaling, to investigate whether there exist additional, and more direct signatures of Anderson localisation.

Universal statistics of decay rates

The scenario sketched in figure 1.1 indicates that the atomic ionisation process depends on the initially prepared electronic population, i.e. on the initial state $|\phi_0\rangle$. One possible route to obtain a characterisation of the problem independently of $|\phi_0\rangle$ is to focus on the quantum spectrum of the atom in the microwave field. The latter is independent of the initial state, and only determined by the field parameters F and ω . Since we aim at the transport to the atomic continuum, the natural quantity for the comparison with Anderson models are the decay rates or the complex poles of the spectrum. They determine the decay of the eigenstates in the field, but may locally depend strongly on the field parameters [109–113]. Precisely for that reason, we perform a comprehensive numerical analysis of the *statistical* properties of the decay rates, and confront our results with predictions from Anderson-localised solid-state models. Even beyond this direct comparison of the spectral properties of the microwave-

driven Rydberg atom and Anderson models, the decay-rate statistics is correlated with the long-time behaviour of the atomic survival probability. The latter also depends on the initial state of the atom, and one question to clarify is how the decay-rate distributions and the properties of $|\phi_0\rangle$ conspire to determine the time-dependence of the survival probability. The survival probability in a microwave field has been extensively studied for real three-dimensional hydrogen as well as for alkali Rydberg states in numerical [95, 114] and laboratory experiments [73, 114]. The survival probability was found to decay asymptotically algebraically in time [95, 114]. Yet, different decay exponents have been extracted which depend on the initial atomic state, and on the field parameters [95, 114]. These findings contradict recent predictions of a *universal* power-law decay for the survival probability [115].

The key point of our analysis is that the survival probability is determined by both, the set of decay rates of the individual eigenstates, and the projection of the specific atomic initial state on the eigenbasis of the full problem. Thereby the rates encode the global spectral information, while the projection contains the local distribution of the initial state in energy space. The clear separation of these two issues allows us to clarify the above mentioned contradiction, and to show that the universality only restricts to the decay-rates statistics.

Moreover, the spectral properties of driven hydrogen Rydberg states may in turn be related to the rich underlying classical phase-space structure [112, 113, 116]. Our statistical analysis of the ionisation rates, therefore, provides not only a direct comparison to Anderson models but also an interpretation of the statistics by means of the phase-space localisation of the corresponding eigenstates. Doing so, different mechanisms which determine the statistical distribution of the decay rates can be discriminated. The thorough understanding of the decay-rate statistics and their mutual impact on the transport mechanisms in the regime of dynamical localisation $\omega_0 > 1$ in figure 1.2, is the goal of the first part of this thesis.

1.2.2 Quantum resonances with δ -kicked atoms

While the first part focuses on the regime of dynamical/Anderson localisation, for which the energy absorption from the external driving is suppressed, the second part of this thesis is devoted to a dynamical regime for which quantum transport is enhanced with respect to the classical analogue. Such enhanced energy absorption, known as quantum resonance, occurs for the δ -kicked model at specific driving frequencies [64, 117, 118]. It leads to an unbounded energy growth of the rotor, which is quadratic in time, and it arises from a perfectly frequency-matched driving [64, 117, 118].

The δ -kicked rotor is a quantum pendulum with a potential which is pulsed on and off periodically in time [6, 9, 17, 63, 64, 80]. The potential depends on the excursion angle of the rotor. The model is sketched in figure 1.3, together with the train of periodic δ -like kicks. The experimental realisation of the δ -kicked rotor model builds on the tools of quantum and atom optics. Atoms provide a

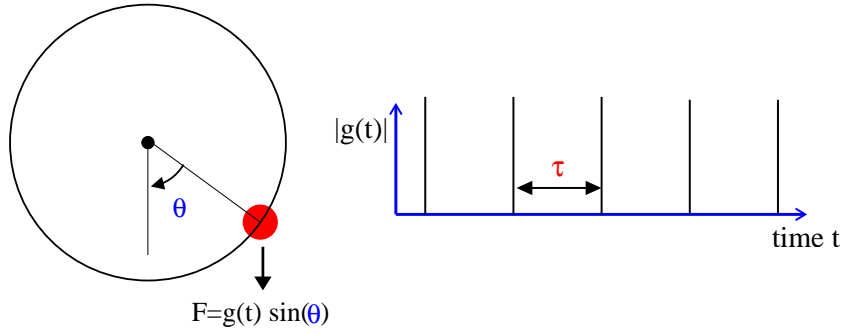


Fig. 1.3: Periodically kicked quantum pendulum, where the kicking force $F(t)$ is periodic in time (with period τ) and in the angle variable θ .

multiple of allowed electronic transitions such that their internal structure can be used to impart momentum on them, and to trap, cool, guide, and also diffract or reflect them by means of optical light fields [119–122]. Techniques which make it possible to manipulate atomic dynamics in a well-defined way, and which provide coherent matter wave sources are of high relevance for active research such as in atomic interferometry [123], for Bose-Einstein condensation [124–126], atom lasers [127–130], and in atomic lithography [131]. Integrated versions of these techniques may be used even to guide atoms along microstructures (“atomic chips”) [132–134]. Although the experimental methods of atom optics are quite standard in modern laboratories, similar high precision manipulations of atoms appeared impossible when the quantum version of the δ -kicked rotor model was studied for the first time [6].

The quantum resonances are very sensitive to variations in the driving frequency, which determines the resonance conditions [64, 117, 118]. Moreover, the quadratic energy growth of a resonantly driven rotor makes it necessary that a large energy window is accessible in experiments. Therefore, it is not surprising that experimental imperfections may lead to deviations from the predictions obtained for the idealised δ -kicked rotor model. Some systematic differences between the model and the experimental realisation can be easily understood. First, the experiments always work with a large number of atoms whose centre-of-mass evolves quantum mechanically. Hence, the experiments necessarily average over many realisations rather than working with one single rotor. Second, the atoms move essentially along a straight line, which is defined by the kicking potential. This leads to an additional freedom which needs to be introduced when mapping the problem of kicked atoms onto the rotor model which in turn moves on a circle (cf. figure 1.3). These two effects, together with experimental imperfections are important when one wants to compare experimental results with theoretical predictions.

In this thesis, a formalism for the exact treatment of an *incoherent* ensemble of kicked-particles which move on a line is developed, which takes care of the two above mentioned systematic differences. In particular, we include in our theory the effect of decoherence on the quantum resonant motion of δ -kicked particles. The decoherence is introduced in a controlled way in the experiments by allow-

ing the atoms to emit spontaneously during the time evolution, and hence to randomly change their centre-of-mass momentum. Several experimental observations at quantum resonance conditions [81–83, 135] which do not match with the standard theory of the δ -kicked rotor will be clarified by taking care of the above stated differences between ideal rotors and their experimental counterparts.

Both parts of the thesis are devoted to the investigation of quantum transport for systems with a complex time evolution. Quantum chaos theory [7–10, 17] is concerned with quantitative measures for the complexity of quantum dynamics. For instance, the classical definition of chaos in dynamical systems – the extreme sensitivity to the choice of initial conditions in phase space, characterised by an exponential divergence of phase space trajectories that were initially in close proximity – is not operable for a quantum system. In a bound quantum problem, unitarity guarantees that the overlap of two wave packets remains constant for all times. Since the notion of trajectories is meaningless in the quantum world [136], the sensitivity cannot be characterised by an exponential divergence [43–45], having in mind the finite resolution given by the uncertainty principle, in other words by the Planck constant. However, one may substitute “sensitivity to initial conditions” by “sensitivity to changes in the Hamiltonian”, an idea which goes back to the early days of quantum chaos [137, 138]. Instead of comparing two trajectories which start in close proximity in phase space, one may compare the time evolution of identical initial states which are propagated by slightly different Hamiltonians. A measure for the sensitivity of quantum dynamics is then the overlap of two such states [138–140]. This overlap is dubbed “quantum fidelity” (see e.g. [141] and references therein), and it can in principle be accessed experimentally for the δ -kicked particle evolution [142, 143]. How the fidelity behaves when quantum resonance conditions are met for an experimental ensemble of kicked atoms will be addressed after the tools to handle the kicked atoms’ dynamics have been developed.

The wish of a deeper understanding of the two time-dependent quantum transport problems introduced in this section is the central motivation for the following two parts of this thesis. While the first part closely links the solid-state concept of Anderson localisation to the decay properties of microwave-driven hydrogen Rydberg states, the second part reconciles experimental observations with the here developed theory for δ -kicked atoms at quantum resonance.

1.3 Outline of the thesis

Chapter 2 preludes with the necessary prerequisites for the theoretical description of periodically driven atoms. The experimental realisation of the δ -kicked rotor and its relevant features for the observation of the quantum resonances are outlined.

Part I

In **Chapter 3** the statistical distributions of the decay rates of periodically driven Rydberg atoms are presented and analysed. Their implications on the time-decay of the survival probability of the atoms are emphasised. The chapter concludes with a discussion of possible experimental tests of the analogy between transport in driven Rydberg atoms and disordered solid states.

Part II

In **chapter 4** analytical formulas for the experimental observables at quantum-resonance conditions are confronted with experimental and numerical data. While section 4.2 restricts to the absence of noise, section 4.3 presents an analytic theory for the stochastic dynamics, where external noise is modelled according to the effects of spontaneous emission.

In **chapter 5** we derive a scaling law in absence and in presence of decoherence (sections 5.2 and 5.3), respectively, that describes the shape of the resonance peaks observed in the mean energy of an atomic ensemble. The derivation is based on a quasi-classical approximation (of the quantum evolution) which was introduced in [144, 145].

Chapter 6 applies the machinery derived in the previous two chapters to the study of quantum fidelity, i.e. the overlap of two initially identical but distinctly evolved quantum states. Results at quantum-resonance conditions are presented, together with preliminary investigations of the time decay of fidelity at small detunings from quantum resonance.

Chapter 7 concludes the thesis with a brief summary of the obtained results and some comments on the direction of future investigations concerning quantum transport in periodically driven systems.

The appendices contain mathematical facts and formulas used in the second part; apart from the last one which collects the author's publications on the topics discussed in this thesis.

Chapter 2

Theoretical and experimental preliminaries

In this chapter we lay the foundations for the presentation and discussions of the central results of this thesis. The atomic systems which we will study in more detail in the following chapters are introduced. We define the basic notations and give the necessary theoretical background. In particular, the differences between kicked atoms in experiments and the abstract δ -kicked rotor model, including relevant experimental imperfections, are discussed.

2.1 Periodicity in time, position, and momentum

Verily I say unto thee. That this night, before the cock crow, thou shalt deny me thrice.

Mt 26,34

2.1.1 Floquet theory

In the subsequent chapters, quantum transport in energy or momentum space is analysed for two open, non-autonomous systems. Both of these systems are subject to a time-periodic external driving force. This particular time dependence allows one to reduce the problems to stationary eigenvalue problems in an extended Hilbert space. More precisely, the Floquet theorem [146–149] guarantees the following: for a time periodic Hamiltonian $\hat{H}(t + T) = \hat{H}(t)$, with

period T , we can write any solution of the Schrödinger equation in the form

$$|\psi(t)\rangle = \sum_{\epsilon} c_{\epsilon} e^{-i\epsilon t} |\epsilon(t)\rangle, \quad (2.1)$$

with $|\epsilon(t)\rangle = |\epsilon(t+T)\rangle,$

where $c_{\epsilon} \in \mathbb{C}$ are time-independent expansion coefficients. The generalised eigenstates $|\epsilon(t)\rangle$ and the corresponding eigenvalues ϵ (the “quasi-energies”) solve the stationary eigenvalue problem

$$\hat{\mathcal{H}}|\epsilon(t)\rangle = \epsilon|\epsilon(t)\rangle \quad (2.2)$$

for $\hat{\mathcal{H}} \equiv \hat{H}(t) - i\partial_t$. $\hat{\mathcal{H}}$ acts in the extended Hilbert space of square-integrable, time-periodic functions $\mathcal{L}_H^2 \otimes \mathcal{L}^2(\mathbb{T}_{\omega})$, where $\mathbb{T}_{\omega} \equiv \mathbb{R}/T\mathbb{Z}$ is the unit circle [150]. The spectrum of the Floquet Hamiltonian $\hat{\mathcal{H}}$ is periodic in energy with period $\omega = 2\pi/T$. Therefore, one may restrict to a single Floquet zone of width $\hbar\omega$ in energy when calculating the quasi-energies ϵ . This is of great use for the diagonalisation of the Floquet problem of microwave-driven Rydberg states (see section 2.4.1 below). For the latter atomic system, the time-periodic eigenstates $|\epsilon(t)\rangle$ are expanded in a Fourier series

$$|\epsilon(t)\rangle = \sum_{m=-\infty}^{\infty} e^{-im\omega t} |\epsilon_m\rangle, \quad (2.3)$$

with time-independent components $|\epsilon_m\rangle$. This expansion allows us to recast the corresponding eigenvalue problem into a time-independent one, with the prize to pay that the matrix dimension is given by the product of the “usual” eigenbasis expansion and the dimension of the Fourier space. In theory, one has to deal with an infinite dimensional matrix. In practice, it can be suitably reduced to finite size, which must be sufficiently large to guarantee numerical convergence [95, 108, 113].

Since the Floquet states $|\epsilon(t)\rangle$ form an orthogonal basis at any time t , the time evolution operator can be expanded in the periodic basis functions [151]

$$\hat{U}(t_2, t_1) = \sum_{\epsilon} e^{-\frac{i}{\hbar}\epsilon(t_2-t_1)} |\epsilon(t_2)\rangle \langle \epsilon(t_1)| \quad (t_1, t_2 \in \mathbb{R}). \quad (2.4)$$

In particular, the periodicity carries over to the evolution operator: $\hat{U}(t_2 + T, t_1 + T) = \hat{U}(t_2, t_1)$, or $\hat{U}(t + mT, t) = \hat{U}(t, t)^m$, for any integer m [152]. The latter relation for \hat{U} is essential for the analytical and numerical treatment of the δ -kicked rotor problem. It means that the time evolution is reduced to a sequential application of the “Floquet operator” $\hat{\mathcal{U}} \equiv \hat{U}(t + T, t)$ to the initial state of the rotor.

2.1.2 Bloch theory in position space

In the experimental realisation of the δ -kicked rotor (see section 2.3), atoms move in a one-dimensional periodic potential in position space. Alike the Floquet theorem in the time domain, the Bloch theorem [153, 154] allows one to

reduce the problem to functions which are periodic in position. Explicitly, for $\hat{H}(x, p) = \hat{H}(x + a, p)$, we write any solution of the Schrödinger equation as a superposition of Bloch states $\exp(i\beta x)\psi_\beta(x)$:

$$\psi(x) = \int_{\beta} d\beta e^{i\beta x} \psi_\beta(x),$$

with $\psi_\beta(x + a) = \psi_\beta(x)$. (2.5)

β is an arbitrary index which can be taken in $[0, 2\pi/a)$, because of $\psi(x + a) = \exp(i\beta a)\psi(x)$ and the periodicity of the phase $\exp(i\beta a)$. The periodic Hamiltonian $\hat{H}(x, p) = \hat{H}(x + a, p)$ only couples eigenstates of the momentum operator with eigenvalues separated by integer multiples of $2\pi/a$. For fixed β , such states form a momentum ladder with $p = \beta + 2\pi m/a$ ($m \in \mathbb{Z}$) and constant spacings $2\pi/a$. Expressing p in units of $2\pi/a$, the fractional part of momentum therefore equals the “quasi-momentum” $\beta = p \bmod(2\pi/a)$. For a free particle with unit mass, the solution of the Schrödinger equation is a plane wave with wave vector k_w , and the eigenenergies follow the dispersion relation $E(k_w) = \hbar^2 k_w^2 / 2$. The Bloch theory guarantees that generic* x -periodic potentials lead to similar extended solutions with a continuous dependence of the energies on momentum. The precise form of the dispersion relation is determined by the potential. The Bloch-state solutions (2.5) allow one to restrict the problem to a single Brillouin zone of widths $2\pi/a$ in momentum, and the corresponding reduced zone scheme leads to the definition of continuous energy bands [153–155].

In section 2.2.3, we will expand the solutions of the δ -kicked problem in Bloch waves of the form (2.5). In the peculiar case of the quantum resonances, yet another periodicity occurs, now in momentum space – besides the periodicity in time (Floquet theorem) and in position space (Bloch theorem). Then the momentum eigenstates of the Floquet operator are extended in momentum space. Details will be explained below, after the δ -kicked rotor has been introduced.

2.2 The δ -kicked rotor

2.2.1 The model

In the sequel, we refer to the δ -kicked rotor as the quantum analogue of the famous Standard Map [43, 156] (also known as Chirikov-Taylor Map). The Standard Map is a two-dimensional (in phase space) Hamiltonian toy model which became important because of its simplicity and the possibility to use it as a local approximation of more complicated systems [43, 59, 156]. It provides a wide range of regular and chaotic types of behaviour which made it a natural

*Exceptional cases are, e.g. an infinite chain of potential wells of finite widths and infinite height; then no tunnelling coupling between neighbouring sites is allowed. Or the so-called anti-resonance of the δ -kicked rotor with infinitely degenerate eigenvalues, i.e. with an energy band of zero width [64].

subject of investigation when studying the quantum-classical correspondence [6, 63, 106]. The Standard Map reads in dimensionless action-angle coordinates [43]

$$p_{j+1} = p_j + k' \sin(\theta_{j+1}) \quad (2.6)$$

$$\theta_{j+1} = \theta_j + \tau' p_j \pmod{2\pi}, \quad (2.7)$$

with the kicking strength k' , the kicking period τ' , and p_j, θ_j the angular momentum and rotation angle just before the $(j+1)$ th kick[†]. The motion described by the map may be viewed as a free evolution in-between the integer times $t = j$ and $t = j + 1$ (equation (2.7)) followed by a momentum shift (kick) occurring at $t = j + 1$ (equation (2.6)). The Standard Map can be quantised [6] (with some freedom in the order of free evolution and kick [64]) and the state evolution from one kick to immediately after the next kick is determined by the unitary Floquet operator [6, 63, 64]

$$\hat{\mathcal{U}} = e^{-\frac{i}{\hbar} k' \cos(\hat{\theta})} e^{-i\tau' \hbar \hat{P}^2 / 2}. \quad (2.8)$$

$\hat{\mathcal{U}}$ describes a free evolution given by $e^{-i\tau' \hbar \hat{P}^2 / 2}$, followed by the kick operator $e^{-\frac{i}{\hbar} k' \cos(\hat{\theta})}$. The time-dependent Hamiltonian of the quantum δ -kicked rotor may be written as

$$\hat{H}(t') = \frac{\hbar^2 \hat{P}^2}{2} + k' \cos(\hat{\theta}) \sum_{m=-\infty}^{+\infty} \delta(t' - m\tau'), \quad (2.9)$$

where $\hat{\theta}, \hat{P}$ are the angle and the angular momentum operator, respectively. After introducing the rescaled variables $k \equiv k'/\hbar$ and $\tau \equiv \hbar\tau', t \equiv \hbar t'$, the Hamiltonian divided by \hbar^2 reads

$$\hat{H}(t) = \frac{\hat{P}^2}{2} + k \cos(\hat{\theta}) \sum_{m=-\infty}^{+\infty} \delta(t - m\tau). \quad (2.10)$$

Both parameters k and τ are necessary in the quantum version of the rotor. The semiclassical limit corresponds to $k \rightarrow \infty, \tau \rightarrow 0$, for fixed classical stochasticity parameter $K = k\tau = \text{const.}$ [63, 64, 80]. The latter constraint expresses that the classical dynamics is unchanged, while $\hbar \rightarrow 0$. The δ function in (2.9-2.10) makes $\hat{P}^2/2$ negligible at the kick, and thus ensures that the free evolution and the kicking part factorise in the Floquet operator (2.8). The iterated application of $\hat{\mathcal{U}}$ yields the dynamics of the rotor in the discrete time given by the kick counter $m \in \mathbb{Z}$. We denote $|\psi\rangle$ the state vector of the rotor, and $\psi(\theta) = \langle \theta | \psi \rangle$, $\bar{\psi}(p) = \langle p | \psi \rangle$ the wave functions in the angle and in the momentum representation, respectively. The δ -kicked rotor describes a free quantum pendulum which is kicked periodically with an angle dependent strength $k \cos \theta$, c.f. figure 1.3. Since the rotor moves on a circle, the periodic boundary condition $\psi(\theta + 2\pi) = \psi(\theta)$ enforces that only integer angular momenta $p = n \in \mathbb{Z}$ are allowed.

[†]The map may be rescaled such that it only depends on the stochasticity parameter $K = k'\tau'$, however, this scaling does not carry over to the quantised map.

2.2.2 Quantum resonances

For the δ -kicked rotor model, the evolution operator is naturally decomposed in a free motion plus an instantaneous application of a kick, and the system evolves freely over the kicking period with phases that are identical to the unperturbed eigenenergies $n^2/2$ ($n \in \mathbb{Z}$). If the timing is such that after one period (for the fundamental resonances $\tau = 4\pi\ell$, ℓ a positive integer) the time evolution shows an exact revival without phase mismatch, then $\exp(-i\tau n^2/2) = 1$ for all $n \in \mathbb{Z}$. Hence, at these “quantum resonances”, the application of m kicks with a strength k is equivalent to the application of one single kick with strength mk . If we deal with kicked particles which move along a straight line, not like a rotor on a circle, then the momentum p may take any value in \mathbb{R} . We can split $p = n + \beta$ in an integer part $[p] = n \in \mathbb{Z}$, and a fractional part $\{p\} = \beta \in [0, 1)$. The free evolution part of the Floquet operator then reads

$$e^{-i\frac{\tau}{2}(n+\beta)^2} = e^{-i\frac{\tau}{2}(n^2+2n\beta+\beta^2)}. \quad (2.11)$$

The phase $\exp(-i\tau\beta^2/2)$ is independent of n , and therefore always cancels when computing quantum expectations. We neglect it in the following. The kick operator can be expanded in the momentum basis [157]:

$$e^{-ik\cos(\hat{\theta})} = \sum_{n=-\infty}^{\infty} (-i)^n J_n(k) e^{in\hat{\theta}}, \quad (2.12)$$

where J_n is the Bessel function of first kind and order n [157]. Thus, the kick does not depend on the fractional part β , which, in fact, is a constant of motion. For $\tau = 2\pi\ell$ ($\ell \in \mathbb{N}$),

$$e^{-i\frac{\tau}{2}(n^2+2n\beta)} = 1, \quad (2.13)$$

if $\beta = 0$ (usual rotor with periodic boundary conditions) and $\ell = 2$, or in general, if $\beta = 1/2 + j/\ell \pmod{1}$, with $j = 0, 1, \dots, \ell-1$. The additional, “adjustable” parameter β allows one to obtain the above mentioned conditions for the fundamental quantum resonances for all kicking periods $\tau = 2\pi\ell$. These are the values at which quantum resonances have been observed in experiments [81–83, 135], and which we will study in detail in the second part of this thesis. Using a plane wave $\psi(0, \theta) = \exp(-in_0\theta)/\sqrt{2\pi}$ ($n_0 \in \mathbb{Z}$) as initial state, it is easily derived that the rotor wave packet spreads ballistically if (2.13) is fulfilled, i.e. the mean value of its energy grows quadratically in time. The rotor’s energy is computed [6]:

$$\begin{aligned} E(t) &\equiv \langle \psi(t, \theta) | -\frac{1}{2} \frac{\partial^2}{\partial \theta^2} | \psi(t, \theta) \rangle = -\frac{1}{4\pi} \int_0^{2\pi} d\theta \psi^*(t, \theta) \frac{\partial^2}{\partial \theta^2} \psi(t, \theta) \\ &= \frac{k^2 t^2}{4} + \frac{n_0^2}{2}, \end{aligned} \quad (2.14)$$

with $\psi(t, \theta) = \exp(-ikt\cos(\theta)) \psi(0, \theta)$ from (2.8) and (2.13). Other choices of the initial state may lead to additional terms growing linearly in time t , which is to be understood here as an *integer* that counts the number of kicks. Moreover,

if the free part of the Floquet operator equals the identity, we immediately see that the quasi-energy spectrum (see section 2.1.1) is continuous. It is given by $\epsilon(\theta) = k \cos(\theta)$. This follows from

$$\hat{U} = e^{-ik \cos(\hat{\theta})} \equiv e^{-i\epsilon(\theta)}, \quad (2.15)$$

where all values $\epsilon(\theta)$ are allowed quasi-energies. For $k \geq 1$, the eigenvalues of \hat{U} cover the whole unit circle in the complex plane. The continuous spectrum originates from a translational invariance of \hat{U} in momentum space. To make this clearer, we recall that the δ -kicked rotor problem can be mapped onto a one-dimensional tight-binding model of the form [61–63, 80]:

$$(W_0 + T_m) u_m + \sum_{r \neq 0} W_{m-r} u_r = 0. \quad (2.16)$$

u_m ($m \in \mathbb{Z}$) are the Fourier coefficients of $1/2[\psi^+(\theta, t) + \psi^-(\theta, t)] = 1/2[1 + \exp(ik \cos(\theta))]\psi^-(\theta, t)$, where ψ^\mp are the time-periodic Floquet states just before and after the δ -kick. We denoted the on-site potential $T_m = \tan(\epsilon\tau/2 - \tau m^2/4)$, and the non-diagonal (“hopping”) terms $W_r = -1/(2\pi) \int_0^{2\pi} d\theta \exp(-ir\theta) \tan(k \cos(\theta)/2)$. A detailed derivation of (2.16) may be found in the literature on quantum chaos [9, 10, 17]. For irrational $\tau/4\pi^\ddagger$, (2.16) corresponds to a one-dimensional disordered tight-binding model with pseudorandom numbers T_m [90]. Therefore, the δ -kicked rotor is mapped onto a standard Anderson problem with disorder, whereby the sites m are identified with integer angular momenta. It was confirmed numerically, that the quasi-energy eigenstates are localised around some lattice site n_j , and they decay exponentially away from that site with a characteristic localisation length ξ , i.e.

$$u_n^{(j)} \propto e^{-\frac{|n-n_j|}{\xi}}. \quad (2.17)$$

A general wave packet also decays exponentially after some initial expansion period t_{break} which is estimated to be $t_{\text{break}} \sim k^2 \sim \xi$ [64, 106, 109].

For the opposite case, $\tau/4\pi = s/q$ (s, q mutually prime integers), the on-site potentials T_m form a periodic sequence in m . Then the corresponding eigenstates of (2.16) are Bloch states of the form:

$$\begin{aligned} \bar{\psi}_{\epsilon(\theta_0)}(n) &= e^{i\theta_0 n} \bar{\psi}_{\theta_0}(n), \\ \text{with } \bar{\psi}_{\theta_0}(n+q) &= \bar{\psi}_{\theta_0}(n). \end{aligned} \quad (2.18)$$

The “quasi-positions” θ_0 can be chosen within the interval $[0, 2\pi/q)$. Therefore, the δ -kicked rotor at quantum resonance is *thrice periodic*, in time, position space, and also in momentum space.

With the phase β in (2.11), an additional constraint on β for the occurrence of quantum resonances is generally given by $\beta = m/2s$, with $0 \leq m < 2s$ an integer [64].

The higher-order quantum resonances, i.e. $q > 1$, support continuous energy

[‡]With a little caveat reported in [158]!

bands whose widths are believed to decay exponentially with increasing q [64]. Therefore, these resonances are much harder to resolve than the fundamental ones. This may be a good reason why only the resonances at $\tau = 2\pi\ell$, with $\ell = 1, 2, 3$, have been detected in experimental realisations using atoms moving on a line [81–83, 159], that is, with the additional freedom $\beta \in [0, 1)$ [145, 160].

2.2.3 Particle vs. rotor: Bloch theory for kicked atoms

Multi enim sunt vocati, pauci vero electi.

Mt 20,16

The periodic boundary conditions for the wave function enforce a discrete ladder of integer (angular) momenta for the rotor, while for a kicked atom also fractional parts of momenta are allowed. The value of these fractional parts are crucial what concerns the quantum resonances, and refined resonance conditions depending on them have been stated in the previous section.

The link between the kicked atom in the experiment, which will be described in section 2.3.2, and the idealised kicked rotor is generated by the spatial periodicity of the potential. The latter periodicity of the driving only allows for transitions (induced by (2.12)) between momenta that differ by integer multiples. Formally speaking, the Floquet operator (2.8) commutes with spatial translations by multiples of 2π , and Bloch theory (section 2.1.2) enforces conservation of quasi-momentum β , which corresponds to the fractional part of momentum p .

For a sharply defined quasi-momentum, the wave function of the particle is a Bloch wave, of the form $\exp(i\beta x)\psi_\beta(x)$, with $\psi_\beta(x)$ a 2π -periodic function. The general particle wave packet is obtained by superposing Bloch waves parametrised by the continuous variable β :

$$\psi(x) = \int_0^1 d\beta e^{i\beta x} \psi_\beta(x), \quad (2.19)$$

where we can restrict to the Bloch zone $\theta \equiv x \bmod(2\pi)$. The simple, yet important observation is now that the Fourier transform of $\psi(x)$, for fixed β , corresponds to the Fourier transform of $\psi_\beta(x)$:

$$\bar{\psi}(n + \beta) = \frac{1}{\sqrt{2\pi}} \int dx e^{-inx} e^{-i\beta x} \psi(x) = \bar{\psi}_\beta(n). \quad (2.20)$$

With (2.20) we have in turn

$$\psi_\beta(\theta) = \frac{1}{\sqrt{2\pi}} \sum_n \bar{\psi}(n + \beta) e^{in\theta} = \frac{1}{\sqrt{2\pi}} \sum_n \bar{\psi}_\beta(n) e^{in\theta}, \quad (2.21)$$

which is the Fourier series of the 2π -periodic function $\psi_\beta(\theta)$. For modelling an experimental initial atomic ensemble, we will later use the special case when the initial state of the particle is a plane wave with momentum $p_0 = n_0 + \beta_0$, where $\beta_0 = \{p_0\}$ and $n_0 = [p_0]$ are the fractional and integer part of p_0 , respectively, i.e. $\overline{\psi}(p) = \delta(\beta - \beta_0)\delta_{n,n_0}$. The wave function in this case reads

$$\psi_\beta(\theta) = \frac{1}{\sqrt{2\pi}}\delta(\beta - \beta_0)e^{in_0\theta}. \quad (2.22)$$

For any given β , $\psi_\beta(\theta)$ may be thought of as the wave function of a rotor with angular coordinate θ , henceforth baptised β -rotor. We denote the corresponding state of the rotor by $|\psi_\beta\rangle$. From (2.8) and (2.21), it follows that $|\psi_\beta\rangle$ evolves into $\hat{U}_\beta|\psi_\beta\rangle$, with the Floquet operator

$$\hat{U}_\beta = e^{-ik\cos(\hat{\theta})} e^{-i\frac{\tau}{2}(\hat{N}+\beta)^2}, \quad (2.23)$$

where \hat{N} is the angular momentum operator, in the θ -representation: $\hat{N} = -id/d\theta$, acting on the Hilbert space of wave functions with periodic boundary conditions in θ . The Floquet operator (2.23) differs from the Floquet operator of the standard δ -kicked rotor [6, 63, 64, 80, 106] by the additional phase β . This phase may be regarded as an external Aharonov-Bohm flux threading the rotor [161], which, for instance, induces strong fluctuations when studying the parametric dependence of survival probabilities [162–164].

The difference between rotors' and a particles' dynamics owing to the presence of a continuum of quasi-momenta is indeed crucial for the observation of quantum resonances in experiments as well as in numerical simulations. Nearly all quasi-momenta involved in a particle's wave packet (2.19) do not show resonant motion, as long as the initial momentum distribution is not prepared in very specific, narrow ranges of quasi-momenta [145, 160]. As stated in section 2.2.2, the occurrence of quantum resonances at $\tau = 2\pi\ell$ ($\ell \in \mathbb{N}$) requires also that $\beta = 1/2 + j/\ell \bmod(1)$, with $j = 0, 1, \dots, \ell - 1$. Only if both conditions on τ and β are fulfilled, the Floquet operator commutes with translations in momentum space by multiples of $q = 1, 2$, respectively. Note that even if $\tau = 2\pi\ell$ ($\ell \in \mathbb{N}$), the number of resonantly driven β -rotors is a set of measure zero in the continuum $[0, 1)$. Therefore, only a tiny fraction of atoms from the initial Gaussian momentum distributions in the experiments reported in [81–83, 159] does obey the second condition on β .

2.3 Experimental realisation of the kicked rotor model

2.3.1 Experimental setup

The quantum system studied in the laboratory to implement the kicked rotor dynamics is a dilute ensemble of laser-cooled alkali atoms (sodium, caesium). Following release from an atomic (magneto-optical) trap [121, 122, 165]

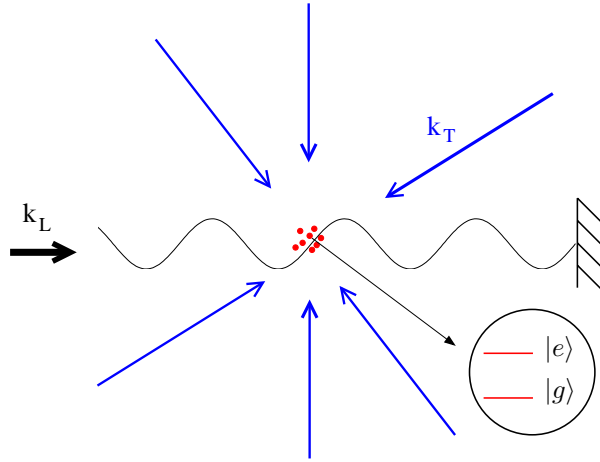


Fig. 2.1: Sketch of the experimental setup used to impart momentum by a standing wave (k_L) on laser cooled atoms (dots); the zoomed view shows the internal two level structure of the atoms with ground state $|g\rangle$ and excited state $|e\rangle$. The cooling beams (k_T) may also be applied to induce spontaneous emission (see section 2.3.3).

these atoms (typically $\sim 10^6$ [15, 83, 166]) are exposed to a spatially periodic potential applied by a standing wave of laser light. To create the standing wave, the output of a tunable laser is retro-reflected by a mirror and the two resulting beams are aligned so as to counter-propagate. Figure 2.1 sketches the experimental setup. The beam intensity is controlled by a switch (in practice an acousto-optical modulator [167]) that allows the beam to be pulsed. This provides a pulsed, spatially periodic potential. Crucial for experiments with long interaction times with the standing wave is that the atoms are “cold” coming from a trapped and cooled dilute ensemble with a small initial spread in momentum. Following application of the standing wave, the atoms are allowed to expand freely. Then their spatial distribution is measured, and knowing the time of free expansion the atoms’ momentum distribution (immediately after the application of the standing wave) can be calculated [135].

The dynamics of a system subject to a time-varying potential, as provided by the pulsed standing wave, approximates that of the δ -kicked rotor. An initial Maxwell-Boltzmann, i.e. Gaussian, distribution of atomic momenta becomes exponential in form for $\tau/4\pi$ irrational, and $k > 1$. The exponential distribution sets in after an interaction time t larger than the “break time” t_{break} (the time at which the quantum nature of the system begins to manifest). This led to the first direct observation of dynamical localisation [54, 168, 169]. From the momentum distributions measured in the experiments one can immediately calculate the average kinetic energy of the atoms as function of the number of applied pulses. In the regime of dynamical localisation, the energy does not show a linear growth with the number of pulses as predicted by a classical diffusion argument [63, 156], it rather saturates after the break time. In particular, in these cold atom experiments momentum distributions and mean energies can be resolved experimentally for very short times up to the break time t_{break} , and

thus in the transition regime when dynamical localisation starts to manifest. Hence, the experimentally observed behaviour demonstrates the quantum suppression of classical diffusion more directly than in experiments with driven Rydberg atoms. There, the only accessible signal is the ionisation yield of the atoms, and short-time observations are limited by the signal-to-noise ratio, and the finite switching time of the microwave field [11, 53].

To allow for a better comparison with experimental literature, we use laboratory units in the subsequent section. There we will show that, under suitable conditions, it is possible to ignore the internal electronic structure of the atoms, and treat them as point particles [170]. The “reduced” atomic dynamics is induced by an effective centre-of-mass Hamiltonian, which in laboratory units reads

$$\hat{H}(t) = \frac{\hat{P}^2}{2M} + V_0 \cos(2k_L \hat{X}) f(t, T_p). \quad (2.24)$$

M denotes the atomic mass, k_L the wave number of the kicking laser, V_0 the potential amplitude (proportional to the laser intensity), and $f(t, T_p)$ its modulation. In a *restricted* momentum region, indeed a periodic δ -like time-dependence can be mimicked $f(t, T_p) \simeq \sum_{l=-\infty}^{+\infty} \delta(t - lT_p)$, with the kicking period T_p . Hence, (2.24) governs the dynamics of a δ -kicked particle. To arrive at the form of the Hamiltonian (2.10) we have to rescale momentum in units of $2\hbar k_L$, position in units of $(2k_L)^{-1}$, mass in units of M . Energy is then given in units of $(2\hbar k_L)^2/M$, time in units of $M/\hbar(2k_L)^2$, and the reduced Planck constant equals unity. In particular we obtain for the kicking period $\tau = \hbar T_p (2k_L)^2/M$, and for the kicking strength $k = V_0 T_{\text{dur}}$, where T_{dur} is the finite width in time of individual pulses. This procedure leads to the Hamiltonian (2.10) with the slight, but crucial difference that \hat{X} is an unbounded operator and its eigenvalues are not to be taken mod(2π), as the angular coordinate of the conventional δ -kicked rotor. This problem has been addressed in section 2.2.3, and it is very important for the understanding of the experiments which work with *atoms* on a line rather than with *rotors* on a circle!

2.3.2 Derivation of the effective Hamiltonian

To derive (2.24) for the experimental realisation, we essentially follow standard arguments in atom optics as provided, for instance, in [122, 135, 171], where a more detailed and contextual description may be found.

To capture the main features of the problem one usually considers a two-level atom moving in a standing wave of light:

$$\vec{E}(\hat{X}, t) = \vec{z} E_0 \cos(k_L \hat{X}) (e^{i\omega_L t} + e^{-i\omega_L t}) \equiv \vec{E}^-(\hat{X}, t) + \vec{E}^+(\hat{X}, t), \quad (2.25)$$

with the amplitude E_0 of the wave, \vec{z} the unit vector in z direction, and ω_L the laser frequency. Time t has to be understood as a continuous variable in this section. The free evolution of the atoms is determined by the Hamiltonian

$$\hat{H}_A = \frac{\hat{P}^2}{2M} + \hbar\omega_0 |e\rangle\langle e|, \quad (2.26)$$

where \hat{P} denotes the (external) centre-of-mass momentum of the atom, and $|e\rangle$ the internal excited state. ω_0 is the frequency of the atomic transition with the zero point of the internal energy chosen at the ground state level, which is denoted by $|g\rangle$, c.f. figure 2.1. The atom-field interaction and its impact on the centre-of-mass motion of the particle is derived using several approximations, called dipole, rotating-wave, and adiabatic approximation, respectively, which we briefly describe in the following.

The dipole approximation states that the field amplitude varies little over the atomic dimensions, an often used and valid assumption for atoms in the ground state and for optical wavelengths, as well as for Rydberg states in the microwave regime (see section 2.4.1). For near-resonant driving $|\omega_L - \omega_0| \ll \omega_L + \omega_0$, we may neglect fast rotating terms of the form $\exp(\pm i(\omega_L + \omega_0)t)$. This results in the atom-field interaction Hamiltonian:

$$\begin{aligned}\hat{H}_{AF} &= -\hat{d}^+ \cdot \vec{E}^+ - \hat{d}^- \cdot \vec{E}^- \\ &= \frac{\hbar\Omega}{2} (\hat{\sigma}^+ e^{-i\omega_L t} + \hat{\sigma}^- e^{i\omega_L t}) \cos(k_L \hat{X}).\end{aligned}\quad (2.27)$$

The atomic dipole operator splits up into two components $\hat{d} \equiv \hat{d}^+ + \hat{d}^- \equiv (\hat{\sigma}^+ + \hat{\sigma}^-) \langle e | \vec{d} | g \rangle$, where \vec{d} is the vectorial dipole moment, and the operator nature is carried by $\hat{\sigma}^- = |g\rangle\langle e|$ and $\hat{\sigma}^+ = |e\rangle\langle g|$. $\Omega \equiv -2\langle e | d_z | g \rangle E_0 / \hbar$ is the Rabi frequency with the dipole matrix element in z direction $\langle e | d_z | g \rangle$, and quantifies the coupling between the atom and the external laser field [172].

To simplify the equations of motion, one usually transforms to the rotating frame of the laser field by defining the atomic excited state $|\tilde{e}\rangle \equiv \exp(i\omega_L t) |e\rangle$ and the stationary field amplitudes $\tilde{E}^\pm \equiv \exp(\pm i\omega_L t) E^\pm$. Notice that $|\tilde{e}\rangle$ is also an eigenstate of the internal component of \hat{H}_A , and in the rotating frame the internal energy equals $-\hbar\Delta_L$, $\Delta_L \equiv \omega_L - \omega_0$. Therefore, we arrive at the following complete Hamiltonian including the internal and external degrees of freedom:

$$\begin{aligned}\hat{H} &= \frac{\hat{P}^2}{2M} - \hbar\Delta_L |\tilde{e}\rangle\langle\tilde{e}| - \hat{d}^+ \cdot \tilde{E}^+ - \hat{d}^- \cdot \tilde{E}^- \\ &= \frac{\hat{P}^2}{2M} - \hbar\Delta_L |\tilde{e}\rangle\langle\tilde{e}| + \frac{\hbar\Omega}{2} (\hat{\sigma}^+ + \hat{\sigma}^-) \cos(k_L \hat{X}).\end{aligned}\quad (2.28)$$

We decompose the atomic state vector $|\psi\rangle$ explicitly into a product of internal and external states, the latter describing the centre-of-mass motion of the atoms:

$$|\psi(t)\rangle = |g\rangle \otimes |\psi_g(t)\rangle + |\tilde{e}\rangle \otimes |\psi_e(t)\rangle. \quad (2.29)$$

Separating the equations of motion induced by \hat{H} into the coefficients of $|e\rangle$ and $|g\rangle$, we obtain the *coupled* pair of equations:

$$i\hbar\partial_t |\psi_e\rangle = \frac{\hat{P}^2}{2M} |\psi_e\rangle + \left(\frac{\hbar\Omega}{2} \cos(k_L \hat{X}) \right) |\psi_g\rangle - \hbar\Delta_L |\psi_e\rangle, \quad (2.30)$$

$$i\hbar\partial_t |\psi_g\rangle = \frac{\hat{P}^2}{2M} |\psi_g\rangle + \left(\frac{\hbar\Omega}{2} \cos(k_L \hat{X}) \right) |\psi_e\rangle. \quad (2.31)$$

We attempt to solve (2.30-2.31) for the centre-of-mass motion of the atom, which occurs on a much slower timescale than those of the internal motion. Therefore, for $|\Delta_L| \gg \Omega$, we may assume that the internal motion damps instantaneously, i.e. $\partial_t |\psi_e\rangle = 0$, such that the excited state probability amplitude follows adiabatically that of the ground state:

$$\left(\hbar\Delta_L - \frac{\hat{P}^2}{2M} \right) |\psi_e\rangle \stackrel{(2.30)}{\simeq} \frac{\hbar\Omega}{2} \cos(k_L \hat{X}) |\psi_g\rangle. \quad (2.32)$$

Inserting this approximation into (2.31) gives

$$i\hbar\partial_t |\psi_g\rangle \simeq \frac{\hat{P}^2}{2M} |\psi_g\rangle + \frac{\hbar\Omega^2}{4\Delta_L} \cos^2(k_L \hat{X}) |\psi_g\rangle, \quad (2.33)$$

where we neglect the centre-of-mass energy term on the left-hand side of (2.32). We already assumed that $|\Delta_L|$ is large, and, therefore, we may also suppose that $\hbar|\Delta_L| \gg |\hat{P}^2|/2M$. For $\Delta_L = -30$ GHz [82] and caesium atoms this constraint corresponds to $p/(2\hbar k_L) \ll 800$ in momentum p . Since such large momenta cannot be reached in experiments because of other reasons (see next section and [15, 83, 135, 173]), the assumption $\hbar|\Delta_L| \gg |\hat{P}^2|/2M$ is well justified. Moreover, $|\Delta_L| \ll \omega_L + \omega_0$, and the rotating wave approximation is still applicable [15, 83, 135, 173]. Then we obtain the Hamiltonian that describes the dynamics of a point particle in a sinusoidal potential:

$$\hat{H} = \frac{\hat{P}^2}{2M} + \frac{\hbar\Omega^2}{4\Delta_L} \cos^2(k_L \hat{X}) = \frac{\hat{P}^2}{2M} + \frac{\hbar\Omega^2}{8\Delta_L} \left(1 + \cos(2k_L \hat{X}) \right), \quad (2.34)$$

where the constant component in the potential can be dropped, to arrive at the final form

$$\hat{H} = \frac{\hat{P}^2}{2M} + V_0 \cos(2k_L \hat{X}), \quad \text{with } V_0 \equiv \frac{\hbar\Omega^2}{8\Delta_L}. \quad (2.35)$$

The position dependent centre-of-mass potential in (2.35) arises from the position dependent shift of the atomic energy levels by virtue of the interaction with the standing wave (ac Stark shift) [172]. From the spatially periodic structure of \hat{H} with period $\lambda_L/2 = \pi/k_L$, we obtain now a clear physical interpretation of the fact that the kicking part of the Floquet operator (2.8) couples only momenta differing by integers [64] (see sections 2.2.2 and 2.2.3). The discrete ladder structure in momentum is imposed by coherent elastic scattering of photons from the standing wave: if the atom absorbs a photon that was travelling in one direction and re-emits it into the counter-propagating mode, the atom will recoil and change its momentum by twice the photon momentum $\hbar k_L$ [§].

If the standing wave is now pulsed in the form of a regularly-spaced sequence in time with period T_p , (2.35) may provide a reasonable approximation to the ideal δ -kicked rotor dynamics induced by (2.10). To this end, the pulse width $\tau_{\text{dur}} = T_{\text{dur}}\hbar(2k_L)^2/M$ must be sufficiently short such that the distance travelled by an atom over T_{dur} is small compared with the spatial period of the standing wave $\lambda_L/2$, i.e. $T_{\text{dur}} \leq \lambda_L M/(2p)$, with the atomic momentum p .

[§]The exchanged momentum must be in either direction of the two counter-propagating waves because of energy and momentum conservation.

2.3.3 Experimental imperfections

Finite pulse width

The most important experimental constraint, when one wants to mimic an idealised δ -kicked system, is given by the fact that experimental pulses used to provide the kicking potential are always of some finite width τ_{dur} in time. From the above arguments (see end of last section) it should be clear that the experimental dynamics fails to approximate ideal kicks for fixed τ_{dur} , in particular, at large atomic momenta. The experimental realisation is the better the larger the mass of the used atomic species. For this reason caesium, the heaviest stable alkali atom, is nowadays used in experiments [174]. The effect of non- δ -like pulses has been studied extensively by Raizen and co-workers in experiments as well as in numerical simulations [15, 169, 173, 174]. Together with theoretical work [175] these results show that the effective potential (kicking strength) is substantially smaller in the region of large momenta ($k_{\text{eff}} \simeq 0.75k_{\text{max}}$ at $p/(2\hbar k_L) = \pm 80$ as compared to the centre $n = 0$, for $T_{\text{dur}} \simeq 300$ nsec [173]). Physically, if the atom is too fast it will start to average over the potential leading to smaller coupling, or, more precisely, the applied pulse (with a certain shape in time) enforces a window function in momentum space depending on the exact pulse shape. For large momenta this effect induces classical and quantum localisation [174–176]. In this region beyond some momentum value n_{ref} , the classical phase space is filled by impenetrable barriers (tori), which survive small perturbations according to the Kolmogorov-Arnold-Moser (KAM) theorem [43–45, 177]. For smooth pulses, the momentum n_{ref} is inversely proportional to the duration of the pulse τ_{dur} , with a pre-factor which depends on the shape of the pulse [175]. Assuming a square pulse shape we obtain, for instance, $k_{\text{eff}} \simeq 2k_{\text{max}} \sin(n\tau_{\text{dur}}/2)/(n\tau_{\text{dur}})$ [169, 173, 178], the window function being the Fourier transform of the pulse.

Other problems

There are many more experimental difficulties which are faced when an idealised one-dimensional δ -kicked particle dynamics [171, 173] should be simulated. For our purposes relevant problems are addressed briefly in the following.

A severe systematic restriction, connected to the discussion of the finite pulse width, originates from the experimental determination of the atoms' momentum distribution. The latter is obtained by counting particles in some relatively small momentum interval centred around $p = 0$. Especially in the wings of the momentum distribution, the signal is weak, calling for an experimental threshold which decides whether to reject the counts or not. Practically two thresholds are applied: i) momenta are only counted in some fixed window, and ii) a “dark count” threshold that discriminates the signal from background noise. For the kicked-rotor experiments reported in [82, 83], the effective mo-

mentum window was chosen $-40 < p/(2\hbar k_L) < +40$ (in most recent data $-60 < p/(2\hbar k_L) < +60$ [159]), and the value of the signal was set to zero for less than 20 counts [83, 135]. These two relevant thresholds are highlighted in figure 4.10 where experimental and theoretical momentum distributions are compared.

The atomic density ($\simeq 10^{11}$ atoms/cm³ in [173]) must be small enough to avoid considerable atom-atom collisions which would spoil the model of independent, structure-less point particles used in the derivation of the effective Hamiltonian (2.35). Based on measurements of collision cross sections for caesium [179], the collision probability is estimated in [173] as 2%/msec. Considering kicking times $t \lesssim 50 \times T_p$, with typical $T_p \simeq 20 \dots 70 \mu\text{sec}$ [81–83], this corresponds to a maximal probability of 7% that one collision occurs during the experiment. Intensity fluctuations in the laser beam producing the standing wave should be kept as small as possible to avoid what is known as amplitude noise [173, 180, 181]. Moreover, since the atoms are initially prepared in a three-dimensional momentum distribution they are not always centred at the spot of the laser. The laser itself has a transverse Gaussian profile what leads to a potential which is the weaker the farther the atoms are away from the centre of the beam. Both of these two independent effects induce a variation of the kicking strength, which is experienced by the atoms [135, 182].

In particular, when additional momentum is imparted on the atoms by allowing them to emit spontaneously in all directions, the particles may move away from the spot of the laser beam. In the experimental situations of [81–83], the transverse spreading (i.e. the deviation from the one-dimensionality of the motion) produced by SE events is smaller than the spread of the initial momentum distribution in the transverse plane to the kicking axis.

The problem of spontaneous emission is for itself worthwhile to investigate: atoms are never two-level systems what makes a treatment necessary which includes the distribution of the atomic population over various sublevels, and also the process of dissipation by spontaneous emission. In the far-detuned case, assumed when deriving the effective Hamiltonian (2.35), the probability of absorbing a photon from the standing wave and emitting it in the vacuum mode is small. A good approximation for the steady-state scattering rate as a result of spontaneous emission (SE) is obtained by $R_{sc} \simeq \gamma_{SE} |\psi_e|^2$, where γ_{SE} is the line width of the excited level with population $|\psi_e|^2$. Using (2.32), we may estimate $|\psi_e|^2 \simeq \Omega^2 / (4\Delta_L^2) \cos^2(k_L x)$ (assuming that only the ground state is significantly populated, i.e. $|\psi_g| \simeq 1$, and $\hbar|\Delta_L| \gg |\hat{P}^2|/2M$ as used above). This leads to $R_{sc} \simeq \gamma_{SE} \Omega^2 / (8\Delta_L^2) \ll 1$ for $\gamma_{SE}, \Omega \ll |\Delta_L|$ after averaging the cosine. For the experiments performed by d’Arcy and co-workers, the mean number of SE events undergone by each atom due to one far-detuned standing wave pulse is estimated to be $n_{SE} \simeq R_{sc} T_p \lesssim 2 \times 10^{-3}$ [83, 135].

Apart from the unwanted effect described above, SE, indeed, provides a controllable way of adding noise to the evolution of the atoms [82, 83, 176, 182–184]. To this end, SE is introduced most flexibly by an additional laser, which is independent of the standing wave (for instance, by the beams used to prepare and cool the atoms before the kicks are applied [82, 83], cf. figure 2.1). The

induced mean number of events can be scanned by varying the intensity (thus the Rabi frequency Ω), the interaction time or the applied detuning from the internal atomic transition [172]. The stochastic time evolution of kicked atoms in presence of SE at quantum resonance is theoretically modelled in section 4.3.2.

2.4 Quantum chaos and microwave-driven Rydberg states

2.4.1 Atomic hydrogen in a microwave field

Like the δ -kicked rotor also the second atomic system which we want to investigate is time-periodic: hydrogen Rydberg atoms exposed to a monochromatic electromagnetic field. A numerically *exact* method to treat this problem with a minimum of (irrelevant) approximations has been developed by Buchleitner and Delande [108, 112, 113, 185], and recently a refined version using large parallel supercomputers has been successfully applied to describe other non-hydrogenic one-electron Rydberg states [95–98].

The highly excited Rydberg electron moves in three-dimensional configuration space in presence of the combined potential of the nucleus and the external time-periodic field. The driving force further excites the electron and eventually may ionise it. Therefore, a complete theoretical treatment must account for the one-electron dynamics within the Coulomb potential, and the spectrum of the atom dressed by the (classical [172]) field, including the coupling to the atomic continuum. The parameter space consists of the quantum numbers of the unperturbed initial electronic state $|\phi_0\rangle = |n_0 \ell_0 m_0\rangle$, the amplitude F , the angular frequency ω of the field, and the interaction time t between atom and field. n_0 denotes the principal quantum number of the initial state, ℓ_0 and m_0 its angular momentum and the projection of the latter onto the field axis, respectively.

In this thesis, we restrict to linearly polarised microwave fields, and assume that the field is constant in space over the atomic dimensions (dipole approximation). We neglect the for our parameter values ($n_0 \gg 1, F \lesssim 1/n_0^4, \omega \simeq 1/n_0^3$) irrelevant relativistic, spin and QED effects, and further assume an infinite mass of the nucleus [108]. In atomic units, the Hamiltonian may be written in several gauges [149, 186]:

$$H = \frac{1}{2}\vec{p}^2 + V(r) + \vec{r} \cdot \vec{F} \cos(\omega t) , \quad \text{length gauge} \quad (2.36)$$

$$H = \frac{1}{2}\vec{p}^2 + V(r) - \frac{\vec{p} \cdot \vec{F}}{\omega} \sin(\omega t) , \quad \text{velocity gauge} \quad (2.37)$$

with the Coulomb potential $V(r) = -1/|\vec{r}|$. Since the spectral properties are *not* affected by the choice of gauge, we have the freedom to choose the most appropriate one for our particular purposes. The numerical calculations use,

for faster convergence, the representation in the velocity gauge [108, 187, 188]. The Floquet theorem allows one to reduce the time-dependent problem given by either of the Hamiltonians (2.36-2.37) to a stationary eigenvalue problem. Using (2.36) and (2.3), the eigenvalue problem (2.2) is recast into a coupled set of time-independent equations:

$$\left(\frac{1}{2}\hat{p}^2 + V(\hat{r}) - m\omega - \epsilon\right) |\epsilon_m\rangle = -\frac{1}{2}\hat{r} \cdot \vec{F} (|\epsilon_{m+1}\rangle + |\epsilon_{m-1}\rangle) \quad (m \in \mathbb{Z}). \quad (2.38)$$

The additional quantum number m counts the number of photons exchanged between the atom and the dressing field [149].

The tridiagonal form of (2.38) in m is reminiscent of the structure of the tight-binding model which is used to describe particle transport in condensed-matter physics [153, 154, 189]. The tight-binding description encountered below in equation (2.16) is exact for the δ -kicked rotor, whereas (2.38) still contains the momentum and position operators, and hence leads to a more complicated matrix structure [95, 113]. A tight-binding model will serve in section 3.1.3 to relate our results on the ionisation probability of the atom to predictions for Anderson-localised solids. We emphasise again, (2.38) explicitly contains the coupling between “nearest neighbour” states $|\epsilon_m\rangle$ in energy space. For vanishing field amplitude $F \rightarrow 0$, the equations decouple, and any Fourier component $|\epsilon_m\rangle$ is a solution of the Schrödinger equation with energy eigenvalue $\epsilon + m\omega$ of the dressed state. With increasing F , the external field starts to couple the different photon channels labelled by m , as depicted in figure 2.2, and we have to solve the full Floquet problem (2.38) in order to obtain the dressed states of the atom.

Since m runs from $-\infty$ to $+\infty$, the dipole term couples all bound states of the field-free Hamiltonian to the atomic continuum. The spectrum of (2.38) no longer separates into two orthogonal subspaces (discrete bound states and continuum), but all bound states turn into resonance states embedded in the atomic continuum [108, 150, 190]. The projection of a resonance state onto a *finite* volume in coordinate space decays with a finite rate Γ_ϵ . The corresponding eigenvalue problem (2.38) can then be solved only for complex quasi-energies $\epsilon = \text{Re}(\epsilon) - \Gamma_\epsilon/2$, because of the non-unitarity of the problem induced by the projection. Precisely the decay rates Γ_ϵ determine the experimentally measured ionisation yield of the driven Rydberg atom.

To extract the complex quasi-energies ϵ , we use a complex scaling transformation [150, 190–195], which allows us to separate the resonance states from the continuous part of the spectrum also for the driven atom. The method of complex scaling is perfectly suited for the present problem of (typically slowly) decaying states, which are non-square-integrable solutions of (2.38). The complex scaling transformation rotates the continuous spectrum away from the real axis into the lower half of the complex plane, and thus uncovers the resonance poles of the metastable states of the atom in the field. The energies ϵ of these resonance states do not depend on the complex rotation angle, which must be sufficiently large to really uncover all the resonance poles [150, 190, 193]. A typical spectrum is plotted in figure 3.8; it illustrates the rotated continuum, and

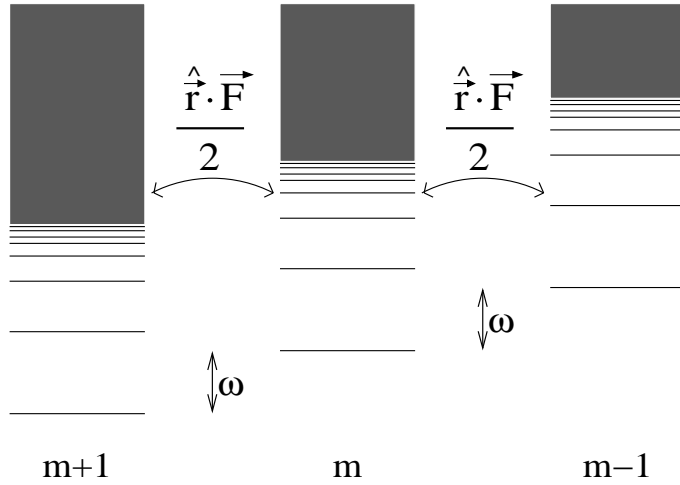


Fig. 2.2: Illustration of the tight-binding structure of equation (2.38) in the photon index m , which labels the number of “dressing” photons: The external microwave field couples the bound states of atomic hydrogen (horizontal lines) through the dipole operator \hat{r} to the atomic continuum (dark areas).

the resonances between the real axis and the continuum.

The complex dilated eigenvalue problem (2.38) is represented in a real Sturmian basis, such that a block-tridiagonal complex symmetric, sparse banded matrix [108, 113] can be diagonalised numerically. The diagonalisation supplies the quasi-energies ϵ , thus also the ionisation rates Γ_ϵ , and the associated eigenbasis of the microwave driven atom [113, 185]. Therefore we have everything at hand for the investigation of the quantum probability transport from an initially bound state $|\phi_0\rangle$ to the atomic continuum.

In section 3.1.3, we are interested in the behaviour of the survival probability of the atom in the microwave field. $P_{\text{surv}}(t)$, i.e. the probability to find the atom in a bound state after an atom-field interaction time $t = t_2 - t_1$, is given by the projection of the propagated initial state $|\phi_0\rangle = |n_0 \ell_0 m_0\rangle$ onto the subspace of all bound states $|\chi\rangle$:

$$P_{\text{surv}}(t) = \sum_{\chi} \left| \langle \chi | \hat{U}(t_2, t_1) | \phi_0 \rangle \right|^2, \quad (2.39)$$

where \hat{U} is the time-evolution operator (cf. (2.4)), generated by the Hamiltonian (2.36-2.37). $\hat{U}(t_2, t_1)$ propagates the wave function from time t_1 to time t_2 when the field interaction is switched on and off, respectively. After averaging the initial and final time t_1 and t_2 over one field cycle $T = 2\pi/\omega$, respectively, while keeping the total interaction time $t = t_2 - t_1$ fixed[¶], (2.39) can be shown to

[¶]The averaging over one field cycle physically represents a phase average for the external field, whose phase – when the atoms start or stop to interact with the microwave – is effectively averaged in state-of-the-art experiments [11, 108].

yield [108, 113]

$$P_{\text{surv}}(t) = \sum_{\epsilon} e^{-\Gamma_{\epsilon} t} w_{\epsilon} . \quad (2.40)$$

The weight factors $w_{\epsilon} \equiv \sum_m |\langle \epsilon_m | \phi_0 \rangle|^2$ are the expansion coefficients of the initial wave packet in the Floquet eigenbasis^{||}. The sum (2.40) runs over the entire spectrum within one Floquet zone of width ω in energy.

2.4.2 Quantum-classical correspondence

As mentioned in the introduction, the experimental findings by Bayfield and Koch on hydrogen Rydberg atoms [4] fostered the understanding of the classical-quantum correspondence of classically chaotic systems. In [4] a very efficient, multi-photon ionisation was reported for field intensities lower than the intensity necessary for a static electric field to ionise the atoms. As evident from figure 1.2, the threshold value $F_0(10\%) \equiv F(10\%)n_0^4$ at which 10% of the atoms ionise, can be reproduced by classical calculations for microwave frequencies less than the classical Kepler frequency, i.e. $\omega < 1/n_0^3$ [11, 94, 100]. For the range $\omega \geq 1/n_0^3$, the behaviour of $F_0(10\%)$ is best explained by dynamical localisation theory [59, 60]. The scaling used in figure 1.2 is the natural scaling of the classical Hamiltonian equations induced by (2.36-2.37). Indeed, the classical equations of motions are invariant under the transformations highlighted in table 2.1 [25, 46].

$\vec{r} \rightarrow \vec{r}/n_0^2$	$\vec{p} \rightarrow \vec{p}n_0$	$t \rightarrow t/n_0^3$
$\vec{F} \rightarrow \vec{F}_0 \equiv \vec{F}n_0^4$	$\omega \rightarrow \omega_0 \equiv \omega n_0^3$	$H \rightarrow Hn_0^2$

Tab. 2.1: Scale transformations which leave the classical Hamiltonian dynamics of periodically driven hydrogen Rydberg states unchanged. n_0 is identified with the principal quantum number of the initial atomic state.

These scaled variables are the basis for the comparison of the classical and the quantum evolution along the lines of the correspondence principle. The classical scale invariance induces an effective Planck constant $\hbar_{\text{eff}} \equiv \hbar/n_0$ through the quantum commutator relation for position and momentum operators:

$$i\hbar = [\hat{r}, \hat{p}] \rightarrow \left[\frac{\hat{r}}{n_0^2}, \hat{p}n_0 \right] = i \frac{\hbar}{n_0} . \quad (2.41)$$

^{||}The weights are actually $w_{\epsilon} = \sum_m \langle \epsilon_m | \phi_0 \rangle^2$, i.e. complex numbers without the absolute square, since the eigenstates are solutions of a complex symmetric, non-Hermitian eigenvalue problem [108, 113, 185]. Here we use a simplified notation to avoid such technical complications.

Precisely this dependence on the initial principal quantum number n_0 – which corresponds to the classical action variable – makes *highly* excited Rydberg states ideal objects for the study of the manifestations of mixed regular-chaotic *classical* dynamics in quantum mechanics. The finite \hbar_{eff} contains the information on the initial state, and the quantum system is able to resolve classical phase-space structures the better, the larger n_0 . Indeed, Floquet states mainly concentrated on either regular regions, e.g. nonlinear resonance islands, or chaotic components of the classical phase space have been identified [77, 87, 93, 100, 112, 113]; see figure 3.11 on page 47 for typical phase-space plots of one-dimensional periodically driven hydrogen.

In the following chapter, we focus on the parameter regime $\omega_0 > 1$ to search for further unambiguous signatures of dynamical/Anderson localisation in periodically driven Rydberg atoms. The phase-space localisation properties of the quantum states will turn out to be essential for the statistical analysis of the ionisation rates Γ_ϵ [116].

Part I:

Signatures of Anderson localisation in the multiphoton ionization of hydrogen Rydberg atoms

Ein historisches Kriterium für die Eigenart der Prinzipien kann auch darin bestehen, daß immer wieder in der Geschichte des philosophischen und naturwissenschaftlichen Erkennens der Versuch hervortritt, ihnen die höchste Form der „Universalität“ zuzusprechen, d.h. sie in irgendeiner Form mit dem allgemeinen Kausalsatz selbst zu identifizieren oder aus ihm unmittelbar abzuleiten. Es zeigt sich hierbei stets von neuem, daß und warum eine solche Ableitung nicht gelingen kann – aber die Tendenz zu ihr bleibt nichtsdestoweniger fortbestehen.

E. Cassierer, in [196]

Chapter 3

Driven Rydberg atoms as an open quantum system

The survival probability (2.40), and hence the thresholds for the field strength $F_0(10\%) \equiv F(10\%)n_0^4$, at which 10% of the atoms ionise owing to the interaction with the external driving (cf. figure 1.2), convolutes the spectral (global) information provided by the decay rates as well as the local information about the initial conditions (i.e. the initial state n_0). The latter is contained in the weight factors w_ϵ in (2.40). To circumvent the mixing of the global spectral properties and of the local expansion coefficients, the straightforward way to proceed is to analyse the ionisation rates Γ_ϵ of the Floquet problem. This allows us to identify unambiguous signatures of dynamical/Anderson localisation in the decay-rate distribution $\rho(\Gamma_\epsilon)$ [116].

A clear indicator for Anderson localisation in transmission problems (i.e. in open quantum systems) is indeed provided by the decay-rate distribution of states exponentially localised within the sample. The distribution of decay rates obeys a power law $\rho(\Gamma) \propto \Gamma^{-1}$ [197]. Such a law is easily derived by assuming that the rates Γ are proportional to the overlap of the corresponding states with the lattice site at the boundary. The boundary is to be identified with the lead in a solid-state transmission problem, or the atomic continuum of driven hydrogen. The tail of the wave functions determines the loss out of the sample in this simplified picture, which is sketched in figure 3.1. We assume a sufficiently large number of sites $j = 1 \dots L$, with $L \gg 1$, and uniformly distributed states along the lattice, i.e. with constant density $\rho_A(j) = 1$ in the limit $L \rightarrow \infty$. Then, if we suppose that the following relation is valid: $\Gamma_n \propto |\psi_{\Gamma_n}(j)|_{j=L}^2 \propto \exp(-2j/\xi)|_{j=L}$, we obtain

$$\rho(\Gamma_n) = \left| \frac{d\Gamma_n}{dj} \right|_{j=L}^{-1} \propto e^{\frac{2j}{\xi}} \Big|_{j=L} \left(\frac{\xi}{2} \right) \propto \frac{1}{\Gamma_n}. \quad (3.1)$$

This follows from the transformation formula for probability densities [198]. L

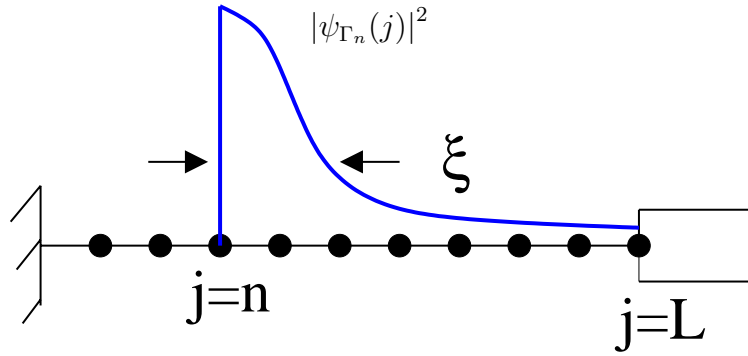


Fig. 3.1: One-lead Anderson model with exponentially decaying state, which is localised at the lattice site $j = n$. On the left we assume a perfectly reflecting wall. The open right end induces decay out of the sample, and the tail of the wave function at the boundary $j = L$ determines the loss rate $\Gamma_n \propto |\psi_{\Gamma_n}(j)|_{j=L}^2$. The localisation length ξ characterises the width of the wave function. The same model will be used in section 3.1.3 to examine the time dependence of the survival probabilities.

denotes the index of the last site at the boundary and ξ the localisation length along the lattice, over which the wave functions are exponentially localised. Using the above argument, the power law (3.1) was predicted also for dynamically localised, classically chaotic model systems [199]. For one-dimensional tight-binding models a similar behaviour $\rho(\Gamma) \propto \Gamma^{-\alpha}$ was found whereby the exponent $\alpha \simeq 1 \dots 2$ turned out to be slightly dependent on the model assumptions and on the degree of localisation [197, 200]. Very recently, the distribution of resonance widths in multiple-light scattering systems was also shown to obey a power law with $\alpha \simeq 1$ in the localised regime [201]. In the subsequent sections, the statistics of the decay-rate distribution are elucidated for the atomic ionisation problem of strongly driven hydrogen Rydberg states.

Generic (physical) Hamiltonian systems are neither completely chaotic nor integrable but show simultaneously both, chaotic and regular motion, which manifests in a mixed classical phase space. Atomic Rydberg states under microwave driving are paradigmatic real objects to investigate the quantum probability decay in presence of tunnelling and of quantum localisation phenomena (Anderson/dynamical localisation [59, 60] and semiclassical localisation in the vicinity of partial phase-space barriers [104, 105]). In addition to the good agreement with the predictions for Anderson-localised systems, our statistical analysis of the distribution of the ionisation rates makes it possible to systematically study the impact of classical phase-space structures on quantum transport in periodically driven Rydberg states.

3.1 Universal statistics of decay rates

3.1.1 Numerical results

The atomic ionisation process of Rydberg states subject to microwave radiation is mapped onto the Anderson model through the localisation parameter $\mathcal{L} = \xi/L$ [59, 60], where the localisation length ξ is measured in units of the photon energy ω . Both transport problems are sketched in figure 1.1. According to the theory of dynamical localisation [59, 60], \mathcal{L} characterises the degree of localisation. For $\mathcal{L} \ll 1$, the electronic wave packet is strongly localised on the energy axis, while for $\mathcal{L} > 1$ considerable coupling to the atomic continuum prevails. The sample length L is the ionisation potential of the initial state $|\phi_0\rangle = |n_0 \ell_0 m_0\rangle$, measured in units of ω :

$$L = \frac{1}{2\omega} \left(\frac{1}{n_0^2} - \frac{1}{n_c^2} \right). \quad (3.2)$$

n_c defines the effective ionisation threshold in the experiments [11, 13, 50] as well as in numerical calculations using a large but finite basis [108]. Provided that n_0 – identified with the principal action of the classical evolution – is chosen within the chaotic component of phase space (assuming only tiny remnants of classically regular motion immersed in the chaotic sea), L measures the extension of the domain of complex transport along the energy axis.

The mapping onto the original Anderson problem – with sample length L – implies a distribution of the decay rates $\rho(\Gamma) \propto \Gamma^{-1}$, in the statistical average over many realisations of disorder at a fixed value of $\mathcal{L} \ll 1$. In the atomic problem, statistically independent realisations of “disorder” with fixed localisation parameter \mathcal{L} are generated by simultaneously varying the field amplitude F and its frequency ω . We use the following prediction of [59, 60]

$$\mathcal{L} \simeq 6.66 F^2 n_0^2 \omega^{-\frac{7}{3}} \left(1 - \frac{n_0^2}{n_c^2} \right)^{-1} \quad (3.3)$$

from the original theory on dynamical localisation in periodically driven, one-dimensional (1D) hydrogen atoms. While this theory, which is based on several approximations, has no quantitative predictive power, it provides at least a qualitatively correct picture, in particular when statistical averages are considered. Possible corrections to (3.3) for the real three-dimensional (3D) atom are discussed in [59], but (3.3) is assumed to hold qualitatively also for quasi-1D realisations of the initial Rydberg state (so-called *extremal parabolic* states [71]). In the sequel, (3.3) is used to guide our choice of the field parameters F, ω for the statistical analysis of the atomic decay-rate distributions.

Figures 3.2-3.5 show the probability densities of the ionisation rates Γ_ϵ of a 1D hydrogen model atom exposed to a microwave field. The rates Γ_ϵ of the quasi-energies within one Floquet zone are presented. The zones are centred around the $n_0 = 40, 70, 100, 140$ Rydberg manifolds, respectively, with

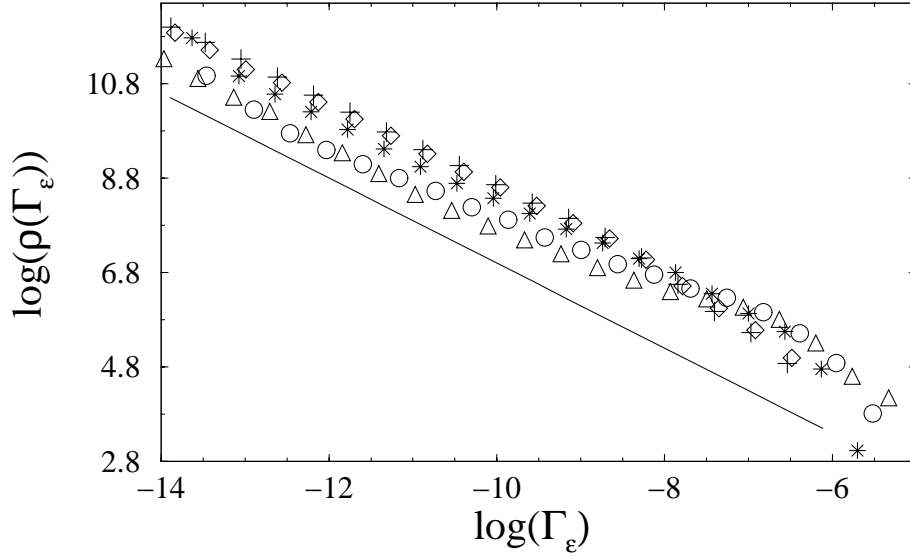


Fig. 3.2: Distribution of the ionisation rates Γ_ϵ of 1D microwave-driven Rydberg states of atomic hydrogen, for different values of the localisation parameter $\mathcal{L} = 0.2$ (plusses) $\mathcal{L} = 0.25$ (diamonds), 0.5 (stars), 1.0 (circles), and 2.0 (pyramids). The distributions were generated, at fixed \mathcal{L} , by sampling the spectra within a Floquet zone of width ω centred around $n_0 = 40$, over the frequency range $\omega_0 = \omega n_0^3 = 2.0 \dots 2.5$. In laboratory (SI) frequency units $\omega/2\pi = 205.63 \dots 257.03$ GHz, with F chosen accordingly to fix \mathcal{L} (3.3) at the given values. The solid line represents the scaling $\rho(\Gamma_\epsilon) \propto \Gamma_\epsilon^{-0.9}$.

$n_c \simeq 2n_0$. By (3.3), at fixed \mathcal{L} , each of these initial quantum numbers corresponds to a different range of field parameters F, ω . In our model, the Rydberg electron is confined to 1D configuration space $z > 0$ defined by the polarisation axis of the field, with the Coulomb singularity at the origin $z = 0$ [77, 108]. The 1D approximation allows to produce vast sets of spectral data on up-to-date workstations in a reasonable amount of calculation time. Much more computer power is needed to simulate the full realistic 3D hydrogen atom. Data for the 3D case centred around $n_0 = 70$ ($n_c = 105$, see (3.3)), and for the selected localisation parameters $\mathcal{L} = 0.25, 0.5, 1$ essentially reproduce the features of the 1D model.

The different values of $\mathcal{L} = 0.2 \dots 2$ (1D), and $\mathcal{L} = 0.25 \dots 1$ (3D) are realised by sampling the spectra over frequency ranges $\omega_0 = \omega n_0^3 = 2 \dots 2.5$ (1D), and $\omega_0 = \omega n_0^3 = 1.854 \dots 1.883$ (3D), and adjusting F accordingly. Because of the dramatically enhanced spectral density of the 3D [95] as compared to the 1D problem – a consequence of the additional angular momentum degree of freedom labelled by ℓ – only ten equidistant frequency values are needed to generate an appropriate statistical sample in the 3D case. The total number of states contributing to the distributions is approximately 25000 (3D), in contrast to up to 100000 states for 500 equidistantly chosen frequencies of the 1D model. Surprisingly enough, only about 5% of the large number of states produce the same distributions. This shows the high stability of the observed statistics. Changes occur with increasing number of sample realisations only in the region

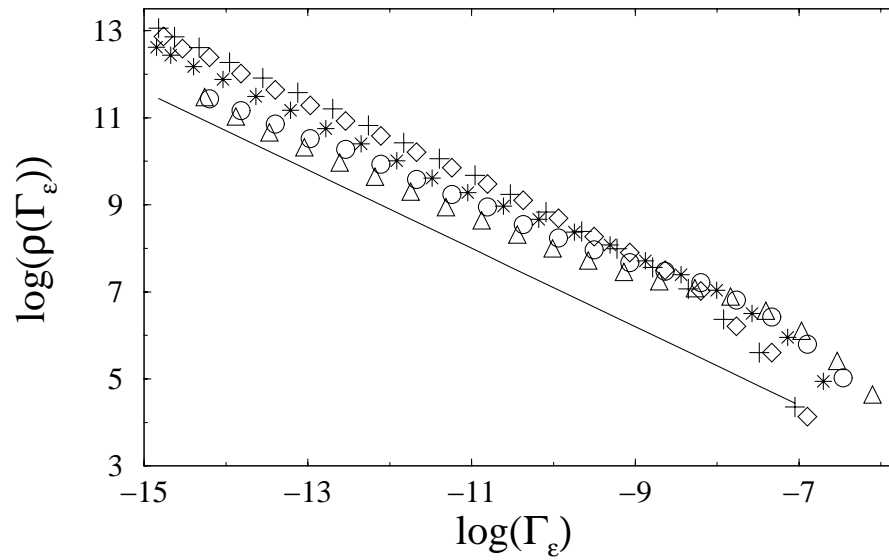


Fig. 3.3: Same as in figure 3.2 for the initial atomic state $n_0 = 70$, corresponding to the frequency range $\omega/2\pi = 38.37 \dots 47.96$ GHz in laboratory units.

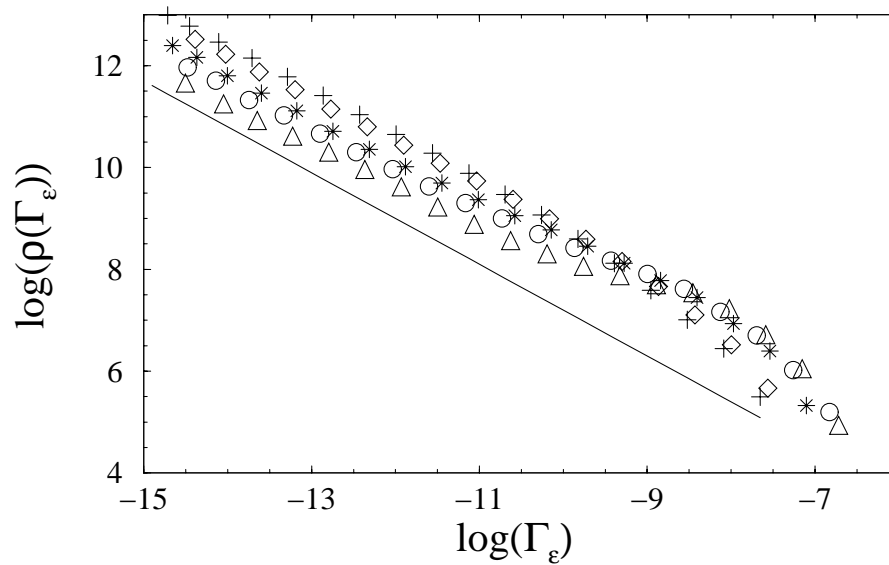


Fig. 3.4: Same as in figure 3.2 for the initial atomic state $n_0 = 100$, corresponding to the frequency range $\omega/2\pi = 13.16 \dots 16.45$ GHz in laboratory units.

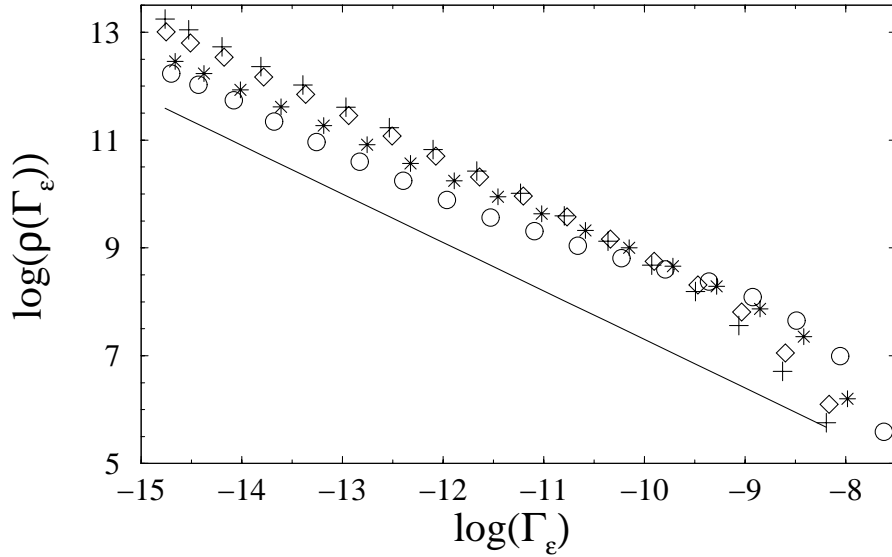


Fig. 3.5: Same as in figure 3.2 for the initial atomic state $n_0 = 140$, corresponding to the frequency range $\omega/2\pi = 4.8 \dots 6.0$ GHz in laboratory units. $\mathcal{L} = 2.0$ is not shown because of the high cost of numerical calculations at very large quantum numbers $n_0 > 100$, even in the 1D case.

of very large decay rates $\Gamma_\epsilon > 10^{-7}$ a.u. for figure 3.2, down to $\Gamma_\epsilon > 10^{-9}$ a.u. for figure 3.5, because of the few Γ_ϵ lying in these regions (for $\mathcal{L} < 1$). The robustness of the distributions (see figure 3.7) is observed either when using only few, but complete spectra (for instance, about 20 – 50 in the 1D case), or a random choice of the full list of decay rates, sampled over the entire frequency range.

Our numerical technique using a complex scaling transformation [108, 113] rotates the continuum into the lower half of the complex energy plane. Doing so, the resonance poles of the resolvent operator are uncovered. The Floquet spectrum is periodic with period ω , and for the 1D model atom the continuum threshold has a well defined position on the real energy axis. It corresponds to the ionisation potential of the initial bound state modulo ω . By rejecting resonance poles Γ_ϵ in the vicinity of the threshold, we ensured that no states from the discretised continuum entered the statistics. Figure 3.8 shows the resonance poles in the complex energy plane, together with the rotated continua. The Floquet zone of width ω contains the poles from which the $\rho(\Gamma_\epsilon)$ distribution is built up. Poles close to the thresholds are not considered.

Figure 3.8 also shows poles which are rejected because of yet another criterion which is based on the values of the overlaps w_ϵ with the initial bound state of the atom. This criterion helps to avoid continuum contributions as well, since these have tiny weights at the initial bound state with quantum number n_0 . For the decay-rate distributions in figures 3.2-3.5, the rejection criterion chosen was that the overlaps had to be larger than 10^{-5} for $\Gamma_\epsilon < 10^{-8}$ a.u., and larger than 10^{-4} for $\Gamma_\epsilon \geq 10^{-8}$ a.u. For smaller values of w_ϵ down to 10^{-8} nearly no changes in the statistics were observed, apart from the rightmost part in the

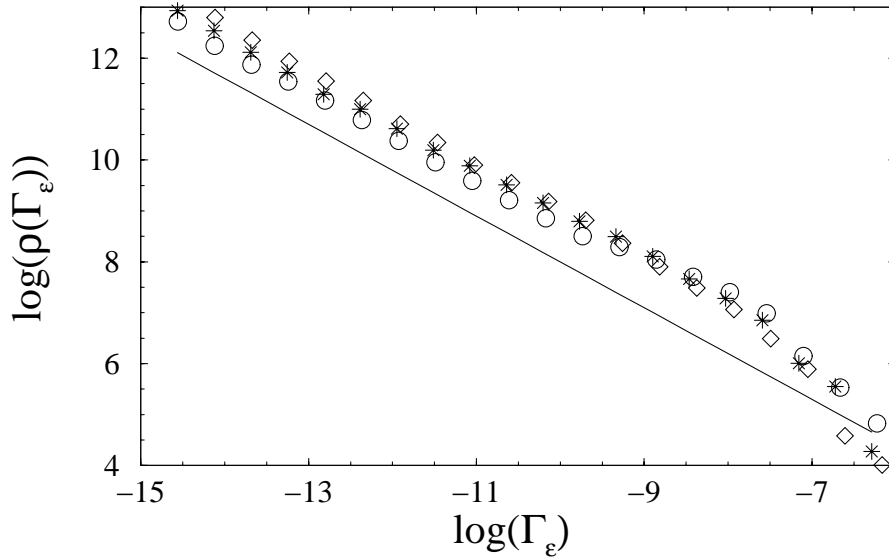


Fig. 3.6: Distribution of the ionisation rates Γ_ϵ of microwave-driven 3D Rydberg states of atomic hydrogen, with linear field polarisation along the z axis, and with angular momentum projection $m_0 = 0$ onto this axis. Localisation parameter are $\mathcal{L} = 0.25$ (diamonds), 0.5 (stars), 1.0 (circles). The distributions were generated, at fixed \mathcal{L} , by sampling the Floquet spectra over the frequency (and corresponding amplitude, F) range $\omega_0 = 1.854 \dots 1.883$, or in laboratory frequency units $\omega/2\pi = 35.5 \dots 36.1$ GHz, within a Floquet zone of width ω centred around $n_0 = 70$. The solid line represents the power-law scaling $\rho(\Gamma_\epsilon) \propto \Gamma_\epsilon^{-0.9}$. Data by courtesy of Andreas Krug [116].

distributions, where continuum states will appear if states with $w_\epsilon < 10^{-4}$ are allowed (typically the rightmost two data points corresponding to the largest rates Γ_ϵ move to the right). On the other hand, eigenstates situated in the regular and elliptic region of classical phase space, deeply below the initial state with principal quantum number n_0 , are also rejected if the overlap criterion is too restrictive. The contribution of such regular states is considerable for large localisation parameter $\mathcal{L} \geq 1$, while for small $\mathcal{L} \leq 0.25$, these states have non-resolvable ionisation rates $\Gamma_\epsilon \lesssim 10^{-15}$ a.u. Figure 3.9 illustrates the effect of states attached to regular/elliptic regions, which is discussed in more detail in the next section 3.1.2.

Since in the 3D calculations the finite numerical basis lifts the degeneracy of the states in angular momentum [113], it is more difficult to automatically exclude continuum states from the width distributions [95]. Contributions from the continuum eigenstates can, however, be excluded by the choice of the lowest allowed overlap value, similar to the procedure in the 1D case. For the distribution plotted in figure 3.6, the criterion was $w_\epsilon > 10^{-5}$. When lowering this threshold down to 10^{-10} the overall relevant structure of the distribution at small and intermediate values of Γ_ϵ is unchanged, while at $\Gamma_\epsilon \geq 10^{-7}$ a.u. new states appear very much as described above for the 1D case.

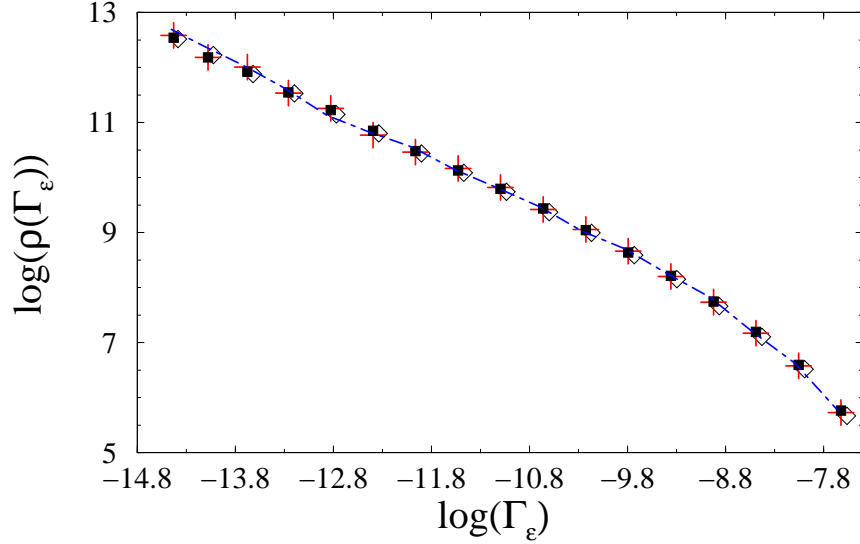


Fig. 3.7: Illustration of the statistical robustness of the ionisation-rate distribution for the data set $\mathcal{L} = 0.25$, from figure 3.4. Shown are the distributions for a random selection of decay rates of the full data set (diamonds), 5% (full squares), 10% (plusses), and for the complete spectra of the first 50 equidistant values of the frequencies $\omega_0 = 2.0 \dots 2.05$ (dash-dotted). No deviation from the full distribution is observable as long as the selected set of decay rates Γ_ϵ contains more than 3000 randomly chosen values. A similarly robust behaviour is found for all distributions plotted in figures 3.2-3.6.

3.1.2 Discussion of decay-rate distributions

The main observation in figures 3.2-3.6 is that in all cases the decay-rate distributions obey an algebraic law

$$\rho(\Gamma_\epsilon) \propto \Gamma_\epsilon^{-\alpha}, \quad (3.4)$$

with exponent $\alpha \leq 1$. For small localisation parameters, both the 1D model atom ($\mathcal{L} = 0.2, 0.25$) as well as the real atom ($\mathcal{L} = 0.25$) exhibit distributions $\rho(\Gamma_\epsilon) \propto \Gamma_\epsilon^{-0.9}$ over about six orders of magnitude, from $\Gamma_\epsilon \simeq 10^{-15}$ a.u. to $\Gamma_\epsilon \simeq 10^{-9}$ a.u. This result is in good agreement with predictions of the decay in a disordered solid, where $\rho(\Gamma) \propto \Gamma^{-\alpha}$, $\alpha \simeq 1 \dots 2$ is predicted in the parameter domain $\exp(-L/\xi) \ll \Gamma/\Delta \leq 1$, Δ being the mean level spacing [197, 200].

However, as the localisation parameter is increased by systematically increasing F over the entire frequency ranges indicated in the previous section, the situation becomes more “complex”. We observe a depletion of the probability densities of small rates, balanced by a decrease of the decay exponent of $\rho(\Gamma_\epsilon)$ in an intermediate range depending slightly on the chosen parameters, or on the chosen initial value of the principal quantum number n_0 . For $n_0 = 40$ (figure 3.2) this range is approximately $\Gamma_\epsilon \simeq 10^{-10} \dots 10^{-7}$ a.u., for $n_0 = 70 - 140$ (1D) (figures 3.3-3.5), and $n_0 = 70$ (3D) $\Gamma_\epsilon \simeq 10^{-10} \dots 10^{-8}$ a.u. (figure 3.6). Such a behaviour is incompatible with the simple assumption of exponentially

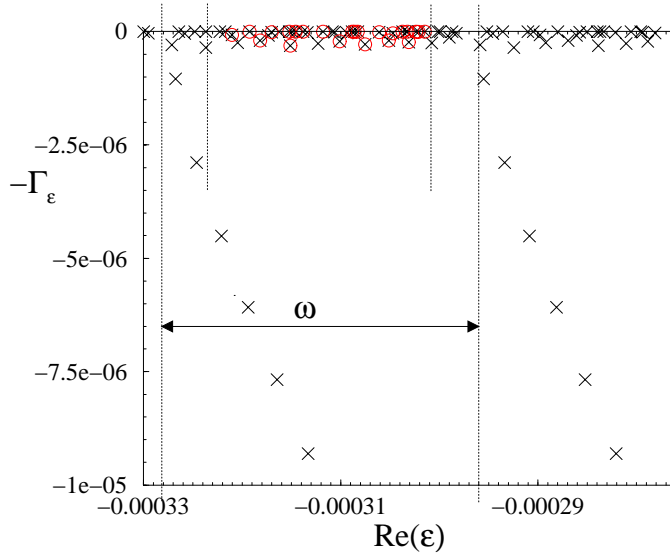


Fig. 3.8: Resonance poles of the resolvent operator for the 1D hydrogen atom. The spectrum is ω periodic, and the continua are rotated into the lower half of the complex energy plane. Crosses represent the full spectrum obtained by the numerical diagonalisation of the Floquet operator (cf. (2.2) and (2.38)), the circles are the poles used to build up the distribution $\rho(\Gamma_\epsilon)$. The regions close to the continuum thresholds (between the long and short dotted line) are not taken into account. In this way, we ensure that no continuum states enter the statistics of the decay rates. The spectrum is shown for $F = 2.0901 \times 10^{-8}$ a.u. and $\omega_0 = 2.0$ ($\omega/2\pi = 205.63$ GHz), in the vicinity of the initial state with quantum number $n_0 = 40$. It corresponds to the distribution plotted in figure 3.2 for $\mathcal{L} = 0.2$.

localised probability densities along the energy axis owing to dynamical localisation of the Floquet eigenstates over the chaotic component of classical phase space [115, 199]. For large localisation parameters $\mathcal{L} \geq 1$, a quantitative change is expected [59, 60], from a regime of localised quantum motion with very little ionisation to diffusive ionisation, similar to the classically predicted diffusion process. With increasing \mathcal{L} , dynamical localisation is gradually destroyed, and alternative transport mechanisms gain importance. Therefore, deviations from the predictions based on purely Anderson-like models do not come as a surprise. For systems with mixed regular-chaotic phase space – like the strongly driven atomic Rydberg states [11, 112–114] and mesoscopic systems [202] – it is known that the eigenstates of the corresponding quantum systems can be classified according to their localisation properties in classical phase space [102, 112, 113, 202–205]. While dynamical localisation occurs for states situated in the chaotic domain of phase space (i), eigenstates can be localised also (ii) on regular or/and elliptic regions, and (iii) along remnants of regular motion immersed in the chaotic sea. In particular, elliptic regions as well as the nearly integrable component are rather robust under changes of some control parameter, such as the field strength in our system [112, 113]. Accordingly, the localisation properties and the decay rates of the associated eigenstates tend to

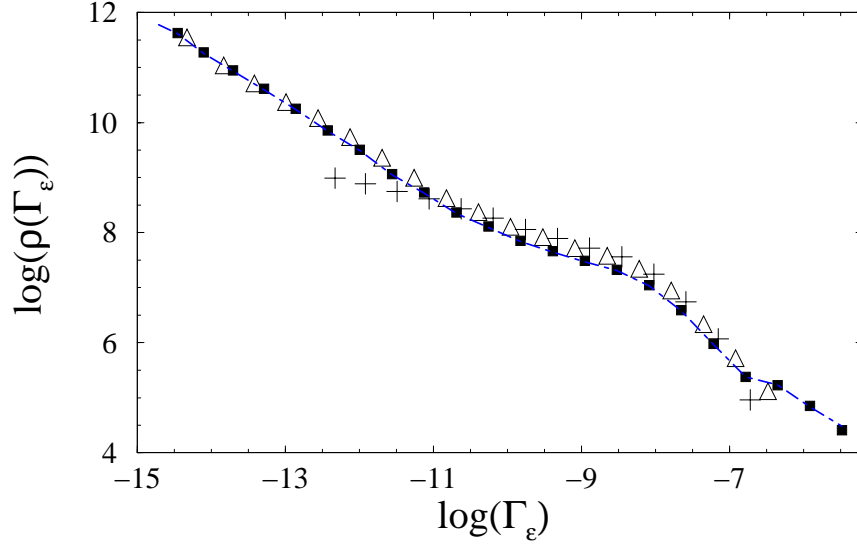


Fig. 3.9: Influence of eigenstates with small decay rates ($\Gamma_\epsilon \leq 10^{-12}$ a.u.), and small overlaps with the initial bound state of the atom. The data set $\mathcal{L} = 2$ from figure 3.4 (pyramids; $w_\epsilon > 10^{-5}$) is compared to different choices of the overlap criterion. The more stringent condition $w_\epsilon > 10^{-4}$ (plusses) excludes many states with small ionisation rates ($\Gamma_\epsilon \leq 10^{-12}$ a.u.) which typically are situated in the regular region of classical phase space, including states attached to the primary nonlinear resonance island. For $w_\epsilon > 10^{-6}$ (full squares) continuum states with large $\Gamma_\epsilon > 10^{-7}$ a.u. appear, and no change in the distribution is observed any more for $w_\epsilon > 10^{-7}$ (dash-dotted) or even smaller lower bounds for w_ϵ . The vicinity of the continuum threshold (cf. previous figure) is *not* excluded from the distributions in this plot, and the same overlap criterion is chosen for the full range in $\Gamma_\epsilon \simeq 5 \times 10^{-15} \dots 10^{-5}$ a.u.

be less sensitive when F changes, while those eigenstates lying in the chaotic domain exhibit rapidly increasing rates Γ_ϵ as the field strength grows. As stated in the previous section, the decay rates of Floquet states in the chaotic component are essentially determined by the localisation parameter \mathcal{L}^* . Hence, deviations from the clean algebraic law $\rho(\Gamma_\epsilon) \propto \Gamma_\epsilon^{-0.9}$ at large values of F are attributed to the rapid increase of the decay rates of class (i) eigenstates with \mathcal{L} . This corresponds to the effective destruction of dynamical localisation, and the observed change in the decay exponent for $\Gamma_\epsilon \gtrsim 10^{-10}$ a.u. On the other hand, class (ii) and (iii) eigenstates move up to intermediate values $\Gamma_\epsilon \lesssim 10^{-10}$ a.u., for the largest \mathcal{L} shown in figures 3.2-3.6.

The above classification of eigenstates is supported by a systematic study of the Floquet eigenstates of the 1D driven hydrogen atom [112,113][†]. Figure 3.10

^{*}This is the expectation for largely averaged quantities such as $\rho(\Gamma_\epsilon)$. For a single realisation or “sample”, large fluctuations, e.g. in the localisation length or in the ionisation probability, may occur around the approximate statistical prediction [109, 111, 206–208].

[†]Nonetheless one must keep in mind that the identification of the decay properties – characterised by the ionisation rates Γ_ϵ – and the localisation in classical phase space is a statistical statement, which is true when averaging over the contribution of many individual eigenstates.

presents generic Floquet eigenstates of the 1D model atom in the Husimi or Q-function representation [16, 112, 113, 211] in phase space. The above classification into (i-iii) states is verified by comparing their decay rates with their position in classical phase space. The latter is shown in figure 3.11 for the different localisation parameters $\mathcal{L} = 0.25$ and $\mathcal{L} = 2$. The phase space is spanned by action angle variables I, Θ of a 1D harmonic oscillator [112, 212][‡].

At small values of $\mathcal{L} < 0.5$, the states of class (ii) and (iii) exhibit tiny ionisation rates below $\Gamma_\epsilon \simeq 10^{-13}$ a.u., or even below the numerical precision $\Gamma_\epsilon \simeq 10^{-15}$ a.u. Therefore, in the regime of strong dynamical localisation, i.e. for small $\mathcal{L} \leq 0.25$, $\rho(\Gamma_\epsilon)$ is dominated by the decay rates of class (i) eigenstates, lying in the chaotic component of classical phase space. The good agreement of the algebraic decay law with predictions from Anderson models suggests that our results are indeed a manifestation of Anderson localisation being at work in the chaotic ionisation process of microwave-driven Rydberg atoms.

The argument at the beginning of this chapter leading to the power-law of the rate distribution is based on the proportionality of the decay rates with the tail of the corresponding eigenstates at the boundary. A similar argument is possible for states which leak out of a regular region in phase space because of tunnelling [199]. The assumption needed for $\rho(\Gamma) \propto \Gamma^{-1}$ is that the decay rates decrease exponentially along the “lattice” of quantised nearly integrable tori[§], i.e. $\Gamma_{\text{regular}} \propto \exp(-|j - j_{\text{max}}|/\xi_{\text{eff}})$. This is formulated on tori, where the integer j denotes the local, and j_{max} the maximal “excitation” of the quantised tori within the regular domain. ξ_{eff} is an effective “tunnelling length”. Such a picture is applicable either to elliptic islands or to the regular regions, with only slightly perturbed tori with respect to the unperturbed hydrogen motion. The assumption of an exponential behaviour induced by tunnelling is certainly true on average. However, ξ_{eff} may be subject to system specific fluctuations which depend on the effective Planck constant [213–217]. For the derivation of the law $\rho(\Gamma) \propto \Gamma^{-1}$, a sufficiently large number of tori j_{max} must be present. This guarantees the necessary limit of many sites on the “lattice” as required in the Anderson problem. If the density of states is too low, finite size effects may spoil the above algebraic behaviour.

Our results nicely confirm the power-law prediction for the decay-rate distribution with $\rho(\Gamma_\epsilon) \propto \Gamma_\epsilon^{-0.9}$ in the region $\Gamma_\epsilon \leq 10^{-11}$ a.u. This part of the distribution is dominated by class (ii) and (iii) states localised along regular structures of phase space for $\mathcal{L} = 1$ and 2 in figures 3.2-3.6. The derivation of $\rho(\Gamma_\epsilon) \propto \Gamma_\epsilon^{-1}$ given above for the tunnelling regime, and at the beginning of this chapter for the Anderson scenario is rather crude. Yet the argument is valid for generic 1D Anderson models in a regime of small Γ [197]. For large

There do exist states for which the better localised in phase space decay faster (larger Γ_ϵ) than those which are more extended in phase space [112]. This reflects the complexity of the problem [110, 112, 209, 210].

[‡]These specific variables are chosen because of the representation of the Floquet problem in a Sturmian basis which is characterised by a scale parameter $\simeq n_0$. The eigenstates are then naturally represented in a harmonic oscillator basis [112, 113, 212]. The action I may be mapped in a well defined way to the principal quantum numbers n [112, 113, 212].

[§]For the 1D as well as the 3D problem, a quantisation procedure à la Einstein-Brillouin-Keller [8, 16, 44] is possible for regular regions locally in phase space [77].

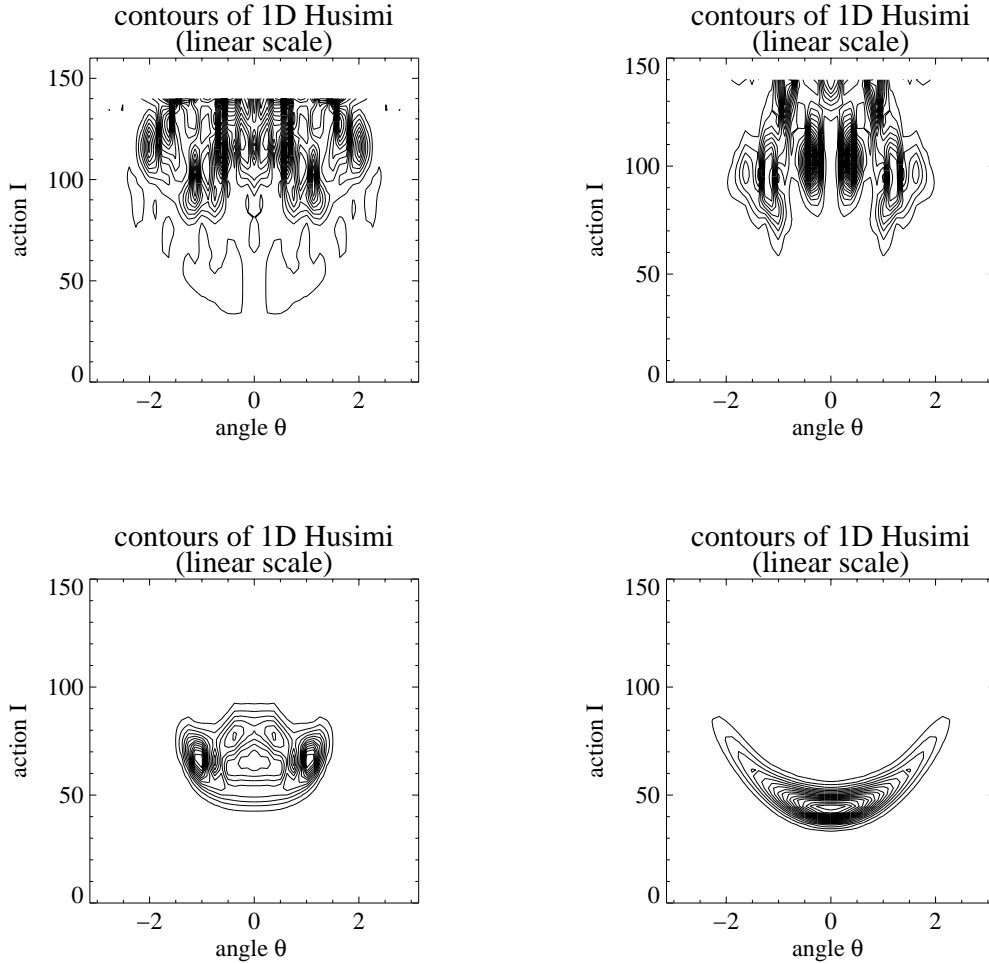


Fig. 3.10: Husimi distributions (contour plots) of four resonance eigenfunctions of the 1D hydrogen atom in a microwave field with amplitude $F = 1.073 \times 10^{-9}$ a.u., and frequency $\omega/2\pi = 13.16$ GHz. For an initial state $n_0 = 100$, the localisation parameter (3.3) is $\mathcal{L} = 2$. The widths of the resonances are $\Gamma_\epsilon \simeq 1.5 \times 10^{-8}$ (top left), $\Gamma_\epsilon \simeq 3 \times 10^{-9}$ (top right), $\Gamma_\epsilon \simeq 2.6 \times 10^{-11}$ (bottom left), $\Gamma_\epsilon \simeq 5 \times 10^{-14}$ (bottom right). These quantum states represent typical eigenstates corresponding to the different Γ_ϵ regions in the distribution of figure 3.4 with $\mathcal{L} = 2$. Comparing to the corresponding classical phase space in figure 3.11(b), we can classify the eigenstates according to their localisation in the chaotic domain (top left, top right), in the separatrix region (bottom left), or on the regular part of phase space (bottom right) [113].

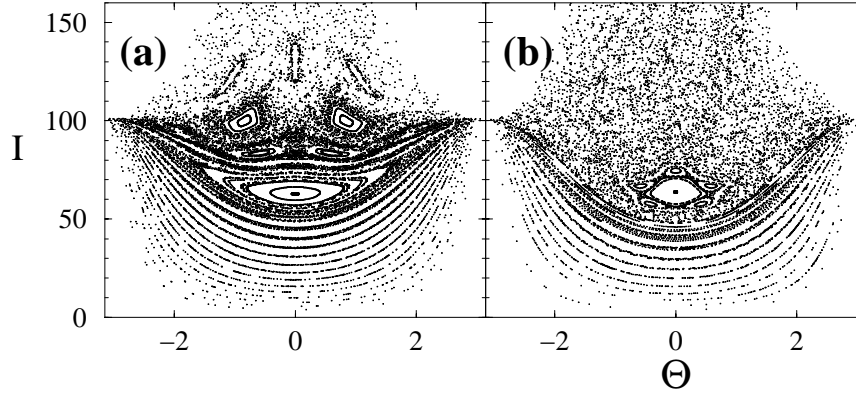


Fig. 3.11: Classical Poincaré surface of section for the 1D microwave-driven hydrogen atom in harmonic oscillator action angle variables I, Θ [112] for weak (a), and strong driving (b). The chosen parameters are $\omega/2\pi = 13.16$ GHz, and $F = 3.774 \times 10^{-10}$ a.u. (a), $F = 1.073 \times 10^{-9}$ a.u. (b). For $n_0 = 100$, this corresponds to a localisation parameter $\mathcal{L} = 0.2$ (a) and 2 (b), respectively.

Γ , the distributions do depend on the specific models [197, 200]. A logarithmic correction to the power law $\rho(\Gamma) \propto \Gamma^{-1}$, based on an additional simplified semiclassical transport mechanism, is derived in [68]. For the complex quantum transport in driven Rydberg states an analytical theory does not exist. But we notice that the universal decay exponent $\alpha \simeq 0.9$ found in our data matches surprisingly well with the predictions from Anderson localisation for $\mathcal{L} \leq 0.25$, or with the tunnelling model in the delocalised regime, respectively.

To conclude the discussion of the decay-rate distributions we comment on a slight, but systematic discrepancy between the 3D and the 1D data. While a clear “knee” like structure develops at intermediate rates, with increasing \mathcal{L} in the 1D model, for the real atom this knee is less pronounced. Let us compare in more detail the distributions for the localisation parameter $\mathcal{L} = 1$: a change in the decay exponent occurs in the region $\Gamma_\epsilon \simeq 10^{-9} \dots 5 \times 10^{-8}$ a.u. (figure 3.3), $\Gamma_\epsilon \simeq 10^{-10} \dots 10^{-8}$ a.u. (figure 3.4), $\Gamma_\epsilon \simeq 10^{-11} \dots 10^{-9}$ a.u. (figure 3.5), and in the 3D atom at $\Gamma_\epsilon \simeq 10^{-10} \dots 10^{-8}$ a.u. (figure 3.6). This regions are dominated by class (i-ii) eigenstates. The observed smoothing of the 3D distribution with respect to the 1D results arises from the additional angular momentum degree of freedom. In the same way as transport occurs along the radial degree of freedom (energy axis in 1D case), also the angular momentum (ℓ -) states are coupled in the real atom. The third degree of freedom, the projections of ℓ onto the field axis, is a constant of motion [71, 218], which is fixed for the spectra plotted in figure 3.6. At small $\mathcal{L} \leq 0.25$, states largely composed of high- ℓ contributions have vanishing decay rates. On the other hand, for strong fields, i.e. $\mathcal{L} \geq 1$, such contributions do come into play because of the strong coupling. They manifest in the distributions $\rho(\Gamma_\epsilon)$ in the range $\Gamma_\epsilon < 10^{-10}$ a.u., they compensate for the reshuffling of states which are mainly composed of low- ℓ contribution, from small to intermediate values of Γ_ϵ . Therefore, the angular momentum degree of freedom is important for the decay-rate distributions, even

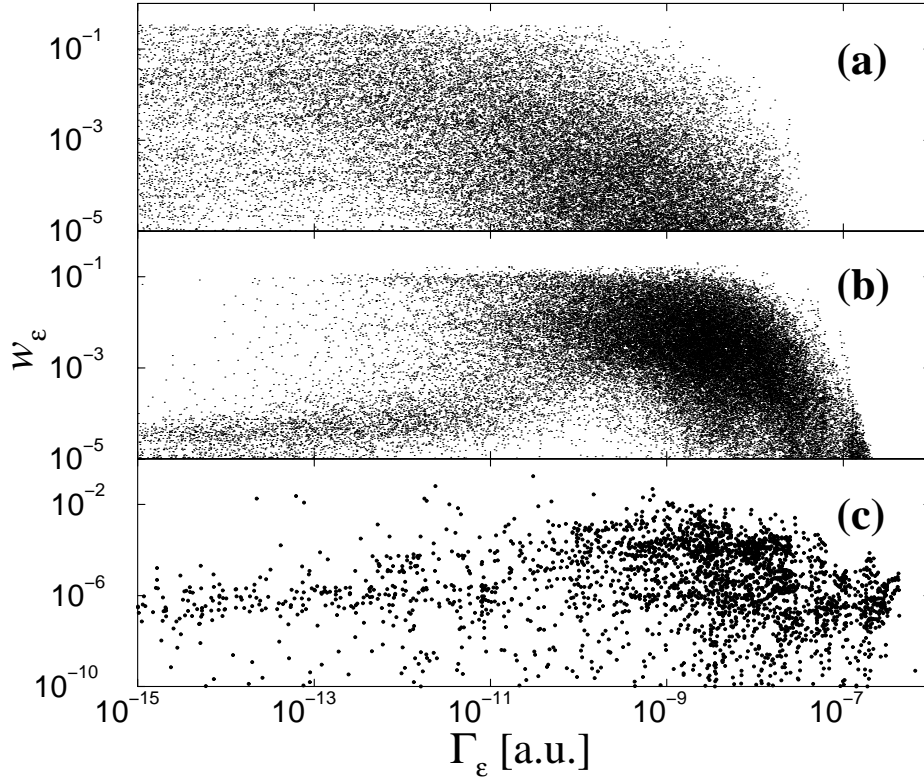


Fig. 3.12: Expansion coefficients w_ϵ of the atomic initial state $|\phi_0\rangle = |n_0 = 100\rangle$ (1D), and $|n_0 = 70, \ell_0 = 0, m_0 = 0\rangle$ (3D) in the Floquet eigenstates $|\epsilon\rangle$ vs. the associated decay rates Γ_ϵ ; for 1D $\mathcal{L} = 0.25$ (a), 1 (b) and $\omega/2\pi = 13.16 \dots 16.45$ GHz (500 spectra), and for 3D (c) with $\mathcal{L} = 1$ and $\omega/2\pi = 35.6$ GHz (one spectrum). (Qualitatively similar results are obtained for microwave driven alkali Rydberg states [95].) There is no definite correlation between the decay rates and w_ϵ , apart from the general observation that with increasing coupling to the atomic continuum (from (a) to (b)), larger Γ_ϵ are assigned larger weights, implying faster decay. 3D data by courtesy of Andreas Krug [116].

if it affects these only slightly.

3.1.3 Algebraic decay of survival probability

The results on the ionisation-rate distributions presented in the preceding sections show how and to what extent chaotic transport mimics signatures of disorder, and induces amendments thereof arising from the peculiar structures of mixed regular-chaotic phase space. The underlying structure of the classical phase space is a feature of dynamical systems, and it has no counterpart in disordered solid-state models.

The aim of the present section is condensed in the following question: how do the observed statistics of the ionisation rates carry over to the survival probability

of an atom in the driving field? The survival probability or its complement, the ionisation probability, is the most directly accessible observable in laboratory experiments. Can one find clear traces of the “universal” decay-rate statistics $\rho(\Gamma_\epsilon) \propto \Gamma_\epsilon^{-0.9}$ in the survival probability of the atom in the field? The answer is *partly* affirmative as we will see in the following. A power-law distribution of the decay rates means that there is a large number of them distributed over many orders of magnitude. If many of these “channels” are involved in the actual decay process an algebraic decay law

$$P_{\text{surv}}(t) \propto t^{-\mu} \quad (3.5)$$

is generally expected [114, 219, 220]. For microwave-driven rubidium Rydberg atoms, experiments have found clear evidence for a power-law with exponent $\mu \simeq 1/2$ [114]. Corresponding numerical studies for alkali as well as hydrogen Rydberg states suggest that asymptotically the power law (3.5) indeed is generic. However, the strong parameter dependence of the exponent ranging from $\mu \simeq 0.5 \dots 2$ [95] contradicts the prediction of a “universal” time decay for the survival probability [115].

The survival probability $P_{\text{surv}}(t)$, i.e. the probability to find the atom in a bound state after an atom-field interaction time t , is given by (2.40). The ionisation process and the number of strongly contributing decay rates is determined also by the weights w_ϵ . The latter represent the initial condition, and contain *local* information on the spectrum to the extent that the initial state $|\phi_0\rangle$ is localised in energy space (see figure 1.1). Therefore, the question whether a power-law like (3.5) holds – and if it holds, over what range of interaction times – depends crucially on the overlaps w_ϵ .

Starting from a general form $\rho(\Gamma_\epsilon) \propto \Gamma_\epsilon^{-\alpha}$, a “universal” time dependence $P_{\text{surv}}(t) \propto t^{\alpha-2}$ has been suggested [115], leaning on the additional assumption $w_\epsilon \propto \Gamma_\epsilon$ [115, 221, 222]. The proportionality of decay rates and weights allows an approximate derivation of the survival probability based on the distribution function $\rho(\Gamma_\epsilon)$. Provided the density of states is sufficiently high, one may substitute the contribution of each resonance to $P_{\text{surv}}(t)$ by an integral average over all possible Γ_ϵ with their weight function $\rho(\Gamma_\epsilon)$ [¶]:

$$P_{\text{surv}}(t) \simeq \int_0^\infty d\Gamma_\epsilon \rho(\Gamma_\epsilon) w_\epsilon e^{-\Gamma_\epsilon t}, \quad (3.6)$$

what reduces to

$$P_{\text{surv}}(t) \propto t^{\alpha-2}, \quad (3.7)$$

for $w_\epsilon \propto \Gamma_\epsilon$, and $\rho(\Gamma_\epsilon) \propto \Gamma_\epsilon^{-\alpha}$ (within the physically relevant window of Γ_ϵ values). Whereas $\rho(\Gamma_\epsilon)$ obeys a nice power law in the dynamically localised regime (see section 3.1.2), the assumption $w_\epsilon \propto \Gamma_\epsilon$ does *not* apply for a generic situation of the ionisation problem. This assumption is justified only if the initial

[¶]Strictly speaking, $\rho(\Gamma_\epsilon)$ is already the density averaged over many realisations/spectra, and for a single spectrum, $P_{\text{surv}}(t)$ is determined by a density distribution of Γ_ϵ which may be amended by finite size effects and local fluctuations. For this reason, the distributions shown in figures 3.2-3.6 collect the decay rates of many spectra.

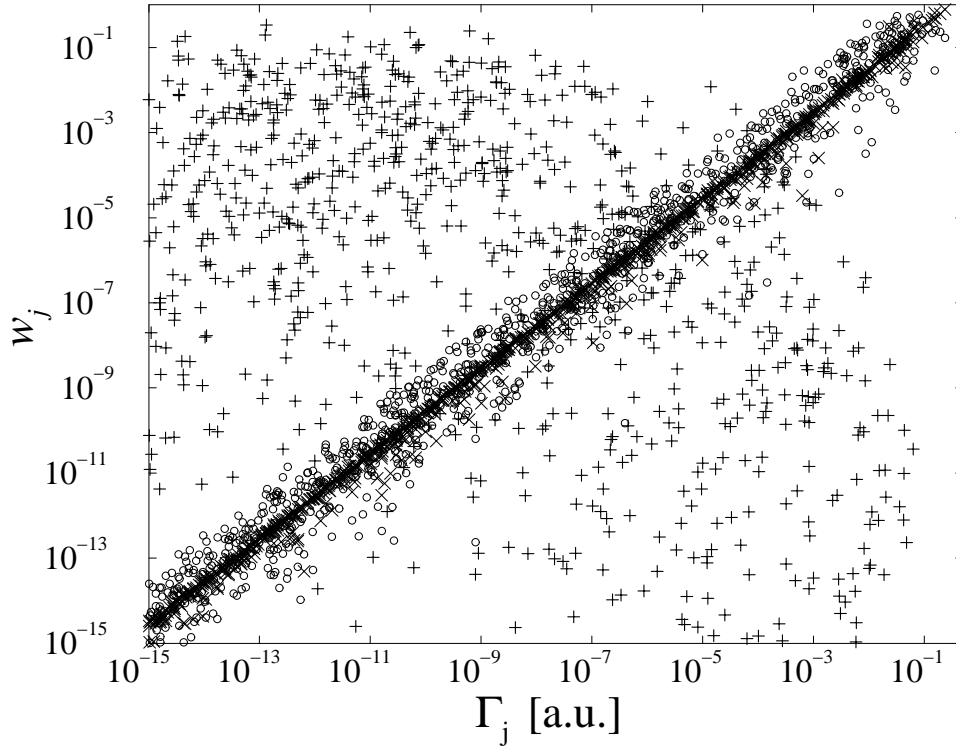


Fig. 3.13: Expansion coefficients w_j vs. decay rates Γ_j for initial states prepared at the sites $j_{\text{init}} = 900$ (plusses), 999 (circles), 1000 (crosses clustered along the diagonal) of a 1D Anderson model of sample length $L = 1000$ (see (3.8) and main text); results for 10 realisations of the random on-site potential are gathered together. Only in the special case of the initial state placed right at the edge of the sample, $j_{\text{init}} = 1000$, there is a one-to-one relation between decay rates and expansion coefficients!

state $|\phi_0\rangle$ is very close to the boundary of the atomic sample, i.e. to the continuum threshold (see figure 1.1). For a generic choice of the initial state within the sample, not very close to the last nearly resonantly coupled bound state below threshold – using the picture of Rydberg levels coupled via multi-photon chains to the continuum – there is no support for a proportionality $w_\epsilon \propto \Gamma_\epsilon$. This is illustrated in figure 3.12, where the distribution of the weights in the $(\Gamma_\epsilon, w_\epsilon)$ plane is shown, on a doubly logarithmic scale, for $|\phi_0\rangle = |n_0 = 100\rangle$ in 1D (a,b), and $|\phi_0\rangle = |n_0 = 70 \ell_0 = 0\rangle$ in 3D driven hydrogen (c). w_ϵ and Γ_ϵ are essentially uncorrelated. This is consistent with the observation that phase space localisation properties and decay rates of strongly driven Rydberg atoms are *not* unambiguously related [112, 113].

To understand better the role of the proportionality of decay rates and weights, we confront our results for the microwave-driven hydrogen problem with a simple, 1D Anderson model [116, 197, 221] which is sketched in figure 3.1. This model easily allows for an arbitrary shift of the initial population inside the

sample. It is defined by the Schrödinger equation

$$i \frac{d\psi_j(t)}{dt} = V_j \psi_j(t) + \psi_{j+1}(t) + \psi_{j-1}(t), \quad (3.8)$$

where the $\psi_j(t)$ are the probability amplitudes for a particle to reside at site j of a 1D sample of length L . The on-site potentials V_j are chosen as a random sequence of uniformly distributed values $\in [-1.5, 1.5]$. This choice models disorder. The coupling to the lead is mediated by requiring absorbing boundary conditions at the right end, i.e. by adding a small imaginary part $-i\gamma = -i0.31$ to V_L on the last site $j = L$. All these choices of parameters are not crucial for the results collected in figure 3.13. They were made such as to mimic a localisation scenario à la Anderson, with significant leakage into the lead at $j = L$. The initial excitation is a δ -like wave packet launched at some site within the sample:

$$\psi_j(t=0) = \begin{cases} 1, & j = j_{\text{init}} \\ 0, & \text{otherwise.} \end{cases} \quad (3.9)$$

We put the initial site systematically closer to the end $j = L$, and the decay rates of the eigenstates of the open tight-binding model are calculated by a diagonalisation routine for symmetric, non-Hermitian matrices (NAG F02GBF routine).

Figure 3.13 shows that the generic situation met in the ionisation of driven hydrogen atomic states (figures 3.2-3.6) continuously evolves into one for which expansion coefficients and decay rates are indeed strongly correlated^{||}. If the initial state is placed well inside the sample, expansion coefficients and decay rates do not show any correlation. However, the distribution in the (Γ, w) plane collapses onto an almost straight line $w_j \propto \Gamma_j$ when the initial state approaches the open end at site $j = L$.

It is the latter situation which was modelled in recent numerical calculations for periodically driven hydrogen atoms additionally subject to an intense static field. Such a field effectively shifts the energy of the initial state closer to the atomic continuum by lowering its ionisation potential. The absorbing boundary conditions used in [115] make contact to the above introduced Anderson model. Choosing the initial state close to the continuum basically reduces the problem to a perturbative relation between the decay rates Γ_j and the expansion coefficients ω_j of the site amplitudes with the lead giving $w_j \propto \Gamma_j$ [221]. The strength of the static field required by [115] to put the threshold in the vicinity of the initial state ($n_0 = 60$ with $n_c = 64$ [115]) would be of the order of the microwave amplitude F . In such a situation, the number of quasi-resonantly coupled states, in the spirit of figure 1.1, is extremely small, what leads a large localisation parameter $\mathcal{L} \simeq 3.5$ [115]. The sample length (3.2) then is $L < 1$ [115], and the limit of many lattice sites necessary for the Anderson scenario is not fulfilled. Therefore, a dynamically localised distribution of the wave

^{||}The correlation indeed was confirmed numerically by standard tests from section 14.5 and 14.6 of [223]: while for the case $j = j_{\text{init}}$ the tests were positive, the correlation found otherwise was not significant (as in the case of hydrogen decay rates and weights).

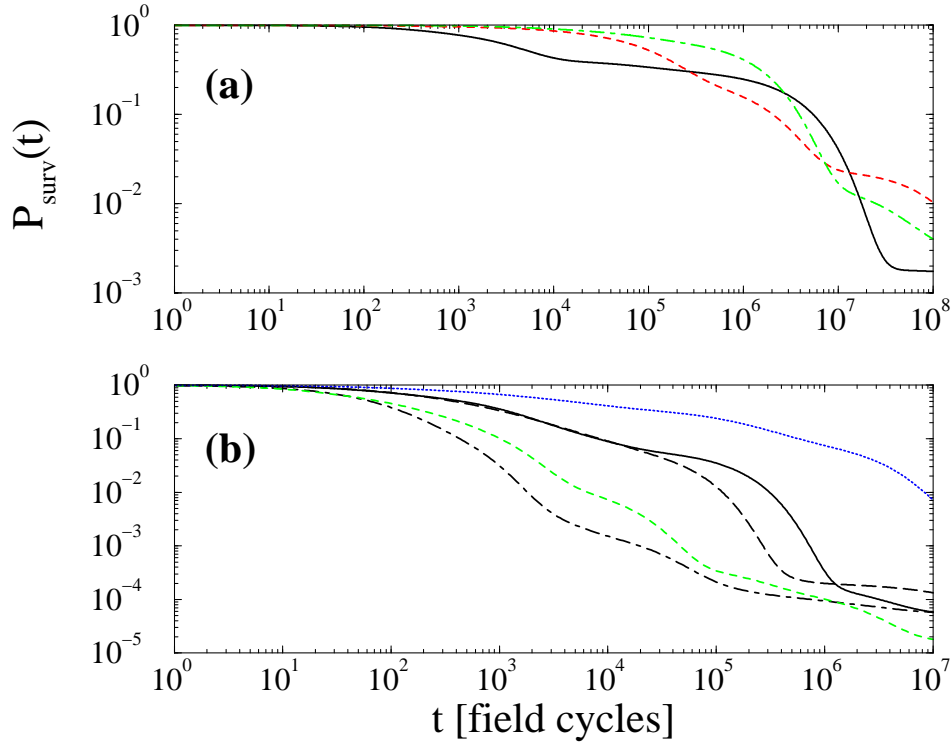


Fig. 3.14: Survival probability $P_{\text{surv}}(t)$ obtained from equation (2.40) for 1D hydrogen. Initial states $|n_0 = 40\rangle$ (a), and $|n_0 = 100\rangle$ (b); localisation parameters and driving frequencies as follows: (a) $\mathcal{L} = 0.2$, $\omega_0 = 2$ (solid line), $\omega_0 = 2.25$ (dashed), $\omega_0 = 2.5$ (dash-dotted); (b) $\mathcal{L} = 0.5$, $\omega_0 = 2.5$ (dotted), $\mathcal{L} = 1$, $\omega_0 = 2$ (solid line), $\omega_0 = 2.5$ (long dashed), and $\mathcal{L} = 2$, $\omega_0 = 2$ (dash-dotted), $\omega_0 = 2.5$ (short dashed).

functions in energy space cannot develop, and the only hope for a decay law $P_{\text{surv}}(t) \propto t^{-1}$ arises from states in the regular region of phase space. After an initial fast drop of the survival probability, which is induced by the one-photon transition to the continuum, the regular states might lead to a t^{-1} -decay.

Given the results in figures 3.12 and 3.13, for a general choice of the initial population, we can no longer expect a universal time decay for the survival probability $P_{\text{surv}}(t)$ of microwave-driven Rydberg atoms, in spite of the universal features of the decay-rate distributions $\rho(\Gamma_\epsilon)$. $P_{\text{surv}}(t)$ is shown in figure 3.14 for the 1D model atom, and in figure 3.15 for real 3D atomic hydrogen. The algebraic decay of $P_{\text{surv}}(t) \propto t^{-\mu}$ is generic, arising from the broad distribution of w_ϵ and Γ_ϵ over many orders of magnitude. Even for one single realisation of field parameters, the numerically computed spectrum consists of about 100...200 eigenstates for the 1D, and of approximately 2500 for the 3D case. All these states are summed in (2.40) to obtain $P_{\text{surv}}(t)$. However, the decay exponent μ varies considerably from one realisation to the other.

We also averaged the survival probability, for fixed \mathcal{L} , over 500 realisations of the parameters ω , F in the 1D case. The averaging smoothes the fluctuations which arise from the sensitive dependence on ω , and F [110–112, 208–210]. In

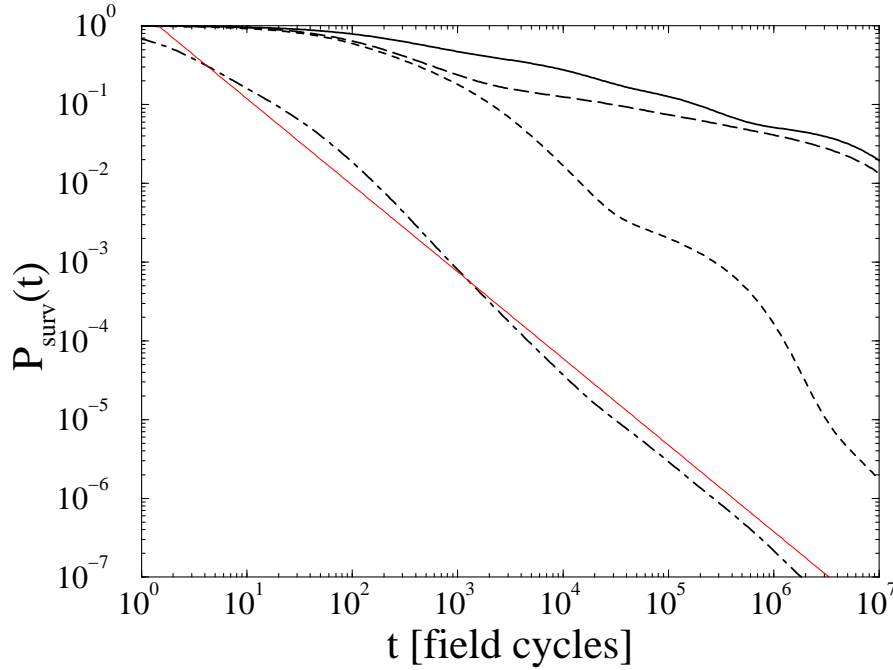


Fig. 3.15: Survival probability $P_{\text{surv}}(t)$ (2.40) of 3D atomic hydrogen, $n_0 = 70$, $m_0 = 0$, $\ell_0 = 0$ (solid line), 15 (long dashed), 45 (short dashed), $\omega_0 = 1.856$ ($\omega/2\pi = 35.6$ GHz), $\mathcal{L} = 1.0$ [116]. Different w_ϵ -distributions are realised by changing the angular momentum ℓ_0 of the initial atomic state, always leading to near-algebraic decay (like in 1D), though with distinct (and *non-universal*) decay exponents. Only fictitious expansion coefficients $w_\epsilon \equiv \Gamma_\epsilon / \langle \Gamma_\epsilon \rangle$ induce asymptotically a “universal” power-law decay $P_{\text{surv}}(t) \sim t^{-\mu}$ (dash-dotted line), $\mu \simeq 2 - \alpha \simeq 1.1$ (indicated by the full line). Γ_ϵ , $\langle \Gamma_\epsilon \rangle$, and $\alpha \simeq 0.9$ are extracted from the $\Gamma_\epsilon \lesssim 10^{-10}$ a.u. part of the $\mathcal{L} = 1.0$ distribution in figure 3.6. The power-law sets in at $t_{\text{on}} \simeq 10^4$ field cycles. This time corresponds to the inverse of the maximum Γ_ϵ up to which $\rho(\Gamma_\epsilon) \propto \Gamma_\epsilon^{-0.9}$ prevails, i.e. $t_{\text{on}} \simeq 10^{10}$ a.u.

the derivation of (3.7), these fluctuations are effectively averaged as well. The results are found in figure 3.16, and they show a much smoother decay in time than the survival probabilities in figure 3.14. Moreover, the averaged curves have a systematically increasing decay exponent μ with increasing \mathcal{L} , and μ is clearly not determined solely by α as suggested by (3.7).

The “universal” exponent $\mu = 2 - \alpha$ (3.7) is observed only in accidental cases [95], or if we artificially reshuffle the expansion coefficients according to $w_\epsilon \rightarrow w_\epsilon \equiv \Gamma_\epsilon / \langle \Gamma_\epsilon \rangle$, with $\langle \Gamma_\epsilon \rangle$ being the mean ionisation rate averaged over the entire Floquet spectrum [116]. In the latter, unrealistic case, illustrated in figure 3.15, $P_{\text{surv}}(t)$ asymptotically decays with exponent $\mu \simeq 1.1$. This perfectly matches the prediction $\mu = 2 - \alpha$ with $\alpha = 0.9$ for the small $\Gamma_\epsilon \lesssim 10^{-10}$ a.u. part of the corresponding distribution $\rho(\Gamma_\epsilon)$ in figure 3.6. The time t_{on} when the power-law decay $P_{\text{surv}}(t) \propto t^{-1.1}$ sets in corresponds to rates $\Gamma_\epsilon \lesssim 10^{-10}$ a.u. Up to these rates $\rho(\Gamma_\epsilon) \propto \Gamma_\epsilon^{-0.9}$ is observed in figure 3.6. In atomic units

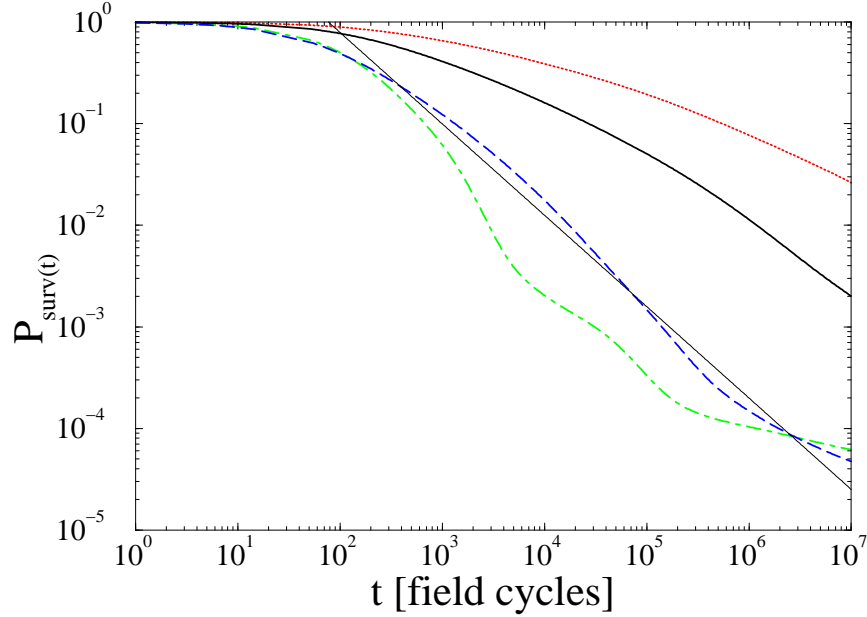


Fig. 3.16: Frequency averaged survival probabilities $P_{\text{surv}}(t)$ of 1D hydrogen. Initial state $|n_0 = 100\rangle$, frequency range $\omega_0 = 2.0 \dots 2.5$, in 500 equidistant steps. Localisation parameters: $\mathcal{L} = 0.5$ (dotted), $\mathcal{L} = 1$ (solid), $\mathcal{L} = 2$ (dashed). A systematic increase of the decay exponent with increasing \mathcal{L} prevails, and the curves are smoother than the data for solely one fixed frequency. For better comparison, the dash-dotted line repeats the survival probability for $\mathcal{L} = 2$ and $\omega_0 = 2.0$ from figure 3.14. The thin line shows a power-law scaling $\propto t^{-0.9}$, which, *in general*, does not match well with the data.

$t_{\text{on}} \simeq 10^{10}$ a.u., which corresponds to $\simeq 10^4$ field cycles in figure 3.15. Since by construction $\Gamma_\epsilon \propto w_\epsilon$, it is not surprising that the asymptotic decay of $P_{\text{surv}}(t)$ is solely determined by the contribution of small Γ_ϵ in $\rho(\Gamma_\epsilon)$. A similar expectation for the “real” survival probabilities is bound to be valid at most approximately, because the weights w_ϵ are then not correlated with the decay rates (see figure 3.12). This leads to a more complex mixture of time-scales induced by the nature of the prepared initial state of the atom.

To summarise the discussion of the decay properties of strongly driven Rydberg atoms, we can state that the *universal* features of the decay-rate statistics (of classically chaotic quantum transport) generally do *not* carry over to the time decay of the survival probability of an initial state prepared at an arbitrary location in phase space. This observation expresses the essential decorrelation between the phase space localisation properties of quantum states, and their asymptotic coupling to the continuum. The ionisation is mediated by *both* sets, the ionisation rates and the overlaps w_ϵ in (2.40). These two uncorrelated sets determine only together the decay in an unambiguous manner.

3.2 Experimental tests

Citius, altius, fortius.
The Olympic motto

Our numerical analysis of the previous section clearly supports the analogy between transport in Anderson-localised models and the ionisation process in driven hydrogen Rydberg atoms. An experimental verification of our results seems feasible. Two experimental options which may quantify the mentioned analogy beyond the threshold scaling in figure 1.2 are discussed in the following.

3.2.1 Status quo

As stated in the introduction (section 1.2.1), the behaviour of the field threshold, at which a certain percentage of atoms ionises, as a function of the scaled microwave frequency $\omega_0 = \omega n_0^3$, may not necessarily originate from dynamical localisation. The experimental results [13, 50, 51] are consistent with the theory of dynamical localisation, but also other mechanism, like the mentioned semiclassical effects, may stabilise the atom against ionisation for $\omega_0 \gtrsim 1$ [72, 77, 87, 103, 104, 106, 107]. Similarly, the experimental data [114] showing an algebraic decay of the survival probability of the atoms in the field, is fully consistent with our findings. In the preceding section, we saw that the slow power-law decay $P_{\text{surv}}(t) \propto t^{-\mu}$ may be caused by the algebraic decay-rate statistics $\rho(\Gamma_\epsilon) \propto \Gamma_\epsilon^{-0.9}$. For $\mathcal{L} \lesssim 0.25$, $\rho(\Gamma_\epsilon)$ was shown to be determined by Floquet states localised in the chaotic component of phase space. Therefore, we can interpret the power-law decay of $P_{\text{surv}}(t)$ as a consequence of dynamical localisation (e.g. the data shown in figure 3.14). However, this finding is again an indirect experimental proof of Anderson localisation. We cannot predict an *exact* exponent μ from arguments based on the ionisation-rate distribution alone. Moreover, also classical model calculations, for systems with mixed regular-chaotic phase space, show an algebraic decay of the asymptotic survival probability [219]. The power-law then results from the multiple time scales involved when trajectories, which are launched in the chaotic component, get trapped in the vicinity of regular regions in phase space [114, 224–234].

3.2.2 Floquet spectroscopy

To confirm the presented numerical results on the decay-rate distributions in experiments, one needs to measure a broad range of ionisation widths. Resonance poles in the complex energy plane were studied experimentally for the wave propagation in microwave cavities [236]. A large number of resonances was obtained from measuring reflection coefficients vs. the initial excitation

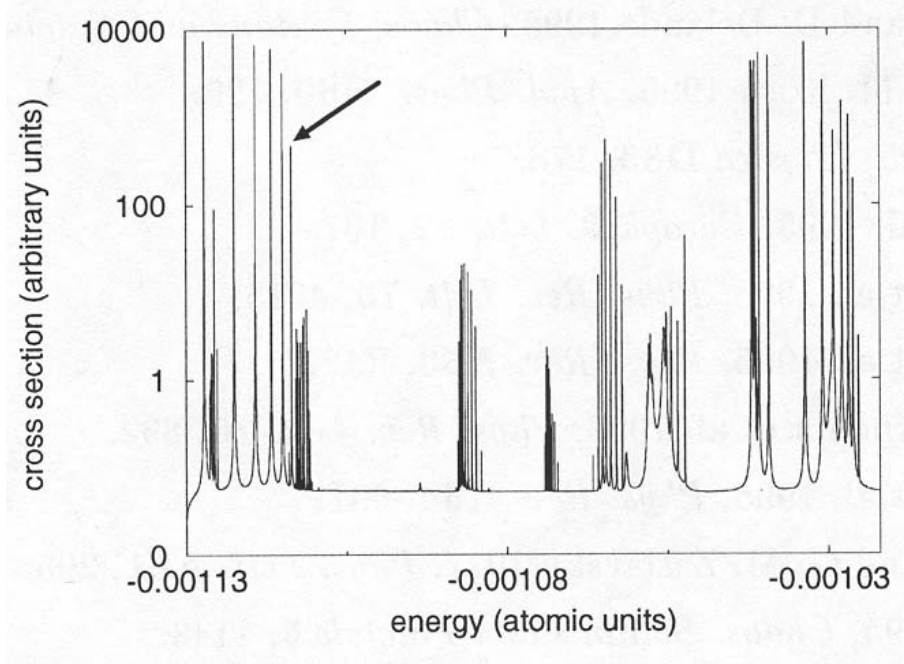


Fig. 3.17: Photo-absorption cross section from the ground state of three-dimensional atomic hydrogen to an energy interval between the $n = 21$ and $n = 22$ manifolds dressed by a microwave field of frequency $\omega \simeq 710$ GHz, and amplitude $F \simeq 1000$ V/cm [235]. The arrow marks a very narrow resonance line corresponding to a Floquet state that is situated mainly within the primary resonance island of classical phase space [77, 235].

energy of such cavities [42, 236, 237].

For beams of Rydberg atoms, which interact with static fields (electric and/or magnetic), photo-excitation spectra were measured by means of laser spectroscopy [26, 29, 34, 71]. From the photo-excitation cross sections one can deduce the decay rates if the resonance peaks do not overlap. This criterion is typically fulfilled for the decay rates of hydrogen Rydberg atoms which are subject to a time-periodic microwave. The distributions in figures 3.2-3.5 show that $\Gamma_\epsilon \lesssim \Delta \simeq n_0^{-3}$, with Δ the average spacing of the energy levels.

For atoms interacting with a microwave field, the spectrum may be probed by an additional laser, which excites atoms starting from a low lying state $|\phi_0\rangle$, e.g. the ground state $|n_0 = 1\rangle$, to some final highly excited Floquet state. This method of Floquet spectroscopy has been proposed in [235, 238–241]. The photo-absorption cross section is given by [185, 241]:

$$\sigma(\Omega_{\text{probe}}) \propto \text{Im} \sum_{\epsilon} \sum_{m=-\infty}^{+\infty} \frac{|\langle \epsilon_m | \hat{T} | \phi_0 \rangle|^2}{\epsilon + m\omega - E_0 - \Omega_{\text{probe}}}, \quad (3.10)$$

where $|\epsilon_m\rangle$ are the Floquet states (see section 2.1.1), and $\hat{T} = \vec{e}\hat{r}$ the electric dipole operator, depending on the polarisation \vec{e} of the probe laser. E_0 is the energy of the initial state $|\phi_0\rangle$, which basically does not couple to the microwave

since the latter is chosen to be negligibly weak, for states with principle quantum numbers $n_0 \simeq 1$. Scanning $\sigma(\Omega_{\text{probe}})$ over the energy range ω (of one photon of the dressing microwave field), a reaction curve as presented in figure 3.17 is obtained. Individual peaks hardly overlap what allows one to extract the resonance widths. The coupling matrix elements in the numerator of (3.10) lead to a biased selection of possibly observable resonances. This bias may be controlled by varying the polarisation of the probe field, and the initial state $|\phi_0\rangle$ to focus on different parts of the spectrum according to their overlaps with $|\phi_0\rangle$ [71]. From the data of the 1D and 3D decay-rate statistics, we saw that the distributions are quite robust with respect to the dimensionality of the problem, the field parameters at fixed \mathcal{L} , and also when selecting only a fraction of the complete spectra (figure 3.7). Hence, we conclude that the decay-rate distributions may be constructed from experimental spectra, given that measurements are performed for a sufficiently large number of realisations, as done in the numerical “experiments”.

3.2.3 Atomic conductance fluctuations

Further quantitative support for the analogy between transport in energy space and the conductance across Anderson-localised one-dimensional wires has been provided recently. In [110] an “atomic conductance” was defined by

$$g \equiv \frac{1}{\Delta} \sum_{\epsilon} \Gamma_{\epsilon} w_{\epsilon}, \quad (3.11)$$

with the mean level spacing Δ . Comprehensive numerical data [111,208] showed that g obeys a log-normal distribution** for localisation parameters $\mathcal{L} < 1$. The statistics was performed in the same manner as for the decay-rate distributions, i.e. by varying the field parameters ω and F , while \mathcal{L} is kept constant. The log-normal distribution was predicted for one-dimensional Anderson models in the localised regime [242–244].

The conductance (3.11) may be interpreted as the “complete” ionisation rate, defined by the weighted sum over the individual decay rates of the Floquet states. Therefore, it contains – alike the ionisation probability – the local information on the initial state. The statistical distributions of the atomic conductance indeed show a systematic dependence on the initial principal quantum number n_0 . For $n_0 \lesssim 60$, finite size effects lead to worse fits of the data with log-normal distributions. The sample length scales like $L \propto n_0$ for fixed $\omega_0 = \omega n_0^3$ (cf. (3.2)), and hence $L(n_0 \leq 60, \omega_0 \geq 2) \lesssim 10$ is too small to quantitatively compare the ionisation problem to the Anderson scenario as suggested by figure 1.1. The decay-rate distribution proved to be rather insensitive to such finite size effects. For $n_0 = 40$ in figure 3.2, a systematic difference as compared to the cases $n_0 \geq 70$ cannot be observed. Consequently, $\rho(\Gamma_{\epsilon})$ is a more direct

**I.e. the logarithm of g is distributed with a Gaussian density. Hence the corresponding fluctuations are huge, and typically range over several orders of magnitude [111,208].

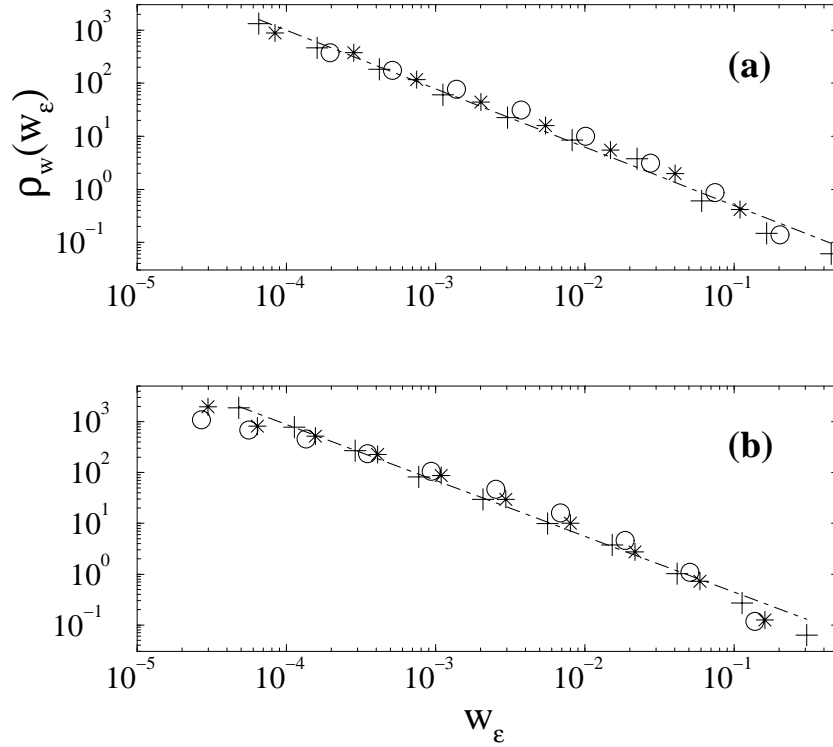


Fig. 3.18: Distribution of the weights w_ϵ (see definition after (2.40)) of the spectral expansion corresponding to the data shown in figures 3.2 and 3.4, respectively; for the initial states $n_0 = 40$ (a), and $n_0 = 100$ (b), and for the localisation parameters $\mathcal{L} = 0.2$ (plusses), $\mathcal{L} = 0.5$ (stars), and $\mathcal{L} = 1$ (circles). The dash-dotted lines show the scaling $\rho_w(w_\epsilon) \propto w_\epsilon^{-1.1}$.

indicator for the analogy to the Anderson problem, because the Floquet spectrum does not depend on the initial bound state. In both statistics, $\rho(\Gamma_\epsilon)$ and of the atomic conductance g , the signatures of localisation à la Anderson are lost for too large localisation parameters $\mathcal{L} \gtrsim 1$. This manifests in the “knee”-like structure which appears in $\rho(\Gamma_\epsilon)$, for $10^{-10} \lesssim \Gamma_\epsilon \lesssim 10^{-8}$, and in the increasing deviation of distribution of g from the log-normal one.

In section 3.1.3 the weights w_ϵ were found to be uncorrelated with the decay rates Γ_ϵ (figure 3.12). Now the w_ϵ enter in the definition of the atomic conductance (3.11), and their statistical behaviour may be extracted from the known distributions of the conductance $\rho_g(\log g)$ [110, 111, 208] and of the decay rates $\rho(\Gamma_\epsilon)$. Figure 3.18 presents numerically obtained distributions $\rho_w(w_\epsilon)$ corresponding to the data shown in figures 3.2 and 3.4. We observe that $\rho_w(w_\epsilon)$ does not significantly depend on the initial state. Moreover, there prevails a slight but systematic dependence on the localisation parameter \mathcal{L} : while, for $\mathcal{L} = 0.2$, $\rho_w(w_\epsilon) \propto w_\epsilon^{-1.1}$ over about 3 orders of magnitude, the distribution changes with increasing \mathcal{L} such that intermediate weights with $10^{-3} \lesssim w_\epsilon \lesssim 10^{-2}$ gain more and more significance. The power-law distribution for the well localised case $\mathcal{L} = 0.2$ may be motivated in the following way. Assuming that $\log g$ and $\log \Gamma_\epsilon$

are independent random variables, as implied by figure 3.12, and furthermore that $g \sim \Gamma_\epsilon w_\epsilon$ it follows [198]:

$$\begin{aligned} \rho(\log w_\epsilon) &\sim \int d \log \Gamma_\epsilon \rho_{\Gamma,g}(\log \Gamma_\epsilon, \log w_\epsilon - \log \Gamma_\epsilon) \\ &= \int d \log \Gamma_\epsilon \rho_\Gamma(\log \Gamma_\epsilon) \rho_g(\log w_\epsilon - \log \Gamma_\epsilon) \\ &\sim \int d \log \Gamma_\epsilon \mathcal{G}(\log w_\epsilon - \log \Gamma_\epsilon) \sim 1, \end{aligned} \quad (3.12)$$

where $\rho_\Gamma(\log \Gamma_\epsilon) = \rho(\Gamma_\epsilon) |d\Gamma_\epsilon/d\log \Gamma_\epsilon| \propto 1$, for $\rho(\Gamma_\epsilon) \propto \Gamma_\epsilon^{-1}$. \mathcal{G} denotes a Gaussian probability density, arising from the log-normal distribution of g . This finally yields

$$\rho_w(w_\epsilon) = \rho(\log w_\epsilon) \left| \frac{d \log w_\epsilon}{dw_\epsilon} \right| \sim \frac{1}{w_\epsilon}, \quad (3.13)$$

neglecting that g (3.11) has to be summed over the entire spectrum. The simplified assumption $g \sim \Gamma_\epsilon w_\epsilon$ leads, however, to a power-law decay as observed in 3.18. The above analysis shows that the distribution of the weights are the *same* as obtained if $\Gamma_\epsilon \propto w_\epsilon$, together with $\rho(\Gamma_\epsilon) \propto \Gamma_\epsilon^{-1}$, is fulfilled, in spite of the fact that the decay rates and the weights are uncorrelated for our system! This suggests that there is more information in the system than it is contained in the statistical distribution of the rates, of the weights, and of the atomic conductance alone.

What is missing is a clear experimental verification of the numerical results on the conductance fluctuations! Experiments with rubidium Rydberg atoms were performed, however, considerable fluctuations have not been detected [245]. The ionisation probability was measured as a function of the scaled frequency, for fixed interaction time t , and approximately constant field amplitudes. The latter depend on the frequency in a waveguide or in a microwave cavity, and must be exactly calibrated. On the other hand, the numerical conductance fluctuations proved to be quite robust with respect to relative uncertainties in the field strength up to about 5%. Therefore, the experimental data most probably did not show fluctuations because the scanned frequency range was too small to observe fluctuations over several orders of magnitude [111].

In the following, we derive a simple estimate for the minimal range in ω over which strong fluctuations are expected. We start from the atomic transport scenario sketched in figure 1.1: the ionisation of the initial state is mediated by a subsequent chain of one-photon transitions connecting resonantly lying levels. A change in the driving frequency ω may be viewed as a shift of the photonic ladder of quasi-resonantly coupled states [91], whereby the most sensitive region is the one closest to the continuum threshold. For small enough changes of the frequency $\delta\omega$, all states on the ladder remain the same, apart from the last unperturbed level n_{ex} just below threshold. The mean level spacing scales as $\Delta \simeq 1/n^3$ (for the 1D atom; for the 3D case, and if the field is strong enough to considerably lift the degeneracy in angular momentum, the scaling is closer to $\Delta \simeq 1/n^4$). Hence, $\delta\omega$ must be larger than n_{ex}^{-3} such as the last ladder level does change when varying ω by $\delta\omega$. Simultaneously, $\omega \gtrsim 1/2n_{\text{ex}}^2$, so that we

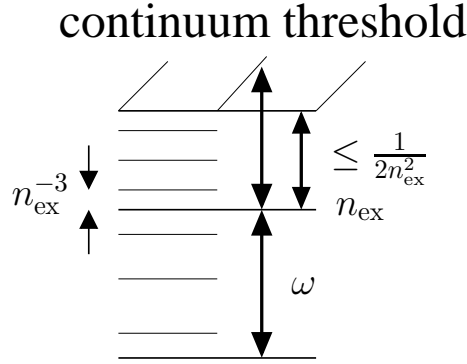


Fig. 3.19: Quasi-resonantly coupled states (long horizontal lines) close to the continuum threshold. The short lines represent the non-coupled unperturbed hydrogen Rydberg states. n_{ex} is the last “ladder” state from which a single one-photon transition leads to ionisation.

arrive at the estimate for the minimal frequency change, which may produce a significantly different ionisation scenario, and hence a large variation in the ionisation probability or the atomic conductance: $\delta\omega \gtrsim (2\omega)^{3/2}$, or in scale units $\delta\omega_0 \gtrsim n_0^{-3/2}(2\omega_0)^{3/2}$. For $n_0 = 100$, and the lower bound $\omega_0 = 2$, this gives $\delta\omega_0 \gtrsim 8 \times 10^{-3}$. Actual numerical computations of the atomic conductance show that dramatic fluctuations over several orders of magnitude occur down to a scale $\delta\omega_0 \simeq 10^{-3}$ for $n_0 = 100$ [111, 208]. For decreasing initial quantum numbers $n_0 < 100$, $\delta\omega_0$ becomes systematically larger. Therefore, an experimental investigation must be performed over a frequency range $\Delta\omega_0 \gg \delta\omega_0$ which is sufficiently broad in order to detect atomic conductance fluctuations (at a resolution of $\delta\omega_0$). The precise value of $\delta\omega_0$ depends on the atomic species used in the experiment, as well as on the chosen initial state. The reason is that the local level spacing depends on the atom (hydrogen, rubidium, etc.), and the ionisation dynamics depends on the prepared initial state via the overlaps w_ϵ in (2.40). Scanning the frequency in a waveguide is simple, but to keep good control over the field amplitude calibration to fulfill the constraint of constant \mathcal{L} is experimentally challenging [53, 73, 246].

The extreme fluctuations of the atomic conductance as a function ω are predicted in a range of microwave amplitudes and frequencies for which the classical transport is suppressed by dynamical localisation. In different contexts it was noticed that classical chaos plays an important role in the theory of quantum scattering, including mesoscopic conductance fluctuations [18, 37, 247]. Self-similar “fractal” fluctuations have been detected for transmission processes through mesoscopic nanostructures [248–250]. They were explained based on a semiclassical theory which is built on the hierarchical structure of mixed regular-chaotic phase space [67, 68, 251, 252]. Another approach [253] predicts well defined conditions on the statistical properties of resonance poles which afford fractal fluctuations, independently of semiclassical arguments: statistically independent sequences of strongly overlapping resonances, which obey a power-law $\rho(\Gamma) \propto \Gamma^{-\alpha}$ ($\alpha > 0$) at small Γ , are proven to be sufficient for the

appearance of fractal fluctuations.

Microwave-driven hydrogen Rydberg atoms are characterised by (a) mixed regular-chaotic phase space, as well as by (b) a power-law distribution of the decay rates. The latter is observed in the regime of dynamical localisation, and for states in the regular region where tunnelling determines the distribution (see section 3.1.2). Nonetheless, self-similar structures of the atomic conductance fluctuations over many orders of magnitude in ω_0 are not observed. One reason is that the resonances are typically non-overlapping, i.e. $\Gamma_\epsilon \lesssim \Delta$, in the range where a clear power-law $\rho(\Gamma_\epsilon)$ dominates. For instance, in figure 3.4, $\rho(\Gamma_\epsilon) \propto \Gamma_\epsilon^{-0.9}$ is obeyed for $\Gamma_\epsilon \simeq 10^{-15} \dots 10^{-9}$ a.u., while $\Delta \simeq 10^{-6}$ a.u. In addition, the above argument based on the photonic ladder picture provides an estimate for a lower bound of the frequency variation below which a significant change in the ionisation signal is not expected. This suggests that a fractal structure over *many* scales in the microwave frequency cannot appear.

Part II:

Quantum resonances and the effect of decoherence in the dynamics of kicked atoms

Creator Deus mathematica ut archetypus secum ab aeterno habuit in abstractione simplicissima et divina, ab ipsis etiam quantitibus materialiter consideratis.

J. Kepler (see [196])

Chapter 4

Kicked-atom dynamics at quantum resonance

4.1 Quantum resonances in experiments

In the two periodically driven systems studied in this thesis, the dynamical evolution may substitute for the intrinsic disorder present in Anderson models. For the δ -kicked rotor, this can be seen directly from the mapping on the tight-binding equations (2.16). Experiments with cold and dilute atomic ensembles, as described in section 2.3, demonstrated the effect of dynamical localisation that manifests (a) in a stationary momentum distribution, and (b) in the cessation of the linear growth of energy as a function of time. Both of these signatures occur after the quantum break time $t_{\text{break}} \sim k^2$ [63, 80, 106].

On the other hand, the quantum resonances of the δ -kicked rotor are much more difficult to access experimentally. A flavour of the experimental limitations has been provided in section 2.3.3. The expected ballistic motion of the atoms (i.e. their energy should increase quadratically in time) is fast. This makes resonant atoms escape the experimentally observable, restricted momentum window on a relatively short time scale. Moreover, while dynamical localisation is a rather robust phenomenon, the quantum resonances are very sensitive to slight detunings in the kicking period τ , and, in addition, they depend on the quasi-momentum β (see end of section 2.2.3).

As a consequence, the correspondence between theoretical expectation and experimental data is much less convincing in the resonant case than in the localised one. In the following, three experimental observations are discussed which do not match directly with the theory of the δ -kicked rotor.

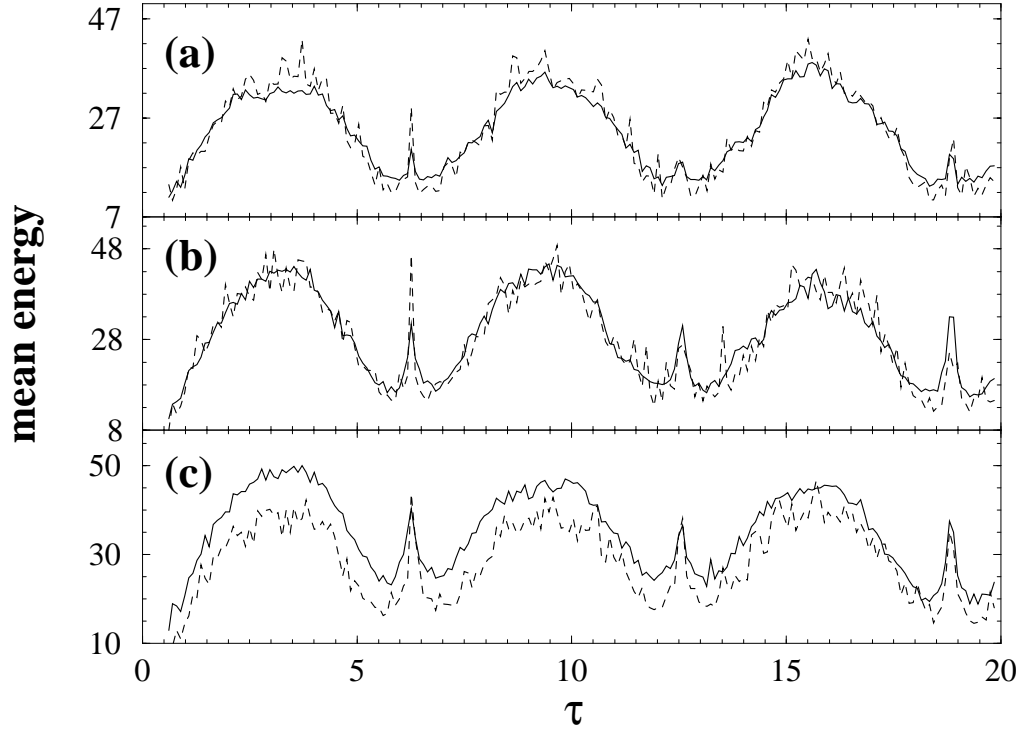


Fig. 4.1: Mean energy (in units of $(2\hbar k_L)^2/M$, c.f. (2.24)) vs. the kicking period τ for an *experimental* ensemble of kicked atoms, after 30 kicks, and with kicking strength $k \simeq 0.8\pi$. (a) no decoherence, mean number of spontaneous emission events per τ : $n_{\text{SE}} \simeq 0$, (b) $n_{\text{SE}} \simeq 0.1$, (c) $n_{\text{SE}} \simeq 0.2$. The duration of the kicking pulses was $\tau_{\text{dur}} = 0.047$. The momentum window used to compute the energies from the momentum distributions was bounded by $n_{\text{cut}} = \pm 40$ (solid) [82], or $n_{\text{cut}} = \pm 60$ (dashed) [159], respectively. The shown range of τ corresponds in laboratory units to $6.5 \dots 210.5 \mu\text{sec}$; any signal above a threshold of 20 counts/atoms in the momentum histogram was included to obtain the energy, and for each value of τ the energy results from an average over 10 (solid) and 3 (dashed) repetitions of the experiment, respectively. The vertical fluctuations as well as the offset with respect to to the numerical data shown in figure 4.6 originates in various experimental problems (see partly section 2.3.3 or [135, 173]). Comparing the two data sets for each value of n_{SE} shows quite plainly how sensitive the mean energy depends on the chosen thresholds and experimental realisations [83, 159]. Experimental data by courtesy of Michael d’Arcy and Gil Summy.

Linear instead of quadratic growth of mean energy?

The first mystery, what concerns the experimental observation of quantum resonances, is related to the momentum distribution of the atomic ensemble. “Ballistic peaks” were reported by Oskay and co-workers [81], arising only from a tiny fraction of the atoms, which indeed shows a quadratically increasing energy. This is in contrast to the bulk of the atomic ensemble that is instead frozen in a rather narrow momentum distribution. In other words, no quadratic growth in the average energy of the atomic ensemble has been observed at $\tau = 2\pi, 4\pi$ in [81], because only a few atoms with the correct quasi-momenta do follow the resonant motion. The resonant values are $\beta = 1/2$, and $\beta = 0, 1/2$, for $\tau = 2\pi$ and $\tau = 4\pi$, respectively (cf. sections 2.2.2 and 2.2.3).

Quantum resonances occur whenever the kicking period is a rational multiple of 4π . In experiments [82, 83, 135, 159], only at the values $\tau = 2\pi, 4\pi, 6\pi$, a special behaviour has been found. Figure 4.1(a) shows experimental data of the mean energy of a large atomic ensemble ($\sim 10^6$ atoms [83, 135]) as a function of the kicking period τ . The quantum resonances correspond to the tiny peaks at the above mentioned values of τ . Only the dashed curve clearly resolves the peak at $\tau = 2\pi$. In the present and the next chapter, we are interested in a detailed understanding of these resonance peaks.

Higher-order quantum resonances?

The overall global structure, apart from signal-to-noise fluctuations, in the mean energy vs. τ is well understood. Time-dependent correlations between subsequent kicks of the δ -kicked rotor evolution induce an effective diffusion constant $D_{\text{eff}} \simeq k^2 \sin^2(\tau/2)$ [57, 227, 254–256], and the mean energy saturates after the quantum break time, i.e. for $t > t_{\text{break}} \sim D_{\text{eff}}$ [6, 56, 63, 64, 80, 256], for all irrational values $\tau/4\pi$. The fine peaks in the experimental data on top of this global structure do change from one experimental run to the other, and hence no higher-order resonances are visible. We suspect that the higher resonances are too sensitive in order to be resolved by the experiments, because their quasi-energy spectra $\epsilon(\theta)$ have a much smaller bandwidth than (2.15) for the fundamental resonances [64]. This means that they manifest clearly only after a relatively long evolution time, which is larger than the typical times of the published experimental data $t \lesssim 30$ kicks [81–83, 135, 159]. In addition, the widths in τ of the higher-order resonance peaks are expected to be even smaller than the ones visible at fundamental resonances $\tau = 2\pi, 4\pi, 6\pi$.

Enhancement of resonance peaks by decoherence?

The third puzzle occurs when adding noise that destroys the phase coherence in-between the imparted kicks. The noise is introduced in a controlled way by forcing the atoms to emit spontaneously in the presence of an additional laser which is near-resonant to an internal electronic transition of the atoms.

This laser may induce a transition, followed by spontaneous emission (SE). The spontaneously emitted photon can depart in an arbitrary direction in position space [211], and the whole process results in a random shift of the centre-of-mass momentum of the atom.

The additional laser beams are switched on immediately after each kick, for a duration $\tau_{\text{SE}} \simeq 0.067\tau$ [82, 83, 135]. The mean number n_{SE} of SE events per atom and per kicking period was varied between $n_{\text{SE}} \simeq 0 \dots 0.2$. The surprising experimental result was that decoherence led to a stabilisation and an enhancement of the resonance peaks in the mean energy vs. τ . Instead of destroying the peaks, decoherence helps them to form as can be seen in figure 4.1, for $n_{\text{SE}} \simeq 0.1$ in (b), and $n_{\text{SE}} \simeq 0.2$ in (c). Qualitatively, we may understand this enhancement effect in the following way. SE events shift the atomic centre-of-mass momenta, as a result of the photon recoil imparted along the relevant axis defined by the kicking potential. These random shifts destroy the conservation of quasi-momenta, see section 2.2.3. Therefore, SE amends the dynamics in a much more intriguing manner than other types of noise (e.g. amplitude noise as random, time-dependent, but spatially uniform fluctuations in the kicking strength k [180, 181]) that do preserve the discrete momentum ladder structure. The latter roots in the spatial periodicity of the kicking potential. Since the quantum resonance conditions depend on quasi-momentum (see end of section 2.2.3), SE shuffles atoms in and out of the resonant motion. That this reshuffling actually leads to an enhancement of the mean energy peaks originates from the form of the full atomic momentum distributions and the experimental imperfections discussed in section 2.3.3.

Our goal is to clarify the above mentioned experimental observations, and to identify quantitatively the physical origin of these puzzles. To this end, we analyse in mathematical detail two characteristic quantities of the dynamical evolution of an atomic ensemble: the momentum distribution of the atoms and their average energy. The particle dynamics is studied at the fundamental quantum resonances $\tau = 2\pi\ell$ ($\ell \in \mathbb{N}$), both in the absence of decoherence, and when external noise is added in the form of SE. The last section of this chapter then tries to reconcile our analytical and numerical results with the experimental findings that inspired the present work.

4.2 Noise-free quantum resonant behaviour

With the help of the Bloch decomposition (2.19), we can first restrict to study the dynamics of a single β -rotor with fixed quasi-momentum β , and average over all quasi-momenta at the end to obtain the experimental observables. At quantum resonance with kicking period $\tau = 2\pi\ell$ ($\ell \in \mathbb{N}$), the wave function of an individual β -rotor can be explicitly derived for all times t . With some mathematical gymnastics, we then obtain the momentum distributions and the average energy of an ensemble of β -rotors from the exact wave functions.

Given a fixed $\beta \in [0, 1)$, the Floquet operator (2.23), at $\tau = 2\pi\ell$ ($\ell > 0$ integer), reads

$$\hat{U}_\beta = e^{-ik \cos(\hat{\theta})} e^{-i\xi \hat{N}} e^{-i\pi\ell\beta^2}, \quad (4.1)$$

where we used the identity $\exp(-i\pi n^2\ell) = \exp(-i\pi n\ell)$, and we defined $\xi \equiv \pi\ell(2\beta \pm 1) \bmod(2\pi)$ to be taken in $[-\pi, \pi)$. The n -independent phase $\exp(-i\pi\ell\beta^2)$ is neglected in the following, since it always cancels when computing quantum expectations. The second operator on the right-hand side of (4.1) will be denoted $\hat{\mathcal{R}}(\xi)$. In the θ -representation it acts as a translation [155] according to:

$$(\hat{\mathcal{R}}(\xi)\psi_\beta)(\theta) = \psi_\beta(\theta - \xi). \quad (4.2)$$

The state of the β -rotor after the t -th kick is then given by the iterated application of (4.1), where $\hat{\mathcal{R}}(\xi)$ only shifts the angle coordinate at each stage:

$$(\hat{U}_\beta^t \psi_\beta)(\theta) = e^{-ik\mathcal{F}(\theta, \xi, t)} \psi_\beta(\theta - t\xi), \quad (4.3)$$

with

$$\mathcal{F}(\theta, \xi, t) = \sum_{s=0}^{t-1} \cos(\theta - s\xi) = |W_t| \cos(\theta + \arg(W_t)), \quad (4.4)$$

where

$$W_t = W_t(\xi) \equiv \sum_{s=0}^{t-1} e^{-is\xi}. \quad (4.5)$$

We denote by n the eigenvalues of the angular momentum \hat{N} . Then, in the \hat{N} representation, the state (4.3) reads (after changing variable from θ to $\theta + \arg(W_t)$):

$$\langle n | \hat{U}_\beta^t \psi_\beta \rangle = e^{in \arg(W_t)} \int_0^{2\pi} \frac{d\theta}{\sqrt{2\pi}} e^{-in\theta - ik|W_t| \cos(\theta)} \psi_\beta(\theta - t\xi - \arg(W_t)). \quad (4.6)$$

If the initial state of the particle is a plane wave (2.22) of momentum $p_0 = n_0 + \beta_0$, ξ takes the constant value $\xi_0 = \pi\ell(2\beta_0 \pm 1) \bmod(2\pi)$. Substituting (2.22) in (4.6), and computing the integral by means of formula (F.1), the momentum distribution for the β_0 -rotor at time t is:

$$P(n, t | n_0, \beta_0) = J_{n-n_0}^2(k|W_t|), \quad (4.7)$$

where $J_n(\cdot)$ is the Bessel function of first kind and order n . Using the identity (F.2), and $J_n(\cdot) = (-)^n J_{-n}(\cdot)$ together with $\sum_n J_n^2(\cdot) = 1$ [157] one computes the expectation value of p^2 (or of the energy by dividing by 2):

$$\begin{aligned} \overline{p^2}(n_0, \beta_0, t) &= \sum_n (n + \beta_0)^2 P(n, t | n_0, \beta_0) \\ &= \sum_m (m + n_0 + \beta_0)^2 J_m^2(k|W_t|) \\ &= \sum_m m^2 J_m^2(k|W_t|) + \sum_m (n_0 + \beta_0)^2 J_m^2(k|W_t|) \\ &= (n_0 + \beta_0)^2 + \frac{1}{2} k^2 |W_t|^2. \end{aligned} \quad (4.8)$$

Already at this stage, we arrived at a very important result. The momentum distribution or its second moment, the mean energy, is determined by the function W_t . In the noise free case, W_t is completely deterministic, and one must average solely over all initial conditions n_0, β_0 to obtain the experimental observables. As will be shown section 4.3, decoherence turns the function W_t into a stochastic process, whose behaviour again completely determines the momentum distribution and the mean energy of the atomic ensemble. Without noise, and for the resonant quasi-momenta, $\beta = 1/2 + j/\ell \bmod(1)$, with $j = 0, 1, \dots, \ell - 1$, and $\xi = 0$, the function $W_t = t$, i.e. all terms in (4.5) add up “in phase”. For non-resonant β and irrational $\xi/2\pi$, the terms in (4.5) add up to a quasi-periodic “walk” in the complex plane. The periodicity is perfect for rational $\xi/2\pi$. Now for $t \rightarrow \infty$, the effect of noise, which randomly changes quasi-momentum, and hence ξ , leads to a *random* walk in the complex plane given by the summation of the phases in (4.5). The resulting asymptotic momentum distribution will be derived in section 4.3.4.

Explicit computation of the geometric series (4.5) yields if $\xi_0 \neq 0$:

$$|W_t| = \left| \frac{e^{-i\xi_0 t} - 1}{e^{-i\xi_0} - 1} \right| = \left| e^{-i\xi_0(t-1)/2} \frac{e^{-i\xi_0 t/2} - e^{i\xi_0 t/2}}{e^{-i\xi_0/2} - e^{i\xi_0/2}} \right| = \left| \frac{\sin(t\xi_0/2)}{\sin(\xi_0/2)} \right|. \quad (4.9)$$

As stated above, for $\xi_0 = 0$ one obtains $|W_t| = t$. Then the distribution (4.7) spreads linearly in time, and the average kinetic energy increases like $k^2 t^2/4$. $\xi_0 = 0$ corresponds to the resonant values of quasi-momentum $\beta_0 = 1/2 + j/\ell \bmod(1)$, $j = 0, 1, \dots, \ell - 1$. For any other value of β , the distribution changes in time in a quasi-periodic manner. It oscillates in time with the approximate period $\pi\xi_0^{-1}$, inverse to the detuning of β_0 from the nearest resonant value. At any time t , the distribution is negligibly small at $|n - n_0| > k |\csc(\xi_0/2)| > k|W_t|$, since the Bessel functions decay faster than exponentially in this case [157, 257].

4.2.1 Momentum distributions

With the conditional distribution (4.7), we can derive the average momentum distribution of an atomic ensemble for a given *initial* momentum distribution of the atoms. The latter is given by the experimental realisation, and in the following we map it to a distribution for the β -rotors with $\beta \in [0, 1)$.

Incoherent ensemble of atoms

If the initial state of the particle is a wave packet, then it is a coherent superposition of continuously many plane waves with different quasi-momenta, which are non-resonant except for a finite set of values $\beta_0 = 1/2 + j/\ell \bmod(1)$, $j = 0, 1, \dots, \ell - 1$. It can then be proven that the asymptotic growth of energy in time is proportional to $k^2 t/4$ [145]. Here we consider the case when

the initial atomic ensemble is an *incoherent* mixture of plane waves. Numerical simulations based on such choices of an initial state have shown satisfactory agreement with experimental data [83,176]. The initial momentum distribution shall be described by a density $f(p)$. We can equivalently consider an ensemble of β -rotors, with β distributed in $[0, 1)$ with the density

$$f_0(\beta) = \sum_{n=-\infty}^{+\infty} f(n + \beta). \quad (4.10)$$

In the case when $f(p)$ is Gaussian with standard deviation σ (a reasonable assumption for the experiments reported in [81–83]), the Poisson summation formula [258, 259] yields

$$\begin{aligned} f_0(\beta) &= \sum_{m=-\infty}^{\infty} \bar{f}(m) e^{i2\pi m\beta} \\ &= \bar{f}(0) + \bar{f}(1) e^{i2\pi\beta} + \bar{f}(-1) e^{-i2\pi\beta} + O(|m| \geq 2) \\ &= 1 + 2e^{-2\pi^2\sigma^2} \cos(2\pi\beta) + O(e^{-8\pi^2\sigma^2}). \end{aligned} \quad (4.11)$$

Here \bar{f} denotes the Fourier transform of the density f . For $\sigma > 1$, that is relevant for the experiments referred to in section 4.1*, it is practically indistinguishable from the uniform distribution $f_0(\beta) = 1$. Each β -rotor is described by a statistical state, which attaches the probability $f_0(\beta)^{-1} f(n + \beta)$ to the momentum eigenstate $|n\rangle$.

The momentum distribution $P(p, t)$ of the particle at time t is obtained as follows. For any given $\beta_0 \in [0, 1)$, averaging (4.7) over the different n_0 of the initial distribution yields the momentum distribution $\bar{P}(n, t|\beta_0)$ for the β_0 -rotor. Weighted by $f_0(\beta_0)$, this is the same as the momentum distribution $P(p, t)$ of the particle over the ladder $p = n + \beta_0$ (β_0 fixed, n variable). The on-ladder distributions corresponding to different β_0 combine like a jigsaw puzzle in building the global momentum distribution for the particle. The result is a complicated function of p which is plotted after $t = 50$ kicks in figure 4.2. The distribution oscillates on the scale $1/t$, which follows from the ξ_0 -dependence of (4.7) and (4.9). Nevertheless, on average, this distribution evolves into a steady-state distribution. This may be shown either by time-averaging [160], or by coarse-graining. In the following section, we present the latter approach in detail, and derive the steady-state distribution that is obtained in the asymptotic limit $t \rightarrow \infty$.

Coarse-grained distribution

Because of the above mentioned complicated local (i.e. within intervals $n < p < n + 1$) structure of the momentum distribution as a function of p , it is hard

*Recently, kicked rotor dynamics showing the influence of timing noise (random fluctuations in the kicking period) on dynamical localisation have been reported with $\sigma < 1$ [166].

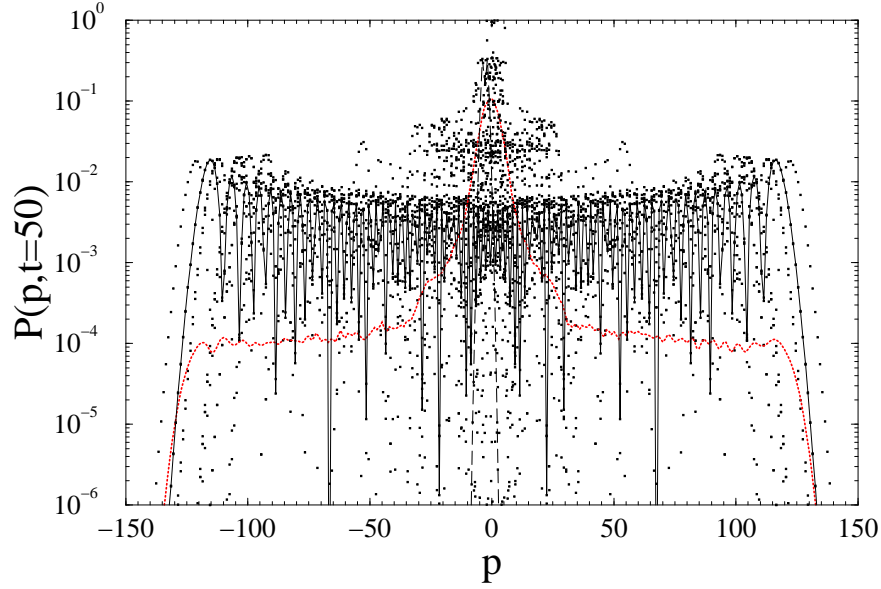


Fig. 4.2: The momentum distribution of an ensemble of 50 particles, with an initial Gaussian distribution of $p_0 = n_0 + \beta_0$ (for the experimentally reported standard deviation $\sigma \simeq 2.7$ [82, 83, 135]). Plotted as dots are the individual β_0 -rotor distributions $|\overline{\psi}_{\beta_0}(t, n)|^2$ (over the corresponding, distinct integer momentum ladders $n = [p]$) vs. $p = n + \beta_0$; after $t = 50$ kicks, $k = 0.8\pi, \tau = 2\pi$. The β_0 -rotors with the smallest detuning from the resonant quasi-momenta follow the resonant motion for longer times, an example is presented by the solid line. The ones with larger detunings stop following the resonant acceleration, after some time $t \ll 50$, see dashed line for such a case. For comparison, the dotted line shows the normalised coarse-grained distribution of a larger ensemble taken from figure 4.3.

to characterise the distribution, and apart from the global structure, it is not useful for the comparison with experimental data. One way of removing the fast oscillations is replacing $P(p, t)$ in each interval $n < p < n+1$ by its integral $P_n(t)$ over that interval. This corresponds to using a bin size $2\hbar k_L$ (c.f. (2.24)) for the observed distributions, which is also the typical resolution in the determination of the momentum distributions in the experiments reported in [82, 83, 159, 260]. Assuming $f(p)$ to be coarse-grained itself, the new distribution is approximately computed in the form:

$$P_n(t) = \sum_m M_{n-m}(t) f(m), \quad (4.12)$$

where

$$M_n(t) = \int_0^1 d\beta J_n^2(k|W_t|). \quad (4.13)$$

Substituting variables and noting that J_n^2 is an even function of its argument we may rewrite

$$M_n(t) = \int_{-\pi\ell}^{\pi\ell} \frac{d\xi}{2\pi\ell} J_n^2 \left(k \left| \sin \left(\frac{t\xi}{2} \right) \csc \left(\frac{\xi}{2} \right) \right| \right) = \int_{-\pi}^{\pi} \frac{dx}{2\pi} J_n^2 (k \sin(tx) \csc(x))$$

$$\stackrel{y=xt}{=} \int_{-\pi}^{\pi} \frac{dy}{(2\pi)^2} \sum_{r=0}^{t-1} \frac{2\pi}{t} J_n^2 \left(k \sin(y) \csc \left(\frac{y}{t} + \frac{2\pi r}{t} \right) \right), \quad (4.14)$$

where in the last step we used the periodicity of the sine. In the limit when $t \rightarrow \infty$ and $2\pi r/t \rightarrow \alpha$, the sum over r approximates the integral over α , and (4.14) converges to

$$M_n^* = \frac{1}{(2\pi)^2} \int_{-\pi}^{\pi} dy \int_0^{2\pi} d\alpha J_n^2 (k \sin(y) \csc(\alpha)). \quad (4.15)$$

The steady-state coarse-grained distribution P_n^* is then obtained by replacing (4.15) in (4.12). We do not know if the double integral may be computed in closed form. In appendix A the following (non-optimal) estimate is derived, for the wings of the momentum distribution, valid for any integer $N > k$:

$$\sum_{|n| \geq N} M_n^* \leq 2 \left(\frac{ke}{16} \right)^{\frac{2N}{2N+1}} N^{\frac{1-2N}{1+2N}} \left(2 + \frac{1}{N} \right). \quad (4.16)$$

Using this estimate it is easy to compute that for $k > 1$ the total probability carried by states $|n| > 4k$ is not larger than $\simeq 0.31$. Therefore, at large kicking strength k , the distribution is rather narrow as compared to the exponentially localised distribution which is observed far from resonance, because the width of the latter scales like k^2 [63, 64, 106]. In appendix A it is further proven that the distribution (4.15) has the following large- $|n|$ asymptotics:

$$M_n^* \sim \frac{4k}{\pi^3 n^2} \text{ as } |n| \rightarrow \infty. \quad (4.17)$$

Such an algebraic decay $\propto 1/n^2$ carries over to the coarse-grained momentum distribution P_n^* whenever the initial momentum distribution $f(p)$ is fast decaying (e.g. like a Gaussian):

$$P_n(t) \rightarrow P_n^* \sim \sum_m \frac{4k}{\pi^3 (n-m)^2} f(m) \text{ as } |n| \rightarrow \infty. \quad (4.18)$$

The convergence of the coarse-grained distributions to the steady-state distribution is illustrated in figure 4.3, where the evolution of statistical ensembles of particles with an initial Gaussian momentum distribution was numerically simulated. The central part of the distribution quite early stabilises in the final form of a narrow peak of width $\sim k$. Away from this peak, the algebraic tail $\propto n^{-2}$ develops over larger and larger momentum ranges as time increases in the wake of two symmetric, tiny ‘‘ballistic peaks’’ that move away linearly in time. The fall of the distribution is quite steep past such peaks. This is easily

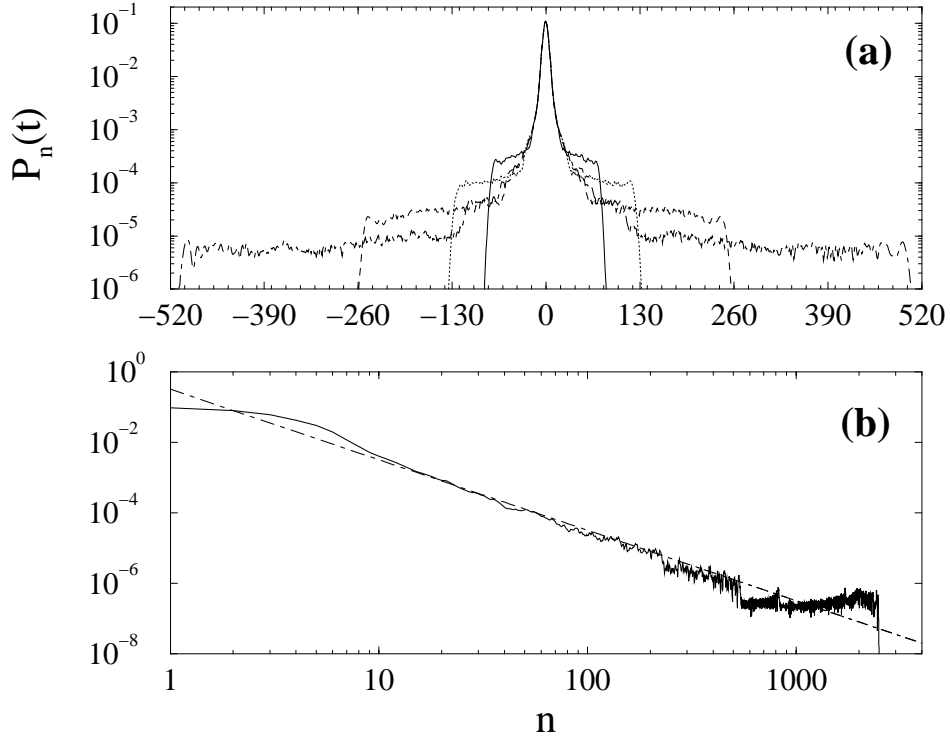


Fig. 4.3: Evolution of coarse-grained momentum distributions (4.12) at quantum resonance with $\tau = 2\pi$, and kicking strength $k = 0.8\pi$, for an ensemble of 10^4 atoms, without decoherence. The initial momentum distribution is centred Gaussian, with root-mean-square deviation $\sigma \simeq 2.7$. (a) Distributions for $t = 30$ (solid lines), $t = 50$ (dotted), $t = 100$ (dashed), $t = 200$ (dash-dotted). (b) Doubly logarithmic plot of the distribution at $t = 1000$ (solid line), compared to the asymptotic formula $4k/(\pi^3 n^2)$ (dash-dotted line) (4.17). No cutoffs are used, so the distributions characterise the ideal behaviour of an ensemble of δ -kicked particles.

understood from the first equation in (4.14): since $|\sin(tx) \csc(x)| \leq \pi t/2$, at $n > \pi kt/2$ the integrand decays faster than exponentially [157, 257]. The distribution in figure 4.3 (b) has stabilised to the limit distribution over a broad momentum range. Apart from the far tail, where the moving peak structure is still apparent, the distribution follows the asymptotic decay (4.17) already for $|n| \gtrsim 15$. Hence, using (4.17), the total probability on states $|n| > 40$ is $\sim 8 \times 10^{-3}$.

From the above analysis, we obtain that all moments of p of order ≥ 1 diverge as $t \rightarrow \infty$, in spite of the onset of the stationary distribution, owing to the slow algebraic decay (4.18) of the latter. For the case of the second moment, which is (apart from a factor 2) just the mean energy of the ensemble, the growth is actually *linear in time*, as we shall presently show.

4.2.2 Average kinetic energy

The mean kinetic energy of an ensemble of rotors at time t is obtained by averaging (4.8) over the initial momentum distribution. In the following, the expectations obtained by averaging over a classical (incoherent) ensemble will be denoted $\mathcal{E}\{\cdot\}$, while quantum expectations of the energy of one individual β -rotor will be denoted \bar{E} . The mean energy then reads

$$\mathcal{E}\{\bar{E}(t)\} = \mathcal{E}\{\bar{E}(0)\} + \frac{k^2}{4} \int_0^1 d\beta f_0(\beta) \frac{\sin^2(t\pi\ell(\beta - 1/2))}{\sin^2(\pi\ell(\beta - 1/2))}. \quad (4.19)$$

As $t \rightarrow \infty$, the fraction in the integrand, multiplied by ℓ/t , tends to a periodic δ function of $(\beta - 1/2)$ with period $1/\ell$. Thus (4.19) has the following $t \rightarrow \infty$ asymptotics:

$$\mathcal{E}\{\bar{E}(t)\} \sim \mathcal{E}\{\bar{E}(0)\} + \frac{k^2 t}{4\ell} \sum_{j=0}^{\ell-1} f_0(\beta^{(j)}), \quad (4.20)$$

where $\beta^{(j)} = 1/2 + j/\ell \pmod{1}$ are the resonant quasi-momenta. In the case when $f_0(\beta) \equiv 1$, i.e. the initial quasi-momentum distribution is uniform in $[0, 1)$, this formula is exact for *all* times t (by (F.13)):

$$\mathcal{E}\{\bar{E}(t)\} = \mathcal{E}\{\bar{E}(0)\} + \frac{k^2 t}{4}. \quad (4.21)$$

With (4.11), (4.21) is practically exact at all times for an initial Gaussian distribution with width $\sigma > 1$ around the origin. Such a distribution corresponds to the initial momentum distribution in the experiments reported in [81–83]. Higher-order energy moments may be likewise computed. For large but finite t , we observe from figure 4.3(a) that the n^{-2} decay of the distribution is truncated at $n \sim kt$, since the speed in momentum of the resonant rotors is determined by square root of (2.14). Consequently, the variance of energy increases like t^3 . The increase of other moments may also be estimated in this way. Higher moments are important for the comparison with the noisy evolution, which we will discuss in the following section.

4.3 Destruction of quantum resonances by decoherence

One major incentive for the present analysis was the rather counter-intuitive experimental observation that, for a given interaction time, the mean energy was found to increase when spontaneous emission (SE) was added, with respect to the absence of external dissipative noise (see figure 4.1 and [82, 83]). The function (4.5) provides some intuition about what will happen when the quasi-momenta are reshuffled in a random manner by SE events. By virtue of the randomisation of the phases ξ (4.5) will turn into a random process, whose

statistics determine the long time asymptotics of the momentum distribution. The statistical assumptions which we use to model the stochastic δ -kicked particle evolution are a compromise between physical adherence and mathematical convenience. By comparing our results with more realistic numerical simulations we demonstrate that their validity does not crucially depend on our technical assumptions. In the following analysis we neglect the delay between absorptions and subsequent SEs. We hence assume that the atom undergoes random momentum changes by virtue of SE at a discrete sequence of random times. Both the SE times and the corresponding momentum changes are modelled by classical random variables, independent of the centre-of-mass motion of the atom. This assumption is reasonable as long as the mean number of SEs n_{SE} is relatively small; otherwise, the atoms may, in the average, be slowed down or cooled – a velocity-dependent effect, which cannot be accounted for under this assumption. On the other hand, at the high field intensity of a quasi-resonant laser beam, which is required for large n_{SE} , stimulated emission would prevail. Stimulated emission would induce biased momentum changes along the axis of the SE inducing laser, and hence act in a similar way as the kicking pulses.

The statistical atom dynamics may be studied by investigating the stochastic Hilbert-space evolution of the atomic state vector [176, 184, 261–264][†]. More specifically, we assume an initial incoherent mixture of plane waves with a distribution $f(p_0)$. We further assume that all the variables describing SE events are given and fixed. Their specification defines a *realisation* of the random SE events. Then we compute the deterministic evolution of the atomic state vectors up to time t . The quantum probability distribution of an observable in the final state depends on the chosen realisation and on the initial state as well; averaging over both yields the final statistical distribution for that observable.

We will see that the dissipative influence of SE on the centre-of-mass motion is typically small and can be described independently from the effect on the phase evolution in (4.5). These two effects of the coupling to the environment are separated by a stochastic gauge transformation, which is introduced in the next section.

4.3.1 Stochastic gauge

This section shows that, although the random SE events destroy the true quasi-momentum conservation, the problem can be formulated in an appropriate gauge for which momentum is not affected by SE. This formally implies the conservation of quasi-momentum, while the random momentum shifts are in-

[†]This approach was first implemented for the study of randomised δ -kicked rotor dynamics in [265]. Please note that in references [176, 184] SE occurs usually during the kicking pulse while in our model – corresponding to the experiments of [82, 83] – SE is induced by a second, independent light field applied after each kick.

incorporated as additional time-dependent phases in the Floquet operator. Let $|\psi(t)\rangle$ be the state vector of the atom immediately after the t -th kick. Let the integer ν_t denote the number of SEs during the subsequent SE-inducing window. Such events are assumed instantaneous. Denote s_{j-1} the delay (in physical time) of the j -th event with respect to the $(j-1)$ -th one, and d_j the momentum change of the atom induced by the j -th SE. For notational convenience a 0-th fictitious SE is assumed to occur immediately after the t -th kick, and a $(\nu_t + 1)$ -th one immediately before the $(t+1)$ -th kick, with $d_0 = d_{\nu_t+1} = 0$.

The state vector immediately after the $(t+1)$ -th kick is, apart from an inessential phase factor,

$$|\psi(t+1)\rangle = \hat{S}(\delta_t) e^{-ik \cos(\hat{X})} e^{-i\tau(\hat{P}+\chi_t)^2/2} |\psi(t)\rangle, \quad (4.22)$$

where:

$$\chi_t = \sum_{j=1}^{\nu_t} \frac{s_j}{\tau} \sum_{k=0}^j d_k, \quad \delta_t = \sum_{j=0}^{\nu_t} d_j, \quad \hat{S}(\cdot) = e^{i(\cdot)\hat{X}}. \quad (4.23)$$

Note that the first and the second operator on the right-hand side of (4.22) commute because both only depend on \hat{X} . In addition, the translation operator \hat{S} has the property $\hat{S}(\alpha+\mu) = \hat{S}(\alpha)\hat{S}(\mu)$. The conservation of quasi-momentum is broken by the operator $\hat{S}(\delta_t)$, which shifts the momentum ladders of the Bloch decomposition (2.19). However, conservation of quasi-momentum may be restored by means of the substitution:

$$|\psi(t)\rangle = \hat{S}(\delta_0 + \delta_1 + \dots + \delta_{t-1}) |\tilde{\psi}(t)\rangle \quad (4.24)$$

which is a time-dependent, momentum shifting gauge transform; the resulting gauge will be termed the *stochastic gauge* in the following. Replacing (4.24) in (4.22), and using

$$e^{-i\tau(\hat{P}+\alpha)^2/2} \hat{S}(\gamma) = \hat{S}(\gamma) e^{-i\tau(\hat{P}+\alpha+\gamma)^2/2},$$

one finds:

$$\begin{aligned} |\psi(t+1)\rangle &= \hat{S}(\delta_t) e^{-ik \cos(\hat{X})} e^{-i\tau(\hat{P}+\chi_t)^2/2} \hat{S}(\delta_0 + \delta_1 + \dots + \delta_{t-1}) |\tilde{\psi}(t)\rangle \\ &= \hat{S}(\delta_0 + \delta_1 + \dots + \delta_t) e^{-ik \cos(\hat{X})} e^{-i\tau\left(\hat{P}+\chi_t + \sum_{s=0}^{t-1} \delta_s\right)^2/2} |\tilde{\psi}(t)\rangle \\ &= \hat{S}(\delta_0 + \delta_1 + \dots + \delta_t) |\tilde{\psi}(t+1)\rangle. \end{aligned} \quad (4.25)$$

Therefore, in the stochastic gauge the state is propagated in the following manner:

$$|\tilde{\psi}(t+1)\rangle = e^{-ik \cos(\hat{X})} e^{-i\tau\left(\hat{P}+\chi_t + \sum_{s=0}^{t-1} \delta_s\right)^2/2} |\tilde{\psi}(t)\rangle. \quad (4.26)$$

This evolution does preserve quasi-momentum (in the same way as does (2.8) by (2.12)), and the reduction to β -rotor dynamics may be performed as described in section 2.2.3, leading to

$$|\tilde{\psi}_\beta(t+1)\rangle = \hat{U}_\beta(t) |\tilde{\psi}_\beta(t)\rangle; \quad \hat{U}_\beta(t) = e^{-ik \cos(\hat{\theta})} e^{-i\tau(\hat{N}+\eta_t)^2/2}, \quad (4.27)$$

where

$$\eta_t = \beta + \chi_t + \sum_{s=0}^{t-1} \delta_s . \quad (4.28)$$

In this way the stochastic evolution (4.23) has been separated in two parts. One of these is described in (4.24) by the operator \hat{S} ; the other is the evolution (4.27) in the stochastic gauge. The former is just a translation (in momentum) by the total momentum imparted by SE during the considered time. It is the latter part that encodes the *stochastic* phase evolution.

4.3.2 Theoretical model for randomised dynamics

In experiments, SE occurred at random times within SE-inducing time windows, and there is one such window immediately after each kick. We shall say that a “*SE event*” occurs at the integer time t , whenever *at least one* SE occurs in the window following the t -th kick. In this way, the number of SEs may be larger than the number of SE events. The probability of a SE event is denoted p_{SE} . The assumptions (S1-3) below build on the separation of different time scales. The experimental time window for SE, $\tau_{\text{SE}} = 0.067\tau = 0.424$, for $\tau = 2\pi$ (or $4.5 \mu\text{sec}$ in [82, 83]), is on the one hand very large compared to the time scales given by the Rabi frequency of the atomic transition and by the inverse SE damping rate [82, 83]. On the other hand, τ_{SE} is very small compared to the kicking period. It is therefore reasonable to neglect memory effects inherent to SE processes [266]. A complete randomisation of quasi-momentum after each SE-inducing cycle occurs when the mean number of SEs per period is large, $n_{\text{SE}} \gg 1$: then effective averaging leads to quasi-independent η_t in (4.28). If n_{SE} is small, then complete randomisation requires that the distribution of the momentum shifts $\delta_t \bmod(1)$ is uniform in $[0, 1)$. On the other hand, δ_t is the sum of a random number of momentum changes owing to single SEs. If these are assumed independent and identically distributed, then each of them has to be uniformly distributed in some interval of integer width. The assumption for the following analysis are now specified as follows:

(S1) SE events occurring at different times are statistically independent. Hence, the random variables δ_t ($t = 0, 1, 2, \dots$) specifying the total (projected onto the axis of the kicking potential) momentum change produced by SE in the t -th kicking period (equation (4.23)) are independent, identically distributed random variables.

(S2) The finite duration of the SE-operating windows is negligibly small compared to the kicking period. Hence, $s_{\nu_t} \approx \tau$ while $s_j \approx 0$ for $j < \nu_t$, so that $\chi_t \approx \delta_t$ in (4.23), and $\eta_t \approx \beta_0 + \sum_{s=0}^t \delta_s$ in (4.28). Different SEs may occur in the same kicking period, each separately contributing to the total momentum change δ_t recorded in that period; nevertheless, their separation in time is neglected.

(S3) The occurrence of a SE event results in total randomisation of the quasi-momentum. Given assumption (S2), this is equivalent to assuming that the conditional distribution of the variable $\delta_t \bmod(1)$, given that a SE event occurs at time t , is uniform in $[0, 1)$ (in units of two photon recoils, see section 2.3.1). We further assume a zero mean for the distribution of δ_t . While no further specification is needed for the formal elaborations below, in numerical simulations we shall in fact use a uniform conditional distribution in $[-1/2, 1/2]$ (in units of two photon recoils).

(S4) As in the SE-free case (section 4.2.1), we assume the initial statistical ensemble to be an incoherent mixture of plane waves.

With (S1-3) we derive now the equivalent of (4.7) in the presence of SE. (S4) is used when computing the average kinetic energy and the asymptotic momentum distributions of an atomic ensemble (section 4.3.3 and 4.3.4).

Let SE events occur after $t_0 \equiv 0$ at integer waiting times $t_1 = \Delta_0, t_2 = \Delta_0 + \Delta_1, \dots, t_j = t_{j-1} + \Delta_{j-1}, \dots$. The variables Δ_j ($j \geq 0$) are integer, independent random variables. Under assumption (S1) they are distributed on the positive integers n with probabilities:

$$\rho(n) = p_{\text{SE}}(1 - p_{\text{SE}})^{n-1} \text{ for } n > 0, \quad \rho(0) = 0, \quad (4.29)$$

where p_{SE} is the probability that at least one SE takes place in one kicking period. For all integers $t > 0$ we define $N_t \equiv \max\{j : t_j \leq t\}$, the number of SE events occurring not later than time t , and $N_0 = 0$. The integer random variables $N_t, t \geq 0$ define a Bernoulli process[‡] [267].

After such preliminaries, we set out to study the evolution in the stochastic gauge, as defined by equations (4.27). The quasi-momentum β of a β -rotor is constant in time, and for each rotor $\eta_0 = \beta$ (SE events are allowed immediately after kicks, and no kick occurs at $t = 0$). In the stochastic gauge, the random propagator from time 0 to time t for the β -rotor is given by the ordered product

$$\hat{U}_{S,\beta}(t) = \prod_{s=0}^{t-1} \hat{U}_{\beta}(s). \quad (4.30)$$

The subscript S on the left-hand side refers to the stochastic gauge. The one-step propagators $\hat{U}_{\beta}(t)$ are defined in equation (4.27). Note that the $\hat{U}_{\beta}(t)$ depend on the time elapsed between $s = 0$ and $s = t - 1$ through the accumulated shifts in η_t (4.28). Similar to what was done in section 4.2.1 at *exact resonance* $\tau = 2\pi\ell$ one may write (cf. equation (4.1)):

$$\hat{U}_{\beta}(t) = e^{-ik \cos(\hat{\theta})} e^{-i\xi_t \hat{N}} \equiv e^{-ik \cos(\hat{\theta})} \hat{\mathcal{R}}(\xi_t), \quad (4.31)$$

where $\xi_t = \pi\ell(2\eta_t \pm 1)$. $\hat{\mathcal{R}}(\xi_s)$ again acts as a translation in the θ -representation. Although η_t is not restricted in the interval $[0, 1)$ in equation (4.27), the resonance condition allows for ξ_t to be taken in $[-\pi, \pi)$ in (4.31). Under assumption

[‡]This process must not be confused with the continuous Poisson process [267] that may be used for the SEs occurring within *one* and the same kicking period; see section 4.3.5.

(S2), ξ_t has a constant value $\tilde{\xi}_j$ in $[-\pi, \pi)$ in-between $t = t_j$ and $t = t_{j+1}$, such that

$$\tilde{\xi}_j \equiv \pi\ell(2\beta_0 \pm 1) + \pi\ell(2\eta_j \pm 1) \bmod(2\pi) = \xi_0 + 2\pi\ell \sum_{m=0}^j \delta_m \bmod(2\pi), \quad (4.32)$$

where δ_m is the total momentum imparted by the m -th SE event. Hence, $\xi_t = \tilde{\xi}_{N_t}$ in-between the t -th kick and the $(t+1)$ -th one. A realisation of the SE events is assigned by specifying the values of all the SE random variables just defined, which we collectively denote by the shorthand notations δ for the random momentum shifts and Δ for the random times of SE events. Once the final observation time t and the realisation are fixed, for notational convenience we re-define $\Delta_{N_{t-1}} = t - t_{N_{t-1}}$. Replacing (4.32) in (4.31), and then in (4.30), we get

$$\hat{U}_{S,\beta}(t) = \prod_{s=0}^{t-1} \left(e^{-ik \cos(\hat{\theta})} \hat{\mathcal{R}}(\tilde{\xi}_{N_s}) \right). \quad (4.33)$$

By repeated use of

$$e^{-ik \cos \hat{\theta}} \hat{\mathcal{R}}(\xi) = \hat{\mathcal{R}}(\xi) e^{-ik \cos(\hat{\theta} + \xi)},$$

all the translation operator are shuffled to the left in (4.33). Then the evolution operator up to time t (4.30) may be rewritten in the form:

$$\hat{U}_{S,\beta}(t) = \hat{\mathcal{R}} \left(\xi_0 + \tilde{\xi}_{N_1} + \dots + \tilde{\xi}_{N_{t-1}} \right) e^{-ik\mathcal{F}(\hat{\theta}, \delta, \Delta, t)}, \quad (4.34)$$

where we defined

$$\mathcal{F}(\hat{\theta}, \delta, \Delta, t) \equiv \sum_{s=0}^{t-1} \cos \left(\hat{\theta} + \sum_{r=0}^s \tilde{\xi}_{N_r} \right). \quad (4.35)$$

$\mathcal{F}(\hat{\theta}, \delta, \Delta, t)$ contains all the shifts in the angle variable in the sum within the cosine. Alike in (4.6) it solely represents a phase in the θ -representation, with the important difference that $\mathcal{F}(\hat{\theta}, \delta, \Delta, t)$ depends on the random variables $\tilde{\xi}_{N_r}$ ($0 \leq r < t$). To arrive at the analogue expression of (4.7) in the case without SE, we next define $\gamma_j = \sum_{m=0}^{j-1} \Delta_m \tilde{\xi}_m$. Replacing s in (4.35) by $s = t_j + l$ with $j = N_s$, and summing over j, l separately, we obtain

$$\mathcal{F}(\hat{\theta}, \delta, \Delta, t) = \sum_{j=0}^{N_{t-1}} \sum_{l=0}^{\Delta_j-1} \cos(\hat{\theta} + \gamma_j + l\tilde{\xi}_j). \quad (4.36)$$

With the definitions

$$z_j = \sum_{r=0}^{\Delta_j-1} e^{i\gamma_j + ir\tilde{\xi}_j}; \quad Z_m = \sum_{j=0}^m z_j; \quad W_t = Z_{N_{t-1}}, \quad (4.37)$$

we finally arrive at

$$\mathcal{F}(\hat{\theta}, \delta, \Delta, t) = |W_t| \cos \left(\hat{\theta} + \arg(W_t) \right).$$

Note that W_t here differs from W_t in equation (4.4). W_t is now a random process, which itself depends on the realisation of the random variables (δ, Δ) . The latter encode the random momentum shifts and the random times of SE events, respectively. By (S4), the initial state of the atom is assumed to have a definite initial momentum, i.e. to be a plane wave of momentum $p_0 = n_0 + \beta_0$. Given a realisation (δ, Δ) , we operate on the corresponding rotor state (2.22) with the propagator (4.34). The (random) state of the rotor at time t is given, in the momentum representation, by:

$$\begin{aligned} \langle n | \hat{\mathcal{U}}_{S, \beta_0}(t) \psi_{\beta_0} \rangle &= e^{i\varphi_t} \int_0^{2\pi} \frac{d\theta}{2\pi} e^{-i(n-n_0)\theta - ik|W_t|\cos(\theta)}, \\ \varphi_t &= (n - n_0)\arg(W_t) - n\gamma_{N(t-1)}. \end{aligned} \quad (4.38)$$

The distribution of momenta n at time t is

$$P(n, t | n_0, \beta_0, \delta, \Delta) = J_{n-n_0}^2(k|W_t|). \quad (4.39)$$

This is formally identical to (4.7), but now W_t depends on the initial quasi-momentum β_0 and on the realisation of the SE events as well. It is a stochastic process and the random state (4.38) performs a random walk in the rotor's Hilbert space. Computation of statistical averages requires averaging over the SE random variables (δ, Δ) , and for an initial atomic ensemble also over the initial momenta $p_0 = n_0 + \beta_0$. Under our assumptions all such variables are classical random variables. Expectations (respectively, conditional expectations) obtained by averaging over such classical variables are denoted $\mathcal{E}\{.\}$ (respectively, $\mathcal{E}\{.\}.$). For instance, $\mathcal{E}\{.|p_0\}$ stands for the average over the SE variables alone, given the value of p_0 , or equivalently of n_0 and β_0 (alternatively $\xi_0 = \pi\ell(2\beta_0 \pm 1)$).

The large- t behaviour of the stochastic process W_t that drives the stochastic rotor evolution is ruled by the large m behaviour of the process Z_m (4.37). The properties of the latter process are completely determined by the assumptions (S2) and (S3). Together with equation (4.32) assumption (S3) entails that the ξ_j are mutually independent random variables, uniformly distributed in $[-\pi, \pi)$ (with the possible exception of ξ_0 , whose distribution is defined by the initial ensemble). This fact has the following consequences, which are derived in the next section and in appendix B: the complex variables z_j, z_k are independent whenever $|j - k| \geq 2$. Moreover z_j, z_k are pairwise uncorrelated whenever $j + k > 1$:

$$\mathcal{E}\{z_j z_k^* | \Delta\} = \delta_{jk} \Delta_j, \quad \mathcal{E}\{z_j z_k | \Delta\} = 0. \quad (4.40)$$

These properties of the z_j allow us to compute the expectations and higher moments of the random process $|W_t|$. Furthermore, this shows that the process Z_m is a random walk in the complex plane, which originates from the summation of random phase terms in (4.37). Equivalently, the distribution of Z_m approaches an isotropic Gaussian distribution in the complex plane as $m \rightarrow \infty$ (see appendix B). On account of the properties of the Bernoulli process, the process W_t at large t has quite similar features: in appendix C we show that as $t \rightarrow \infty$, the distribution of $|W_t|$ approaches an isotropic Gaussian distribution

in the complex plane centred at 0.

The random walk property manifests in a linear growth of the mean energy in time t , as well as in a Gaussian momentum distribution for large t [160]. The asymptotic momentum distribution will be derived in section 4.3.4 below. In the next section, we will prove that the mean energy indeed increases almost alike without SE (4.21), for a uniform initial distribution of quasi-momentum, i.e. for $f_0(\beta_0) = 1$:

$$\mathcal{E}\{\bar{E}(t)\} = \mathcal{E}\{\bar{E}(0)\} + \frac{1}{4}k^2t + \frac{1}{2}D(t-1). \quad (4.41)$$

The additional term $D(t-1)/2$ arises from the “heating” effect of SE events, which do not only change quasi-momentum, but also the integer part of momentum. In experiments, this heating is typically very small, and its diffusion constant D depends on the mean number of SEs per kicking period (see section 4.3.5). We conclude that the growth of the mean energy is but *weakly* affected by SE, in contrast to what is observed in the experiments, cf. figure 4.1. This discrepancy between the experimental data and the theoretical prediction will be discussed in detail in section 4.3.6. In the sequel, a more general expression than (4.41) is proven rigorously for an arbitrary initial momentum distribution.

4.3.3 Average kinetic energy

The statistical moments of the random process W_t may be explicitly computed at all t . For instance,

$$\mathcal{E}\{|W_t|^2 \mid \Delta\} = \sum_{j,k=0}^{N_t-1} \mathcal{E}\{z_j z_k^* \mid \Delta\} \quad (4.42)$$

is calculated by using the relations (4.40), which are proven in the following. We denote:

$$\alpha_j = e^{i\tilde{\xi}_j}, \quad \varphi_j = \sum_{r=0}^{\Delta_j-1} \alpha_j^r,$$

so that

$$\begin{aligned} z_j z_k^* &= e^{i(\gamma_j - \gamma_k)} \sum_{r=0}^{\Delta_j-1} \sum_{s=0}^{\Delta_k-1} \alpha_j^r \alpha_j^{-s} \\ &= e^{i\left(\sum_{m=0}^{j-1} \Delta_m \tilde{\xi}_m - \sum_{l=0}^{k-1} \Delta_l \tilde{\xi}_l\right)} \varphi_j \varphi_k^* \\ &= \varphi_j \varphi_k^* \prod_{l=0}^{j-1} \alpha_l^{\Delta_l} \prod_{m=0}^{k-1} \alpha_m^{-\Delta_m}. \end{aligned} \quad (4.43)$$

Let $j > k$, $j + k > 1$. Then $j > 1$, and the first product has the factor $\alpha_{j-1}^{\Delta_{j-1}}$. Hence (4.43) depends on $\tilde{\xi}_{j-1}$ via this factor alone (if $j \neq k + 1$), or via

this factor multiplied by φ_{j-1}^* (if $j = k + 1$), leading to a factor $e^{i\tilde{\xi}_{j-1}(\Delta_{j-1}-l)}$ with $l \leq \Delta_{j-1} - 1$. In both cases averaging over the uniformly distributed random variable $\tilde{\xi}_{j-1}$ yields zero (by (4.32) and assumption (S3) $\tilde{\xi}_{j-1}$ is indeed uniformly distributed whenever $j > 1$). The case $j < k$ then follows by complex conjugation in (4.43). For combinations of the form $z_j z_k$, we observe from (4.43) that the factors dependent on $\alpha_{j,m}$ can never cancel each other, and therefore they average to zero. This proves the second claim made in (4.40). If, on the other hand, $j = k$, then

$$|z_j|^2 = \left(\sum_{r=0}^{\Delta_j-1} \alpha_j^r \right)^2 = \frac{\sin^2(\tilde{\xi}_j \Delta_j / 2)}{\sin^2(\tilde{\xi}_j / 2)}, \quad (4.44)$$

similarly to (4.9). This gives for the expectation

$$\mathcal{E}\{|z_j|^2 | \Delta\} = \int_{-\pi}^{\pi} dP(\tilde{\xi}_j) \frac{\sin^2(\tilde{\xi}_j \Delta_j / 2)}{\sin^2(\tilde{\xi}_j / 2)}, \quad (4.45)$$

where $dP(\tilde{\xi}_j)$ is the distribution of ξ_j . For $j > 0$, this distribution is uniform: $dP(\tilde{\xi}_j) = d\tilde{\xi}_j / (2\pi)$, and the integral is computed according to (F.13): $\mathcal{E}\{|z_j|^2 | \Delta\} = \Delta_j$. For $j = 0$, we define

$$\mathcal{E}\{|z_0|^2 | \Delta\} = \mathcal{M}(\Delta_0) \equiv \int_{-\pi}^{\pi} dP(\xi_0) \frac{\sin^2(\xi_0 \Delta_0 / 2)}{\sin^2(\xi_0 / 2)} \quad (4.46)$$

where

$$dP(\xi_0) = (2\pi\ell)^{-1} d\xi_0 \sum_{j=0}^{l-1} f_0(\beta_j), \quad \beta_j \equiv \frac{\xi_0}{2\pi\ell} + \frac{1}{2} + \frac{j}{l} \pmod{1} \quad (4.47)$$

is the distribution of ξ_0 , and f_0 is the probability density of the initial quasi-momentum (4.10).

With these results (4.42) becomes

$$\sum_{j=0}^{N_{t-1}} \mathcal{E}\{|z_j|^2 | \Delta\} + 2\chi(N_{t-1}) \operatorname{Re}(\mathcal{E}\{z_1 z_0^* | \Delta\}), \quad (4.48)$$

where $\chi(\cdot)$ is the characteristic function of the strictly positive integers. For the last term one obtains from (4.37) by averaging over the uniformly distributed $\tilde{\xi}_1$

$$z_1 z_0^* = \sum_{s=0}^{\Delta_1-1} e^{is\tilde{\xi}_1} e^{i\Delta_0 \xi_0} \sum_{r=0}^{\Delta_0-1} e^{-ir\xi_0} \xrightarrow{\text{average}} \tilde{\xi}_1 \left. e^{is\tilde{\xi}_1} \right|_{s=0} \sum_{r=1}^{\Delta_0} e^{ir\xi_0}, \quad (4.49)$$

and hence:

$$\mathcal{E}\{z_1 z_0^* | \Delta\} = \mathcal{N}(\Delta_0) \equiv \sum_{r=1}^{\Delta_0} \int_{-\pi}^{\pi} dP(\xi_0) e^{ir\xi_0}. \quad (4.50)$$

The variables Δ_j were defined such that $\sum_{j=0}^{N_{t-1}} \Delta_j = t$; hence, with the help of (4.46) and (4.50) we find:

$$\begin{aligned} \mathcal{E} \{ |W_t|^2 \mid \Delta \} &= \mathcal{M}(\Delta_0) + \sum_{j=1}^{N_{t-1}} \Delta_j + \Delta_0 - \Delta_0 + 2\chi(N_{t-1}) \operatorname{Re}\mathcal{N}(\Delta_0) \\ &= \mathcal{M}(\Delta_0) - \Delta_0 + t + 2\chi(N_{t-1}) \operatorname{Re}\mathcal{N}(\Delta_0) . \end{aligned} \quad (4.51)$$

To obtain the mean energy of an atomic ensemble subject to SE, we must average over the random SE times Δ . The special case when no event happens up to time t , i.e. $\Delta_0 = t$ if $t_1 > t$ (with t_1 the time of the first SE event), implies $N_{t-1} = 0$, and this gives

$$\mathcal{E} \{ |W_t|^2 \mid \Delta \} = \mathcal{M}(t) . \quad (4.52)$$

In general, $N_{t-1} = 0$ is equivalent to $t_1 \geq t$, and t_1 is distributed according to (4.29). Therefore, using that the probability for $t_1 \leq t$ is given by $q_{\text{SE}}^t = (1 - p_{\text{SE}})^t$, and its complement by $1 - q_{\text{SE}}^t$ the mean energy equals:

$$\mathcal{E} \{ |W_t|^2 \} = q_{\text{SE}}^t \mathcal{M}(t) + t(1 - q_{\text{SE}}^t) + C(t, p_{\text{SE}}) \quad (4.53)$$

where

$$C(t, p_{\text{SE}}) = \sum_{n=1}^t \rho(n) [\mathcal{M}(n) - n + 2\operatorname{Re}\mathcal{N}(n)] . \quad (4.54)$$

In the case of a uniform initial quasi-momentum distribution, $\mathcal{M}(t) = t$ by (F.13) and (4.50) vanishes, hence also $C(t, p_{\text{SE}}) = 0$, and

$$\mathcal{E} \{ |W_t|^2 \} = t , \quad (4.55)$$

like in the case without SE.

With a smooth initial quasi-momentum distribution (4.10) it follows from the definitions (4.46) and (4.50) of \mathcal{M} and \mathcal{N} that

$$\begin{aligned} |C(t, p_{\text{SE}})| &\leq \left| \sum_{n=1}^t \rho(n) \mathcal{M}(n) + 2\operatorname{Re}\mathcal{N}(n) + \sum_{n=1}^t n\rho(n) \right| \\ &\leq 3(\delta f_0) \sum_{n=1}^t n\rho(n) , \end{aligned} \quad (4.56)$$

where (δf_0) is the maximum of $|f_0(\beta) - 1|$ in $[0, 1)$. In the last step, we used for (4.50) the upper bound

$$\left| \sum_{r=1}^{\Delta_0} \int_{-\pi}^{\pi} dP(\xi_0) e^{ir\xi_0} \right| \leq (\delta f_0) \left| \sum_{r=1}^{\Delta_0} e^{ir\xi_0} \right| \leq (\delta f_0) \left| \sum_{r=0}^{\Delta_0-1} e^{ir\xi_0} \right| \leq (\delta f_0) \Delta_0 .$$

With a non-uniform initial quasi-momentum distribution, letting $p_{\text{SE}} \rightarrow 0$ at fixed t causes the second and the third term on the right-hand side of (4.53)

to vanish. If instead $t \rightarrow \infty$ at fixed $p_{\text{SE}} > 0$, then the second and the first term on the right-hand side approach t and zero respectively, exponentially fast; the third term remains bounded according to (4.56). So the result which is obtained with a uniform quasi-momentum distribution is always approached asymptotically.

Assuming that the initial state and the SE realisation are given, and denoting $\tilde{\delta}_t = \sum_{s=0}^{t-1} \delta_s$, the quantum expectation of the energy of the atom at time t may be written as:

$$\begin{aligned} \bar{E}(t) &= \frac{1}{2} \int dp p^2 |\langle p | \psi(t) \rangle|^2 = \frac{1}{2} \int dp (p + \tilde{\delta}_t)^2 |\langle p | \tilde{\psi}(t) \rangle|^2 \\ &= \frac{1}{2} \int dp p^2 |\langle p | \tilde{\psi}(t) \rangle|^2 + \frac{1}{2} \tilde{\delta}_t^2 + \tilde{\delta}_t \int dp p |\langle p | \tilde{\psi}(t) \rangle|^2, \end{aligned} \quad (4.57)$$

where (4.24) was used. This expression has to be averaged over the initial statistical ensemble and over all SE realisations. Then the standard random walk result (applicable because of the assumptions (S1-3)) is

$$\mathcal{E}\{\tilde{\delta}_t^2\} = D(t-1), \quad \mathcal{E}\{\tilde{\delta}_t\} = 0, \quad (4.58)$$

where $D = \mathcal{E}\{\delta_t^2\}$ is the mean square momentum change per period owing to spontaneous emission. For an initial plane wave (2.22) of momentum $p_0 = n_0 + \beta_0$, with the help of (4.39) one finds

$$\begin{aligned} \int dp p |\langle p | \tilde{\psi}(t) \rangle|^2 &= \sum_n \int_0^1 d\beta (n + \beta) |\langle n | \tilde{\psi}_\beta(t) \rangle|^2 \\ &= \sum_n (n + \beta_0) J_{n-n_0}^2(k|W_t|) \\ &= \sum_m (m + n_0 + \beta_0) J_m^2(k|W_t|) = n_0 + \beta_0. \end{aligned} \quad (4.59)$$

where $J_n(\cdot) = (-)^n J_{-n}(\cdot)$ and $\sum_n J_n^2(\cdot) = 1$ [157] were used. Similarly,

$$\int dp p^2 |\langle p | \tilde{\psi}(t) \rangle|^2 = \sum_n (n + \beta_0)^2 J_{n-n_0}^2(k|W_t|), \quad (4.60)$$

whence, using (F.2),

$$\int dp p^2 |\langle p | \tilde{\psi}(t) \rangle|^2 = \frac{1}{2} k^2 |W_t|^2 + (n_0 + \beta_0)^2. \quad (4.61)$$

Replacing (4.59) in (4.57), the expectation of the last term in (4.57) vanishes by virtue of (4.58). The expectation of (4.61) is found with the help of (4.53). Thus the final result for the mean energy is

$$\mathcal{E}\{\bar{E}(t) - \bar{E}(0)\} = \frac{1}{4} k^2 [t(1 - q_{\text{SE}}^t) + \mathcal{M}(t)q_{\text{SE}}^t + C(t, p_{\text{SE}})] + \frac{1}{2} D(t-1). \quad (4.62)$$

(4.62) reduces to the SE-free one equation (4.19) for $q_{\text{SE}} = 1$. The term on the right-hand side which includes k^2 as a factor is the mean energy in the

stochastic gauge. With a uniform quasi-momentum distribution, (4.62) reduces to (4.41), which is *identical* to the result obtained in the SE-free case, except for the last term in (4.62). However, a similar, albeit cumbersome computation of higher-order moments would reveal sharp differences, which reflect totally *different* ways of the spreading of the *momentum distribution* in the two cases. While, in the noise free case, the second moment of energy, for instance, increases with t^3 in time (see discussion after (4.21)), it would grow like t^2 in the asymptotic limit where a Gaussian momentum distribution develops (see next section).

Under assumption (S3), the quasi-momentum distribution of the atoms is immediately turned uniform by the first SE event. The time scale for uniformisation of the quasi-momentum distribution is then $t_c = -1/\ln(1 - p_{\text{SE}})$. Equation (4.62) shows that for $t \gg t_c$ the growth of energy is linear with the coefficient $k^2/4 + D/2$, like in the case of a uniform quasi-momentum distribution. On the other hand, since $C(t, p_{\text{SE}})$ is bounded in time, for $(\delta f_0)t_c \ll t \ll t_c^{\S}$ the growth of energy is dominated by the term $\mathcal{M}(t)$, which is the same as in the SE-free, non-uniform case.

4.3.4 Asymptotic momentum distribution

In this section we assume an initial momentum distribution with $n_0 = 0$. For initial distributions with values $n_0 \neq 0$, we may average the final result over the initial integer grid points similarly as done in (4.12). We denote $P(p, t)$ the momentum distribution at time t , and show that, as $t \rightarrow \infty$, $P(p, t)$ approaches a Gaussian distribution with mean value 0; in the sense that, for an arbitrary smooth function $\phi(p)$,

$$\begin{aligned} \lim_{t \rightarrow \infty} \langle \phi \rangle_t &\equiv \lim_{t \rightarrow \infty} \int dp P(p, t) \phi\left(\frac{p}{\sqrt{t}}\right) = \lim_{t \rightarrow \infty} \sqrt{t} \int dp P(p\sqrt{t}, t) \phi(p) \\ &= \int dp \phi(p) \mathcal{G}_{D+k^2/2}(p) \end{aligned} \quad (4.63)$$

where $\mathcal{G}_{\sigma^2}(p)$ denotes the normal distribution with zero mean and variance σ^2 . To this end we compute by applying the stochastic gauge (4.24), with $\tilde{\delta}_t = \sum_{s=0}^{t-1} \delta_s$ as defined in the previous section:

$$\begin{aligned} \langle \phi \rangle_t &= \mathcal{E} \left\{ \int dp |\langle p | \psi(t) \rangle|^2 \phi\left(\frac{p}{\sqrt{t}}\right) \right\} \\ &= \mathcal{E} \left\{ \int dp |\langle p | \tilde{\psi}(t) \rangle|^2 \phi\left(\frac{p + \tilde{\delta}_t}{\sqrt{t}}\right) \right\} \\ &\stackrel{(4.39)}{=} \mathcal{E} \left\{ \sum_n J_n^2(k|W_t|) \phi\left(\frac{n + \beta_0 + \tilde{\delta}_t}{\sqrt{t}}\right) \right\}. \end{aligned} \quad (4.64)$$

^{\S}Note that for a distribution $f_0(\beta_0)$ close to uniform, $(\delta f_0) \gtrsim 0$.

For $t \gg 1$ one may neglect corrections of order $1/\sqrt{t}$, hence β_0/\sqrt{t} in the argument of the smooth function ϕ , so

$$\langle \phi \rangle_t \approx \mathcal{E} \left\{ \sum_n J_n^2(k|W_t|) \phi \left(\frac{n + [\tilde{\delta}_t]}{\sqrt{t}} \right) \right\}, \quad (4.65)$$

where $[\cdot]$ denotes the integer part. Asymptotically as $t \rightarrow \infty$, the statistics of W_t are determined by the *fractional* parts of sums of many δ_s (cf. (4.32) and (4.37)). Such sums of a large number of independent terms have a broad distribution, so their integer and fractional parts tend to be independent of each other as the number of terms in the sums diverges. The squared Bessel functions and the function ϕ in the last equation may then be separately averaged. Denoting

$$\phi_t(p) \equiv \mathcal{E} \left\{ \phi \left(\frac{p + [\tilde{\delta}_t]}{\sqrt{t}} \right) \right\} \quad (4.66)$$

we may write

$$\langle \phi \rangle_t \approx \sum_n \mathcal{E} \{ J_n^2(k|W_t|) \} \phi_t \left(\frac{n}{\sqrt{t}} \right). \quad (4.67)$$

As shown in appendix C, the distribution of $\rho = |W_t|$ is asymptotically at large t given by $dF_t(\rho) = 2t^{-1}\rho d\rho \exp(-\rho^2/t)$. Consequently,

$$\begin{aligned} \langle \phi \rangle_t &\approx \int_0^\infty dF_t(\rho) \sum_n J_n^2(k\rho) \phi_t \left(\frac{n}{\sqrt{t}} \right) \\ &= 2 \int_0^\infty dx x e^{-x^2} \sum_n J_n^2(kx\sqrt{t}) \phi_t \left(\frac{n}{\sqrt{t}} \right). \end{aligned} \quad (4.68)$$

The integral over ρ is a classical expectation, but the sum over n is a quantum expectation instead. With (2.12) it may be formally written as

$$I_t(kx) \equiv \sum_n J_n^2(kx\sqrt{t}) \phi_t \left(\frac{n}{\sqrt{t}} \right) = \langle 0 | \hat{\mathcal{K}}^\dagger \phi_t(t^{-1/2} \hat{\mathcal{N}}) \hat{\mathcal{K}} | 0 \rangle, \quad (4.69)$$

where

$$\hat{\mathcal{K}} = e^{-ikx\sqrt{t}\cos(\theta)}. \quad (4.70)$$

If we regard $t^{-1/2}$ as the Planck constant, then $t \rightarrow \infty$ is equivalent to a classical limit. In that limit $t^{-1/2}\hat{\mathcal{N}}$ corresponds to (angular) momentum p , and $\hat{\mathcal{K}}$ corresponds to $p \rightarrow p + kx \sin(\theta)$, by comparison with (2.6) and (2.8). Therefore, the ‘‘classical’’ limit ($t \rightarrow \infty$) for the momentum distribution in the state $\hat{\mathcal{K}}|0\rangle$ is given by the distribution of $kx \sin(\theta)$, with θ uniformly distributed in $[0, 2\pi]$. Replacing the quantum expectation (4.69) by the average over the related classical distribution yields

$$\lim_{t \rightarrow \infty} I_t(kx) = \int_{-\pi}^{\pi} \frac{d\theta}{2\pi} \phi_\infty(kx \sin \theta) \stackrel{p=kx \sin(\theta)}{=} 2 \int_{-kx}^{kx} \frac{dp}{2\pi} \frac{\phi_\infty(p)}{\sqrt{k^2 x^2 - p^2}}. \quad (4.71)$$

Substituting this in (4.68), interchanging the integrals, and computing the integral over x gives

$$\begin{aligned} \lim_{t \rightarrow \infty} \langle \phi \rangle_t &= 2 \int_0^\infty dx x e^{-x^2} I_\infty(kx) = \frac{2}{\pi} \int_{-\infty}^\infty dp \phi_\infty(p) \int_{|p|/k}^\infty dx \frac{x e^{-x^2}}{\sqrt{k^2 x^2 - p^2}} \\ &\stackrel{y^2 = (kx)^2 - p^2}{=} \frac{1}{k\pi} \int dp \phi_\infty(p) e^{-\frac{p^2}{k^2}} \int dy \frac{e^{-y}}{\sqrt{y}} = \frac{\Gamma(\frac{1}{2})}{k\pi} \int dp \phi_\infty(p) e^{-\frac{p^2}{k^2}} \\ &= \frac{1}{k\sqrt{\pi}} \int dp \phi_\infty(p) e^{-\frac{p^2}{k^2}}, \end{aligned} \quad (4.72)$$

with the Γ function $\Gamma(1/2) = \sqrt{\pi}$ [268]. On the other hand, from the definition (4.66) it follows that

$$\phi_\infty(p) = \int dp' \phi(p-p') \mathcal{G}_D(p'), \quad (4.73)$$

where \mathcal{G}_D is the limit ($t \rightarrow \infty$) normal distribution of $\tilde{\delta}_t/\sqrt{t}$. Recalling (4.72) and the definition of $\langle \phi \rangle_t$ given in (4.63), we immediately obtain the result claimed there. Hence, $P(p, t)$ is asymptotically equivalent to a Gaussian with zero mean and variance $k^2 t/2 + Dt$. Being just the leading term in the asymptotic approximation as $t \rightarrow \infty$, this misses those terms in the exact result (4.62) which are bounded in time. The way (4.72) was derived from (4.67) shows that decoherence turns the dynamics classical by causing the effective Planck constant to decrease with time. An exact derivation of (4.72) from (4.67), which does not refer to the semiclassical argument from above, is obtained by starting from (4.68), and replacing $\phi_t(n/\sqrt{t})$ by its Fourier transform $\bar{\phi}_t(u)$:

$$\phi_t\left(\frac{n}{\sqrt{t}}\right) = \frac{1}{\sqrt{2\pi}} \int du \bar{\phi}_t(u) e^{inu\sqrt{t}}. \quad (4.74)$$

Using the Bessel function identity (F.5),

$$\begin{aligned} \langle \phi \rangle_t &= \frac{1}{\sqrt{2\pi}} \int_0^\infty dF_t(\rho) \int du \bar{\phi}_t(u) J_0\left(2k\rho \sin\left(\frac{u}{2\sqrt{t}}\right)\right) \\ &\stackrel{x=\rho/\sqrt{t}}{=} \frac{2}{\sqrt{2\pi}} \int_0^\infty dx x e^{-x^2} \int du \bar{\phi}_t(u) J_0\left(2kx\sqrt{t} \sin\left(\frac{u}{2\sqrt{t}}\right)\right). \end{aligned} \quad (4.75)$$

With (F.9) this yields in the limit $t \rightarrow \infty$

$$\langle \phi \rangle_\infty = \frac{2}{\sqrt{2\pi}} \int_0^\infty dx x e^{-x^2} \int du \bar{\phi}_\infty(u) J_0(kxu). \quad (4.76)$$

Substitution of

$$\bar{\phi}_\infty(u) = \frac{1}{\sqrt{2\pi}} \int dp \phi_\infty(p) e^{-ipu} \quad (4.77)$$

and of (F.6) yields

$$\langle \phi \rangle_\infty = \frac{1}{\sqrt{\pi^2}} \int_0^\infty dx x e^{-x^2} \int_{-1}^1 dy \frac{1}{\sqrt{1-y^2}} 2\pi \delta(p - kxy), \quad (4.78)$$

and finally

$$\langle \phi \rangle_\infty = \frac{2}{\pi} \int_0^\infty dx x e^{-x^2} \int_{-kx}^{kx} dp \frac{\phi_\infty(p)}{\sqrt{k^2 x^2 - p^2}}. \quad (4.79)$$

Interchanging integrals, we obtain the same result as above (equation (4.72)) by different means.

4.3.5 Theoretical model vs. numerical results

In the preceding sections, we derived the mean energy growth and the asymptotic momentum distribution for an ensemble of δ -kicked atoms in the presence of SE. Our theoretical model was based on the assumptions (S1-S3) stated in section 4.3.2. We now test the result thus obtained by a direct comparison to numerical simulations that mimic a more realistic stochastic evolution of the initial states.

In general, for a single transition in a three-dimensional atom, the probability distribution of momentum shifts produced by SEs is not isotropic [269]. This in particular implies that the distribution of single SE, projected momentum shifts δp is *not* uniform. In the case when the SE-inducing beam is orthogonal to the kicking direction, it has the parabolic form:

$$\mathcal{P}_0(\delta p) = \begin{cases} C \left(\frac{9}{8} - \frac{3(\delta p)^2}{2} \right) & , \quad |\delta p| \leq \frac{k_T}{2k_L} \\ 0 & , \quad \text{otherwise,} \end{cases} \quad (4.80)$$

where C is a normalisation constant, and $\vec{k}_T \perp \vec{k}_L$ are the (assumed to be orthogonal) wave vectors of the SE-inducing light and of the kicking light, respectively. This distribution is derived for a situation where SE from a $\Delta m = \pm 1$ atomic transition is induced by circularly polarised light [269]. The allowed change in momentum δp is restricted within the interval $[-k_T/2k_L, k_T/2k_L]$, with $k_T/2k_L \simeq 1/2$ (resulting in $C \simeq 1$) in [82, 83]. With a non-uniform distribution such as (4.80) a correlation in time may be established between quasi-momenta in different periods of the evolution. The mean momentum change as a result of absorption followed by SE is $\hbar \vec{k}_T$ for a single SE-inducing beam with wave vector \vec{k}_T . Our assumption of zero mean (along the kicking direction) is justified either when $\vec{k}_T \perp \vec{k}_L$, or when the experimental arrangement uses two or more appropriately directed beams, whereby the atoms may be excited with equal probability. In such cases, the distribution of the projected δp is more complicated (and closer to uniformity) than (4.80). Since the experiments use a large ensemble of caesium atoms, and SEs involve several hyperfine sublevels [83, 135], the assumption of a nearly uniform distribution of momentum changes seems, however, most appropriate. We shall nonetheless use (4.80) as a term of comparison in “type (II) simulations” (see below) in order to test the effects of deviations from uniformity. Such numerical data demonstrate that our assumption of a uniform distribution in an exactly integer interval of allowed momentum changes does not affect the results, for experimentally relevant times at least.

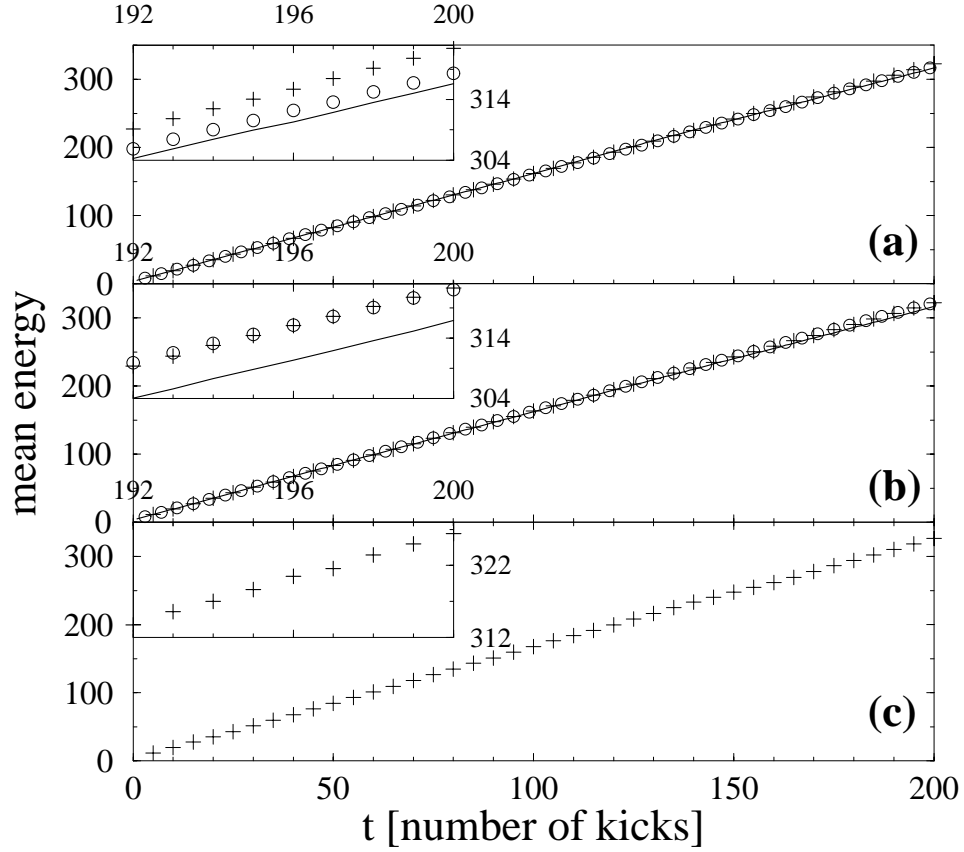


Fig. 4.4: Average energy vs. time t at exact resonance $\tau = 2\pi$ for the same ensemble of atoms as in figure 4.3, for $k = 0.8\pi$, in the presence of SE events simulated in different ways as described in the text: (a) type (I) simulation: a random number of SEs occur immediately after kicks, each causing a momentum change δp uniformly distributed in $[-1/2, 1/2]$. (b) type (II): SE times are Poisson-distributed in a window $\tau_{\text{SE}} = 0.067\tau$, with free evolution in-between them; δp is distributed as in (a). (c) type (III): SE times as in (a), but δp has the parabolic distribution (4.80) with $k_L/2k_T \simeq 0.476$. Rates of spontaneous emission $p_{\text{SE}} = 0.05$ (solid), $p_{\text{SE}} = 0.1$ (circles), $p_{\text{SE}} = 0.2$ (plusses). The theoretical prediction (see text) for the coefficient of linear growth D_{dec} is approximately 1.59, whereas the data lead to $D_{\text{dec}} \approx 1.58 - 1.60$ except in (b) for $p_{\text{SE}} = 0.05$ where it takes the value 1.55 (strong fluctuations arising from a too small statistical sample at this smallest SE rate). The insets zoom into the region close to $t = 200$. No momentum cutoffs are used.

For the uniform distribution of δp in the interval $[-1/2, 1/2]$, $\langle \delta p^2 \rangle = 1/12$, so the coefficient D in (4.58) is $D = n_{\text{SE}}/12$. With the distribution (4.80) $\langle \delta p^2 \rangle = 3/40$, and $D = n_{\text{SE}}3/40$. In the theoretical model based on assumption (S2) the distribution of the random times at which single SEs occur within *one* kicking period is totally irrelevant, so p_{SE} and n_{SE} enter as *independent* parameters. They have to be related to each other in order to make contact with experiments. A seemingly natural way assumes a Poisson distribution for the SEs occurring within one operating window, at least for not too large p_{SE} . In that case, $p_{\text{SE}} = 1 - \exp(-n_{\text{SE}})$.

We have performed numerical simulations of three types: for type (I) we used all assumptions (S1-3), whereas for type (II-III) the assumptions (S2) and (S3) were replaced by more realistic ones. Type (II) allowed for free evolution in-between successive SEs occurring in the same kicking period. For type (III) the distribution (4.80) of δp was used. Type (I) simulations serve as a demonstration of the theoretical exact results, and much more as a term of comparison with type (II-III) simulations. The essential agreement between the three types demonstrates that our theoretical conclusions remain valid, under less stringent premises. Both types of numerical results were obtained by independently evolving rotors in a given initial Gaussian ensemble, and by incoherently averaging the final results. Random SE events were simulated as follows. After choosing values for τ_{SE} and $p_{\text{SE}} = 1 - \exp(-n_{\text{SE}})$, random SE times were generated in each kicking period from a Poisson distribution with the characteristic time $\tau_{\text{SE}}/n_{\text{SE}}$ within the time window $(t\tau, t\tau + \tau_{\text{SE}})$. To each random time a random momentum jump was associated, from the chosen distribution (uniform or parabolic). In type (I) simulations, such jumps were added to the quasi-momentum the rotor had at (integer) time t . The integer part of the result determined a corresponding shift in the computational basis of angular momentum eigenstates (i.e. if the sum of quasi-momentum and the shift exceeded one or was negative then $\bar{\psi}_\beta(n) \rightarrow \bar{\psi}_\beta(n \pm 1)$, respectively, with integers n). The fractional part was used as quasi-momentum for a full one-period free rotor evolution. In all cases *the computational basis of momentum eigenstates was chosen as large as possible* in order to model as faithfully as possible the ideal models analysed in previous sections.

Figure 4.4 shows a long-time plot for different rates $p_{\text{SE}} = 0.05 \dots 0.2$, and for the two cases: type (I) with SEs happening immediately after the kicks (a), and type (II) with SEs within a finite time window ($\tau_{\text{SE}} = 0.067\tau = 0.424$ [83]) (b). For $p_{\text{SE}} = 0.2$ data is given in figure 4.4 (c) for the parabolic distribution (4.80), i.e. for the type (III) model. The energy growth is *in all cases* linear with the predicted slope $D_{\text{dec}} \simeq k^2/4 + D/2$, as discussed above (see equation (4.62)). Figure 4.5 presents the coarse-grained momentum distributions $P_n(t)$ (see section 4.2.1) defined as the probability that the momentum p of an atom at time t lies in $[n, n + 1)$ (in units of two photon recoils). They are computed for $\tau = 2\pi$ and different SE rates; SE events are modelled after type (I-III). With added decoherence, the distribution keeps spreading as a whole all the time, looking more and more Gaussian-like while it flattens out. Apart from statistically induced fluctuations in the wings of the distributions no significant difference between the different simulations (figures 4.4-4.5) is detectable, and

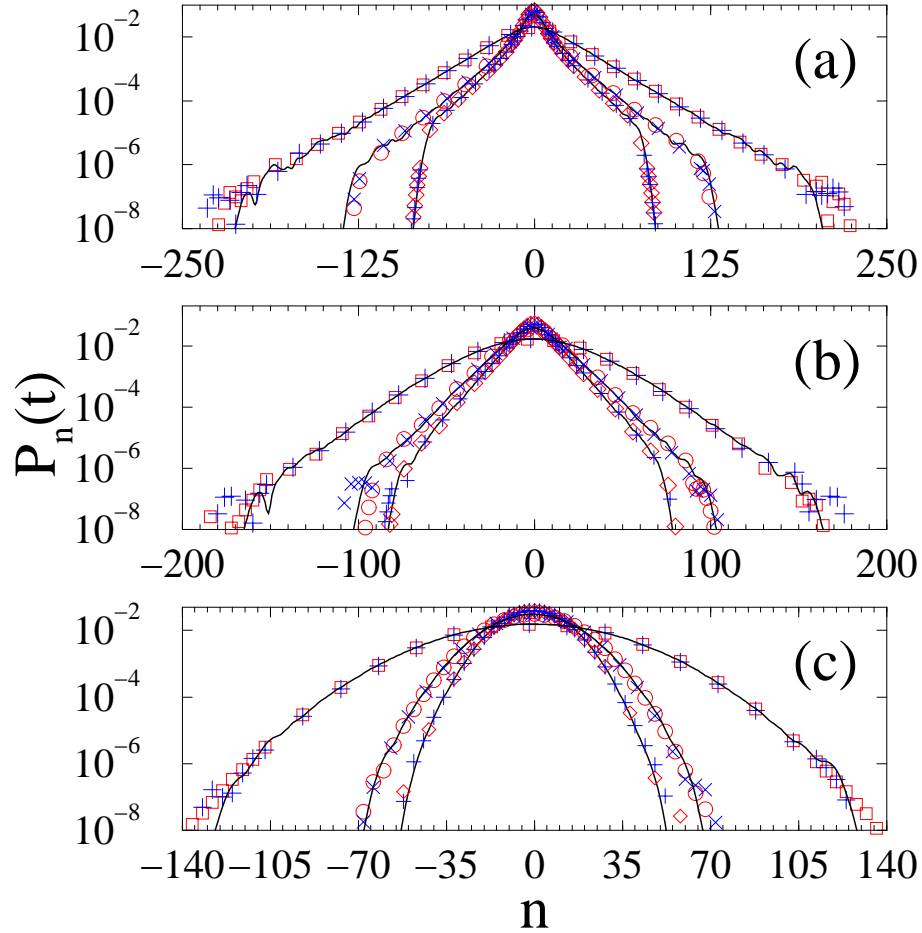


Fig. 4.5: Evolution in time of coarse-grained momentum distributions for the same initial ensemble as in figure 4.3, and for $k = 0.8$, in the presence of SE. (a) $p_{\text{SE}} = 0.1$, (b) $p_{\text{SE}} = 0.2$, (c) $p_{\text{SE}} = 0.8$, for $t = 30$, $t = 50$, and $t = 200$. The SE events are simulated in different ways. Solid lines were computed like in (a) in the previous figure; diamonds, circles and squares, like in (b); pluses and crosses, like in (c) there. Differences in the wings, in particular at $t = 200$, where $P_n(t) \lesssim 10^{-7}$, are attributed to the finite statistical sample in the simulation of the SE events. For strong noise in (c), the momentum distributions are already similar to a Gaussian distribution as predicted for $t \rightarrow \infty$ in section 4.3.4.

our conclusions from the preceding sections remain valid in all cases. We conclude that the results obtained in the present work are not very sensitive to assumptions (S1-3) that made the analytical treatment possible. In the sequel, the analytical and numerical findings presented in this chapter are confronted with the experimental results of [82, 83, 135]. In particular, the puzzle about the observed enhancement of the quantum resonance peaks when adding SE will be resolved [159].

4.3.6 Reconciliation with experimental observations

Omnis actio et omnis mutatio est de contrario in contrarium.

G. Bruno, La cena de le ceneri

In the presence of decoherence induced by spontaneous emission, experimentally measured energies at fixed observation time t_{obs} were found to exhibit resonance peaks near the resonant values $\tau = 2\pi, 4\pi, 6\pi$ that were *higher* than in the SE-free case (figure 4.1). On the other hand, our analytical analysis (equations (4.21) and (4.62)), together with numerical data (figures 4.4 and 4.6), predicts in both cases, with and without added noise by SE, a linear increase of the average energy as a function of time, and in addition with an almost negligible difference in the pre-factor for the experimentally used parameters ($D/2 \lesssim 0.2/24$, for the data in figure 4.1). Such observations may have been suggestive of an enhancement of quantum resonances owing to decoherence: however, such a phenomenon has no match in the theory developed in the previous sections. This paradox will be resolved in this section. It will be shown that certain restrictions, that are unavoidably present in real experiments, depress the ideal resonant behaviour in a way that is most severe *in the absence of SE*. So the explanation rather lies with the experimentally measured, SE-free peaks being *lower* with respect to the ideal case, than with the SE ones being higher. The most important experimental features not taken into account in the foregoing theoretical analysis have been mentioned already in section 2.3.3:

(EXI) experimental kicks are not δ -like. The ideal model is then only valid as long as the distance travelled by the atoms over the finite duration τ_{dur} of the kick is much smaller than the spatial period of the potential ($T_{\text{dur}} = 0.5 \mu\text{sec}$ in [82, 83]). In dimensionless units of (2.10) $\tau_{\text{dur}} = T_{\text{dur}}\hbar(2k_L)^2/M \simeq 0.047$. At large momenta this requirement is violated, and the atomic motion starts averaging over the potential, while the small momentum regime is practically not affected by the replacement of the δ -function by a pulse of finite width. The resulting dependence of the kicking strength on momentum destroys the translational invariance in momentum space required for quantum resonant motion. At large momenta, the effect of the finite pulse width induces a momentum

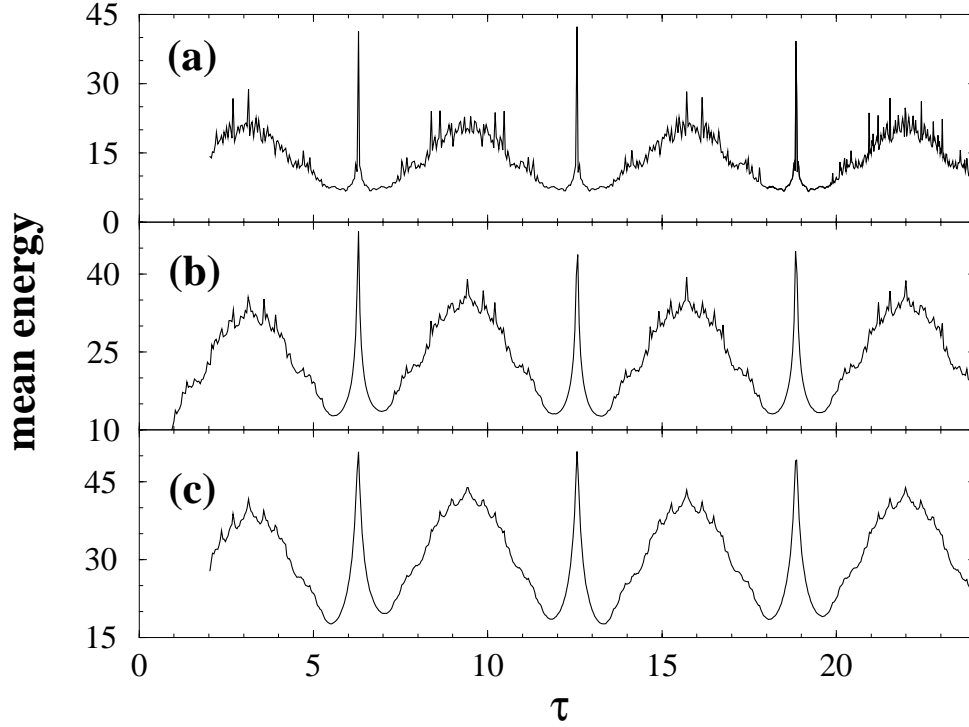


Fig. 4.6: Mean energy (in units of $(2\hbar k_L)^2/M$, c.f. (2.24)) vs. kicking period τ after $t = 30$ kicks, and for a type (I) simulation starting with an ensemble of 10^5 δ -kicked atoms, with Gaussian initial momentum distribution ($\sigma \simeq 2.7$) and $k = 0.8\pi$. (a) no decoherence $p_{SE} = 0$, (b) $p_{SE} = 0.1$, (c) $p_{SE} = 0.2$. The shown range of τ corresponds in laboratory units to $21.2 \dots 254.7 \mu\text{sec}$ (a,c), and to $10.1 \dots 254.7 \mu\text{sec}$ (b). The peaks appear lower in (a) because the used computational grid in τ had a too low resolution to hit the value $\tau = 2\pi, 4\pi, \dots$ exactly, while the peaks in (b,c) are broader and therefore less sensitive. (The sensitivity decreases with increasing p_{SE} , see section 5.3.)

boundary which we denoted n_{ref} in section 2.3.3. The atom dynamics mimics the ideal lowest-order resonances for a (possibly long) while [175], but not the higher-order ones whose period (in momentum) is not very small compared to n_{ref} [64,117,118]. This is an additional reason preventing experimental detection of high-order resonances, no matter how long the observation time (cf. discussion in section 4.1). Figure 4.7 shows a simulation for an ensemble of rotors, with a rectangular pulse shape of width τ_p . This does not include the smooth switching on/off of pulses, as described e.g. in [180]; no substantial difference is however expected in the dynamics on relatively small time scales. In each kicking interval the rotors freely evolved over a physical time $\tau - \tau_{\text{dur}}$. During the remaining time τ_p they evolved according to the pendulum Hamiltonian $(\hat{N} + \beta)^2/2 + k \cos(\hat{\theta})$. The latter evolution was computed by a Trotter-Kato discretisation [270] of the Floquet operator (this split-operator method [16] is equivalent to replacing the pulse by a thick sequence of δ -subkicks).

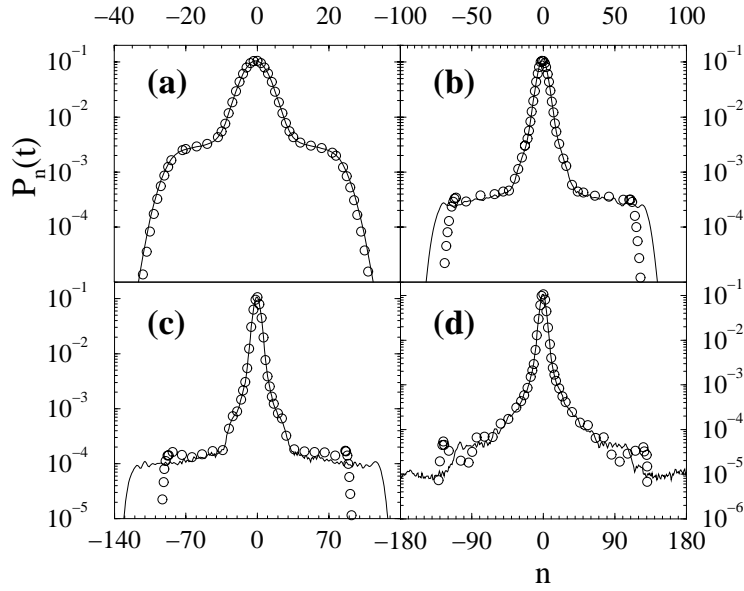


Fig. 4.7: Coarse-grained momentum distributions for the same initial ensemble as in figure 4.3 and without SE, for $k = 0.8\pi$ and $\tau = 2\pi$. The ideal case of δ -kicks (solid line) is compared to the case of rectangular pulses with $\tau_{\text{dur}} = 0.047$ (open circles). Times are $t = 10$ (a), 30 (b), 50 (c), 200 (d).

(EXII) The experimental signal-to-noise ratio allows only a finite reliable interval of momenta to be observed; in [83] this border was $n_{\text{cut}} = 40$ (data with counteracted gravity; in most recent data $n_{\text{cut}} = 60$ [159]). Momenta with $n > n_{\text{cut}}$ are not included in the mean energy data of [83], cf. figure 4.10. Therefore, the theoretical momentum distributions have to be appropriately weighted prior to the computation of the mean energy and to the comparison with experimental data. The crudest way is cutting the theoretical distributions beyond n_{cut} and renormalising the probability to 1.

The effect of (EXI) and (EXII) on the ideal behaviour discussed in the previous section is easily understood in qualitative terms. We start with the SE-free case. The resonant growth of energy is stopped as soon as the ballistic peak in the tail approaches the closest of the two borders that are the effective cutoffs: (EXI) n_{ref} and (EXII) n_{cut} . If this happens earlier than the observation time, then the resonance peak is significantly depressed in comparison to the ideal case. We shall presently argue that such depression mainly arises from the cut-off (EXII) for the experimental data in [83, 135].

In the case of a rectangular pulse, n_{ref} is not a precisely defined quantity because of the slow decay of the Fourier harmonics of the pulse. It has to be meant in an effective sense. We hence resort to numerical simulations. In figures 4.7 numerically computed momentum distributions are compared with those obtained in the ideal δ -kicked rotor case; according to such data, the effective n_{ref} should be located in the momentum range 70 – 120. The second cutoff n_{cut}

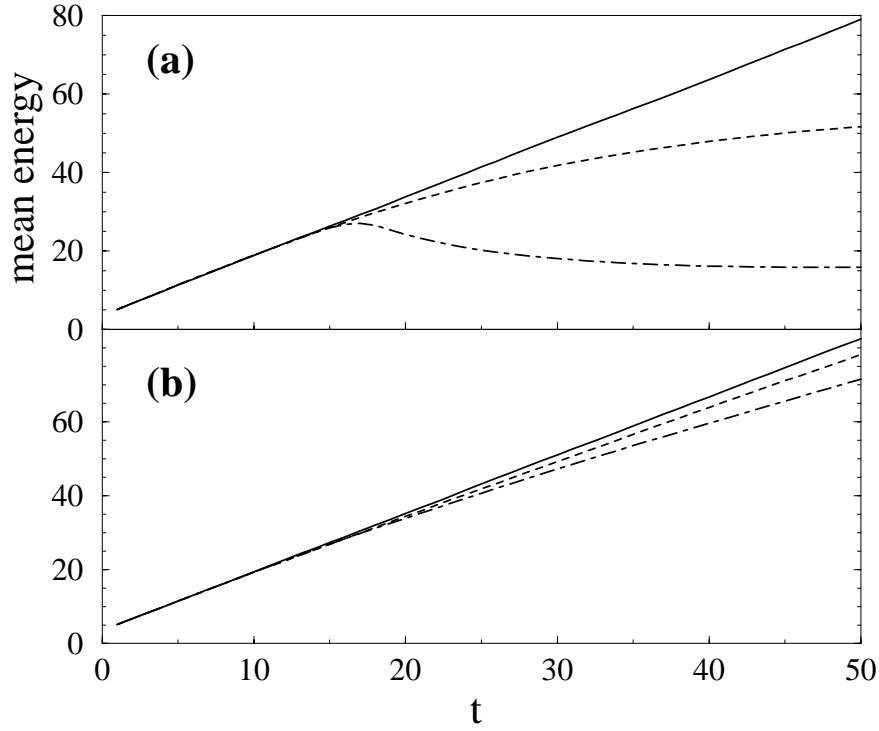


Fig. 4.8: Effect of finite pulse width and of momentum cutoff on the growth of the mean energy for the same initial ensemble as in figures 4.3 and 4.7, for kicking strength $k = 0.8\pi$ and period $\tau = 2\pi$, without SE (a) and with $p_{\text{SE}} = 0.2$ (b). Solid lines are for the ideal δ -kicks and no momentum cutoff; dashed lines for rectangular pulses, no cutoff; dash-dotted lines for rectangular pulses and momentum cutoff at $n_{\text{cut}} = 40$. In (a) the energy is significantly depressed by the cutoff after $t > 20$, not so in (b).

is simulated by not counting momenta higher than n_{cut} when calculating energies (the computational basis of momentum eigenstates is however much larger than n_{cut}). Following experimental parameters [83, 135] we choose $n_{\text{cut}} = 40$, the distributions are renormalised to unity after disregarding states with momenta larger/smaller than $n = \pm 40$. In figures 4.8 the effect of this cutoff on the growth of the mean energy is shown. In the presence of n_{cut} the deviation from the ideal case appears somewhat earlier, as expected from $n_{\text{cut}} < n_{\text{ref}}$; moreover, the deviation at $t \gtrsim 20$ is strongly enhanced in the presence of n_{cut} (and in the absence of SE). As shown in figures 4.9 (a), the momentum distributions including both cutoffs (EXI) and (EXII) are stable in time, not moving at all in the centre around $n = 0$. The slight enhancement at $|n| \simeq 15 - 40$ as compared to the case without cutoffs (shown in figures 4.7) is only due to n_{ref} which to some extent acts like a reflecting boundary. The ballistic peak, however, which moves in momentum like $n \sim \pi kt/2$ (see discussion after (4.18)) is lost already after about $t \simeq 40/k \simeq 16$ kicks, cf. figure 4.8. The peak is then beyond the cutoff (EXII). The estimated loss after about 16 kicks is consistent with the saturation of the mean energy vs. time at quantum resonance which has been

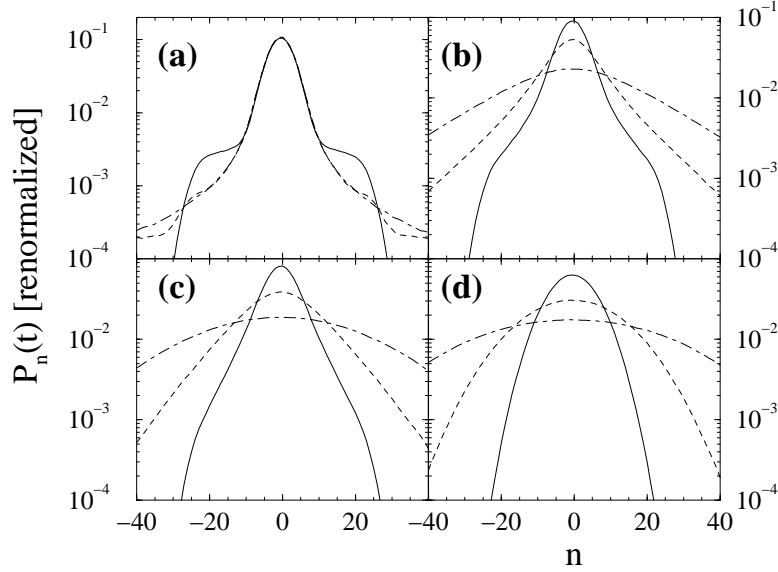


Fig. 4.9: Evolution of coarse-grained momentum distribution for the same ensemble as in figures 4.3 and 4.7, for $\tau = 2\pi$ and $k = 0.8\pi$, with rectangular pulses ($\tau_{\text{dur}} = 0.047$) and momentum cutoff at $n_{\text{cut}} = 40$. The distributions are renormalised within the shown momentum window. (a) $p_{\text{SE}} = 0$, (b) $p_{\text{SE}} = 0.1$, (c) $p_{\text{SE}} = 0.2$, (d) $p_{\text{SE}} = 0.8$, after $t = 10$ (solid lines), $t = 50$ (dashed), $t = 200$ (dash-dotted).

observed in [82, 135], for $t > 15$, in the experimental results as well as in the theoretical modelling (figure 4 in [82]).

The dependence of the mean energy on the kicking period τ is strongly influenced by the cutoffs at exact resonance. This dependence in the absence of SE, with rectangular pulses and cutoff at n_{cut} is shown in figure 4.11(a). By comparing to figure 4.6(a) (ideal case without cutoffs), we directly see that the only substantial difference is at resonant values $\tau = 2\pi, 4\pi, 6\pi$: cutoffs lead to lower resonance peaks. When the cutoff (EXII) $n_{\text{cut}} = 40$ is applied in the ideal case of δ -kicks, no differences can be detected from the results plotted in figure 4.11(a), again confirming that cutoff (EXII) is the crucial one. The resonance peaks are smaller, because the resonant growth of energy stops, as soon as the ballistically moving rotors hit the boundary (cf. figure 4.8). Then the mean energy very quickly falls below its ideal value (after about 16 kicks in the plotted case), as can be seen in figure 4.8.

Added SE totally changes this picture. The energy growth originates now in the overall broadening of the distribution, and not just in the ballistic peaks in the tail, as can be seen comparing the various parts of figure 4.5, where kicks are δ -like, and no cutoff is present. The distributions with weak SE are broader in the tails as compared to those with strong SE; the latter are however flatter in the centre, which is why they have roughly the same root-mean-square deviation. As already commented, in the SE-free case the quasi-momentum is constant in time, and atoms with quasi-momenta close to $1/2$ travel faster, thus

producing the long tails and the ballistic peaks at their edges. In the presence of SE, no atom may persist a long time in the fast-travelling quasi-momentum range, whence it is removed the sooner, the larger p_{SE} . Therefore with SE, the cutoffs are “felt” much later by the evolving distribution (figures 4.5 and 4.9). Whereas the cutoffs still prevent observation of the fastest atoms, they do not significantly affect the growth of energy until large times. Even then, the momentum distribution normalised within $|n| < n_{\text{cut}}$ approaches the flat distribution in $|n| < n_{\text{cut}}$ (figure 4.9(b,c,d)), which has a limit value for the second moment significantly higher than the SE-free steady-state distribution in the presence of the cutoff. Figure 4.10 compares the ideal momentum distributions which are taken from figures 4.3(a) and 4.5(a) to recent experimental results at $t = 30$ kicks. Note that the numerical simulation shows the “ballistic” wings of the distributions at $p_{\text{SE}} = 0$, which are swamped by the noise background in the experimental data. Nonetheless, both experimental and theoretical data agree very well in the central (stationary) part of the distribution. The same is true for the case with SE where we chose $p_{\text{SE}} = 0.1$ ($n_{\text{SE}} = -\ln(1 - p_{\text{SE}}) \simeq 0.105$) which compares best to the experimental data for which $n_{\text{SE}} \simeq 0.14 \pm 0.04$ [159] is estimated. The latter estimate is rather rough and depends on several absorption processes in the experimental setup, and on fluctuations in the intensity of the SE inducing laser [159, 260]. SE occurs not only in the direction of the kicks (cf. discussion in section 4.3.5). Hence, we cannot exclude a possible enhancement of the effect that different atoms may also experience different intensities of the kicking pulses (see section 2.3.3). The atoms are then subject to a range of kicking strengths which has not been taken into account numerically. Those atoms which do experience a low intensity yield an enhanced population near to zero momentum which might look like a numerical distribution in which the SE rate is lower.

In contrast to the SE-free case, the dependence of the mean energy on the kicking period τ after 30 kicks is but slightly affected by the cutoffs when SE is present. This is shown in figure 4.11 (b,c), to be compared to figure 4.6(b,c). In the experiments (see figure 4.1 here, and figure 2 in [82], figure 6 in [83]), the peaks for all cases (a-c) are still smaller than in our figure 4.11, which can be explained by the extreme sensitivity of the energy at exact resonance to all sort of perturbations besides those included in our present analysis, and also by difficulties in experimentally tuning to the exactly resonant values of τ . Additional experimental restrictions, e.g. the experienced fluctuations of the potential depth and the resulting averaging over slightly different experimental realisations [83, 135, 182], may lead to a further reduction of the peak, especially in the case without decoherence which is most sensitive to any kind of disturbance.

Our analytical results of this chapter are exclusively obtained for the exact resonance condition in the kicking period $\tau = 2\pi\ell$ ($\ell \in \mathbb{N}$). The experimental and, in particular, the numerical data of the mean energy vs. τ also show that the widths of the resonance peaks changes systematically when SE is introduced (cf. figures 4.1 and 4.6). The shape of these peaks is responsible also for their experimentally observed stabilisation with increasing noise. An analytical

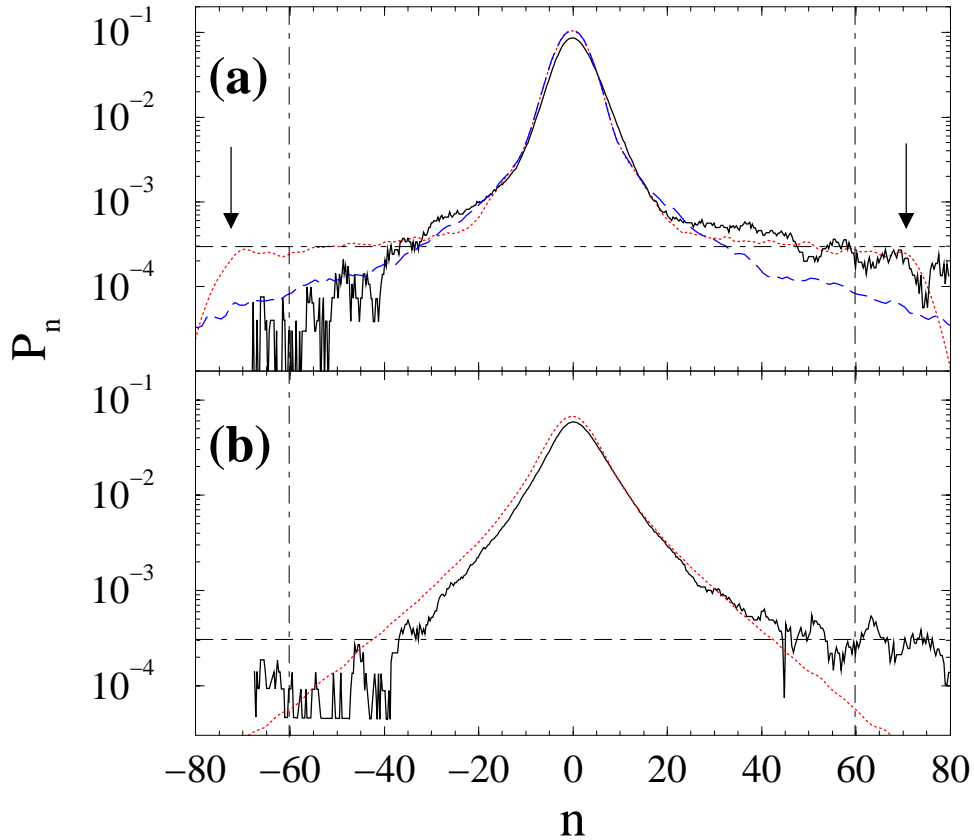


Fig. 4.10: Coarse-grained momentum distributions at quantum resonance $\tau = 2\pi$ (type (I) simulations) from figures 4.3(a) and 4.5(a) (dotted), as compared to experimental data [159] (full lines), for $p_{\text{SE}} = 0$ (a) and $p_{\text{SE}} = 0.1$ ($n_{\text{SE}} = -\ln(1 - p_{\text{SE}}) \simeq 0.105$), experimental estimate $n_{\text{SE}} \simeq 0.14 \pm 0.04$ (b); kicking strength $k = 0.8\pi$, at $t = 30$ kicks. The arrows mark the ballistic wings in the case without SE. The dashed line in (a) shows the steady-state distribution (for $t = 1000$) taken from figure 4.3(b). The dash-dotted lines show the signal threshold and momentum cuts ($n_{\text{cut}} = 60$) imposed on the experimental data when calculating mean energies as plotted in figure 4.1. The asymmetry in the experimental distribution around $n = 0$ is caused by the non-ideal compensation of gravity which acts in the direction of the standing wave, in the experimental realisation [82, 83, 135, 159].

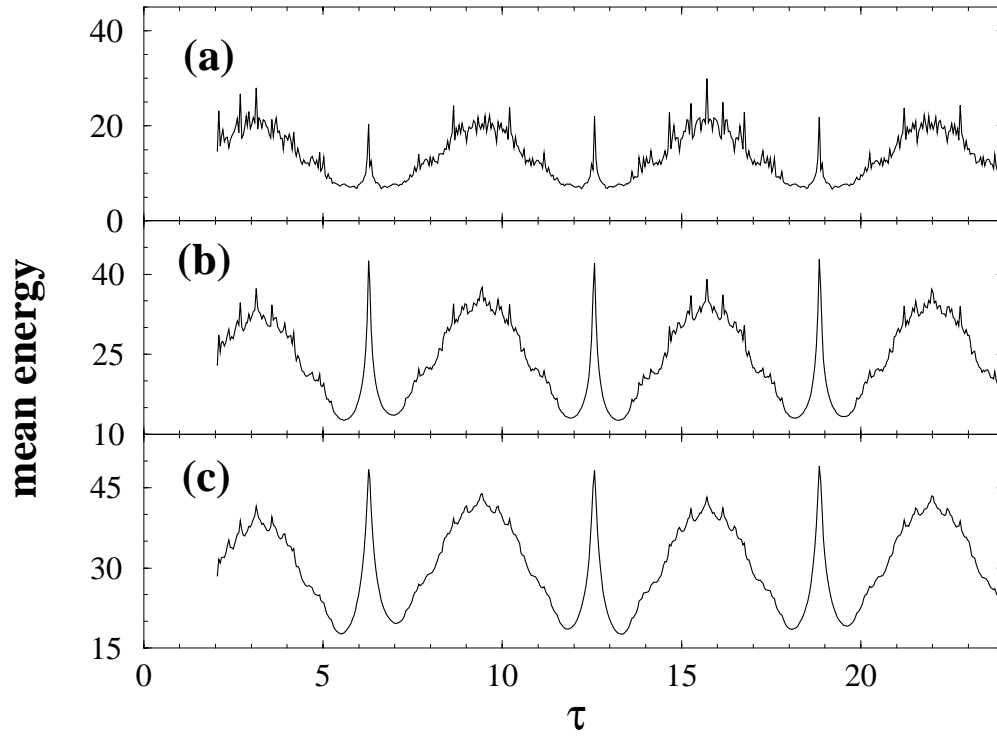


Fig. 4.11: Numerical simulation of the mean energy as a function of the kicking period τ for the same ensemble of SE and the same initial distribution of atoms as in figure 4.6, after 30 kicks, and with kicking strength $k = 0.8\pi$. (a) no decoherence $p_{\text{SE}} = 0$, (b) $p_{\text{SE}} = 0.1$, (c) $p_{\text{SE}} = 0.2$. The width of the rectangular pulse is $\tau_{\text{dur}} = 0.047$ and $n_{\text{cut}} = 40$, as for the experimental data [82, 83] shown in figure 4.1.

theory for arbitrary irrational $\tau/2\pi$ does not exist, but in the next chapter we develop an approximate description for the vicinity of the resonance peaks for $\tau = 2\pi\ell + \epsilon$, with $|\epsilon| \ll 1$.

Chapter 5

Dynamics near to quantum resonance

In the previous chapter, we derived analytical results for the momentum distribution and the average kinetic energy of an initial atomic ensemble, and compared them to numerical simulations and the experimental data. In the following, we go beyond the case of the exact resonance condition for the kicking period τ , and study the vicinity and, in particular, the shape of the resonance peaks, which are observed in the mean energy after a fixed observation time t_{obs} . For irrational values of $\tau/(4\pi)$, dynamical localisation sets in (cf. section 2.2.2), that is, on increasing t_{obs} beyond a break-time t_{break} , the observed energy values should not increase any more*. If t_{obs} is significantly larger than t_{break} , a scan of the measured energy vs. the kicking period τ yields plots alike in figure 4.1(a), and figure 4.6(a). In 4.6(a) peaks are clearly observed at the resonant values $\tau = 2\pi, 4\pi, 6\pi$. For continuity reasons, the resonance peaks have a width, determined by the finite value of t_{obs} . In the ideal case, they would shrink on increasing t_{obs} , and further, narrower peaks associated with higher-order resonances would appear for large t_{obs} . In this chapter, we derive a description of the structure of the peaks around $\tau = 2\pi\ell$ ($\ell \in \mathbb{N}$), based on a finite time, small- ϵ asymptotics, where $\tau = 2\pi\ell + \epsilon$. This technique was introduced in [144, 145], and partially anticipated in [271, 272], where the special role of the combination $k|\epsilon|$ of the two parameters k , the kicking strength, and ϵ , the detuning from the resonance, was first realised.

In particular, we find that the width of the resonance peak scales like $(kt_{\text{obs}}^2)^{-1}$, so that, at large t_{obs} , the peak is much narrower than the naive expectation $\propto 1/t_{\text{obs}}$. Such sharp sub-Fourier resonances reflect the high sensitivity of the quantum-chaotic δ -kicked rotor with respect to slight variations in the detun-

*Unbounded growth was also proven for a dense set of close-to-commensurate values of τ [158]. Extremely long times are however required to resolve such arithmetic subtleties.

ing from resonance, and they may be relevant for high-resolution experiments[†].

5.1 ϵ -quasi-classical approximation

The most elementary *classical resonances* are met when a system, such as an oscillator, is driven by a force that is periodic in time with frequency equal to the natural frequency of the system. In linear systems, a classical resonance leads to unbounded energy absorption, e.g. for a resonantly driven harmonic oscillator (see, for instance, section 1.6a in [44]). For nonlinear systems, however, this is typically not the case because the unperturbed frequencies depend on the system's energy, so the system is rapidly driven off resonance by the initially resonant excitation itself. Similarly, for a quantum system the resonant excitation is eventually stopped owing to the anharmonicity of the unperturbed spectrum.

The quantum resonances of the δ -kicked rotor are rare examples of unbounded excitation in the deep quantum regime. For instance, the experimental and numerical data presented in the previous chapter were obtained for $\tau \propto \hbar = O(1)$, and $k \propto \hbar^{-1} = O(1)$, cf. section 2.2.2 for the definition of the parameters k and τ in the quantum model. As discussed there, the quantum resonances arise for particular kicking periods which are commensurable with 4π . They have no direct counterpart in the corresponding classical system, and are totally unrelated to resonances of the classical rotor[‡].

In the following, we present a quasi-classical analysis of the quantum resonances of the δ -kicked particle and their vicinity. This seemingly self-contradictory task is accomplished by establishing a direct correspondence between the quantum resonances and the classical *nonlinear* resonances of a related model. This classical system is *not* obtained in the conventional classical limit of vanishing Planck constant $\hbar \propto \tau \rightarrow 0$, but rather in the limit when the detuning ϵ from the resonant periods $\tau = 2\pi\ell$ ($\ell \in \mathbb{N}$) approaches zero. In our quasi-classical approximation, the role of Planck's constant is played by the detuning ϵ from exact resonance in the kicking period τ . This approximation allows us to describe the near-to-resonant quantum motion in terms of a Standard Map [156], which is different in parameter values from the one that is obtained in the conventional classical limit of the δ -kicked rotor, i.e. when the real effective Planck constant $\tau \rightarrow 0$, and $k \rightarrow \infty$ simultaneously [63]. The quantum resonances of the δ -kicked rotor then correspond to the primary nonlinear resonance of this

[†]In a similar context, the sub-Fourier sensitivity of the kicked-rotor dynamics on periodicity conditions was used to sharply discriminate dynamical localisation from diffusive quantum transport [273].

[‡]There do exist classical accelerator modes of the δ -kicked rotor that lead to ballistic motion [43]. E.g., for $k\tau = 2\pi$, and $(p_0 = 0, \theta_0 = \pi/2)$, it is easily checked from (2.6) and (2.7) that momentum grows linearly in time $p_t = 2\pi t$. However, these modes are of a different nature, and occur for very specific initial values (p_0, θ_0) , while the quantum resonances do not depend on the initial conditions [43], if there is no additional degree of freedom, like the quasi-momentum β for the kicked particles.

quasi-classical Standard Map. The stable elliptic island associated with the nonlinear resonance [43–45] accounts for the structure of the resonance peak in the quantum mean energy vs. τ curves (see figures 4.1 and 4.6).

To derive the quasi-classical approximation [145, 160], we rescale the kicking strength $k = \tilde{k}/|\epsilon|$, and define

$$\hat{I} = |\epsilon|\hat{\mathcal{N}} = -i|\epsilon|\frac{d}{d\theta}. \quad (5.1)$$

The free evolution part of the Floquet operator for the β -rotor (2.23) may be rewritten as follows:

$$\begin{aligned} e^{-i\frac{\tau}{2}(n+\beta)^2} &= e^{-i\pi\ell n^2} e^{-i\frac{\epsilon}{2}n^2} e^{-i\tau n\beta} e^{-i\frac{\tau}{2}\beta^2} \\ &= e^{-i\pi\ell\frac{I}{|\epsilon|}} e^{-i\text{sign}(\epsilon)\frac{I^2}{2|\epsilon|}} e^{-i\tau\beta\frac{I}{|\epsilon|}} e^{-i\frac{\tau}{2}\beta^2}, \end{aligned} \quad (5.2)$$

where the last factor does not depend on I and may be dropped. Similarly, we obtain for the kick operator in (2.23)

$$e^{-ik\cos(\hat{\theta})} = e^{-\frac{i}{|\epsilon|}\tilde{k}\cos(\hat{\theta})}, \quad (5.3)$$

and then the Floquet operator reads

$$\hat{\mathcal{U}}_\beta(t) = e^{-\frac{i}{|\epsilon|}\tilde{k}\cos(\hat{\theta})} e^{-\frac{i}{|\epsilon|}\hat{\mathcal{H}}_\beta}, \quad (5.4)$$

with

$$\hat{\mathcal{H}}_\beta(\hat{I}, t) = \frac{1}{2}\text{sign}(\epsilon)\hat{I}^2 + \hat{I}(\pi\ell + \tau\beta). \quad (5.5)$$

If $|\epsilon|$ is regarded as the Planck constant, then (5.1) together with (5.4) is the formal quantisation of either of the following classical maps:

$$I_{t+1} = I_t + \tilde{k}\sin(\theta_{t+1}), \quad \theta_{t+1} = \theta_t \pm I_t + \pi\ell + \tau\beta \pmod{2\pi} \quad (5.6)$$

where \pm has to be chosen according to the sign of ϵ . We stress that “classical” here is not related to the $\tau \propto \hbar \rightarrow 0$ limit but to the limit $\epsilon \rightarrow 0$ instead. The small- $|\epsilon|$ asymptotics of the quantum β -rotor is thus equivalent to a quasi-classical approximation based on the “classical” dynamics (5.6), that will be termed ϵ -classical in the following. Changing variables to $J = \pm I + \pi\ell + \tau\beta$, $\vartheta = \theta + \pi(1 - \text{sign}(\epsilon))/2$ turns the maps (5.6) into a single Standard Map (c.f. (2.6-2.7)), independent of the value of β :

$$J_{t+1} = J_t + \tilde{k}\sin(\vartheta_{t+1}) \quad (5.7)$$

$$\vartheta_{t+1} = \vartheta_t + J_t. \quad (5.8)$$

This will be called the ϵ -classical Standard Map (ϵ SM) in what follows. In figure 5.1(a) quantum energy curves vs. τ in a neighbourhood of $\tau = 2\pi$ are compared with energy curves computed using the ϵ -classical map (5.6).

For any given particle in the initial ensemble, the map (5.6) with β equal to the quasi-momentum of the particle was used to compute a set of trajectories started at $I = n_0|\epsilon|$ with homogeneously distributed $\theta_0 \in [0, 2\pi)$. The final

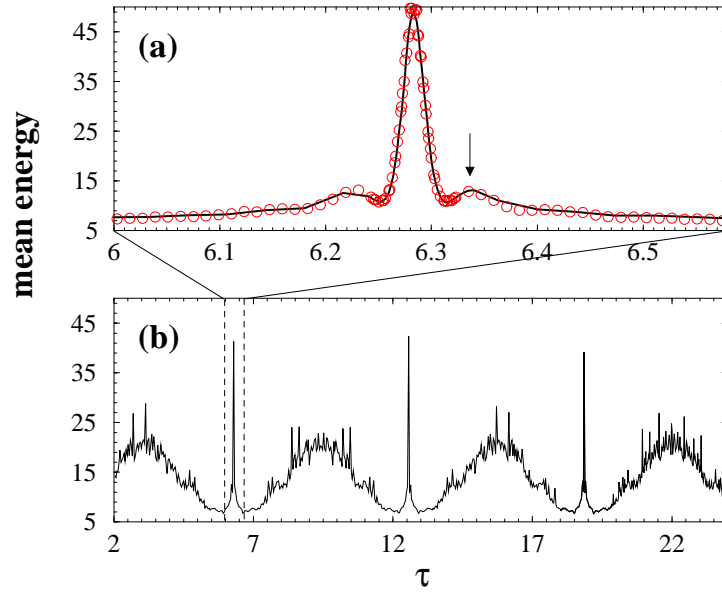


Fig. 5.1: (a) shows the mean energy vs. kicking period τ , after $t = 30$ kicks, and for kicking strength $k = 0.8\pi$; magnification near the quantum resonance $\tau = 2\pi$. Quantum data taken from figure 4.6(a) (for better comparison repeated in the lower panel (b)) (solid lines) are compared with the mean energies of an ensemble of 10^6 ϵ -classical atoms (circles) with the same initial momentum distribution, evolving under the ϵ -classical dynamics (5.6). The value of τ corresponding to the small peak on the right of the resonant spike is marked by an arrow for reference to figures 5.4 and 5.6.

energies $\epsilon^{-2}I_t^2/2$ at $t = t_{\text{obs}}$ of the individual trajectories were averaged over θ_0, β, n_0 with the appropriate weights. This is equivalent to using the ϵ SM in all cases, with different initial ensembles $J_0 = \text{const.} = \pm n_0|\epsilon| + \pi\ell + \tau\beta_0$. As β_0 is varied, such ensembles sweep the full unit cell of the ϵ SM, so sampling different β_0 's amounts to probing different regions of the ϵ -classical phase space as illustrated in figure 5.2. The average energy $\langle E_t \rangle = \epsilon^{-2}\langle I_t^2 \rangle/2$ is plotted vs. $\tau = 2\pi + \epsilon$ in figure 5.1(a), along with results of the corresponding quantal computations. The main qualitative features emerging of figure 5.1 are: (i) on a gross scale the curves are shaped in the form of a basin with a high, narrow spike in the centre, closely flanked by a much smaller peak on either side. (ii) quantum and ϵ -classical curves nicely agree at small $|\epsilon|$, in particular the structure of the spike is the same. Their behaviour at large $|\epsilon|$, i.e. for $\tau \gtrsim 6.6$ and $\tau \lesssim 6$ is qualitatively similar but quantitatively different (see figure 5.8 in section 5.2.2). This overall qualitative behaviour may be explained in ϵ -classical terms, and an approximate scaling law for the t, k, ϵ dependence of the mean energy close to resonance can be obtained, as shown in the next section.

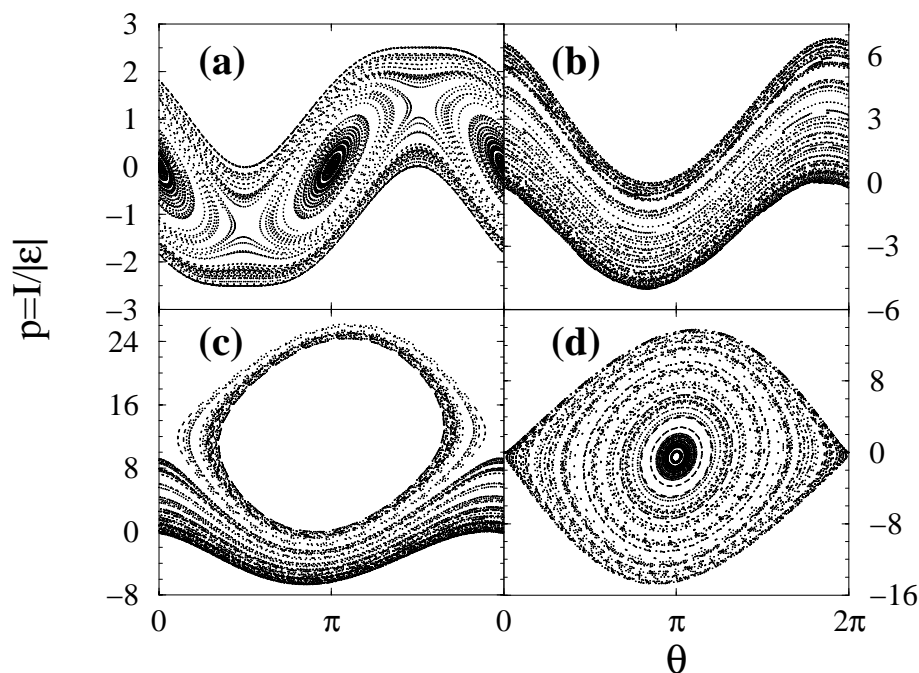


Fig. 5.2: Poincaré surface of sections for the map (5.6), and $k = 0.8\pi$, $\epsilon = 0.05$, $\beta = 0$ (a), $\beta = 0.35$ (b), $\beta = 0.4$ (c), $\beta = 0.5$ (d). Plotted are the true momenta $p = I/|\epsilon|$ to emphasise the much larger contribution to the mean energy from the (nonlinear) resonant zone for $\beta \simeq 1/2$, whose width is approximately given by $\delta p \simeq 4\sqrt{k/|\epsilon|}$. For $\beta = 0.5$, the period-1 fixed point of the map (5.6) is close to 0 (in fact at $p = -1/2$), so all trajectories launched at $p_0 = \beta$, move along the island, leading to large excursions in p . As β decreases to 0, the period-1 fixed point [43] moves away from $p = 0$, and is not hit by trajectories started at $p_0 = \beta$ ($n_0 = 0$). The trajectories in (b) and at $p \leq 8, \theta = 0$ in (c) are rotational orbits, corresponding to the regular regions outside the primary resonance island in figure 5.3 (right panels). (a) contains a higher-order period-2 resonance embedded in the otherwise rotational motion. In the coordinates of the map (5.6), the effective Planck cell $2\pi\epsilon \simeq 0.314$ is larger than the area of the period-2 islands, which is estimated by $k\epsilon \simeq 0.126$ (see [43]). Higher-order resonances are neglected in our analysis since they affect much smaller regions in phase space than the dominant primary island (in (d)). The full phase space in the coordinates of the ϵ SM is shown in the next figure (right panels).

5.2 Classical scaling theory for quantum resonances

5.2.1 ϵ -quasi-classical analysis of the resonance peaks

The ϵ -classical standard map is different from the map obtained in the classical limit proper $\tau \propto \hbar \rightarrow 0$ of the kicked rotor. In particular, if $\tau k > 1$, then the classical and the ϵ -classical dynamics are at sharp variance whenever $\tilde{k} < 1$. In the former unbounded diffusion occurs, while in the latter the dynamics is quasi-integrable instead. In this quasi-integrable system, the ϵ -classical trajectories remain trapped forever in-between impenetrable phase space barriers, which survive small perturbations according to the Kolmogorov-Arnold-Moser (KAM) theorem [43–45, 177]. It is exactly the deep changes which occur in the ϵ -classical phase space (cf. figure 5.3) as τ is varied at constant k that account for the energy vs. τ dependence at fixed time $t = t_{\text{obs}}$. In the following discussion, we assume for simplicity an initially flat distribution of $p_0 \in [0, 1)$; then $I_0 = 0$, and $J_0 = \pi\ell + \tau\beta_0$ with β_0 uniformly distributed in $[0, 1)$. Without loss of generality we also consider $\ell = 1$. Hence if $|\epsilon| \ll 1$ then J_0 is uniformly distributed over one period (in action) $(\pi, 3\pi)$ of the ϵ SM.

Since $J_t = \pm I_t + \pi + \tau\beta$, and $I_0 = 0$, the mean energy of the rotor at time t is:

$$\langle E_{t,\epsilon} \rangle = \epsilon^{-2} \langle I_t^2 \rangle / 2 = \frac{\langle (\delta J_t)^2 \rangle}{2\epsilon^2}, \quad \delta J_t = J_t - J_0.$$

The exact quantum resonance $\epsilon = 0$ corresponds to the integrable limit of the ϵ SM, where $\delta J_t = 0$. However, $\langle E_{t,\epsilon} \rangle$ is scaled by ϵ^{-2} , so in order to compute it at $\epsilon = 0$ one has to compute δJ_t at first order in ϵ . This is done by substituting the 0-th ϵ -order of (5.8), i.e. $\vartheta_t \simeq \vartheta_0$, into (5.7). This leads to

$$\delta J_t = |\epsilon|k \sum_{s=0}^{t-1} \sin(\theta_0 + J_0 s) + r(\epsilon, t) \quad (5.9)$$

where $r(\epsilon, t) = O(\epsilon)$ as $\epsilon \rightarrow 0$ at any fixed t . The energy at time t is found from (5.9) by taking squares, averaging over θ_0, J_0 , dividing by $2|\epsilon|^2$, and finally letting $\epsilon \rightarrow 0$:

$$\begin{aligned} \langle E_{t,\epsilon} \rangle &= \frac{1}{8\pi^2} \int_0^{2\pi} d\theta_0 \int_{\pi}^{3\pi} dJ_0 \frac{(\delta J_t)^2}{\epsilon^2} \\ &\xrightarrow{\epsilon \rightarrow 0} \frac{k^2}{8\pi^2} \int_0^{2\pi} d\theta_0 \int_{\pi}^{3\pi} dJ_0 \left(\sum_{s=0}^{t-1} \sin(\theta_0 + J_0 s) \right)^2 \\ &\stackrel{(4.9)}{=} \frac{k^2}{8\pi} \int_{\pi}^{3\pi} dJ_0 \frac{\sin^2(J_0 t/2)}{\sin^2(J_0/2)}. \end{aligned} \quad (5.10)$$

With the help of (F.13), this calculation yields:

$$\langle E_{t,0} \rangle = \frac{k^2}{4} t. \quad (5.11)$$

The small contribution of the initial quasi-momentum in the atom's energy was neglected. Apart from that, (5.11) is the same result as was found by the exact quantum mechanical calculation performed at $\epsilon = 0$ in section 4.2.2 for the case of a uniform quasi-momentum distribution. Thus the ϵ -quasi-classical approximation reproduces the quantum behaviour at exact quantum resonance. The integral over J_0 in (5.10) collects contributions from all the invariant curves $J_0 = \text{const.}$ of the ϵ SM at $\epsilon = 0$. Of these, the one at $J_0 = 2\pi$ leads to quadratic energy growth because it consists of (period 1) fixed points [43]. This is called a classical nonlinear resonance. It is responsible for the linear growth of energy (5.11), because the main contribution to the integral in (5.10) comes from a small interval $\sim 2\pi/t$ of actions around $J_0 = 2\pi$. Note that $J_0 = 2\pi$ corresponds to $\beta_0 = 1/2$, the quantum resonant value of quasi-momentum. It is hence seen that the ϵ -quasi-classical approximation explains the *quantum* resonances of the kicked rotor in terms of the *classical* resonances of the Standard Map.

In the sequel, we estimate $\langle E_{t,\epsilon} \rangle$ for $|\epsilon| > 0$, where the dynamics is maximally distorted (with respect to the $\epsilon = 0$ one) for J_0 in the vicinity of the elliptic fixed points [43] of the ϵ SM, i.e. of the $2n\pi$, in the very region which is mostly responsible for the linear growth of energy at $\epsilon = 0$. Being formed of period-1 fixed points, the $J_0 = 2n\pi$, $\epsilon = 0$ invariant curves break at $|\epsilon| > 0$ as described by the Poincaré-Birkhoff theorem [43]. The motion is then strongly distorted inside regions of size (in action) δJ_{res} astride $J = 2n\pi$. Such regions are termed the primary resonances of the ϵ SM, and a well-known estimate is $\delta J_{\text{res}} \approx 4(k|\epsilon|)^{1/2}$ [43]. Inside these resonances, the approximation (5.9) fails quite quickly, so their contribution $\langle E_{t,\epsilon} \rangle_{\text{res}}$ to the mean energy has to be estimated differently. The dynamical situation is illustrated in figure 5.3 by Poincaré surface of sections for the dynamics induced by (5.7-5.8).

In the remaining part of the ϵ -classical phase space the motion mostly follows KAM invariant curves [43–45], slightly deformed with respect to the $\epsilon = 0$ ones, still with the same rotation angles (see figure 5.3). The contribution of such invariant curves to the mean energy is therefore roughly similar to that considered in the integral (5.10), provided J_0 is therein meant as the rotation angle[§]. On such grounds, in order to roughly estimate $\langle E_{t,\epsilon} \rangle$ we remove from the integral (5.10) the contribution of the resonant action interval near $J_0 = 2\pi$, and replace it by $\langle E_{t,\epsilon} \rangle_{\text{res}}$:

$$\langle E_{t,\epsilon} \rangle \sim \frac{k^2}{4}t - \Phi(t) + \langle E_{t,\epsilon} \rangle_{\text{res}} , \quad (5.12)$$

where

$$\Phi(t) = \frac{k^2}{8\pi} \int_{-\delta J_{\text{res}}/2}^{\delta J_{\text{res}}/2} dJ' \frac{\sin^2(tJ'/2)}{\sin^2(J'/2)} , \quad (5.13)$$

and J' is the deviation from the resonant value 2π . The contribution $\langle E_{t,\epsilon} \rangle_{\text{res}}$ may be estimated by means of the pendulum approximation [43, 44]. The pen-

[§]Higher resonances appear near all values of J_0 commensurate to 2π . At small $|\epsilon|$ such higher-order resonances affect regions of phase space that are negligibly small with respect to the primary resonance, see figures 5.2 and 5.3. The higher resonances are altogether ignored in the present discussion. Also note that structures that are small compared to the “Planck constant” $|\epsilon|$ are irrelevant for the purposes of the ϵ -classical approximation.

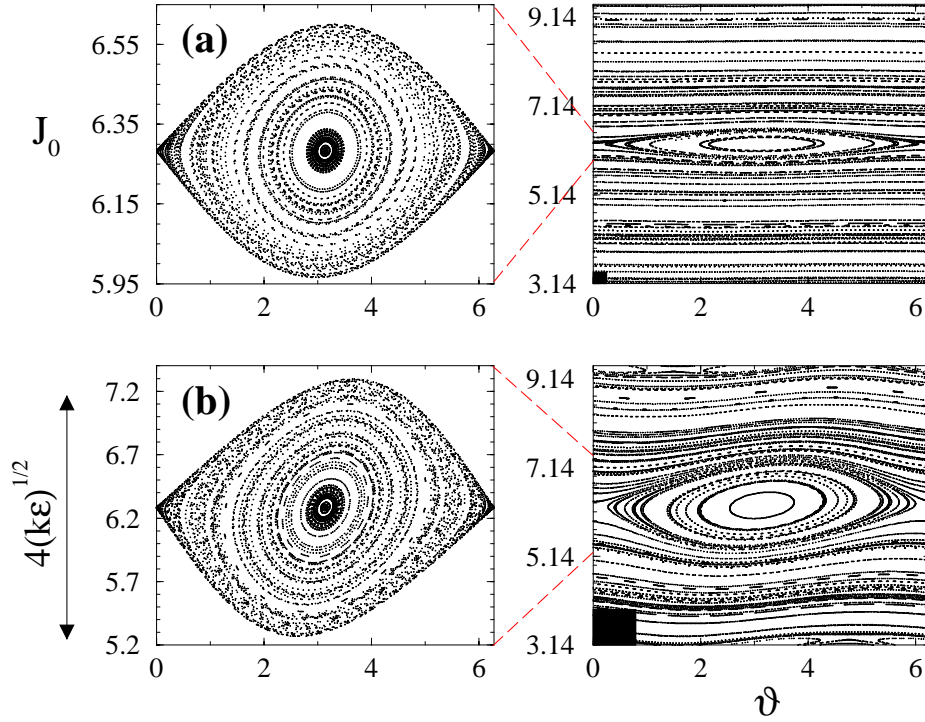


Fig. 5.3: Poincaré surface of sections for the Standard Map (5.7-5.8), and $k = 0.8\pi$, $\epsilon = 0.01$ (a), $\epsilon = 0.1$ (b). As ϵ increases, the invariant curves (right panels) become more and more distorted, and the contribution of trajectories around the primary resonance island (left panels), with a width of $\delta J_{\text{res}} \approx 4(k|\epsilon|)^{1/2}$, to the energy must be calculated separately (see equation (5.12)). The black boxes in the right panels represent the Planck cell $2\pi|\epsilon|$. In the coordinates of (5.7-5.8) sweeping β from 0 to 1 is equivalent to scanning J_0 from π to 3π , with the primary resonance island centred at $J_0 = 2\pi$. The four plots (a-d) in the previous figure effectively correspond to a scan from $J_0 \simeq \pi$ (figure 5.2(a)) upwards to $J_0 \simeq 2\pi$ (figure 5.2(d)).

dulum Hamiltonian emerges from the Fourier analysis of the kick perturbation: $|\epsilon|k \cos(\vartheta) \sum_m \delta(t-m) = |\epsilon|k \sum_m \cos(\vartheta - 2\pi mt)$ (note that for the ϵ SM (5.7-5.8) the kicking period is 1). In the time average, higher Fourier components may be neglected near the ϵ SM resonance [43, 44], and the motion is thus described (in *continuous* time) by the following pendulum Hamiltonian in the canonical coordinates J', ϑ :

$$H_{\text{res}} = \frac{1}{2}(J')^2 + |\epsilon|k \cos(\vartheta). \quad (5.14)$$

The resonance width δJ_{res} is estimated by the separation (in action) between the separatrices of the pendulum motion. The period of the small pendulum oscillations is $2\pi t_{\text{res}}$ where $t_{\text{res}} = (k|\epsilon|)^{-1/2}$ [43, 44], so we use t_{res} as a characteristic time scale for the elliptic motion in the resonant zone. One may altogether remove $|\epsilon|$ from the Hamilton equations, by scaling momentum and time by

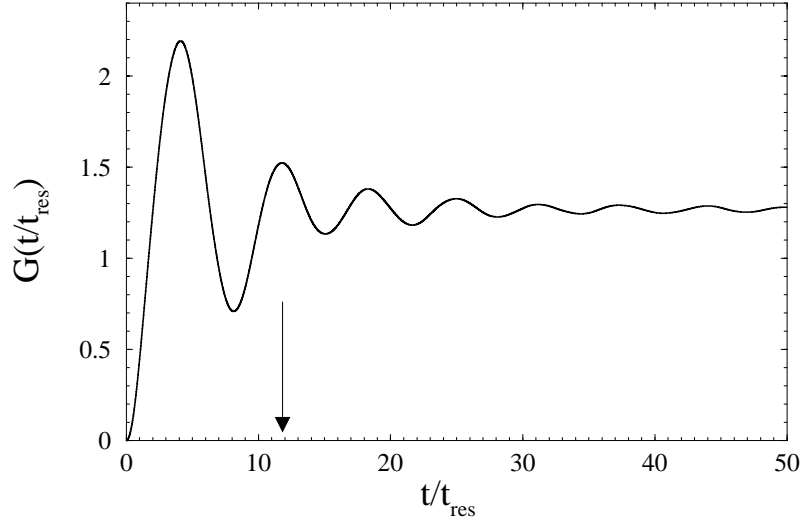


Fig. 5.4: The function G (5.16) vs. the scaled time variable t/t_{res} . It increases quadratically as the momentum of a harmonic oscillator for short times, then the continuum of frequencies of different periods of the nonlinear pendulum motion leads to dephasing, and G saturates with damped oscillations for large argument $t/t_{\text{res}} \gg 1$. The arrow marks the position of the “horn” in figures 5.1 and 5.6.

factors $(k|\epsilon|)^{-1/2} = 4/\delta J_{\text{res}}$, $(k|\epsilon|)^{1/2} = 1/t_{\text{res}}$ respectively. Therefore,

$$\langle (\delta J_t)^2 \rangle = \langle (J'_t - J'_0)^2 \rangle \sim k|\epsilon| G(t\sqrt{k|\epsilon|}), \quad (5.15)$$

for an ensemble of orbits started inside the resonant zone, where $G(\cdot)$ is a parameter-free function, whose explicit expression involves elliptic integrals [44]. $G(\cdot)$ represents the average energy contribution from trajectories in the primary island of the ϵSM , i.e.

$$G(t\sqrt{k|\epsilon|}) \simeq \frac{1}{8\pi} \int_0^{2\pi} d\theta \int_{-2}^2 dJ'_0 J' \left(t\sqrt{k|\epsilon|}, \theta_0, J'_0 \right)^2. \quad (5.16)$$

Hence, this function results from averaging over nonlinear pendulum motions with a continuum of different periods, so it saturates to a constant value when its argument $\gg 1$. At small values ($\ll 1$) of the argument, it behaves quadratically. This behaviour is illustrated in figure 5.4, where G is plotted vs. the scaled variable t/t_{res} . The contribution to the total energy is then obtained on multiplying (5.15) by $|\epsilon|^{-2} \delta J_{\text{res}} / (4\pi)$, because only a fraction $\sim \delta J_{\text{res}} / (2\pi)$ of the initial ensemble is trapped in the resonant zone. As a result

$$\langle E_{t,\epsilon} \rangle_{\text{res}} \sim \frac{\delta J_{\text{res}}}{4\pi} \frac{\langle (\delta J_t)^2 \rangle}{2\epsilon^2} \sim \frac{k^2}{\pi k \sqrt{|\epsilon|}} G \left(t\sqrt{k|\epsilon|} \right). \quad (5.17)$$

When δJ_{res} is small, $\sin^2(J'/2)$ may be replaced by $J'^2/4$ in the integrand in (5.13), leading to

$$\Phi(t) \sim \frac{k^2}{4} t \Phi_0(t\sqrt{k|\epsilon|})$$

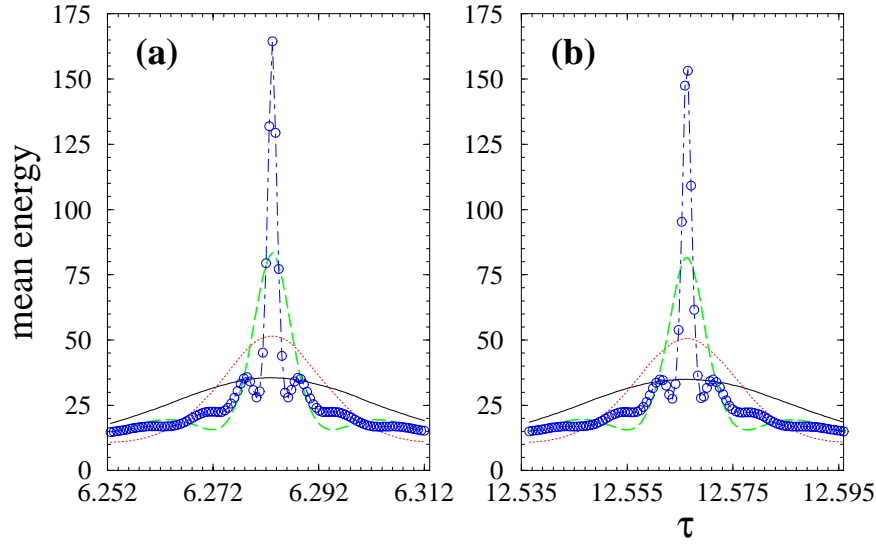


Fig. 5.5: Mean energy (in units of $(2\hbar k_L)^2/M$, c.f. (2.24)) vs. the kicking period $\tau \simeq 2\pi$ (a), and $\tau \simeq 4\pi$ (b), after $t = 20$ (solid), $t = 30$ (dotted), $t = 50$ (dashed), $t = 100$ (circles connected by dash-dotted line) kicks; for an ensemble of 10^5 δ -kicked atoms with Gaussian initial momentum distribution ($\sigma \simeq 2.7$) and kicking strength $k = 0.8\pi$.

with

$$\Phi_0(x) \equiv \frac{2}{\pi} \int_0^x ds \frac{\sin^2(s)}{s^2}.$$

Replacing in (5.12), we obtain the central result of this chapter:

$$R(t, k, \epsilon) \equiv \frac{\langle E_{t,\epsilon} \rangle}{\langle E_{t,0} \rangle} \sim H(x) \equiv 1 - \Phi_0(x) + \frac{4}{\pi x} G(x),$$

$$x = t\sqrt{k|\epsilon|} = t/t_{\text{res}}. \quad (5.18)$$

Hence $R(t, k, \epsilon)$ depends on t, k, ϵ only through the scaling variable $x = t/t_{\text{res}}$. This is natural, since the main ingredient in the derivation of (5.18) is the pendulum motion around the nonlinear island of the ϵ SM. The pendulum dynamics for (5.14) is governed by a single parameter which is the coupling strength $k|\epsilon|$, or the frequency of small oscillations around the elliptic fixed point $\omega_{\text{res}}(k|\epsilon|) \equiv \sqrt{k|\epsilon|}$, respectively [43, 44].

Because of (5.18) the width in ϵ of the resonance peak scales like $(kt^2)^{-1}$. This implies that for fixed k , the width of the resonance peak shrinks very quickly in time, as illustrated in figure 5.5 for an experimental relevant ensemble of β -rotors.

The scaling law (5.18) is demonstrated by numerical data shown in figure 5.6. The function $H(x)$ was calculated numerically; in particular, $G(x)$ was computed by a standard Runge-Kutta integration of the pendulum dynamics (5.14). The scaling function $H(x)$ decays proportional to x^{-1} at large x , because so do $1 - \Phi_0(x)$ and $4G(x)/(\pi x)$; the latter owing to the saturation of G . From

figure 5.6 it is seen that Φ_0 is quite slowly varying at $x > 4$. The structures observed in that region are then due to $G(x)$, which describes the resonant island. Figure 5.4 shows that $G(x)$ saturates via a chain of oscillations of decreasing amplitude around the asymptotic value. These give rise to three local maxima in the graph of $x^{-1}G(x)$, followed by a chain of gentle oscillations in the tail. The first and most pronounced maximum lies in the small- x region, and is not resolved by the scaling function $H(x)$, apparently because it is effaced by the rapid decay of $1 - \Phi_0(x)$. The subsequent maximum and its symmetric partner at $\epsilon < 0$ are instead resolved and precisely correspond to the “horns”, the right-hand one of which is marked by the arrow in figures 5.1(a) and 5.4. The oscillations in the tail of $x^{-1}G(x)$ are also well reproduced in the tail of $H(x)$. The scaling law shows that at given k, t the energy curve $\langle E_{t,\epsilon} \rangle$ vs. ϵ decays proportional to $|\epsilon|^{-1/2}$ past the “horns”. As t increases the horns rise higher while moving closer and closer to $\tau = 2\pi$, because they are located at a constant value of $x = t\sqrt{k|\epsilon|}$. Thus an overall $|\epsilon|^{-1/2}$ dependence eventually develops (cf. figures 5.1 and 5.6).

In the case when the smooth initial momentum distribution includes values $n_0 \neq 0$ and/or is appreciably non-uniform in quasi-momentum, the statistical weights of the various phase-space regions are different. Scaling in the single variable t/t_{res} still holds, but the scaling functions Φ_0 and G may be different. For a Gaussian initial distribution with mean square deviation $\sigma \simeq 2.7$, as used in the experiments reported in [82, 83, 135, 159], a scaling like in figure 5.6 was found numerically. The initial energy, which is negligible in the case of $p_0 \in [0, 1)$, must be subtracted such that the scaling holds, i.e. $(\langle E_{t,\epsilon} \rangle - \langle p_0^2/2 \rangle) / \langle E_{t,0} \rangle$ obeys the scaling law (5.18), as shown in figure 5.7 for a Gaussian initial momentum distribution.

Our analysis shows that the structure of the resonant peak is essentially determined by the primary resonant island of the ϵ SM. It neglects higher-harmonics resonances of the ϵ SM, higher-order islands, and especially the growth of the stochastic layer surrounding the primary resonance. Such structures grow with $|\epsilon|$ and are expected to introduce deviations from the scaling law (5.18). Hence this analysis is valid only if $|\epsilon|$ is sufficiently small, such that $k|\epsilon|_{cr} \ll 1$. On trespassing the threshold for global chaotic motion $k|\epsilon|_{cr} \approx 1$, the *critical regime* of the ϵ SM is entered. No isolating KAM curve survives [43], so the energy curve rises in time for $|\epsilon| > |\epsilon|_{cr}$ (see figure 5.8). Estimating the mean energy at relatively short times and below the threshold for global chaos in the ϵ SM, i.e. $|\epsilon|k < 4.5$ [43], is difficult, because unbounded, non-homogeneous diffusion and elliptic motion inside residual stable islands coexist. The increase of the curve with $|\epsilon|$ at constant t is a result of the decreasing size of the latter islands, and of the rapid increase of the diffusion coefficient (proportional to $(|\epsilon| - |\epsilon|_{cr})^\gamma$, $\gamma \simeq 3$ at large enough t [225, 274]).

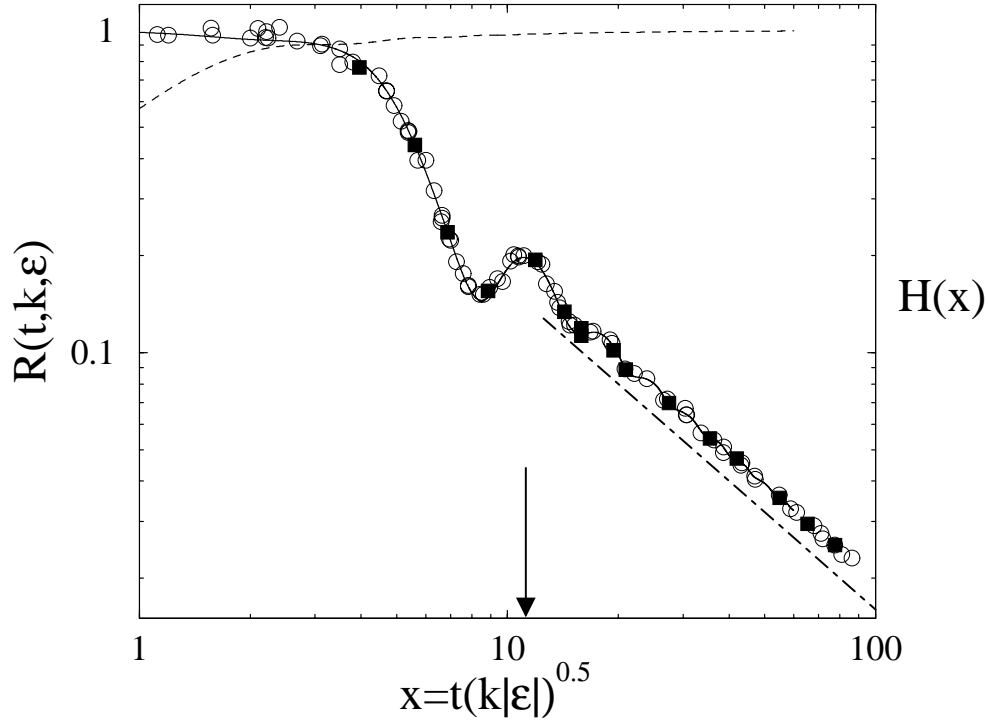


Fig. 5.6: Demonstrating the scaling (5.18) of the resonant peak, in a right neighbourhood of $\tau = 2\pi$. Open circles correspond to different values of the parameters ϵ, k, t , randomly generated in the ranges $1 < t < 200$, $0.001 < \epsilon < 0.1$, $0.1 < k < 50$ with the constraint $0.01 < k\epsilon < 0.2$. In each case an ensemble of 2×10^6 ϵ -classical rotors was used to numerically compute the scaled energy $R(t, k, \epsilon)$ (5.18), with a uniform distribution of initial momenta in $[0, 1)$ and a uniform distribution of initial θ in $[0, 2\pi)$. Full squares present quantum data for $k = 0.8\pi$, $t = 50$ and $t = 200$. The solid line through the data is the scaling function $H(x)$ of (5.18) obtained by direct numerical computation of the functions $\Phi_0(x)$ and $G(x)$. The dashed line represents the function $\Phi_0(x)$; the dash-dotted line has slope -1 and emphasises the x^{-1} decay described in the text. The arrow marks the value of the scaled detuning x which corresponds to the arrow in figure 5.1.

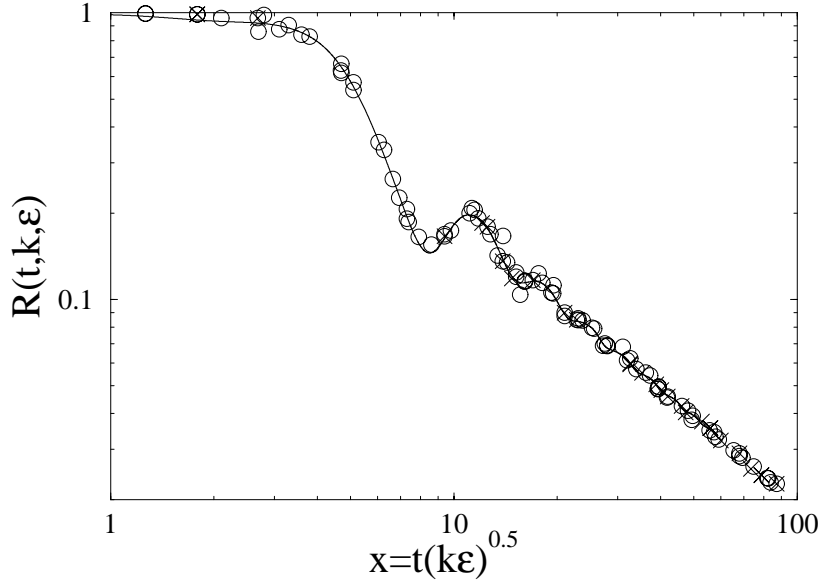


Fig. 5.7: Same as figure 5.6 for Gaussian initial momentum distribution with mean square deviation $\sigma \simeq 2.7$ (open circles, crosses), similar to experimental initial distribution in [82, 83, 135, 159]. The circles present ϵ -classical data where the initial energy of an individual atom was subtracted before computing the average energy value, while the crosses show ϵ -classical data where the mean initial energy was subtracted from the average energy value of the atomic ensemble after some fixed time t . The latter is the experimentally accessible method, and no difference between the two methods can be observed what concerns the scaling of the data. The solid line is the scaling function $H(x)$ from (5.18).

5.2.2 Validity of the ϵ -quasi-classical approximation

The ϵ -quasi-classical approximation is exact at all times for $\epsilon = 0$, as shown above. At nonzero ϵ , it is valid for not too large times t , and it is in the long run spoiled by quantum, non ϵ -classical effects. At $|\epsilon| < |\epsilon|_{cr}$ the ϵ -classical motion is bounded by KAM curves, so the main quantum mechanism leading to non- ϵ -classical behaviour is tunnelling across the regular regions. Estimating the related time scales is a non-trivial problem, because the 2π -periodicity in action of the ϵ -classical phase space may enhance tunnelling, and even result in delocalisation, depending on the degree of commensuration between 2π and the “Planck constant” $|\epsilon|$. For instance, if $|\epsilon|/2\pi$ is rational, then the quantum motion will be ballistic asymptotically in time. This is just the ordinary quantum resonance of the quantum kicked rotor (see section 2.2.2). In order that one such resonance with $|\epsilon| = 4\pi s/q$ exists at $|\epsilon|$ less than some $|\epsilon_0|$, it is necessary that $q > 4\pi/|\epsilon_0|$. It will show up after a time roughly estimated by $|\epsilon|$ times the inverse bandwidth. The bandwidth is estimated to decrease faster than exponentially at large q [64, 118], so one may infer that the time of validity of the ϵ -quasi-classical approximation is at least exponentially increasing with

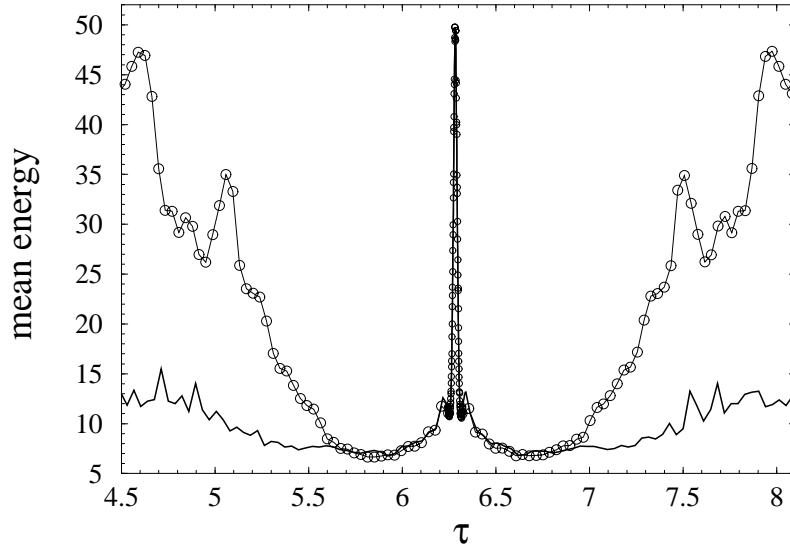


Fig. 5.8: Same as figure 5.1, however plotted in a broader window in τ around the quantum resonance peak at $\tau = 2\pi$. For larger detuning $|\epsilon| > 0.25$, the ϵ -classical approximation (circles and thin line) leads to larger energies than the quantum simulation (thick solid line). At $|\epsilon| > 0.25$ classical diffusion occurs, and the classical curves rise as a function of time t , while the quantum energies basically remain unchanged (for not too large times for which higher-order quantum resonances may be important).

$1/|\epsilon|$ as the exact resonance at $\epsilon = 0$ is approached.

At $|\epsilon| > |\epsilon|_{cr}$ the ϵ -classical motion is unbounded, and the difference between ϵ -classical and quantal energy curves vs. τ is basically set by various quantum localisation effects, including localisation by cantori close to the $|\epsilon|_{cr}$ [275, 276]. As a consequence, if t is large enough, then the ϵ -classical curve lies much higher than the quantum one (cf. figure 5.8). Nevertheless the latter still rises with $|\epsilon|$ at constant t , because of the growth of the localisation length $\sim D_{\text{eff}} \simeq k^2 \sin^2(\tau/2)$ [57, 227, 254–256], with $\tau = 2\pi\ell + \epsilon$ ($\ell \in \mathbb{N}$).

5.3 Classical scaling in presence of decoherence

The scaling law (5.18) derived in the previous section shows that the only relevant time scale for the evolution of the quantum motion sufficiently near to $\tau = 2\pi\ell$ ($\ell \in \mathbb{N}$) is given by $t_{\text{res}} = 1/\sqrt{k|\epsilon|}$. If we allow for a noisy time evolution as discussed in section 4.3, an additional time scale comes into play that characterises the strength of the noise [277]. In the following, we indeed find an equivalent of the scaling law (5.18) in the presence of noise, which is based on the two time scales t_{res} and t_c , where t_c is the mean waiting time between two spontaneous emission (SE) events.

The ϵ -quasi-classical approximation introduced in section 5.1 for the study of

the coherent nearly resonant quantum motion may be adapted to include SE, because the effects of SE were modelled by a totally classical noise. In the stochastic gauge (section 4.3.1), the ϵ -classical approximation may be implemented in the β -rotor propagators (4.27) much in the same way as in section 5.1. The resulting ϵ -classical map corresponding to (5.6) is:

$$I_{t+1} = I_t + \tilde{k} \sin(\theta_{t+1}) \quad , \quad \theta_{t+1} = \theta_t \pm I_t + \pi\ell + \tau\eta_t \quad . \quad (5.19)$$

We now exploit assumption (S2) of section 4.3.2 and write $\eta_t = \beta + \tilde{\delta}_t$, where $\tilde{\delta}_t = \sum_{s=1}^t \delta_s$ is the total momentum imparted by SE up to time t . In order to turn off the stochastic gauge, we need to recover the accumulated SE momentum change, hence we change variables to $I_t^* = I_t + |\epsilon|\tilde{\delta}_t$. The momentum of the atom at time t is then $|\epsilon|^{-1}I_t^* + \beta$, where β is the initial quasi-momentum. Denoting $\eta_t^* = \eta_t + \epsilon\beta/(2\pi\ell)$, and changing variables from (I_t, η_t) to (I_t^*, η_t^*) in 5.19, we obtain the following map:

$$\begin{aligned} I_{t+1}^* &= I_t^* + |\epsilon|\delta_{t+1} + \tilde{k} \sin(\theta_{t+1}) \quad , \\ \theta_{t+1} &= \theta_t \pm I_t^* + \pi\ell + 2\pi\ell\eta_t^* \quad , \\ \eta_{t+1}^* &= \eta_t^* + \delta_{t+1} \quad , \\ \eta_0^* &= \frac{\tau\beta}{2\pi\ell} \quad . \end{aligned} \quad (5.20)$$

The δ_t are independent random variables, whose distribution is determined by the statistics of SE.

Numerical simulations of such noisy ϵ -classical maps are shown in figure 5.9, and very well match with the quantal computations at small $|\epsilon|$. Under the substitution $J_t = \pm I_t^* + \pi\ell + 2\pi\ell\eta_t^*$, the map (5.20) reduces to a noisy ϵ SM, which differs from the ϵ SM by a random shift $\tau\delta_t$ of the action J at each step. We assume an initially uniform quasi-momentum distribution. At any SE time t_j , the distribution of the ensemble in the phase space of the ϵ SM is reshuffled by the random action change. Under the assumption of homogeneous distribution of single SEs in an interval of integer length (assumption (S3) in section 4.3.2), the resulting distribution of $J \bmod(2\pi)$ is approximately homogeneous over the unit cell of the ϵ SM. Such randomisation may be assumed to wash out correlations between the past and the subsequent random dynamics. Hence the scaling (5.18) may be used to write the energy at time t as

$$\langle E_{t,\epsilon} \rangle \sim \frac{k^2}{4} \left\langle \sum_{j=0}^{N_t-1} \Delta_j H(\Delta_j/t_{\text{res}}) \right\rangle + \frac{1}{2} D' n_{\text{SE}} t \quad , \quad (5.21)$$

where $\langle \cdot \rangle$ stands for the average over all the Bernoulli realisations of the times of SE events, according to the discussion after (4.29). n_{SE} is the average number of SE per period, and $D' = n_{\text{SE}}^{-1} \langle \delta_t^2 \rangle$ is the mean square momentum imparted by a single SE. For an individual realisation, (5.21) states that the energy is given by the sum of the SE-free scaling function H of the evolutions over time intervals Δ_j . The SE resets the evolution after each event at times Δ_j , apart from the momentum shift contained in the second term in (5.21). If t_c is sufficiently large

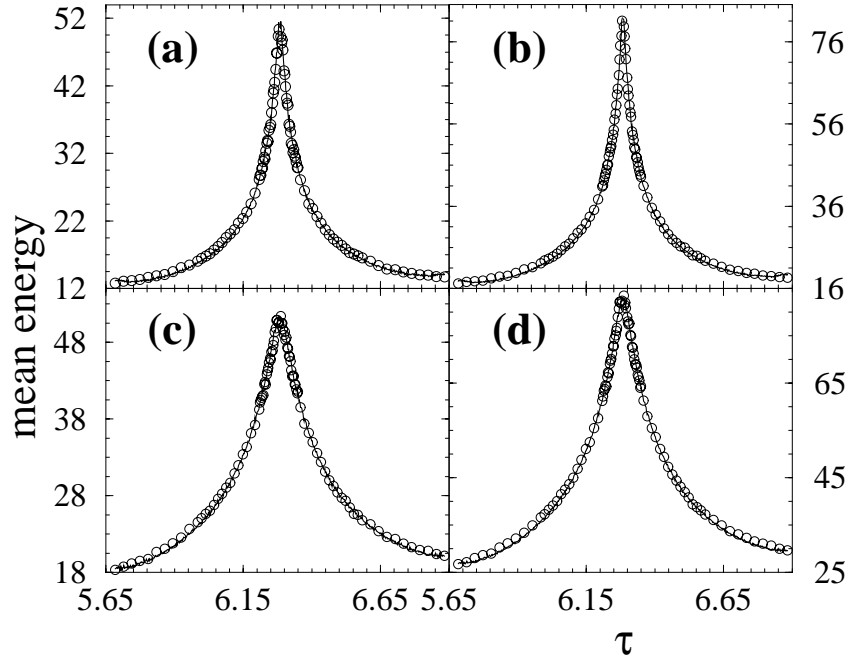


Fig. 5.9: Analogue of figure 5.1(a), with the same initial ensemble, for $k = 0.8\pi$, in the presence of SE. Results of full quantum calculations (circles) and of ϵ -classical ones (solid lines) in the presence of SE are compared near the resonance $\tau = 2\pi$, for different times and different rates of SE: (a) $p_{\text{SE}} = 0.1, t = 30$, (b) $p_{\text{SE}} = 0.1, t = 50$, (c) $p_{\text{SE}} = 0.2, t = 30$, and (d) $p_{\text{SE}} = 0.2, t = 50$. The quantum simulation was type (I) (see section 4.3.5), while the ϵ -classical simulations used the map (5.20).

compared to 1, one may replace the Bernoulli process by the continuous time Poisson process with the characteristic time $t_c = -1/(\ln(1 - p_{\text{SE}})) = 1/n_{\text{SE}}$. This process has the delays Δ distributed with the density $t_c^{-1} \exp(-\Delta/t_c)$. Its statistics reduces to that of the unit Poisson process (with $t_c = 1$) by just rescaling all times by the factor $1/t_c$. This entails

$$\left\langle \sum_{j=0}^{N_{t-1}} \Delta_j H(\Delta_j/t_{\text{res}}) \right\rangle \approx 4t_c Q(t/t_c, t_c/t_{\text{res}}), \quad (5.22)$$

where

$$Q(u, v) \equiv \frac{1}{4} \left\langle \sum_{j=0}^{N_u^1} \Delta_j^1 H(\Delta_j^1 v) \right\rangle. \quad (5.23)$$

The superscript 1 specifies that the average is now over the realisations of the unit Poisson process: each realisation has the continuous time interval $[0, u]$ divided in subintervals Δ_j^1 by a random number N_u^1 of Poisson events. We are

hence led to the following scaling law:

$$\langle E_{t,\epsilon} \rangle \sim D' \frac{t}{2t_c} + k^2 t_c Q\left(\frac{t}{t_c}, \frac{t_c}{t_{\text{res}}}\right) \quad (5.24)$$

or, equivalently,

$$\frac{2\langle E_{t,\epsilon} \rangle - D't/t_c}{2k^2 t_c} \sim Q(u, v) \quad , \quad u = t/t_c \quad , \quad v = t_c/t_{\text{res}} \quad . \quad (5.25)$$

The scaling function $Q(u, v)$ may be explicitly written in terms of the function $H(x)$ as reported in appendix D:

$$4Q(u, v) = uH(uv)e^{-u} + \int_0^u dx e^{-x} x H(xv)(2 + u - x) \quad . \quad (5.26)$$

Limiting behaviours of the scaling function $Q(u, v)$ immediately follow from this equation, or from (5.23) itself. On one hand, for $u = t/t_c \gg 1$ the right-hand side in (5.23) is a sum of a large number $\sim t/t_c$ of terms. In that limit, such terms are quite weakly correlated and may be independently averaged, leading to:

$$u \gg 1 : \quad Q(u, v) \sim \frac{1}{4} u \int_0^\infty dx H(vx) x e^{-x} \quad . \quad (5.27)$$

On the other hand, for $t/t_c \ll 1$, the sum reduces to the single term $j = 0$, with $\Delta_0^1 = t/t_c$; hence

$$u \ll 1 : \quad Q(u, v) \sim \frac{1}{4} u H(uv) \quad . \quad (5.28)$$

In particular, (5.28) shows that (5.24) coincides with (5.18) in the SE-free limit $t_c \rightarrow \infty$. In the opposite limit, (5.27) shows that, if k is fixed, then the width in ϵ of the resonant spike will not shrink any more with time when $t \gg t_c$, and its width thereafter scales like $(t_c^2 k)^{-1}$. The spike is therefore erased (that is, it is absorbed in the background) in the strong noise limit $t_c \sim 1$. In the latter limit, the method developed above breaks down, because on average after each kick a SE event happens, which does not let the time evolution recover for some time interval. The result is then a completely random motion which does not depend on the system specific dynamics, and hence not on the value of the kicking period τ .

The spreading of the resonance peaks with increasing noise, as can be seen nicely in figure 5.9, explains why they are more stable and easier to observe experimentally than in the case without noise. Together with the results of the last chapter, this resolves now the puzzles put forward by the experimental data in figure 4.1 or in [82, 83, 135]. An intuitive argument for the spreading of the resonance peaks is that for a fixed value of ϵ , due to SE there is an enhanced chance to find a quasi-momentum β , such that the free evolution part of the Floquet operator is approximately the identity. This is the condition for quantum resonant motion at $\tau = 2\pi\ell$ ($\ell \in \mathbb{N}$), as discussed in section 2.2.2.

Numerical simulations in figure 5.10 satisfactorily support the scaling law (5.24). Data were obtained in a similar manner as for the case without SE; however, one of the parameters u, v is varied, while keeping fixed either the other parameter or the ratio u/v . The theoretical scaling function $Q(u, v)$ was calculated

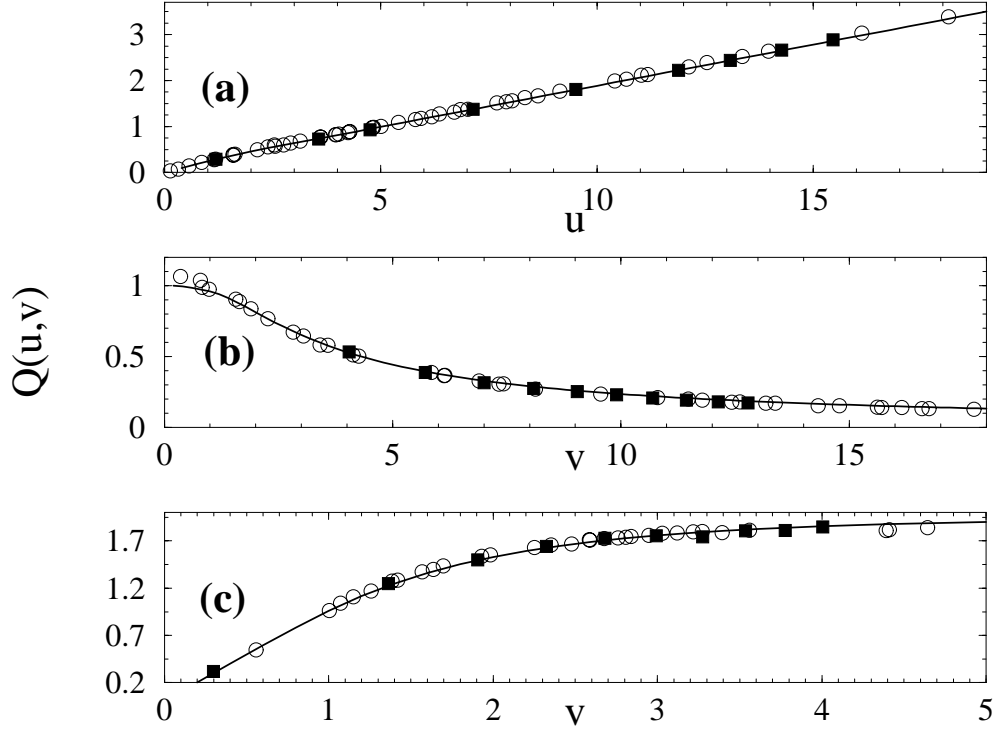


Fig. 5.10: Demonstrating the scaling law (5.24) in a right neighbourhood of $\tau = 2\pi$. In (a), (b) the quantity on the left-hand side of (5.25) is plotted vs. one of the parameters $u = t/t_c$ or $v = t_c/t_{\text{res}}$ while keeping the other fixed: (a) $v = 2$, (b) $u = 4$. In (c) the ratio $u/v = 4$ is fixed. Open symbols correspond to different values of the parameters t, t_c, k, ϵ , randomly generated in the ranges $1 < t < 200$, $5 < t_c < 60$, $0.001 < \epsilon < 0.1$, $0.1 < k < 20$, with the constraints $0.001 < k\epsilon < 0.2$ and $t_c\sqrt{k\epsilon} = 2$ in (a), $t/t_c = 4$ in (b), $t = 4t_c^2\sqrt{k\epsilon}$ in (c). In each case an ensemble of 2×10^6 ϵ -classical rotors was used, with a uniform distribution of initial momenta in $[0, 1)$ and a uniform distribution of initial θ in $[0, 2\pi)$. The random momentum shifts at each step of the ϵ -classical evolution (5.20) were generated from the uniform distribution in $[-1/2, 1/2]$. Full squares represent quantum data for $k = 0.8\pi$, and $\epsilon = 0.01$ in (a), $\epsilon = 0.05$ in (c), and $t = 50$ and $t = 100$ in (b). The solid lines correspond to the theoretical formula (5.26).

numerically using in (5.26) the function $H(x)$ computed as described in section 5.2.

If $f_0(\beta_0)$ is smooth but not uniform, the scaling in absence of SE of the form (5.18) holds but with a different scaling function H as explained in section 5.2. Therefore the arguments of the present section leading to (5.24) should hold also in this case.

Chapter 6

Decay of fidelity for δ -kicked atoms

What a fuss people make about fidelity!

O. Wilde, The picture of Dorian Gray

In the previous two chapters, a powerful machinery was developed for a comprehensive understanding of the dynamics of δ -kicked atoms, at the fundamental quantum resonances and in their vicinity.

In the present chapter, the theory of chapter 4 as well as the ϵ -quasi-classical approximation of chapter 5 are applied to calculate and/or estimate the overlap of two initially identical states which are subject to two distinct evolutions. The overlap function, the “quantum fidelity”, is studied at exact resonance conditions (with kicking period $\tau = 2\pi\ell$, $\ell \in \mathbb{N}$), and for small detunings ϵ at $\tau = 2\pi\ell + \epsilon$. In contrast to the derivation of the momentum distributions, and their second moment, the average energies, the fidelity depends crucially on the phases of the evolved wave functions. In section 6.2.2 the destruction of coherence by added decoherence – in form of spontaneous emission (SE) – builds on the stochastic wave function (4.38), and the method developed in section 4.3 is a useful tool to calculate the evolution of wave packets, including their phases.

6.1 Stability of quantum dynamics and experimental proposal

When discussing the atomic conductance fluctuations (section 3.2.3), a characteristic feature emanating from classical chaos displayed: the extreme sensitivity

with respect to changes of the system's parameters [109–111, 140, 278]. In the case of the atomic conductance the control parameter was the driving frequency. How can one quantify the sensitivity with respect to parameter variation, i.e. to changes in the Hamiltonian?

A measure for the stability of quantum dynamics was introduced in [138]: the overlap of two initially identical quantum states which are exposed to two different time evolutions [138–140]. The overlap, or the quantum fidelity, is defined as

$$F(t) = \left| \langle \psi | e^{i\hat{H}_\delta t/\hbar} e^{-i\hat{H}_0 t/\hbar} | \psi \rangle \right|^2 \quad (6.1)$$

where \hat{H}_0 , and $\hat{H}_\delta = \hat{H}_0 + \delta\hat{V}$ represent the Hamiltonians of a reference system and of its slightly perturbed variant, respectively, with the perturbation parameter δ . The decay of fidelity in time was studied for classically chaotic quantum systems, usually for relatively small perturbations $\delta \ll 1$. Depending on the strength of the perturbation, several regimes of Gaussian and exponential decay were identified [279–283]. For a classically quasi-regular system, a power-law decay has been found [284]. The quantum-classical correspondence, however, is still subject of some controversy [141].

For an initial statistical mixture of pure states $|\psi_n\rangle$, appearing with probabilities ρ_n , the fidelity may be defined in terms of the statistical density operator $\hat{\rho} = \sum_n \rho_n |\psi_n\rangle\langle\psi_n|$ [155, 285]:

$$F(t) = \left| \text{Tr} \left\{ \hat{\rho} \hat{U}_{-t}^\delta \hat{U}_t \right\} \right|^2. \quad (6.2)$$

\hat{U}_t and \hat{U}_t^δ represent the evolution operators corresponding to the Hamiltonians \hat{H}_0 and \hat{H}_δ , respectively. This definition will be used below when dealing with incoherent initial ensembles of momentum states (see equation (6.7) and (E.8)). An experiment which accesses the fidelity for the δ -kicked oscillator was proposed in [286, 287], and investigations with δ -kicked atoms were reported in [143, 288]. The experiment is based on the actual sublevel structure of the atoms' ground and excited state which are used to induce the kicking potential (see section 2.3.2). Before the relevant dynamics starts, two ground state sublevels are equally populated, and couple differently to the external driving because of the different detuning with respect to the transition to the corresponding excited level ($V_0 \propto 1/\Delta_L$ in (2.35)). The splitting of the populations and the reversal after the dynamical evolution is performed by a Ramsey-type interferometer technique [172, 289]. In the absence of coherence-destroying spontaneous emission, the contrast of the measured interference fringes is related to the overlap of two initially identical states evolved under different Hamiltonians. The difference occurs in the coupling parameter, the kicking strength.

The experimental setup is illustrated in figure 6.1: caesium atoms are initially prepared in the hyperfine level $F = 3, m_F = 0$ of the $6^2S_{1/2}$ ground state. The first microwave (Ramsey) pulse creates an equal superposition of the atom's internal states, $F = 3, m_F = 0$ and $F = 4, m_F = 0$. Now the atoms are exposed to the δ -kicked evolution, before a second Ramsey pulse reshuffles the population of the two relevant ground state levels. The phase delay between

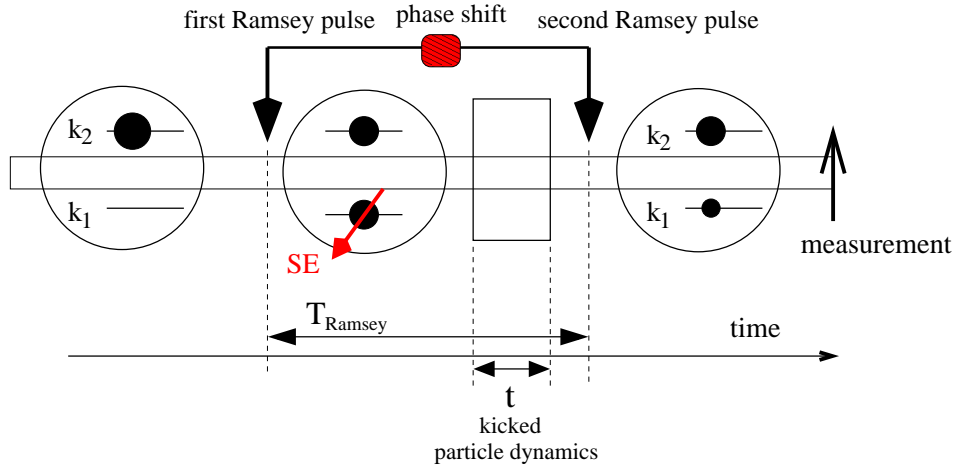


Fig. 6.1: Scheme of the experimental setup of [135, 143, 288]. Each atom is prepared in the upper state (left), then a $\pi/2$ Ramsey pulse is applied before the time evolution starts (kicked-particle dynamics with/without gravity) for a coherent superposition of the upper (with corresponding kicking strength $k = k_2$) and lower ($k = k_1$) level. The dynamics lasts for a time interval t , afterwards a second $\pi/2$ Ramsey pulse (with time delay to the first one T_{Ramsey}) is applied which reshuffles the population in the upper and lower level according to the value of the Ramsey phase. We allow additional spontaneous emission (SE) events to happen during the time interval t in our scheme.

the two Ramsey pulses, which determines the final population of the levels, is experimentally tunable [288]. Finally, the (centre-of-mass) momentum distribution of *one* of the ground state levels is measured – corresponding to a state projection onto this level. From the experimental signal, the overlap of the two distinctly evolved states may be extracted as an *average* over all atoms used in the experiment.

To increase the efficiency of the experiment, when focusing on certain dynamical regimes, and, in particular, to minimise the effect of averaging, the actual proposal [135, 143, 288] was to use a variant of the δ -kicked atom dynamics. This variant is subject to an additional linear potential which is provided by gravity. The constant field modifies the dynamics considerably because it alters the phases of the states accumulated between consecutive kicks. Very robust quantum accelerator modes have been observed in specific parameter ranges around the quantum resonances [83, 290, 291] discussed in the previous chapters. Using a slightly amended ϵ -quasi-classical approximation with respect to the one presented in chapter 5, a large number of these modes could be identified [144] and measured [288]. Apart from the last section 6.4, where preliminary results on the quantum fidelity in the “ δ -kicked accelerator” are reported, we restrict to the conventional δ -kicked particle dynamics at the fundamental quantum resonances ($\tau = 2\pi\ell$, $\ell \in \mathbb{N}$) and in their vicinity.

6.2 Fidelity at quantum resonance

6.2.1 Dynamical stability in absence of noise

Before the discussion of the fidelity, which will be defined in equation (6.7) in a form useful for our purposes, we show how to extract it from the data obtained by experiments [143, 288]. The following arguments are based on the intuitive interferometric picture suggested by figure 6.1. A more elegant presentation of (6.3-6.7) may be found in appendix E.

Let us assume we start the experiment at time $T = 0$. One $\pi/2$ Ramsey pulse [172, 289, 292] acts on the upper atomic level $|2\rangle \rightarrow (|1\rangle + |2\rangle)/\sqrt{2}$, and on the lower level $|1\rangle \rightarrow (|1\rangle - |2\rangle)/\sqrt{2}$, respectively. E_1, E_2 are the energies of the atomic levels ($\hbar \equiv 1$ is assumed). After a time delay T_{Ramsey} , the second pulse produces the transformations $|2\rangle \rightarrow (\exp(i\phi)|1\rangle + |2\rangle)/\sqrt{2}$, $|1\rangle \rightarrow (|1\rangle - \exp(-i\phi)|2\rangle)/\sqrt{2}$, with ϕ being a controllable phase of the Ramsey pulse source [172, 288, 292]. The rotor states are expanded in the momentum basis, where the expansion coefficients between the two pulses are different for the two arms of the interferometer, because of the two different time evolutions, characterised by k_1 and k_2 , respectively. In the sequel, $\psi_\beta(t, n, k_{1,2})$ denotes the time-dependent wave function of a β -rotor in the momentum representation (the bar in (2.20) is dropped; the integer t denotes the number of applied kicks). Initially, a momentum distribution is prepared in the level $|2\rangle$, and the free evolution after the first Ramsey pulse leads to

$$T = 0 : \sum_{n_0} \psi_\beta(n_0) |n_0\rangle \otimes |2\rangle \rightarrow \frac{1}{\sqrt{2}} \sum_{n_0} \psi_\beta(n_0) |n_0\rangle \otimes (|1\rangle + |2\rangle)$$

$$0 < T < T_{\text{KR}} : \frac{1}{\sqrt{2}} \sum_{n_0} \psi_\beta(n_0) |n_0\rangle \otimes (e^{-iE_1 T} |1\rangle + e^{-iE_2 T} |2\rangle) .$$

At time $T = T_{\text{KR}}$ (corresponding to $t = 0$) the kicked-particle evolution starts with the kick counter t . The kicks effectively act only on the external centre-of-mass motion, not on the electronic degrees of freedom (see section 2.3.2), and hence the state vector up to the second Ramsey pulse reads

$$T_{\text{KR}} < T < T_{\text{Ramsey}} :$$

$$\frac{1}{\sqrt{2}} \sum_n \psi_\beta(t, n, k_1) |n\rangle \otimes e^{-iE_1 T} |1\rangle + \psi_\beta(t, n, k_2) |n\rangle \otimes e^{-iE_2 T} |2\rangle .$$

At time $T \geq T_{\text{Ramsey}}$ the distribution is reshuffled according to the above mentioned rule

$$|\psi_{\beta, \text{end}(t, n)}\rangle = \frac{1}{2} e^{-iE_1 T} \left[|1\rangle \left(\psi_\beta(t, n, k_1) + \psi_\beta(t, n, k_2) e^{-i\phi_{\text{Ramsey}}} \right) + e^{-iE_2 T} |2\rangle \left(-e^{i\phi_{\text{Ramsey}}} \psi_\beta(t, n, k_1) + \psi_\beta(t, n, k_2) \right) \right] . \quad (6.3)$$

The Ramsey phase $\phi_{\text{Ramsey}} \equiv (E_2 - E_1)T_{\text{Ramsey}} - \phi$ describes the phase difference accumulated between the pulse source and the internal atomic phase evolution

in the time interval T_{Ramsey} [172, 292]. We now assume that the projection onto a specific momentum state and onto the lower internal level $|1\rangle$ is measured. We average incoherently over a given initial momentum distribution of independent β -rotors. The probability of finding the atom in a momentum eigenstate with eigenvalue $p \simeq n$ (i.e. a coarse-grained integer value, see section 4.2.1) depends on the number of applied kicks t , and on the two kicking strengths k_1 and k_2 :

$$\begin{aligned} P_n(t, k_1, k_2) &= \frac{1}{4} \int d\beta f_0(\beta) [|\psi_\beta(t, n, k_1)|^2 + |\psi_\beta(t, n, k_2)|^2] \\ &\quad + \frac{1}{2} \left| \int d\beta f_0(\beta) \psi_\beta^*(t, n, k_1) \psi_\beta(t, n, k_2) \right| \\ &\quad \times \cos \left(\phi_{k_1, k_2}^{(n)} + \phi_{\text{Ramsey}} \right), \end{aligned} \quad (6.4)$$

where $\phi_{k_1, k_2}^{(n)}$ is the phase of the interference term, i.e.

$$\begin{aligned} &\int d\beta f_0(\beta) \psi_\beta^*(t, n, k_1) \psi_\beta(t, n, k_2) \\ &= \left| \int d\beta f_0(\beta) \psi_\beta^*(t, n, k_1) \psi_\beta(t, n, k_2) \right| e^{i\phi_{k_1, k_2}^{(n)}}. \end{aligned} \quad (6.5)$$

The initial momentum distribution (typically Gaussian with $\sigma \simeq 2.7$ [83]) implies an ensemble of β -rotors with density $f_0(\beta)$ (see section 4.2.1). The third (interference) term in equation (6.4) is responsible for the appearance of oscillatory fringes in the visibility. The latter is defined by the difference between the maximum and minimum of the experimental signal as a function of the Ramsey phase, for all other parameters fixed [288]. We denote the amplitude of the modulation in $P_n(t, k_1, k_2)$ by $A(k_1, k_2, n) = \left| \int d\beta f_0(\beta) \psi_\beta^*(t, n, k_1) \psi_\beta(t, n, k_2) \right|$. In [288]

$$O(k_1, k_2) = \sum_{n=-\infty}^{+\infty} A(k_1, k_2, n)^2 \quad (6.6)$$

was identified as the “quantum stability measure of Peres” [138]. For reasons of proper normalisation*, the quantity $O(k_1, k_2)$ is problematic, because of the absolute square taken *before* the average over all momenta. In the following, we define the quantum fidelity as

$$F(t, k_1, k_2) \equiv \left| \sum_{n=-\infty}^{+\infty} \int d\beta f_0(\beta) \psi_\beta^*(t, n, k_1) \psi_\beta(t, n, k_2) \right|^2. \quad (6.7)$$

In our definition, the absolute square is taken *after* all averages, and it coincides with the standard definition (6.2) of fidelity involving ensemble averages (see appendix E). In the experiment, only (6.4) is directly accessible, and therefore only $A(k_1, k_2, n)$. However, from the form of (6.4) it is clear that scanning the Ramsey phase over a sufficiently wide range (maximally over an interval of 2π) it should be possible to reconstruct the unknown phase $\phi_{k_1, k_2}^{(n)}$, and hence to

*For identical evolutions in the two “arms” of the Ramsey interferometer, the fidelity as defined in (6.7) keeps the value 1 for all times.

access the fidelity (6.7).

To compute the fidelity (6.7) we must calculate the product of two states of the form (4.6), for two different values of the kicking strength, and then sum over all integer momenta n :

$$\begin{aligned}
& \sum_{n=-\infty}^{+\infty} \psi_{\beta}^*(t, n, k_2) \psi_{\beta}(t, n, k_1) \\
&= \sum_{n=-\infty}^{+\infty} \frac{1}{(2\pi)^2} \int_0^{2\pi} d\zeta \int_0^{2\pi} d\theta e^{-in(\theta-\zeta) - i(k_1 \cos(\theta) - k_2 \cos(\zeta)) |W_t|} \\
&= \frac{1}{2\pi} \int_0^{2\pi} d\theta e^{-i(k_1 - k_2) \cos(\theta) |W_t|} , \tag{6.8}
\end{aligned}$$

where we used $|\psi_{\beta}(\theta - t\xi - \arg(W_t))|^2 = 1/(2\pi)$ for the special case when the initial state of the particle is a plane wave with momentum $p_0 = n_0 + \beta$ (cf. equation (2.22)). With (F.1) the overlap (6.8) reads

$$\sum_{n=-\infty}^{+\infty} \psi_{\beta}^*(t, n, k_2) \psi_{\beta}(t, n, k_1) = J_0(|W_t|(k_2 - k_1)) , \tag{6.9}$$

leading to the result for the fidelity of one individual β -rotor:

$$\begin{aligned}
F_{\beta}(t) &= \left| \sum_{n=-\infty}^{+\infty} \psi_{\beta}^*(t, n, k_2) \psi_{\beta}(t, n, k_1) \right|^2 \\
&= J_0^2(|W_t|(k_2 - k_1)) . \tag{6.10}
\end{aligned}$$

For $\Delta k \equiv k_1 - k_2 = 0$, this gives $F_{\beta} = F_{\beta}(t) = 1$. For the resonant values of quasi-momentum $\beta_{\text{res}} = 1/2 + j/\ell \bmod(1)$, with $j = 0, 1, \dots, \ell - 1$, $|W_t| = t$, and we can use the asymptotic expansion formula (F.8). The fidelity for large times at quantum resonance is then:

$$F_{\beta_{\text{res}}}(t) \simeq \frac{2}{\pi t \Delta k} \cos^2\left(t \Delta k - \frac{\pi}{4}\right) . \tag{6.11}$$

This shows that the fidelity falls off like $1/t$ for the resonantly driven rotors. A numerical computation of the quantum evolution (figure 6.2) agrees with this asymptotic result already at times $t \geq 2$. The situation is less clear for general values of the quasi-momentum, because (6.10) sensitively depends on β through W_t in (4.9). Another particular case is given for $\beta = 0$ or $\xi_0 = \pi$:

$$F_{\beta=0}(t) = J_0^2\left(\left|\sin\left(t\frac{\pi}{2}\right)\right|(k_2 - k_1)\right) , \tag{6.12}$$

which at $t = 1$ depends only on the difference Δk of the two kicking strengths. Then (6.12) can be made arbitrarily small by choosing $\Delta k \simeq z_0$, where $z_0 \simeq 2.40$ is the first zero of J_0 .

To compute the full fidelity

$$F(t, k_1, k_2) = \left| \int_0^1 d\beta J_0(|W_t|(k_2 - k_1)) \right|^2 , \tag{6.13}$$

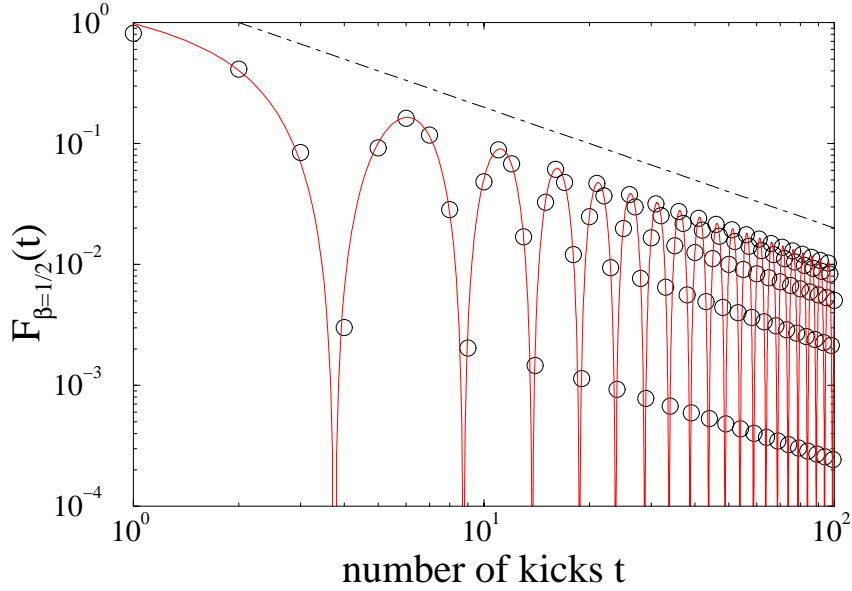


Fig. 6.2: Numerically computed evolution of one resonant β -rotor for $\tau = 2\pi$, and initial momentum $p_0 = \beta = 1/2$. The corresponding fidelity $F_{\beta=1/2}(t, k_1 = 0.8\pi, k_2 = 0.6\pi)$ vs. time t is shown (circles) together with the asymptotic formula (6.11) (solid line). The dot-dashed line indicates the $1/t$ decay.

for a uniform distribution of quasi-momenta with $f_0(\beta) \equiv 1$, we must perform the average over the different quasi-momenta, i.e.

$$\begin{aligned} & \int_0^1 d\beta J_0(|W_t|(k_2 - k_1)) = \int_{-\pi}^{\pi} \frac{dx}{2\pi} J_0(\Delta k \sin(tx) \csc(x)) \\ &= \int_{-\pi}^{\pi} \frac{dx}{4\pi^2} \sum_{r=0}^{t-1} \frac{2\pi}{t} J_0(\Delta k \sin(x) \csc(xt^{-1} + 2\pi r t^{-1})). \end{aligned} \quad (6.14)$$

As shown in section 4.2.1, in the limit when $t \rightarrow \infty$ and $2\pi r/t \rightarrow \alpha$, the sum over r approximates the integral over α , and (6.14) converges to

$$\begin{aligned} & \int_0^1 d\beta J_0(|W_t|(k_2 - k_1)) \\ & \rightarrow \frac{1}{(2\pi)^2} \int_{-\pi}^{\pi} dx \int_0^{2\pi} d\alpha J_0(\Delta k \sin(x) \csc(\alpha)). \end{aligned} \quad (6.15)$$

With (F.4) we obtain the final result for the asymptotic value of the fidelity:

$$F^*(\Delta k) \equiv \frac{1}{(2\pi)^2} \left(\int_0^{2\pi} d\alpha J_0^2 \left(\frac{\Delta k \csc(\alpha)}{2} \right) \right)^2. \quad (6.16)$$

The dependence on Δk of the formula (6.16) is shown in figure 6.3 together with explicit numerical calculations. There are local maxima, which means that the asymptotic fidelity F^* does not fall off monotonically as a function of

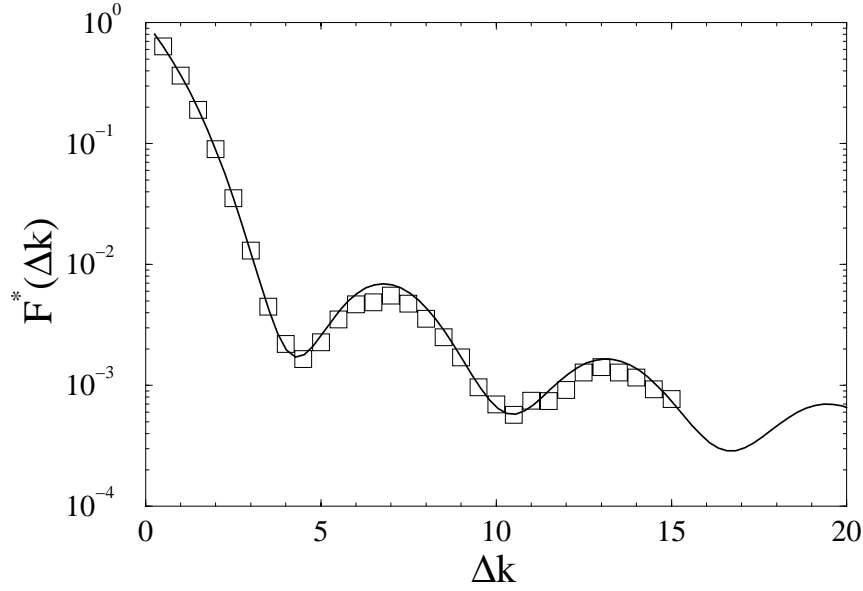


Fig. 6.3: Asymptotic fidelity at quantum resonance (6.16) vs. Δk (solid line), compared with numerical data obtained by evolving ensembles of 10^4 β -rotors with uniform initial momentum distribution in $[0, 1)$, and $\tau = 2\pi$ (open squares). The data is shown for all Δk at $t = 50$, when it typically has reached its asymptotic value (see figure 6.4).

the perturbation, which is given by Δk . Note that a finite saturation value F^* is always reached, i.e. the fidelity at exact quantum resonances $\tau = 2\pi\ell$ always saturates, where the saturation time may depend on the choice of k_1, k_2 .

In figure 6.4 numerical data for the fidelity $F(t, \Delta k)$ is presented for various values of the difference Δk between the two kicking amplitudes. Experimentally feasible should be values of $\Delta k/k \simeq 0.05 \dots 0.5$ [260], and the results reported in [288] were obtained for $k_1 \simeq 0.8\pi$ and $k_2 \simeq 0.6\pi$ (the laser amplitude depends on the position of the atoms with respect to the beam centre; this introduces some spread in the kicking strength, cf. section 2.3.3). The latter values are used as a guidance in the following discussions. The minima in figure 6.4 are given by the minima of (6.13). Differentiating with respect to Δk gives

$$\frac{dF}{d(\Delta k)} = - \left\{ \int_0^1 d\beta J_0(|W_t|\Delta k) \right\} \int_0^1 d\beta J_1(|W_t|\Delta k) |W_t|. \quad (6.17)$$

For $t \gg 1$, $|W_t|^2/t$ approaches $\delta(\beta - 1/2)$ (see (4.19)), and hence, we approximately obtain:

$$\frac{dF}{d(\Delta k)} \sim - \left\{ \int_0^1 d\beta J_0(|W_t|\Delta k) \right\} J_1(t\Delta k). \quad (6.18)$$

Without loss of generality we restricted to $\tau = 2\pi$, with only one resonant value $\beta_{\text{res}} = 1/2$ (for $\tau = 2\pi\ell$, we obtain the same result for all $\ell > 0$, see section 4.2.2). Therefore, the first zero of the Bessel function $J_1(z)$ ($z = z_1 \simeq 3.83$) is responsible for the minimum in figure 6.4. This is demonstrated by plotting

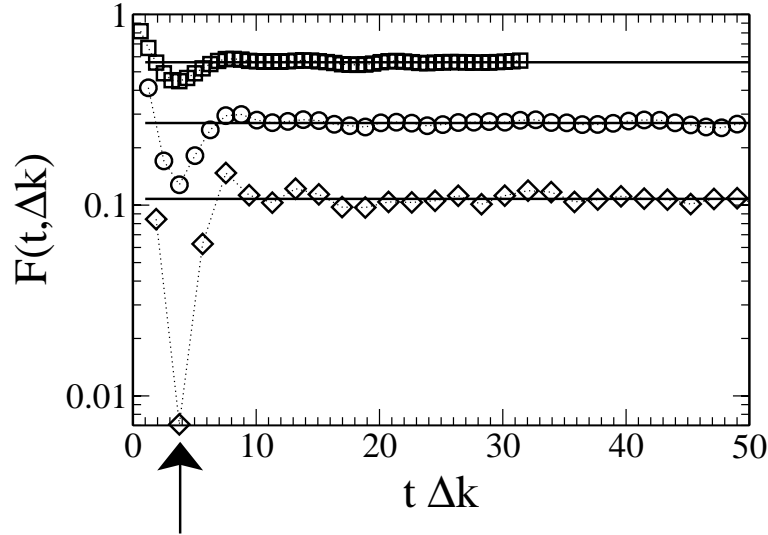


Fig. 6.4: Numerically computed fidelity (6.13) at quantum resonance ($\tau = 2\pi$) vs. $t\Delta k$, with reference kicking strength $k_1 = 0.8\pi$ and fixed $\Delta k = 0.6283$ (squares) 1.257 (circles) and 1.885 (diamonds), and the same initial ensemble as in figure 6.3. The position of the minima corresponds to the time $t_{\min} \simeq 3.83/\Delta k$ (marked by the arrow). The fidelity saturates for times $t \gtrsim 25$ at a constant value, which is indicated by the horizontal lines.

$F(t, \Delta k)$ vs. $t\Delta k$. On the other hand, $\int_0^1 d\beta J_0(|W_t|\Delta k) = 0$, hence fidelity zero, was found numerically only at $t \simeq 1.31$ with fixed $t\Delta k = z_1$, what is excluded for integer kick counters t .

6.2.2 Fidelity in presence of decoherence

We start with the scenario in which SE can happen only in *one* of the two “arms” of the Ramsey interferometer (figure 6.1). SE is induced by an additional near resonant (to one interferometer path, i.e. the k_1 arm) laser, which is switched on for a time τ_{SE} immediately after each kick. As described in section 4.3, the additional laser induces transitions to the excited state of the atom from which it may decay spontaneously, leading to random momentum shifts. If a SE event happens, we in principal know along which path of the interferometer the atom went, and a measurement of the emitted photon would correspond to a which-path detection [211]. This information destroys the coherence of the Ramsey evolution [172], and the fidelity is expected to decay exponentially. For calculating the fidelity of a state subject to SE with the “deterministic” state (4.6) the phases $\varphi_t \equiv n \arg(W_t)$ in (4.6) are substituted by random processes (in the case without SE the phases cancelled because they do not depend on the kicking strength). If now a SE event happens, we must perform an ensemble average over the randomised phase φ_t in the state (4.38) subject to SE, what gives zero. The probability that up to time t no event occurs is given by

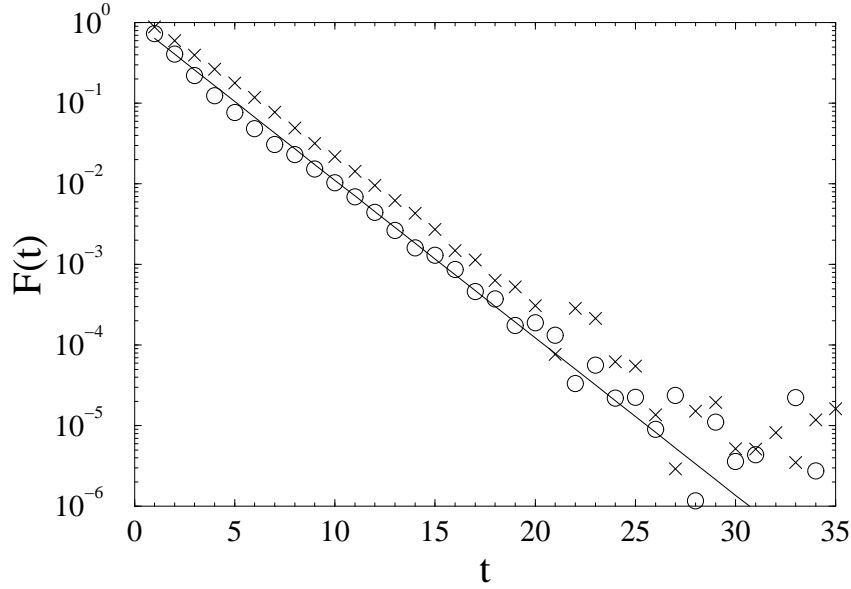


Fig. 6.5: Fidelity vs. number of applied kicks t at $\tau = 2\pi$, for the same initial ensemble as in figure 6.3, and with added spontaneous emission (type (I) simulation, cf. section 4.3.5) in only the k_1 -arm of the Ramsey interferometer (figure 6.1); kicking strengths: $k_1 = 0.8\pi, k_2 = 0.6\pi$ (circles), $k_2 = 0.75\pi$ (crosses), and for an event probability per kick $p_{\text{SE}} = 0.2$. The decay exponent (solid line) $2/t_c = 0.45 \simeq -2 \ln(1 - p_{\text{SE}}) = 0.446$ is independent of Δk . The horizontal offset of the two curves arises from the initial, Δk -dependent drop of fidelity (see previous figure), and is not a feature of noise.

$(1 - p_{\text{SE}})^t$, with the event probability per kick p_{SE} . Hence, we estimate

$$F(t, k_1, k_2) \propto e^{-2t/t_c} \quad \text{with } t_c \equiv -\frac{1}{\ln(1 - p_{\text{SE}})}, \quad (6.19)$$

for $t \gtrsim t_c$, what is in excellent agreement with numerical data for $p_{\text{SE}} = 0.2$ in figure 6.5, and for $p_{\text{SE}} = 0.05 \dots 0.8$ in figure 6.6. It shall be emphasised that the fidelity decays at a rate $2/t_c$ which does not depend on the difference Δk , which on the other hand characterises the “separation” of the two distinct evolutions. For a finite number of β -rotors and a finite number of SE events, the phase average over $\exp(i\varphi_t)$ does give a typically small, but finite value $\langle \exp(i\varphi_t) \rangle = 1/N_{\text{tot}} \sum_{j=0}^{N_{\text{tot}}} \exp(i\varphi_t^{(j)}) \simeq N_{\text{tot}}^{-1/2}$, and N_{tot} can be estimated by $N_{\text{rot}}t/t_c$, for independent realisation of $\varphi_t^{(j)}$. In figure 6.6(a), the estimate for the statistical error is $1/(N_{\text{rot}}t/t_c) \simeq 1.7 \times 10^{-5}$ which agrees with the data for $t \geq 30$.

If SE occurs in *both* arms of the Ramsey interferometer, our model [160] which builds on the stochastic wave function (4.38) cannot be used directly because possible SE entangles the time evolutions between the Ramsey pulses. Only for the special case, when in both arms the SE rates p_{SE} are identical, i.e. both arms experience the same random process (which leads to the cancelling of the phases responsible for the fast exponential decay (6.19)), we obtain an estimate

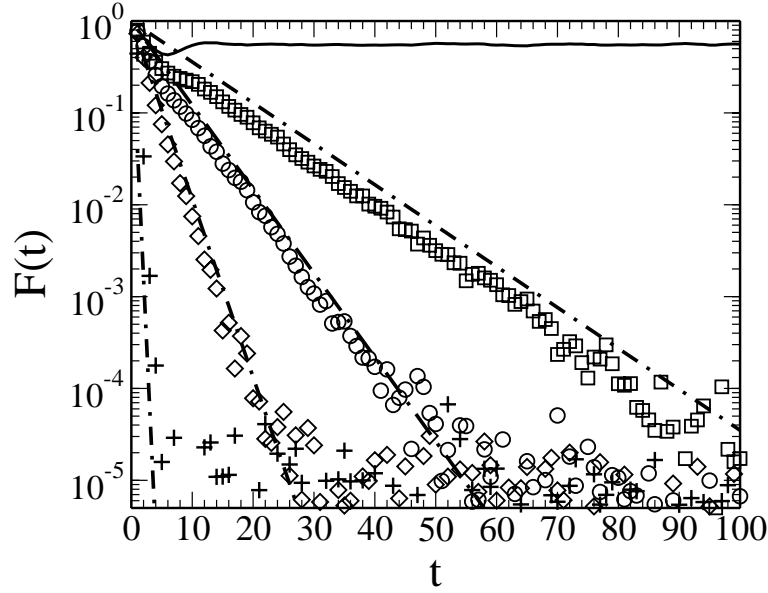


Fig. 6.6: Same as previous figure 6.5 for $k_1 = 0.8\pi, k_2 = 0.6\pi$, and $p_{\text{SE}} = 0$ (full line), $p_{\text{SE}} = 0.05$ (squares), $p_{\text{SE}} = 0.1$ (circles), $p_{\text{SE}} = 0.2$ (diamonds), $p_{\text{SE}} = 0.8$ (pluses). The slopes (dash-dotted) follow the prediction (6.19): $1/t_c = 0.05$ ($p_{\text{SE}} = 0.05$), $1/t_c = 0.1$ ($p_{\text{SE}} = 0.1$), $1/t_c = 0.23$ ($p_{\text{SE}} = 0.2$), $1/t_c = 3.2$ ($p_{\text{SE}} = 0.8$).

for $t \rightarrow \infty$. In appendix C, the random process $\rho \equiv |W_t|$ is shown to obey the distribution $2\rho \exp(-\rho^2/t)/t$ for $t \rightarrow \infty$, which it does not depend on quasi-momentum. Then we may average (6.13) over the random process to obtain the asymptotic ($t \rightarrow \infty$) result:

$$\begin{aligned}
 F(t, k_1, k_2) &\sim \langle J_0^2(\Delta k \rho) \rangle_{\text{SE}} = \frac{2}{t} \int d\rho \rho e^{-\frac{\rho^2}{t}} J_0^2(\rho \Delta k) \\
 &\stackrel{y=\rho^2/t}{=} \int dy e^{-y} J_0^2(\sqrt{yt} \Delta k) = J_0 \left(i \frac{t \Delta k^2}{2} \right) e^{-\frac{t \Delta k^2}{2}} \\
 &\stackrel{\text{(F.8)}}{\rightarrow} \frac{1}{\Delta k \sqrt{\pi t}}, \tag{6.20}
 \end{aligned}$$

where we used the integral formula (F.12). Hence, for this special case, we expect the fidelity to decay algebraically, i.e. much slower than the exponential decay (6.19).

Up to now all results focused on the regime of the fundamental quantum resonances $\tau = 2\pi\ell$ ($\ell \in \mathbb{N}$). In the next section we use the ϵ -quasi-classical approximation introduced in chapter 5 to investigate the fidelity in the vicinity of the quantum resonances.

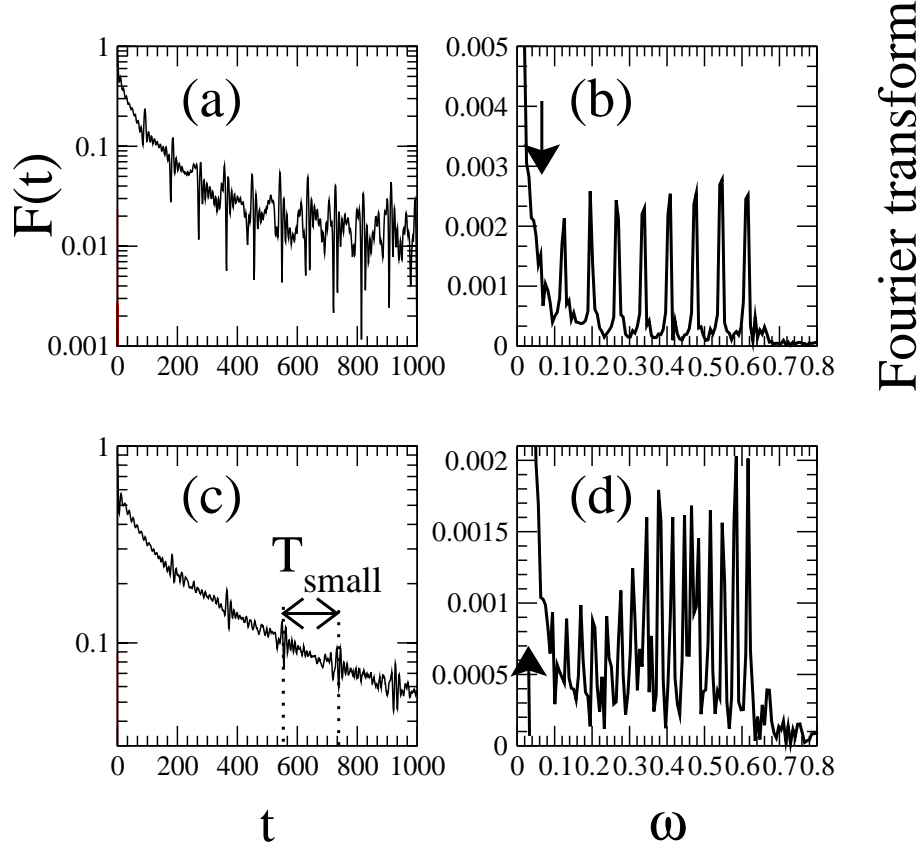


Fig. 6.7: Numerical simulations of the fidelity (6.7) as a function of the applied number of kicks t , for an ensemble of 10^4 atoms with initial uniform momentum distribution in $[0, 1)$; parameters are $k_1 = 0.8\pi, k_2 = 0.6\pi$ and $\tau = 2\pi + \epsilon$ with $\epsilon = 0.1$ (a), and $\epsilon = 0.025$ (c). The corresponding Fourier transforms are shown in (b) and (d), respectively. The peaks in (b,d) show essentially a constant spacing, which is related to the lowest frequency $\Delta\omega_{\text{small}}$ in the data (a,c), with $\Delta\omega_{\text{small}} = 2\pi/T_{\text{small}} \simeq 0.066$ for $\epsilon = 0.1$, and $\Delta\omega_{\text{small}} \simeq 0.033$ for $\epsilon = 0.025$. The highest frequencies $\lesssim 0.63$ are related to a period $T_{\text{fast}} \sim 10$ which occurs for short times $t < 100$ in the fidelity oscillations (a,c), c.f. figure 6.8(a). The arrows in (b,d) mark the position of $\omega = \Delta\omega_{\text{small}}$, but the peaks are not resolved, only in (b) there is a tiny trace of the Fourier peak at the lowest frequency which is predicted by the estimate (6.21).

6.3 Fidelity near to quantum resonance

For computing the fidelity as defined in (6.7), one must calculate the scalar product of two wave functions. In general, these are not known analytically for the δ -kicked particle dynamics. An exception are the quantum resonances studied in the previous sections. For kicking periods $\tau = 2\pi + \epsilon$ with finite $\epsilon \neq 0$, generally a direct calculation of (6.7) is not possible. However, we can restrict to the ϵ -quasi-classical model introduced in chapter 5. Figure 6.7(a,c) shows data for the fidelity of an atomic ensemble (uniform initial momentum distribution in $[0, 1)$) for $\tau = 2\pi + \epsilon$. We observe characteristic fluctuations which we study by calculating the Fourier spectrum of the signal in the frequency domain, see figure 6.7(b,d). For large times, the lowest frequency in the Fourier spectrum dominates. The latter is related to the difference of the two characteristic frequencies of the nonlinear resonance of the ϵ -quasi-classical phase space. In section 5.2.1 the important role of the characteristic time scale $t_{\text{res}} = (|\epsilon|k)^{-1/2} \equiv 1/\omega_{\text{res}}$ was pointed out. It determines the motion for the quantum system for sufficiently small detunings ϵ . Since two different kicking strengths have to be compared this corresponds to compare the motion of two ϵ -classical systems with slightly different t_{res} . In the harmonic approximation, the basic frequency is defined by the beating frequency, i.e. the difference of the two fixed-point frequencies:

$$\Delta\omega_{\text{small}} = \omega_{\text{res},1} - \omega_{\text{res},2} = \sqrt{|\epsilon|}(\sqrt{k_1} - \sqrt{k_2}). \quad (6.21)$$

The dominant fidelity oscillations for large times $t > 100$ are indeed determined by $\Delta\omega_{\text{small}}$ as one can see in figure 6.7. Table 6.1 collects values of $\Delta\omega_{\text{small}}$ obtained from figure 6.7 and similar cases, showing the correspondence between the estimate (6.21) and the numerical simulations.

ϵ	$\omega_{\text{res},1}$	$\omega_{\text{res},2}$	$\Delta\omega_{\text{small}}$	$T_{\text{small}} = 2\pi/\Delta\omega_{\text{small}}$	$T_{\text{small}}^{\text{data}}$
0.025	0.2507	0.2171	0.0336	187	190
0.05	0.3545	0.3070	0.0475	132	130
0.075	0.4342	0.3760	0.0582	108	105
0.1	0.5013	0.4342	0.0671	94	$\lesssim 100$

Tab. 6.1: Table of periods of fidelity oscillations (cf. equation (6.21)) for $k_1 = 0.8\pi$, $k_2 = 0.6\pi$ and $\tau = 2\pi + \epsilon$, and for large times $t > 100$. Presented are the estimated periods T_{small} , and the mean periods $T_{\text{small}}^{\text{data}}$ obtained from the data in figure 6.7, and from similar simulations for $\epsilon = 0.05, 0.075$.

At small times $10 < t < 100$, we observe in figure 6.8(a) (similar for data in figure 6.7(c)) oscillations with a varying amplitude for increasing time. However, we do not know yet, how different harmonics or frequencies conspire in the fidelity oscillations in the region $10 < t < 100$.

Taking only rotors close to the resonant value of quasi-momentum $\beta = 1/2$, i.e. in the range $\beta \in [0.4, 0.6]$, we observe that the highest frequencies dominate

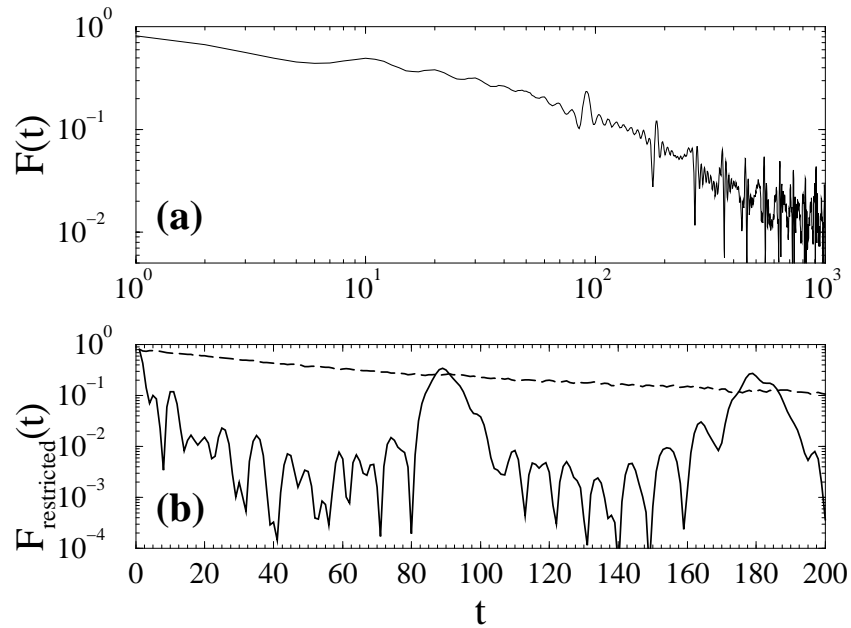


Fig. 6.8: (a) reproduces data from figure 6.7(a) to show the short time behaviour on a log-log scale. (b) shows fidelity as in (a) but with the restriction $\beta \in [0.4, 0.6]$ (solid line), and $\beta \notin [0.4, 0.6]$ (dashed). While the resonant values of quasi-momentum lead to fast oscillations with periods corresponding to the maximum frequencies observed in the Fourier spectrum (figure 6.7), the non-resonant ones show a fidelity decay without oscillations. The curve in (a) results from the average over all $\beta \in [0, 1)$, c.f. definition of fidelity in (6.7).

in the fidelity oscillations, while for non-resonant $\beta \notin [0.4, 0.6]$ the fidelity decays without considerable oscillations (see figure 6.8). The maximum frequency $\omega_{\max} \simeq 0.62$ in figure 6.7 seems to be universal for all studied $\epsilon = 0.05 \dots 0.1$, and its origin is still to be clarified.

6.4 Fidelity with quantum accelerator modes

Since the quantum accelerator modes mentioned in section 6.1 provide a useful tool to prepare atoms in a certain region in momentum space or even in phase space [135, 143, 145, 288], we present some preliminary results on the theoretically more complicated problem with added linear field. The quantum accelerator modes are found in the vicinity of the fundamental quantum resonances studied in this thesis, i.e. for kicking periods $\tau = 2\pi\ell + \epsilon$ ($\ell \in \mathbb{N}$). Therefore, a similar qualitative analysis as in the previous section may be used to describe the behaviour of the fidelity as a function of time, and the parameters k_1, k_2, ϵ, η – where η characterises the linear constant potential (the gravity in appropriate units [145]). The accelerator modes are explained by the islands

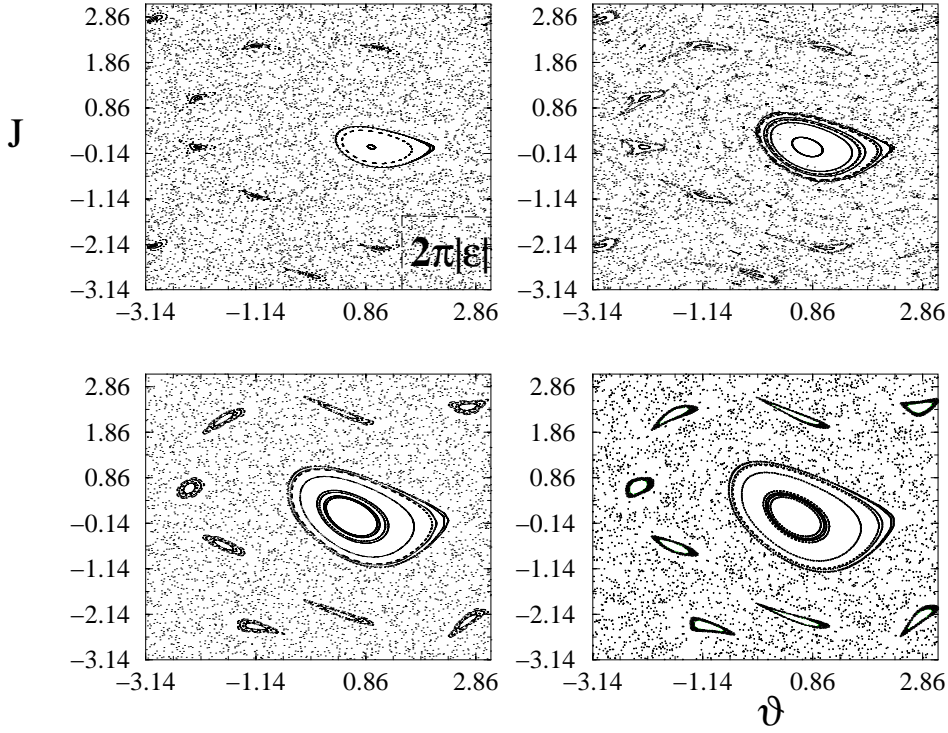


Fig. 6.9: Poincaré surface of sections determined by the map (6.22) for $\tau = 5.86$, $k = 0.5\pi$ (upper left), $k = 0.6\pi$ (upper right), $k = 0.75\pi$ (lower left), $k = 0.8\pi$ (lower right). The gravity parameter is chosen $\eta = 0.01579\tau$ (corresponding to the gravity acceleration in laboratory units [145]). The size and the *position* of the main island, corresponding to the accelerator mode (1,0) [145], depends on k [145]. Higher-order modes, represented by the island chains around the main (large) islands, are neglected in our discussion. This is partly justified by the large value of the effective Planck constant $2\pi|\epsilon|$.

of stability in the phase space of an appropriate ϵ -classical map, which can be reduced to a two-dimensional map defined on the 2-torus yielding for negative ϵ [145]:

$$\begin{aligned} J_{t+1} &= J_t + \tilde{k} \sin(\vartheta_{t+1}) - \tau\eta \\ \vartheta_{t+1} &= \vartheta_t - J_t. \end{aligned} \quad (6.22)$$

This map is the analogue of (5.7-5.8) with the additional term $\tau\eta$ (remember that $\tilde{k} = |\epsilon|k$).

Figure 6.9 shows typical phase-space plots generated by iterating (6.22). The islands support the accelerator modes much in the same manner as the non-linear resonances support the quantum resonances in chapter 5. The fidelity is obtained by numerical calculations of the quantum evolution of an ensemble of β -rotors subject to the δ -kicked accelerator. It is presented in figure 6.10 as a function of time t . As in the previous section, we observe characteristic fluctuations which are related to the structure of the ϵ -classical phase space.

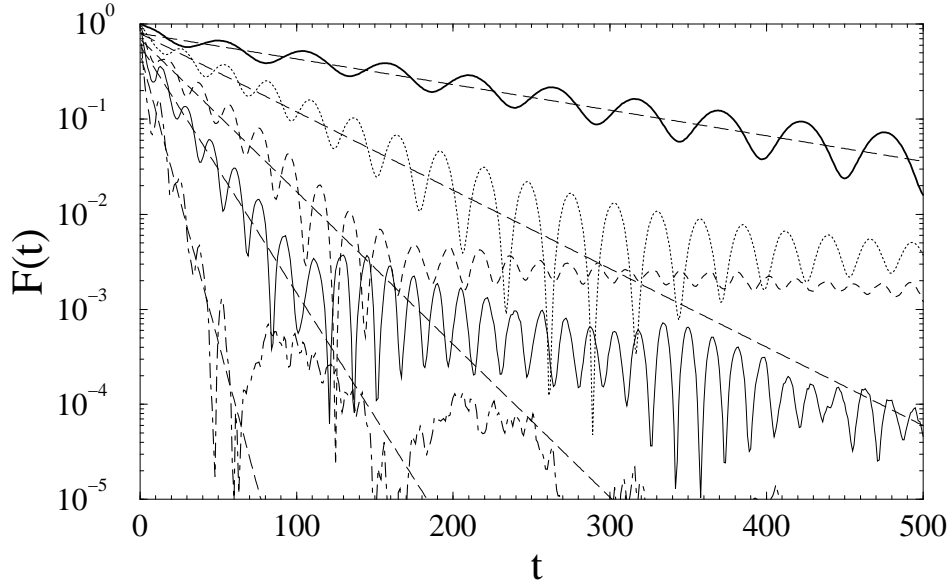


Fig. 6.10: Numerical simulation of the fidelity vs. the number of applied kicks t for the quantum evolution of the δ -kicked accelerator. The initial momentum distribution was chosen as in figure 6.7, parameters are $\tau = 5.86$, $\eta = 0.01579\tau$, $k_1 = 0.8\pi$, $k_2 = 0.75\pi$ (solid line), $k_2 = 0.7\pi$ (dotted), $k_2 = 0.65\pi$ (dashed), $k_2 = 0.6\pi$ (thin line), $k_2 = 0.5\pi$ (dot-dashed). The thin dashed lines show the overall exponential decay in the regime of not too large times.

The fixed-point frequencies ω_{FP1} and ω_{FP2} (corresponding to ω_{res} in the previous section) are not directly related to the oscillations observed in figure 6.10. However, a stability analysis around the elliptic fixed point (whose position depends on k , see figure 6.9) like in the case without gravity (6.21) must be amended by the relative shift of the island centres of the main accelerator modes visible in figure 6.9. In [145] it was shown that the velocity of the modes is independent of the kicking strength, which is the only difference in the two dynamical situations that we compare in the present discussion. A crude estimate for the frequencies of oscillations is given by

$$\omega_{\text{acc}} \simeq |\omega_{\text{FP1}} - \omega_{\text{FP2}}| + \Delta\vartheta_{\text{FP}}, \quad (6.23)$$

where $\Delta\vartheta_{\text{FP}}$ is the distance in the angle coordinate of the corresponding island centres. This shift of the frequency can be understood in the following way: for the elliptic motion in one island the trajectory is ahead, whereas for the elliptic motion in the other island the trajectory is behind, so they get closer to each other and rephase after a shorter period than in the case when both islands lie concentric[†]. The shift, which we estimate by $\Delta\vartheta_{\text{FP}}$, depends on the precise geometry of the two islands, and the overlapping area. A better estimate can certainly be derived for a *specific* island configuration. The periods

[†]In the fidelity, one of the distinctly evolved states enters in complex conjugated form, hence the phase has a different sign with respect to the second state; therefore one trajectory is ahead while the second, corresponding one lacks behind in the classical picture.

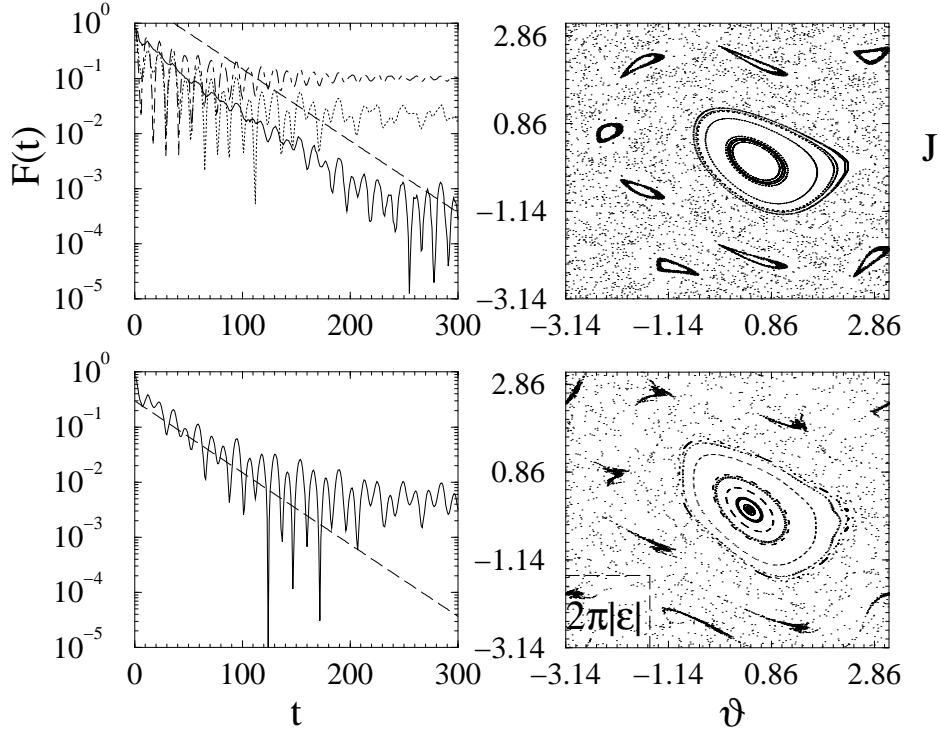


Fig. 6.11: Upper left: fidelity vs. number of kicks t , for $\tau = 5.86$, $k_1 = 0.8\pi$, $k_2 = \pi$, and a prepared initial coherent state centred at $J_0 = 0$, $\vartheta_0 = 0.5$ with a spread in the angle coordinate of $d = 0.1$ (dash-dotted), $J_0 = 0$, $\vartheta_0 = 0.5$, $d = 1$ (dotted), $J_0 = 0$, $\vartheta_0 = -3$, $d = 1$ (solid) (the evolution is averaged over 100 quasi-momenta uniformly distributed in $[0, 1)$). Lower left: Fidelity for same parameters but with uniform initial ensemble of 10^4 plane wave β -rotors with $p_0 = \beta_0 \in [0, 1)$ (like in figure 6.10). The slope (dashed) is 0.03, and it is determined by the states having strong overlap with the chaotic component of ϵ -classical phase space plotted for $k_1 = 0.8\pi$ in the upper right, and for $k_2 = \pi$ in the lower right panel. The effective Planck constant $2\pi|\epsilon| \simeq 2.66$ is indicated by the square.

won by the numerical data from figure 6.10 compare well (yet not perfectly) with the prediction from (6.23).

To further investigate the overall decay of the fidelity vs. time we focus on a case where the islands are as large as possible for the given values $\tau = 5.86$, $k \simeq 0.8\pi$, namely $k_1 = 0.8\pi$ and $k_2 = \pi$ in figure 6.11. The fidelity shows beating arising from several frequencies. On the other hand, the decay can be shown to originate solely from the chaotic motion in ϵ -classical phase space. Launching a coherent state wave packet [16, 211] centred at either the ϵ -classical island or in the chaotic sea, we observe that in the first case, the oscillations are dominated by one frequency only, and after some short decay the mean value saturates (probably decaying further owing to tunnelling, see short discussion below), while the fidelity decays exponentially for much longer times in the latter case. We thus conclude that the initial decay of the fidelity is governed

by states in the chaotic component of ϵ -classical phase space and/or by states sitting only partly at the accelerator mode island. These states get lost for the accelerator mode, possibly on different time scales, but much faster than states sitting mainly within the island. The latter can only escape via tunnelling out of the island which is a much slower process, and we assume that the fidelity decay after the first stage – after the plateau sets in – is indeed determined by such tunnelling processes. The tunnelling regime is very interesting from the theoretical point of view, however, in the experimental setup we referred to in section 6.1, this long-time regime ($t \geq 100$) is hardly attainable.

The slope of the initial fidelity decay is by a factor of 6 smaller than the Lyapunov exponent [43] calculated for the map (6.22). Therefore, we assume that the quantum coarse-graining of the phase space dynamics smears out the fast decay to arrive at a much smaller decay rate than expected by purely ϵ -classical means. Note that to observe the structure (clear exponential decay amended by more or less well-defined oscillations) in the fidelity in figures 6.10 and 6.11, it is necessary to average over some finite (possibly small) interval of quasi-momenta around the values which support the accelerator mode [145].

Calculating the fidelity in a window in momentum space around the origin $n = 0$ (not counting the contributions from outside the window), the overall decay in the initial stage is not affected, as can be seen from figure 6.12. However, the oscillations with frequencies estimated by (6.23) are destroyed as soon as the accelerator part of the momentum distribution is outside the window. This stresses again the role of the nonlinear island in ϵ -classical phase space, corresponding to the accelerator mode, which is responsible for the fluctuations. We also used a window in momentum around the accelerator mode peak in the momentum distribution. The window is moving with the peak at a speed $\tau\eta/|\epsilon|$ [145], and its effect is that there no longer prevails a clear initial exponential decay. Only the second stage occurs earlier, with exponential decay but much smaller slope (which is the *same* as for the data without any window, see figure 6.12). The latter decay is amended by fast oscillations, which are seen for all cases plotted in figure 6.10 using a window around the accelerator mode peak. The frequency of these fast oscillations is close to the two individual fixed point frequencies ω_{FP1} or ω_{FP2} , but so far we have no explanation for its occurrence yet.

The presented results on the the fidelity in presence of the additional linear potential await a proper theoretical analysis. Such a treatment should include the mentioned problems of determining the decay slopes in both exponential regimes, and the development of a semiclassical theory for the tunnelling out of the accelerator mode island in ϵ -classical phase space.

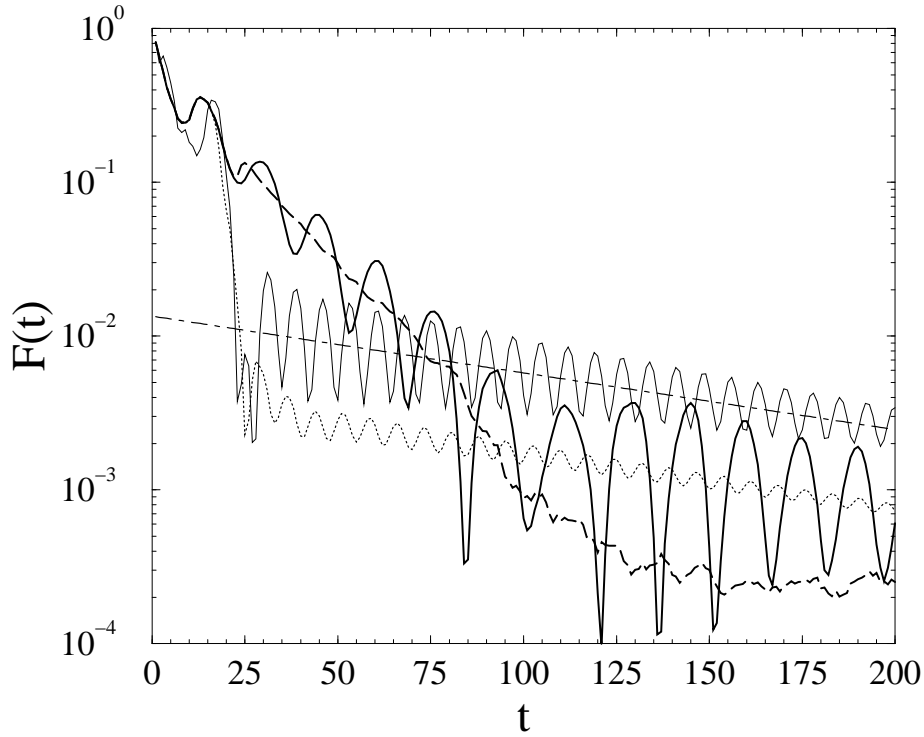


Fig. 6.12: Fidelity vs. number of applied kicks t for $\tau = 5.86, k_1 = 0.8\pi, k_2 = 0.6\pi$: data from figure 6.10 (thick solid) compared with data when the sum in momentum n extends only over a finite window in equation (6.7), $-30 < n < 30$ (dashed) and $n_{\text{acc}} - 30 < n < n_{\text{acc}} + 30$ (dotted). The centre of the accelerator mode peak in the momentum distribution n_{acc} moves with the velocity $\tau\eta/|\epsilon|$, which is independent of k [145]. The thin solid line shows data like the dotted line for restricted initial momenta $p_0 = \beta_0 \in [0.49, 0.51]$. While the cutoff around zero momentum destroys the oscillations as soon as the accelerated peak has reached the boundary (at $t \simeq 22$), the overall exponential decay (up to $t \simeq 100$) is the same as in the data without cutoff. The window around the accelerator mode peak has a completely different effect: it leads to a huge drop in the fidelity because of probability loss for $t \gtrsim t_{\text{loss}} \simeq 16$ (dotted line), and what remains decays with the *same* slope (dot-dashed) as the thick solid line for $t \gtrsim 100$, probably related to tunnelling. Puzzling are the fast oscillations of the dotted curve for $t \gtrsim 25$; their amplitude is increased using only a small range of initial quasi-momenta around the one supporting the accelerator mode (thin solid line).

Chapter 7

Résumé

7.1 Summary of results

In this thesis transport in energy or momentum space, arising from the energy absorption from an external time periodic driving force, is studied focusing on quantum effects relevant on the atomic scale.

The first part of the thesis presents novel quantitative support for the hypothesis that the energy transport in periodically driven hydrogen Rydberg atoms is determined by dynamical localisation. The latter implies the quantum suppression of classical diffusion, and is based on the mechanism of Anderson localisation [61, 88, 89]. The distributions of ionisation rates of the driven Rydberg states allow for a clear identification of signatures of Anderson localisation. In the statistical average, the ionisation rates Γ_ϵ follow a universal algebraic distribution $\rho(\Gamma_\epsilon) \propto \Gamma_\epsilon^{-0.9}$ (cf. section 3.1). This result is in good agreement with quasi-one-dimensional Anderson models [197]. The corresponding eigenstates are dominantly located in the chaotic component of phase space, which is exactly the domain where dynamical localisation suppresses the transport to the atomic continuum [60]. In addition to the identification of Anderson localisation through the ionisation-rate statistics, the latter provide evidence for other mechanisms hindering quantum transport such as tunnelling out of the regular regions in phase space. We were able to separate dynamical localisation and localisation induced by regular phase-space structures by investigating the localisation properties of the Floquet eigenstates in phase space. Driven Rydberg atoms are real systems perfectly suited for the investigation of the mixed regular-chaotic phase-space dynamics, and the classical-quantum correspondence is essential for a clear understanding of the underlying physical phenomena.

Our statistical analysis of the decay rates may be experimentally verified by

spectroscopic techniques similar to the ones extensively used in measuring the (dc) Stark spectrum of Rydberg atoms [71].

In contrast to recent predictions [115], the ionisation probability as a function of time does *not* behave universally – in spite of the universal decay-rate statistics. The more or less algebraic, but highly non-universal decay arises from the *local* property of the expansion coefficients in (2.40) contrary to the *global* spectral information carried by the ionisation rates. Since the latter and the corresponding coefficients are essentially uncorrelated (see figure 3.12), the universality in $\rho(\Gamma_\epsilon)$ does not imply universality in the ionisation or survival probability as a function of time. Experiments with rubidium Rydberg states [114] as well as extensive numerical simulations on lithium and rubidium Rydberg atoms [95] support our results on hydrogen.

In the second part of this thesis, we have clarified several experimental findings on the quantum resonant dynamics of atoms subject to time periodic δ -like pulses. Thereby the particle nature of the atoms, which move on a line, and not on a circle as assumed for the kicked-rotor model, plays a crucial role. The atoms in the experiment are non-interacting, and thus they are modelled in our theory as a *classical* ensemble of *quantum* particles.

The puzzling enhancement of resonance peaks in the mean energy (of the atomic ensemble) vs. the kicking period [82, 83] is identified as an experimental artefact [159]. The latter arises from cutoffs which inevitably impair the quantum resonant motion in absence of decoherence by spontaneous emission. Our analytical results show that the mean energy increases in both cases – with and without spontaneous emission – linearly with the number of kicking pulses (equations (4.20) and (4.62)).

However, the momentum distributions of the atomic ensemble behave completely differently in the two cases: without decoherence the main contribution to the energy growth originates from a tiny fraction of resonantly driven atoms (the residual ones are strongly localised around the initial momenta close to zero). On the other hand, the energy increase in presence of spontaneous emission emerges because the momentum distribution spreads as a whole. Decoherence acts as expected and destroys the coherent dynamics, what makes the distribution become Gaussian in the asymptotic limit of large times, characteristic of a diffusive random walk in momentum space.

Based on a quasi-classical approximation, we have derived a scaling law for the resonance peaks in the mean energy in the absence and presence of decoherence. From these scaling laws (equations (5.18) and (5.25)) the widths of the peaks as function of the detuning from the resonance follow, including their time dependence. The experimentally observed stabilisation of the peaks by adding a small amount of noise corresponds to their broadening arising from the reshuffling of atoms in and out of the resonance conditions. This enhances the probability of following the resonant motion, also for small detunings from the exact resonant kicking period. The presented scaling allows the experimentalist to collect data from different parameter ranges, and average them in order to enhance the experimental resolution.

Our treatment of the spontaneous emission by a quantum Monte Carlo method,

or equivalently by a random walk in the rotor's Hilbert space, not only permits an exact analysis of the kicked atoms' dynamics in presence of noise but also shows that periodically kicked atoms provide an interesting system for the study of decoherence. Most recent experiments [142] make it possible to compare two slightly distinct time evolutions, and to study the influence of the underlying dynamical regime on the overlap function of two initially identical but differently evolved wave packets. Using the results derived at the exact quantum resonance conditions as well as the quasi-classical approximation which describes the system close to the resonances, the overlap function, i.e. the fidelity, has been investigated. In the absence of decoherence, the fidelity characterises the stability of the quantum motion subject to slight perturbations. Varying the dynamical regime (e.g. quantum resonant, dynamically localised, or dynamics with added linear potential) alters the time dependence of fidelity. Since the δ -kicked rotor affords a variety of dynamical scenarios building on its mixed classical phase space, its atom optical realisation provides an exciting system to study the influence of decoherence and noise competing with classical chaos or its quantum manifestations [293, 294]. Our preliminary results support the intuition that the fidelity offers a route for the *quantitative* study of the destruction of quantum coherences via its behaviour on time and on the underlying dynamics.

7.2 Future perspectives

This thesis describes the dynamics of atomic degrees of freedom which are directly accessible to experiments: electronic states in driven Rydberg atoms and external centre-of-mass motion in kicked atoms. The presented discussions gathered tools of classical and quantum transport theory to describe experimental systems prepared and controlled by quantum and atom optical techniques. New experimental methods are offered by cooling atoms even below the temperatures as used so far for the kicked-particle experiments [55, 81, 83, 135, 143, 166, 174, 184, 290]. The coherent atomic ensemble of a Bose-Einstein condensate [124–126, 295] may be used to prepare very well defined initial conditions, for instance, initial momentum distributions of atoms. It is possible to reach spreads in momentum of $p_0 = \beta_0 \leq 0.05$ (in units of two photon recoils), which are sufficiently small to strongly populate atoms in the conditions required for the quantum-resonances (see section 2.2.3). The “ballistic” peaks in the momentum distribution may be clearly visible in such an experiment if in addition the problem of finite-pulse widths in the kicks is minimised (cf. section 4.3.6). Moreover, one may hope to observe higher-order quantum resonances which have not been unambiguously resolved in experiments yet [159]. To observe them it is necessary to guarantee a high resolution in the kicking period as well as a large population of the quasi-momenta near to the corresponding resonant values [64].

The influence of the atom-atom interaction in the coherent Bose-Einstein con-

densate [124] on the dynamical evolution is certainly an exciting problem to investigate. The particle nature (as compared to the rotor moving on a circle) is important for the quantum resonances but also for initial *coherent* superpositions of momentum eigenstates what concerns the kicked-atoms' dynamics in presence of an additional linear potential. The effect of interferences on the quantum accelerator modes occurring when such an additional potential is present is partly discussed in [145], and a more complete theoretical understanding together with an experimental exploration of coherent ensemble dynamics would be of great interest.

The presented quasi-classical approximation not only allows one to grasp the main features of the kicked-atom dynamics near to the fundamental quantum resonances. It offers a new tool for the study of quantum effects in the quasi-classical limit of small detunings from the resonant kicking period. In section 6.4, the decay of fidelity was partly related to the chaotic component, and to tunnelling out of the main nonlinear island in the quasi-classical phase space. As the latter is typically nicely separated in a regular island, corresponding to the quantum accelerator mode [145], and a chaotic motion, the quasi-classical approximation provides an ideal playground for the investigation of tunnelling phenomena, such as dynamical [296–299] or chaos-assisted tunnelling [210, 216, 217, 235, 300, 301]. On the experimental side, these are challenging perspectives since very well-defined initial conditions are an essential prerequisite to observe relatively weak signals such as tunnelling oscillations [297, 298].

The noisy transport problem in microwave-driven atomic Rydberg states has been explored in several experiments with focus on the destruction of dynamical localisation [13, 52, 53, 72]. The influence of spontaneous emission on one-dimensional Rydberg wave packets, which otherwise show no or little dispersion owing to very weak decay to the continuum, was investigated [77, 302, 303]. Such studies may be extended to a comprehensive analysis of the survival probabilities, as studied in section 3.1.3. These are certainly affected by noise arising from spontaneous emission, in particular for the large interaction times plotted, for instance, in figure 3.15.

A merger of the two systems studied in this thesis, which can also be realised experimentally [304, 305], is provided by periodically δ -kicked Rydberg atoms [306, 307]. Here, the kicking pulses excite the internal electronic degrees of freedom in the same way as for monochromatically driven Rydberg states (as opposed to our δ -kicked rotor realisation, where the atoms' centre-of-mass motion is affected). In addition, the δ -kicks contain all harmonics of the basic frequency $\omega = 2\pi/\tau$, with the kicking period τ . Therefore, many decay channels to the atomic continuum, including direct one-photon ionisation, are present. Recent results [308, 309] show analogies to the Rydberg problem discussed in this thesis, and in particular, fluctuations in the ionisation probabilities which are reminiscent of the atomic conductance fluctuations mentioned in section 3.2.3. Moreover, since direct one or few-photon ionisation is possible, very large decay rates appear besides the rates connected to multi-photon transport. This implies that parametric fractal fluctuations in the survival probability or in an

analogue of the atomic conductance (3.11) may be observable in an experimentally accessible situation.

The presented new aspects of the analogy between periodically-driven Rydberg states and Anderson-localised solids may also be investigated in more complex systems than one-electron problems. More precisely, one may study systems in which more (strongly coupled) degrees of freedom are present. Can one identify transport mechanisms similar to the ones discussed in this thesis also for systems such as the driven three-body helium problem [76, 310, 311]? The additional particle-particle interaction offers new perspectives in the analogy between atomic problems with many degrees of freedom and many-body solid state systems.

Appendix A

Analysis of the Steady State Distribution (4.15)

A.1 Proof of estimate (4.16)

From (4.15) it follows that

$$\sum_{|n| \geq N} M_n^*(t) = \frac{1}{2\pi^2} \int_{-\pi}^{\pi} dx \int_{-\pi/2}^{\pi/2} d\alpha \sum_{|n| \geq N} J_n^2(z)$$

with $z \equiv k \sin(x) \csc(\alpha)$, (A.1)

for any positive integer N . In A.2 we show that

$$\sum_{|n| \geq N} J_n^2(z) \leq 2 \left(\frac{ez}{2N} \right)^{2N} .$$
 (A.2)

With this inequality, we derive an upper bound for the sum in the inner integral in (A.1) when $|\alpha| > \epsilon/2$, for $0 < \epsilon < \pi$. If $|\alpha|$ does not fulfill this condition, we use the upper bound 1 for $\sum_{n=-\infty}^{\infty} J_n^2 \leq 1$ (cf. F.3), and that by (A.1) leads to the first term on the right in (A.3). Noting that $|z| < k|\csc(\alpha)| < \pi k/(2\epsilon)$ whenever $\pi/2 > |\alpha| > \epsilon$, one obtains altogether

$$\sum_{|n| \geq N} M_n^*(t) \leq \frac{\epsilon}{\pi} + 2 \left(\frac{k\pi e}{4N\epsilon} \right)^{2N} .$$
 (A.3)

We now minimise the right-hand side by requiring

$$\frac{1}{\pi} - 4N \left(\frac{k\pi e}{4N\epsilon} \right) \epsilon^{-2N-1} = 0 .$$
 (A.4)

Solving for ϵ , we obtain

$$\epsilon = \frac{ek\pi}{4N} \left(\frac{16N^2}{ek} \right)^{\frac{1}{2N+1}}$$
 (A.5)

(which is indeed not larger than π whenever $N > k \times 1.03 \dots$). Replacing (A.5) in (A.3) yields the estimate (4.16):

$$\sum_{|n| \geq N} M_n^* \leq 2 \left(\frac{ke}{16} \right)^{\frac{2N}{2N+1}} N^{\frac{1-2N}{2N+1}} \left(2 + \frac{1}{N} \right). \quad (\text{A.6})$$

A.2 Proof of inequality (A.2)

Using twice the bound (F.7) and the power series expansion of Bessel functions [157],

$$\sum_{n=0}^{\infty} J_n^2(z) e^{nr} \leq \sum_{n=0}^{\infty} \left(\frac{|z|e^{r/2}}{2} \right)^{2n} \frac{1}{(n!)^2} = J_0(i|z|e^{r/2}) \leq e^{|z|e^{r/2}}, \quad (\text{A.7})$$

for any real r . It follows that

$$\sum_{n=N}^{\infty} J_n^2(z) \leq e^{-Nr} e^{|z|e^{r/2}}. \quad (\text{A.8})$$

Inequality (A.2) follows upon optimising, i.e. minimising, with respect to r what gives $r = 2 \ln(2N/|z|)$. Then

$$e^{-Nr} e^{|z|e^{r/2}} \Big|_{r=2 \ln(2N/|z|)} = \left(\frac{|z|}{2N} \right) e^{2N},$$

and since $z \in \mathbb{R}$, and taking into account a factor of two for the equivalent of (A.8) with negative n , the inequality (A.2) follows.

A.3 Proof of the asymptotic formula (4.17)

For $z \in [-1, 1]$ we define:

$$f(z) \equiv \frac{1}{2\pi} \int_{-\pi/2}^{\pi/2} d\alpha J_0^2(kz \csc(\alpha)) \text{ for } z \neq 0; \quad f(0) = \frac{1}{2}. \quad (\text{A.9})$$

The integrand in (A.9) is meant = 0 for $\alpha = 0, z \neq 0$. Using the integral identity (F.3) for Bessel functions, (4.15) may be rewritten as:

$$M_n^* = \frac{1}{\pi} \int_0^{2\pi} dx \cos(2nx) f(\sin(x)), \quad (\text{A.10})$$

so, for $|n| > 0$, M_n^* is the $2n$ -th coefficient in the cosine expansion of $f(\sin(x))$. The function $f(z)$ is differentiable in $[-1, 1] \setminus \{0\}$. It will be presently shown that

$$f'(0+) = \lim_{z \rightarrow 0+} f'(z) = -\frac{4k}{\pi^2} \neq 0.$$

Since $f(z)$ is an even function, it will follow that its first derivative is discontinuous at $z = 0$. We choose $\epsilon > 0$ and write

$$f(z) = f_\epsilon(z) + g_\epsilon(z) , \quad f_\epsilon(z) \equiv \frac{1}{2\pi} \int_{-\epsilon}^{\epsilon} d\alpha J_0^2(kz \csc(\alpha)) . \quad (\text{A.11})$$

Then g_ϵ is differentiable around 0, with $g'_\epsilon(0) = 0$. Hence, $f'(0+) = f'_\epsilon(0+)$. Next we note that if $z > 0$,

$$f'_\epsilon(z) = \pi^{-1} z^{-1} \int_{-\epsilon}^{\epsilon} d\alpha F(kz \csc(\alpha)) ,$$

where $F(x) \equiv x J_0(x) J'_0(x)$. Noting that

$$|\csc(\alpha) - \alpha^{-1}| < c_1 \alpha$$

for $0 < |\alpha| < \pi/2$ and some numerical constant c_1 , one easily finds

$$\begin{aligned} f'_\epsilon(z) &= \pi^{-1} z^{-1} \int_{-\epsilon}^{\epsilon} d\alpha F(kz \alpha^{-1}) + O(\epsilon) \\ &= -2k\pi^{-1} \int_{kz/\epsilon}^{\infty} du u^{-1} J_0(u) J_1(u) + O(\epsilon) , \end{aligned} \quad (\text{A.12})$$

where $J'_0(z) = -J_1(z)$ was used. Letting $z \rightarrow 0+$ and thereafter $\epsilon \rightarrow 0+$ we obtain:

$$f'(0+) = \lim_{\epsilon \rightarrow 0+} f'_\epsilon(0+) = -2k\pi^{-1} \int_0^{\infty} du u^{-1} J_0(u) J_1(u) = -\frac{4k}{\pi^2} .$$

The integral was computed by using (F.6) and then formula 11.4.36 in [157].

Next we recall from (A.10)

$$f(\sin x) = \frac{1}{2} M_0^* + \sum_{n=1}^{\infty} M_n^* \cos(2nx) .$$

According to the above analysis, the derivative of this function jumps by $-8k/\pi^2$ at $x = j\pi$ (j any integer). Hence the second derivative has the singular part $-8k\pi^{-2} \sum_j \delta(x - j\pi)$, leading to the asymptotic value $-16k\pi^{-3}$ for the coefficients in its cosine expansion. This yields

$$M_n^* \sim \frac{4k}{\pi^3 n^2} \text{ as } n \rightarrow \infty . \quad (\text{A.13})$$

Appendix B

Statistics of the process Z_m

B.1 Independence of the variables z_j

We show that, for any integers n, m , ($m > n$), the variables (z_n, \dots, z_m) are independent of the variables (z_0, \dots, z_k) whenever $k \leq n - 2$. It suffices to show that (z_n, \dots, z_m) are independent of $(\tilde{\xi}_0, \dots, \tilde{\xi}_k, \Delta_0, \dots, \Delta_k)$. To see this, let f be an arbitrary (Borel) function of $m - n + 1$ complex variables, and consider

$$\mathcal{M}_k \equiv \mathcal{E}\{f(z_n, \dots, z_m) | \tilde{\xi}_0, \dots, \tilde{\xi}_k, \Delta_0, \dots, \Delta_k\}. \quad (\text{B.1})$$

Looking at (4.37), and recalling that the $\tilde{\xi}_j$ are mutually independent, one notes that (z_n, \dots, z_m) depend on $\tilde{\xi}_j, \Delta_j$ ($0 \leq j \leq k$) through the factor $\exp(i \sum_0^k \tilde{\xi}_j \Delta_j)$, hence only through $\sum_{j=0}^k \tilde{\xi}_j \Delta_j \pmod{2\pi}$. Therefore, (B.1) is a function of the variable $\mu_k \equiv \sum_0^k \tilde{\xi}_j \Delta_j \pmod{2\pi}$ alone, i.e. $\mathcal{M}_k = \mathcal{M}_k(\mu_k)$. Furthermore, since $k + 1 < n$,

$$\begin{aligned} \mathcal{M}_k(\mu_k) &= \int dP(\tilde{\xi}_{k+1}, \Delta_{k+1}) \mathcal{M}_{k+1}(\mu_{k+1}) \\ &= \int dP(\tilde{\xi}_{k+1}, \Delta_{k+1}) \mathcal{M}_{k+1}(\mu_k + \tilde{\xi}_{k+1} \Delta_{k+1}) \end{aligned} \quad (\text{B.2})$$

because $\tilde{\xi}_{k+1}, \Delta_{k+1}$ are independent of past variables; here $dP(\cdot, \cdot)$ is their joint distribution. Now $\tilde{\xi}_{k+1}$ is independent of the integer Δ_{k+1} , and it is uniformly distributed in $[-\pi, \pi)$. Then the integral does not depend on μ_k , so

$$\mathcal{E}\{f(z_n, \dots, z_m) | \tilde{\xi}_0, \dots, \tilde{\xi}_k, \Delta_0, \dots, \Delta_k\} = \mathcal{E}\{f(z_n, \dots, z_m)\},$$

what proves the announced independence property.

B.2 Central Limit property

The properties of the process Z_m allow to conclude that its distribution is asymptotically Gaussian, thanks to known results about the Central Limit Theorem for weakly dependent sequences [312]. Isotropy of the limit Gaussian distribution follows from computing the mean square displacement along an arbitrary direction θ in N steps, i.e.

$$\mathcal{E} \left\{ \operatorname{Re}^2 \left(\sum_{j=0}^N e^{-i\theta} z_j \right) \right\}$$

since

$$\operatorname{Re}(e^{-i\theta} Z_N) = \operatorname{Re}(Z_N) \cos(\theta) + \operatorname{Im}(Z_N) \sin(\theta) .$$

Using $\mathcal{E}\{z_j z_k^* | \Delta\} = \delta_{jk} \Delta_j$ for any $j, k \geq 0$ such that $j + k > 1$ (see (4.40) and section 4.3.3), the result is independent of θ , hence the limit distribution is isotropic in the complex plane.

Appendix C

Asymptotic distribution of the process $|W_t|$

We show that as $t \rightarrow \infty$, the distribution of $|W_t|$ approaches a Gaussian distribution in the complex plane centred at 0. To this end we assume for simplicity that W_t and Z_m (4.37) are real; the argument carries through by replicating it for the real and the imaginary parts separately. We define $\tilde{W}_t = W_t/\sqrt{t}$, and prove that the characteristic function [259, 267] of \tilde{W}_t , i.e.

$$\Phi(\tilde{W}_t) \equiv \mathcal{E} \left\{ e^{iy\tilde{W}_t} \right\}, \quad (\text{C.1})$$

is a Gaussian for $t \rightarrow \infty$. From the definition of the process N_t after equation (4.29), it follows that $N_t \rightarrow \infty$ for $t \rightarrow \infty$ with probability 1 if $p_{\text{SE}} > 0$. The previous appendix shows further that the conditional distribution of Z_{N_t} , at given N_t , is asymptotically Gaussian as $N_t \rightarrow \infty$ with variance $\propto N_t$. Therefore, one obtains

$$\mathcal{E} \left\{ e^{iy\tilde{W}_t} \middle| N_t \right\} = \mathcal{E} \left\{ e^{i\frac{yZ_{N_t}}{\sqrt{t}}} \middle| N_t \right\} \xrightarrow{t \rightarrow \infty} c_1 e^{-\frac{c_2 y^2 N_t}{t}}, \quad (\text{C.2})$$

with constants c_1, c_2 . To obtain $\Phi(\tilde{W}_t)$ we must average (C.2) over the distribution of N_t which is Bernoullian (see its definition after (4.29)). Consequently,

$$\begin{aligned} \Phi(\tilde{W}_t) &\sim c_1 \mathcal{E} \left\{ e^{-\frac{c_2 y^2 N_t}{t}} \right\} \\ &= c_1 \sum_{m=0}^t \frac{t!}{m!(t-m)!} \left(p_{\text{SE}} e^{-\frac{c_2 y^2}{t}} \right)^m (1-p_{\text{SE}})^{t-m}. \end{aligned} \quad (\text{C.3})$$

With the binomial formula (F.10), this gives

$$\begin{aligned} \Phi(\tilde{W}_t) &\sim c_1 \left(1 - p_{\text{SE}} \left(1 - e^{-\frac{c_2 y^2}{t}} \right) \right)^t \\ &\sim c_1 \left(1 - \frac{p_{\text{SE}} c_2 y^2}{t} \right)^t \xrightarrow{t \rightarrow \infty} c_1 e^{-p_{\text{SE}} c_2 y^2}, \end{aligned} \quad (\text{C.4})$$

where (F.11) was used. Since the Fourier transform of a Gaussian is again a Gaussian with inverse variance, it follows that asymptotically \tilde{W}_t obeys a Gaussian distribution with variance $\propto 1$, hence also W_t with variance $\propto t$. From the discussion in section 4.3.3, i.e. with (4.55) which is in all cases approached for $t \rightarrow \infty$, the variance is exactly t . This finally tells us that $\rho = |W_t|$ is asymptotically distributed with a density $dF_t(\rho) = 2t^{-1}\rho d\rho \exp(-\rho^2/t)$, i.e. a two-dimensional isotropic Gaussian in the complex plane.

Appendix D

Derivation of equation (5.26)

Let Δ_j^1 , ($j = 0, 1, \dots$) be real nonnegative, independent random variables exponentially distributed with $\mathcal{E}\{\Delta_j^1\} = 1$. For j a nonnegative integer denote $s_j = \sum_{k=0}^j \Delta_k$, and $s_{-1} \equiv 0$. For given $u > 0$ let $N_u^1 \equiv \max\{j : s_j < u\}$. We shall compute the expectation of the random variable

$$f_u \equiv \sum_{j=0}^{N_u^1} f(\Delta_j^1) + f(u - s_{N_u^1}), \quad (\text{D.1})$$

where $f(x)$ is a given nonrandom function; the sum in equation (5.23) is of this form, with $f(x) = xH(xv)$. We write $f_u = \sum_{j=0}^{\infty} f_{u,j}$, where

$$\begin{aligned} f_{u,j} &\equiv \chi(u - s_{j-1})[\chi(u - s_{j-1} - \Delta_j^1)f(\Delta_j^1) + \\ &+ \chi(\Delta_j^1 + s_{j-1} - u)f(u - s_{j-1})], \end{aligned} \quad (\text{D.2})$$

and $\chi(\cdot)$ is the unit step function. Then, denoting $G(x) = \int_0^x ds f(s)e^{-s}$,

$$\mathcal{E}\{f_{u,j}|s_{j-1}\} = \chi(r)[G(r) + f(r)e^{-r}] \quad , \quad r = u - s_{j-1} . \quad (\text{D.3})$$

Therefore,

$$\begin{aligned} \mathcal{E}\{f_u\} &= \sum_{j=0}^{\infty} \mathcal{E}\{\mathcal{E}\{f_{u,j}|s_{j-1}\}\} = G(u) + f(u)e^{-u} + \\ &+ \sum_{j=1}^{\infty} \int_0^u dP_j(x) [G(u-x) + f(u-x)e^{x-u}] , \end{aligned} \quad (\text{D.4})$$

where $dP_j(x) = dx e^{-x}x^{j-1}/(j-1)!$ is the distribution of s_{j-1} for $j > 0$. Summing over j and replacing the definition of $G(x)$ we finally obtain

$$\mathcal{E}\{f_u\} = 2 \int_0^u dx e^{-x} f(x) + f(u)e^{-u} + \int_0^u dx e^{-x} f(x)(u-x) . \quad (\text{D.5})$$

Equation (5.26) in the text is obtained on substituting $f(x) = xH(xv)$.

Appendix E

Extraction of fidelity from Ramsey fringes

Let us consider a two-level atom. The state space is $\mathcal{H} \otimes \mathbb{C}^2$ where \mathcal{H} is the state space of a point particle on a line. The states are then represented by spinors (ψ_1, ψ_2) where $\psi_{1,2} \in \mathcal{H}$ represent the internal levels of the atom. E_1, E_2 are the energies of the levels ($\hbar \equiv 1$ is assumed). Applying to the atomic transition between these levels two successive $\pi/2$ Ramsey pulses at a frequency $\omega_{\text{RA}} \simeq E_2 - E_1$, one has a Ramsey separated field interferometer [172, 289, 292], see figure 6.1. We denote with ϕ the phase of the Ramsey pulse source. For notational convenience, we assume that there is no time delay between the Ramsey pulses and the start and the end of the kicked-particle evolution, respectively. A Ramsey pulse then produces the following instantaneous change of the state vector ($\phi = 0$ for the first pulse at time 0):

$$\begin{pmatrix} \psi_1 \\ \psi_2 \end{pmatrix} \rightarrow \frac{1}{\sqrt{2}} \begin{pmatrix} 1 & e^{i\phi} \\ -e^{-i\phi} & 1 \end{pmatrix} \begin{pmatrix} \psi_1 \\ \psi_2 \end{pmatrix} \equiv \hat{R}_\phi \begin{pmatrix} \psi_1 \\ \psi_2 \end{pmatrix}. \quad (\text{E.1})$$

The evolution operator from time 0 to time t which includes the kicked-particle dynamics then reads

$$\hat{U}_{t,\phi} \equiv \hat{R}_\phi \hat{W}_t \hat{R}_0,$$

where

$$\hat{W}_t = \begin{pmatrix} e^{-iE_1 t} \hat{U}_{1,t} & 0 \\ 0 & e^{-iE_2 t} \hat{U}_{2,t} \end{pmatrix}. \quad (\text{E.2})$$

$\hat{U}_{1,2,t}$ are the kicked-particle evolution operators in the upper and in the lower atomic level, respectively. With the initial state $\psi_1 = 0, \psi_2 = \psi$, the state after the final Ramsey pulse then reads

$$\begin{aligned} \psi_{1,\phi}(t) &= \frac{1}{2} e^{-iE_1 t} (\hat{U}_{1,t} + e^{-i\phi_{\text{Ramsey}}} \hat{U}_{2,t}) \psi \\ \psi_{2,\phi}(t) &= \frac{1}{2} e^{-iE_2 t} (-\hat{U}_{1,t} e^{i\phi_{\text{Ramsey}}} + \hat{U}_{2,t}) \psi, \end{aligned} \quad (\text{E.3})$$

with the phase $\phi_{\text{Ramsey}} \equiv (E_2 - E_1)t - \phi$. The momentum distribution in the lower state ψ_1 is given by

$$P_1(p, t, \phi_{\text{Ramsey}}) = \frac{1}{4} \left| \langle p | \hat{U}_{1,t} \psi \rangle \right|^2 + \frac{1}{4} \left| \langle p | \hat{U}_{2,t} \psi \rangle \right|^2 + \frac{1}{2} \text{Re} \left\{ e^{-i\phi_{\text{Ramsey}}} \langle \hat{U}_{1,t} \psi | p \rangle \langle p | \hat{U}_{2,t} \psi \rangle \right\}. \quad (\text{E.4})$$

Integrating over p , the total probability in the lower level is obtained:

$$P_1(t, \phi_{\text{Ramsey}}) = \frac{1}{2} \left[1 + \text{Re} \left\{ e^{-i\phi_{\text{Ramsey}}} \langle \hat{U}_{1,t} \psi | \hat{U}_{2,t} \psi \rangle \right\} \right]. \quad (\text{E.5})$$

We now consider the case when the initial pure state ψ (of atomic motion) is replaced by a mixture which is described by the following statistical density operator

$$\hat{\rho} = \sum_n \rho_n |\psi_n\rangle \langle \psi_n|.$$

The final population in the lower level is then

$$\bar{P}_1(t, \phi_{\text{Ramsey}}) = \frac{1}{2} \{ 1 + G(t, \phi_{\text{Ramsey}}) \}, \quad (\text{E.6})$$

with

$$\begin{aligned} G(t, \phi_{\text{Ramsey}}) &\equiv \sum_n \rho_n \text{Re} \left\{ e^{-i\phi_{\text{Ramsey}}} \langle \hat{U}_{1,t} \psi_n | \hat{U}_{2,t} \psi_n \rangle \right\} \\ &\equiv \sqrt{F(t)} \cos(\phi''), \end{aligned} \quad (\text{E.7})$$

where, at fixed time t , ϕ'' differs from ϕ_{Ramsey} , as well as from ϕ by a constant shift, and

$$\begin{aligned} F(t) &= \left| \sum_n \rho_n \langle \hat{U}_{1,t} \psi_n | \hat{U}_{2,t} \psi_n \rangle \right|^2 = \left| \sum_n \rho_n \langle \psi_n | \hat{U}_{1,t}^{-1} \hat{U}_{2,t} \psi_n \rangle \right|^2 \\ &= \left| \text{Tr} \left\{ \hat{\rho} \hat{U}_{1,t}^{-1} \hat{U}_{2,t} \right\} \right|^2 \end{aligned} \quad (\text{E.8})$$

is the fidelity, cf. equation (6.2). From equation (E.6) and subsequent ones, we see that the fidelity is equal to the difference between the maximum and the minimum values taken by $\bar{P}_1(t, \phi)$ while the original phase ϕ varies in $[0, 2\pi)$. We arrive at the conclusion that the fidelity is accessible in principle by an experimental setup as used in [142], cf. figure 6.1. Equation (E.8) coincides with the fidelity defined in (6.7) when identifying $|\psi_n\rangle$ with the β -rotor states $|\psi_\beta\rangle$ (cf. sections 2.2.3 and 4.2.1).

Appendix F

Some formulas used in Part II

The following formulas involving Bessel functions are used in part II of this thesis and previous appendices; these are taken from [157] or derived from formulas there (we give the corresponding numbers from [157] in []):

$$\frac{1}{2\pi} \int_{\alpha}^{\alpha+2\pi} d\theta e^{iz \cos \theta} e^{-in\theta} = i^n J_n(z) \quad [9.1.21] \quad (\text{F.1})$$

$$\sum_{n=-\infty}^{\infty} n^2 J_n^2(x) = \frac{1}{2} x^2 \quad [9.1.76] \quad (\text{F.2})$$

$$\int_0^{2\pi} dx J_n^2(b \sin(x)) = \int_0^{2\pi} dx \cos(2nx) J_0^2(b \sin(x)) \quad [11.4.7/8] \quad (\text{F.3})$$

$$\int_{-\pi}^{\pi} dx J_{2n}(2z \sin(x)) = 2\pi J_n^2(z) \quad [11.4.7] \quad (\text{F.4})$$

$$\sum_n J_n^2(z) e^{int} = J_0(2z \sin(t/2)) \quad [11.4.8] \quad (\text{F.5})$$

$$J_0(z) = \frac{1}{\pi} \int_{-1}^1 dx \frac{\cos(zx)}{\sqrt{1-x^2}} \quad [9.1.18] \quad (\text{F.6})$$

$$|J_n(z)| \leq \frac{1}{n!} \left| \frac{z}{2} \right|^{|n|} e^{\mathcal{I}m(z)} \quad [9.1.62] \quad (\text{F.7})$$

$$J_0(z) \xrightarrow{|z| \rightarrow \infty} \sqrt{\frac{2}{\pi z}} \cos(z - \pi/4) \quad [9.2.1] \quad (\text{F.8})$$

From [157], we further collect:

$$\frac{\sin(x)}{x} \xrightarrow{x \rightarrow 0} 1 \quad [4.3.74] \quad (\text{F.9})$$

$$(a+b)^m = \sum_{k=0}^m \frac{m!}{k!(m-k)!} a^k b^{m-k} \quad [3.1.1] \quad (\text{F.10})$$

$$\left(1 + \frac{x}{n}\right)^n \xrightarrow{n \rightarrow \infty} e^x \quad [4.2.21] \quad (\text{F.11})$$

In section 6.2.2 we used an integral for the Bessel function J_0 adapted from [6.615] in [257]:

$$\int_0^\infty dy e^{-ay} J_0^2(2b\sqrt{y}) = \frac{1}{a} J_0\left(i\frac{2b^2}{a}\right) e^{-\frac{2b^2}{a}} . \quad (\text{F.12})$$

The following integral is used, for instance, when calculating the average energy in section 4.2.2:

$$\int_0^{2\pi} dx \frac{\sin^2(tx)}{\sin^2(x)} = 2\pi t . \quad (\text{F.13})$$

Appendix G

Publications

Publications of the author related to the topics covered in this thesis:

- *A classical scaling theory of quantum resonances*
Sandro Wimberger, Italo Guarneri, and Shmuel Fishman
to appear in Phys. Rev. Lett.
- *Decoherence as a probe of coherent quantum dynamics*
Michael B. d'Arcy, Rachel M. Godun, Gil S. Summy, Italo Guarneri,
Sandro Wimberger, Shmuel Fishman, and Andreas Buchleitner
to appear in Phys. Rev. E.
- *Decay, interference, and chaos: How simple atoms mimic disorder*
Andreas Krug, Sandro Wimberger, and Andreas Buchleitner
Eur. Phys. J. D, **26**, 21 (2003).
- *Quantum resonances and decoherence for δ -kicked atoms*
Sandro Wimberger, Italo Guarneri, and Shmuel Fishman
Nonlinearity **16**, 1381 (2003).
- *Decay rates and survival probabilities in open quantum systems*
Sandro Wimberger, Andreas Krug, and Andreas Buchleitner
Phys. Rev. Lett. **89**, 263601 (2002).
- *Signatures of Anderson localization in the ionization rates of periodically driven Rydberg states*
Sandro Wimberger and Andreas Buchleitner
J. Phys. A **34**, 7181 (2001).

Bibliography

- [1] P. W. Anderson, *More is different*, Science **177**, 393 (1972).
- [2] *The physics of complex systems*, Vol. Course XIX of *Proceedings of the International School of Physics 'E. Fermi'*, edited by F. Mallamace and H. E. Stanley (IOS Press, Amsterdam, 1996).
- [3] S. Solomon and E. Shir, *Complexity; a science at 30*, Europhys. News **34**, 54 (2003).
- [4] J. E. Bayfield and P. M. Koch, *Multiphoton Ionization of Highly Excited Hydrogen Atoms*, Phys. Rev. Lett. **33**, 258 (1974).
- [5] J. E. Bayfield, L. D. Gardner, and P. M. Koch, *Observation of Resonances in the Microwave-Stimulated Multiphoton Excitation and Ionization of Highly Excited Hydrogen Atoms*, Phys. Rev. Lett. **39**, 76 (1977).
- [6] G. Casati, B. V. Chirikov, J. Ford, and F. M. Izrailev, in *Stochastic Behavior in Classical and Quantum Hamiltonian Systems*, Vol. 93 of *Lecture Notes in Physics*, edited by G. Casati and J. Ford (Springer-Verlag, Berlin, 1979), p. 334.
- [7] M. C. Gutzwiller, *Chaos in Classical and Quantum Mechanics*, Vol. 1 of *Interdisciplinary Applied Mathematics* (Springer-Verlag, Berlin, 1990).
- [8] *Chaos and quantum physics*, Vol. Session **LII** of *Les Houches Lectures, 1989*, edited by M.-J. Giannoni, A. Voros, and J. Zinn-Justin (North-Holland, Amsterdam, 1991).
- [9] F. Haake, *Quantum Signatures of Chaos*, Vol. 54 of *Springer Series in Synergetics* (Springer-Verlag, Berlin, 1991).
- [10] *Quantum chaos: between order and disorder*, edited by G. Casati and B. Chirikov (Cambridge Univ. Press, Cambridge, 1995).
- [11] P. M. Koch and K. A. H. van Leeuwen, *The importance of resonances in microwave 'ionization' of excited hydrogen atoms*, Phys. Rep. **255**, 289 (1995).

- [12] C.-H. Iu, G. R. Welch, M. M. Kash, D. Kleppner, D. Delande, and J. C. Gay, *Diamagnetic Rydberg atom: Confrontation of calculated and observed spectra*, Phys. Rev. Lett. **66**, 145 (1991).
- [13] M. Arndt, A. Buchleitner, R. N. Mantegna, and H. Walther, *Experimental Studies of Quantum and Classical Limits in Microwave Ionization of Rubidium Rydberg Atoms*, Phys. Rev. Lett. **67**, 2435 (1991).
- [14] G. Raithel and H. Walther, *Ionization energy of rubidium Rydberg atoms in strong crossed electric and magnetic fields*, Phys. Rev. A **49**, 1646 (1994).
- [15] M. G. Raizen, V. Milner, W. H. Oskay, and D. A. Steck, in *New Directions in Quantum Chaos, Proceedings of the International School of Physics 'E. Fermi'*, edited by G. Casati, I. Guarneri, and U. Smilansky (IOS Press, Amsterdam, 2000), Vol. Course CXLIII, p. 299.
- [16] Bayfield, *Quantum Evolution: An Introduction to Time-Dependent Quantum Mechanics* (John Wiley & Sons, New York, 1999).
- [17] H.-J. Stöckmann, *Quantum Chaos, An Introduction* (Cambridge Univ. Press, Cambridge, 1999).
- [18] R. A. Jalabert, in *New Directions in Quantum Chaos, Proceedings of the International School of Physics 'E. Fermi'*, edited by G. Casati, I. Guarneri, and U. Smilansky (IOP Press, Amsterdam, 2000), Vol. Course CXLIII, p. 145.
- [19] *Statistical Theories of Spectra: Fluctuations*, edited by C. E. Porter (Academic Press, New York, 1965).
- [20] O. Bohigas, in *Chaos and quantum physics*, Vol. Session **LII** of *Les Houches Lectures, 1989*, edited by M.-J. Giannoni, A. Voros, and J. Zinn-Justin (North-Holland, Amsterdam, 1991), p. 87.
- [21] M. L. Mehta, *Random Matrices* (Academic Press, Boston, 1991).
- [22] C. W. J. Beenakker, *Random-matrix theory of quantum transport*, Rev. Mod. Phys. **69**, 731 (1997).
- [23] T. Guhr, A. Müller-Groeling, and H. A. Weidenmüller, *Random-matrix theories in quantum physics: common concepts*, Phys. Rep. **299**, 189 (1998).
- [24] W. R. S. Garton and F. S. Tomkins, *Diamagnetic Zeeman Effect and Magnetic Configuration Mixing in Long Spectral Series of BA I*, Astrophys. J. **158**, 839 (1969).
- [25] D. Delande, in *Chaos and quantum physics*, Vol. Session **LII** of *Les Houches Lectures, 1989*, edited by M.-J. Giannoni, A. Voros, and J. Zinn-Justin (North-Holland, Amsterdam, 1991), p. 665.

- [26] A. Holle, J. Main, G. Wiebusch, H. Rottke, and K. H. Welge, *Quasi-Landau spectrum of the chaotic diamagnetic hydrogen atom*, Phys. Rev. Lett. **61**, 161 (1988).
- [27] H. Hasegawa, M. Robnik, and G. Wunner, *Classical and Quantal Chaos in the Diamagnetic Kepler-Problem*, Prog. Theor. Phys. Suppl. **98**, 198 (1989).
- [28] H. Friedrich and D. Wintgen, *The hydrogen atom in a uniform magnetic field – An example of chaos*, Phys. Rep. **183**, 37 (1989).
- [29] J. Main, G. Wiebusch, K. Welge, J. Shaw, and J. B. Delos, *Recurrence spectroscopy: Observation and interpretation of large-scale structure in the absorption spectra of atoms in magnetic fields*, Phys. Rev. A **49**, 847 (1994).
- [30] J. Main and G. Wunner, *Ericson fluctuations in the chaotic ionization of the hydrogen atom in crossed magnetic and electric fields*, Phys. Rev. Lett. **69**, 586 (1992).
- [31] J. v. Milczewski and T. Uzer, *Chaos and order in crossed fields*, Phys. Rev. E **55**, 6540 (1997).
- [32] X. M. Tong and S.-I. Chu, *Time-dependent approach to high-resolution spectroscopy and quantum dynamics of Rydberg atoms in crossed magnetic and electric fields*, Phys. Rev. A **61**, 031401(R) (2000).
- [33] J. Rao, D. Delande, and K. T. Taylor, *Quantum manifestations of closed orbits in the photoexcitation scaled spectrum of the hydrogen atom in crossed fields*, J. Phys. B **34**, L391 (2001).
- [34] S. Freund, R. Ubert, E. Flöthmann, K. Welge, D. M. Wang, and J. B. Delos, *Absorption and recurrence spectra of hydrogen in crossed electric and magnetic fields*, Phys. Rev. A **65**, 053408 (2002).
- [35] T. Ericson, *Fluctuations of nuclear cross sections in the ‘continuum’ region*, Phys. Rev. Lett. **5**, 430 (1960).
- [36] T. Ericson, *A theory of fluctuations in nuclear cross-sections*, Ann. Phys. **23**, 390 (1963).
- [37] U. Smilansky, in *Chaos and quantum physics*, Vol. Session **LII** of *Les Houches Lectures, 1989*, edited by M.-J. Giannoni, A. Voros, and J. Zinn-Justin (North-Holland, Amsterdam, 1991), p. 371.
- [38] J. U. Nöckel and A. D. Stone, *Ray and wave chaos in asymmetric resonant optical cavities*, Nature **385**, 45 (1997).
- [39] Q. A. Starykh, P. R. Jacquod, E. E. Narimanov, and A. D. Stone, *Signature of dynamical localization in the resonance width distribution of wave-chaotic dielectric cavities*, Phys. Rev. E **62**, 2078 (2000).

- [40] H. J. Stöckmann and J. Stein, “*Quantum*” chaos in billiards studied by microwave absorption, *Phys. Rev. Lett.* **64**, 2215 (1990).
- [41] C. Dembowski, H.-D. Gräf, R. Hofferbert, H. Rehfeld, A. Richter, and T. Weiland, *Anderson localization in a string of microwave cavities*, *Phys. Rev. E* **60**, 3942 (1999).
- [42] K. Pance, W. Lu, and S. Sridhar, *Quantum Fingerprints of Classical Ruelle-Pollicott Resonances*, *Phys. Rev. Lett.* **85**, 2737 (2000).
- [43] A. J. Lichtenberg and M. A. Lieberman, *Regular and Chaotic Dynamics*, Vol. 38 of *Applied Mathematical Sciences* (Springer-Verlag, Berlin, 1992).
- [44] M. Tabor, *Chaos and Integrability in Nonlinear Dynamics* (Wiley, New York, 1989).
- [45] E. Ott, *Chaos in Dynamical Systems* (Cambridge Univ. Press, Cambridge, 1993).
- [46] J. G. Leopold and I. C. Percival, *Microwave Ionization and Excitation of Rydberg Atoms*, *Phys. Rev. Lett.* **41**, 944 (1978).
- [47] N. B. Delone, B. P. Krainov, and D. L. Shepelyansky, *Highly excited atoms in the electromagnetic field*, *Sov. Phs. Usp.* **26**, 551 (1983).
- [48] R. V. Jensen, *Stochastic Ionization of Surface-State Electrons*, *Phys. Rev. Lett.* **49**, 1365 (1982).
- [49] R. V. Jensen, *Stochastic ionization of surface-state electrons: Classical theory*, *Phys. Rev. A* **30**, 386 (1984).
- [50] E. J. Galvez, J. E. Sauer, L. Moorman, P. M. Koch, and D. Richards, *Microwave Ionization of H Atoms: Breakdown of Classical Dynamics for High Frequencies*, *Phys. Rev. Lett.* **61**, 2011 (1988).
- [51] J. E. Bayfield, G. Casati, I. Guarneri, and D. W. Sokol, *Localization of Classically Chaotic Diffusion for Hydrogen Atoms in Microwave Fields*, *Phys. Rev. Lett.* **63**, 364 (1989).
- [52] R. Blümel, R. Graham, L. Sirko, U. Smilansky, H. Walther, and K. Yamada, *Microwave Excitation of Rydberg Atoms in the Presence of Noise*, *Phys. Rev. Lett.* **62**, 341 (1989).
- [53] R. Blümel, A. Buchleitner, R. Graham, L. Sirko, U. Smilansky, and H. Walther, *Dynamical localization in the microwave interaction of Rydberg atoms: The influence of noise*, *Phys. Rev. A* **44**, 4521 (1991).
- [54] F. L. Moore, J. C. Robinson, C. F. Bharucha, P. E. Williams, and M. G. Raizen, *Observation of Dynamical Localization in Atomic Momentum Transfer: A New Testing Ground for Quantum Chaos*, *Phys. Rev. Lett.* **73**, 2974 (1994).

- [55] F. L. Moore, J. C. Robinson, C. F. Bharucha, B. Sundaram, and M. G. Raizen, *Atom Optics Realization of the Quantum δ -Kicked Rotor*, Phys. Rev. Lett. **75**, 4598 (1995).
- [56] B. V. Chirikov, F. M. Izrailev, and D. L. Shepelyansky, *Dynamical Stochasticity in Classical and Quantum Mechanics*, Soviet. Sci. Rev. C **2**, 209 (1981).
- [57] D. L. Shepelyansky, *Some statistical properties of simple classically stochastic quantum systems*, Physica D **8**, 208 (1983).
- [58] D. L. Shepelyansky, in *Chaotic Behavior in Quantum Systems*, Vol. 120 of *NATO ASI Series B*, edited by G. Casati (Plenum Press, New York, 1985), p. 187.
- [59] G. Casati, V. Chirikov, D. L. Shepelyansky, and I. Guarneri, *Relevance of classical chaos in quantum mechanics: The hydrogen atom in a monochromatic field*, Phys. Rep. **154**, 77 (1987).
- [60] G. Casati, I. Guarneri, and D. L. Shepelyansky, *Hydrogen Atom in Monochromatic Field: Chaos and Dynamical Photonic Localization*, IEEE J. Quantum Electron. **24**, 1420 (1988).
- [61] S. Fishman, D. R. Grempel, and R. E. Prange, *Chaos, Quantum Recurrences, and Anderson Localization*, Phys. Rev. Lett. **49**, 509 (1982).
- [62] S. Fishman, D. R. Grempel, and R. E. Prange, *Quantum dynamics of a nonintegrable system*, Phys. Rev. A **29**, 1639 (1984).
- [63] S. Fishman, in *Quantum Chaos*, Vol. Course CXIX of *Proceedings of the International School of Physics 'E. Fermi'*, edited by G. Casati, I. Guarneri, and U. Smilansky (North Holland, Amsterdam, 1993), p. 187.
- [64] F. M. Izrailev, *Simple Models of Quantum Chaos: Spectrum and Eigenfunctions*, Phys. Rep. **196**, 299 (1990).
- [65] Y. V. Fyodorov and H.-J. Sommers, *Statistics of resonance poles, phase shifts and time delay in quantum chaotic scattering: Random matrix approach for systems with broken time-reversal invariance*, J. Math. Phys. **38**, 1918 (1997).
- [66] P. Gaspard and S. A. Rice, *Exact quantization of the scattering from a classical chaotic repeller*, J. Chem. Phys. **90**, 2255 (1989).
- [67] B. Huckestein, R. Ketzmerick, and C. H. Lewenkopf, *Quantum Transport through Ballistic Cavities: Soft vs Hard Quantum Chaos*, Phys. Rev. Lett. **84**, 5504 (2000).
- [68] M. W. L. Hufnagel, R. Ketzmerick, *Conductance Fluctuations of Generic Billiards: Fractal or Isolated?*, Europhys. Lett. **54**, 703 (2001).

- [69] A. Bäcker, A. Manze, B. Huckestein, and R. Ketzmerick, *Isolated resonances in conductance fluctuations and hierarchical states*, Phys. Rev. E **66**, 016211 (2002).
- [70] K. Richter, *Semiclassical Theory of Mesoscopic Quantum Systems*, Vol. 161 of *Springer Tracts in Modern Physics* (Springer-Verlag, Berlin, 2000).
- [71] T. F. Gallagher, *Rydberg atoms*, Vol. 3 of *Cambridge monographs on atomic, molecular, and chemical physics* (Cambridge Univ. Press, Cambridge, 1994).
- [72] O. Benson, A. Buchleitner, G. Raither, M. Arndt, R. N. Mantegna, and H. Walther, *From coherent to noise-induced microwave ionization of Rydberg atoms*, Phys. Rev. A **51**, 4862 (1995).
- [73] M. W. Noel, W. M. Griffith, and T. F. Gallagher, *Classical subharmonic resonances in microwave ionization of lithium Rydberg atoms*, Phys. Rev. A **62**, 063401 (2000).
- [74] C. L. Stokely, J. C. Lancaster, F. B. Dunning, D. G. Arbó, C. O. Reinhold, and J. Burgdörfer, *Production of quasi-one-dimensional very-high- n Rydberg atoms*, Phys. Rev. A **67**, 013403 (2003).
- [75] P. A. Braun, *Discrete semiclassical methods in the theory of Rydberg atoms in external fields*, Rev. Mod. Phys. **65**, 115 (1993).
- [76] G. Tanner, K. Richter, and J.-M. Rost, *The theory of two-electron atoms: between ground state and complete fragmentation*, Rev. Mod. Phys. **72**, 497 (2000).
- [77] A. Buchleitner, D. Delande, and J. Zakrzewski, *Non-dispersive wave packets in periodically driven quantum systems*, Phys. Rep. **368**, 409 (2002).
- [78] S. Wiggins, *Chaotic transport in dynamical systems*, Vol. XIII of *Interdisciplinary applied mathematics; 2* (Springer-Verlag, Berlin, 1992).
- [79] P. W. Anderson, *Local moments and localized states*, Rev. Mod. Phys. **50**, 191 (1978).
- [80] S. Fishman, in *Quantum Dynamics of Simple Systems, Proc. of the 44-th Scottish Universities Summer School in Physics, Stirling, Aug. 1994*, edited by G. Oppo, S. Barnett, E. Riis, and M. Wilkinson (SUSSP Publications and Institute of Physics, Bristol, 1996), p. 115.
- [81] W. H. Oskay, D. A. Steck, V. Milner, B. G. Klappauf, and M. G. Raizen, *Ballistic peaks at quantum resonance*, Opt. Commun. **179**, 137 (2000).
- [82] M. B. d'Arcy, R. M. Godun, M. K. Oberthaler, D. Cassettari, and G. S. Summy, *Quantum Enhancement of Momentum Diffusion in the Delta-Kicked Rotor*, Phys. Rev. Lett. **87**, 074102 (2001).

- [83] M. B. d'Arcy, R. M. Godun, M. K. Oberthaler, G. S. Summy, K. Burnett, and S. A. Gardiner, *Approaching Classicality in Quantum Accelerator Modes through Decoherence*, Phys. Rev. E **64**, 056233 (2001).
- [84] R. Blümel and U. Smilansky, *Quantum Mechanical Suppression of Classical Stochasticity in the Dynamics of Periodically Perturbed Surface-State Electrons*, Phys. Rev. Lett. **52**, 137 (1984).
- [85] H. P. Breuer and M. Holthaus, *Adiabatic processes in the ionization of highly excited hydrogen atoms*, Z. Phys. D **11**, 1 (1989).
- [86] J. G. Leopold and D. Richards, *A semiclassical ionization mechanism for excited hydrogen in high-frequency fields*, J. Phys. B **24**, 1209 (1991).
- [87] R. V. Jensen, S. M. Susskind, and M. M. Sanders, *Chaotic ionization of highly excited hydrogen atoms: Comparison of classical and quantum theory with experiment*, Phys. Rep. **201**, 1 (1991).
- [88] P. W. Anderson, *Absence of Diffusion in Certain Random Lattices*, Phys. Rev. **109**, 1492 (1958).
- [89] K. Ishii, *Localization of Eigenstates and Transport Phenomena in the One-Dimensional Disordered System*, Suppl. Prog. Theor. Phys. **53**, 77 (1973).
- [90] N. Brenner and S. Fishman, *Pseudo-randomness and localization*, Nonlinearity **5**, 211 (1992).
- [91] N. Brenner and S. Fishman, *High-frequency excitation of quantum systems with adiabatic nonlinearity*, J. Phys. A **29**, 7199 (1996).
- [92] H. P. Breuer, K. Dietz, and M. Holthaus, *Highly excited hydrogen atoms in strong microwave fields*, Z. Phys. D **18**, 239 (1991).
- [93] H. P. Breuer and M. Holthaus, *A semiclassical theory of quasienergies and Floquet wave functions*, Ann. Phys. (New York) **211**, 249 (1991).
- [94] K. A. H. van Leeuwen, G. v. Oppen, S. Renwick, J. B. Bowlin, P. M. Koch, R. J. Jensen, O. Rath, D. Richards, and J. G. Leopold, *Microwave Ionization of Hydrogen Atoms: Experiment versus Classical Dynamics*, Phys. Rev. Lett. **55**, 2231 (1985).
- [95] A. Krug, *Alkali Rydberg States in Electromagnetic Fields: Computational Physics Meets Experiment*, Ph.D. thesis, Ludwig-Maximilians-Universität, Munich (2001).
- [96] A. Krug and A. Buchleitner, *Chaotic Ionization of Nonhydrogenic Alkali Rydberg States*, Phys. Rev. Lett. **86**, 3538 (2001).
- [97] A. Krug and A. Buchleitner, *Microwave ionization of alkali-metal Rydberg states in a realistic numerical experiment*, Phys. Rev. A **66**, 053416 (2002).

- [98] A. Krug and A. Buchleitner, *Chaotic ionization of non-classical alkali Rydberg states – computational physics beats experiment*, *Comp. Phys. Comm.* **147**, 394 (2002).
- [99] T. F. Gallagher, *Rydberg Atoms in Microwave Fields*, 2003, 296. WE-Heraeus Seminar: Chaos and Quantum Transport, organised by A. Buchleitner.
- [100] R. V. Jensen, S. M. Susskind, and M. M. Sanders, *Microwave ionization of highly excited hydrogen atoms: a test of the correspondence principle*, *Phys. Rev. Lett.* **62**, 1476 (1989).
- [101] J. G. Leopold and D. Richards, *The effect of a resonant electric field on a one-dimensional classical hydrogen atom*, *J. Phys. B* **18**, 3369 (1985).
- [102] J. G. Leopold and D. Richards, *Robust scarred states*, *J. Phys. B* **27**, 2169 (1994).
- [103] R. V. Jensen, M. M. Sanders, M. Saraceno, and B. Sundaram, *Inhibition of quantum transport due to “scars” of unstable periodic orbits*, *Phys. Rev. Lett.* **63**, 2771 (1989).
- [104] R. Graham, *Comments on dynamical localization, dissipation, and repeated measurements*, *Comm. At. Mol. Phys.* **25**, 219 (1991).
- [105] T. Geisel, G. Radons, and J. Rubner, *Kolmogorov-Arnold-Moser barriers in the quantum dynamics of chaotic systems*, *Phys. Rev. Lett.* **57**, 2883 (1986).
- [106] B. V. Chirikov, in *Chaos and quantum physics*, Vol. Session **LII** of *Les Houches Lectures, 1989*, edited by M.-J. Giannoni, A. Voros, and J. Zinn-Justin (North-Holland, Amsterdam, 1991), p. 443.
- [107] K. Vant, G. Ball, H. Ammann, and N. Christensen, *Experimental evidence for the role of cantori as barriers in a quantum system*, *Phys. Rev. E* **59**, 2846 (1999).
- [108] A. Buchleitner, D. Delande, and J.-C. Gay, *Microwave ionization of three-dimensional hydrogen atoms in a realistic numerical experiment*, *J. Opt. Soc. Am. B* **12**, 505 (1995).
- [109] G. Casati, in *Chaos and quantum physics*, Vol. Session **LII** of *Les Houches Lectures, 1989*, edited by M.-J. Giannoni, A. Voros, and J. Zinn-Justin (North-Holland, Amsterdam, 1991), p. 761.
- [110] A. Buchleitner, I. Guarneri, and J. Zakrzewski, *Conductance fluctuations in microwave-driven Rydberg atoms*, *Europhys. Lett.* **44**, 162 (1998).
- [111] S. Wimberger and A. Buchleitner, *Signatures of Anderson localization in the ionization rates of periodically driven Rydberg states*, *J. Phys. A* **34**, 7181 (2001).

- [112] A. Buchleitner and D. Delande, *Spectral Aspects of the Microwave Ionization of Atomic Rydberg States*, *Chaos, Solitons & Fractals* **5**, 1125 (1995).
- [113] A. Buchleitner, *Atomes de Rydberg en champ microwave: regularite et chaos*, Thèse de Doctorate, Université Pierre et Marie Curie, Paris (1993).
- [114] A. Buchleitner, D. Delande, J. Zakrzewski, R. N. Mantegna, M. Arndt, and H. Walther, *Multiple Time Scales in the Microwave Ionization of Rydberg Atoms*, *Phys. Rev. Lett.* **75**, 3818 (1995).
- [115] G. Benenti, G. Casati, G. Maspero, and D. L. Shepelyansky, *Quantum Poincaré Recurrences for a Hydrogen Atom in a Microwave Field*, *Phys. Rev. Lett.* **84**, 4088 (2000).
- [116] S. Wimberger, A. Krug, and A. Buchleitner, *Decay rates and survival probabilities in open quantum systems*, *Phys. Rev. Lett.* **89**, 263601 (2002).
- [117] F. M. Izrailev and D. L. Shepelyansky, *Quantum resonance for the rotor in a non-linear periodic field*, *Dok. Akad. Nauk SSSR* **249**, 1103 (1979).
- [118] F. M. Izrailev and D. L. Shepelyansky, *Quantum resonance for a rotator in a non-linear periodic field*, *Theor. Math. Phys.* **43**, 353 (1980).
- [119] C. S. Adams, M. Sigel, and J. Mlynek, *Atom optics*, *Phys. Rep.* **240**, 143 (1994).
- [120] C. N. Cohen-Tannoudji, *Nobel Lecture: Manipulating atoms with photons*, *Rev. Mod. Phys.* **70**, 707 (1998).
- [121] S. Chu, *Nobel Lecture: The manipulation of neutral particles*, *Rev. Mod. Phys.* **70**, 685 (1998).
- [122] P. Meystre, *Atom Optics* (Springer-Verlag, New York, 2001).
- [123] B. Dubetsky and P. R. Berman, *Atomic interferometry* (Academic Press, Chestnut Hill, 1997).
- [124] C. J. Pethick and H. Smith, *Bose-Einstein Condensation in Dilute Gases* (Cambridge Univ. Press, Cambridge, 2002).
- [125] E. A. Cornell and C. E. Wieman, *Nobel Lecture: Bose-Einstein condensation in a dilute gas, the first 70 years and some recent experiments*, *Rev. Mod. Phys.* **74**, 875 (2002).
- [126] W. Ketterle, *Nobel Lecture: When atoms behave as waves: Bose-Einstein condensation and the atom laser*, *Rev. Mod. Phys.* **74**, 1131 (2002).
- [127] M.-O. Mewes, M. R. Andrews, D. M. Kurn, D. S. Durfee, C. G. Townsend, and W. Ketterle, *Output Coupler for Bose-Einstein Condensed Atoms*, *Phys. Rev. Lett.* **78**, 582 (1997).

- [128] B. P. Anderson and M. A. Kasevich, *Macroscopic Quantum Interference from Atomic Tunnel Arrays*, *Science* **282**, 1686 (1998).
- [129] E. W. Hagley, L. Deng, M. Kozuma, J. Wen, K. Helmerson, S. L. Rolston, and W. D. Phillip, *A Well-Collimated Quasi-Continuous Atom Laser*, *science* **283**, 1706 (1999).
- [130] I. Bloch, T. W. Hänsch, and T. Esslinger, *Atom Laser with a cw Output Coupler*, *Phys. Rev. Lett.* **82**, 3008 (1999).
- [131] C. J. Lee, *Quantum-mechanical analysis of atom lithography*, *Phys. Rev. A* **61**, 063604 (2000), and references therein.
- [132] R. Folman, D. C. P. Krüger, B. Hessmo, T. Maier, and J. Schmiedmayer, *Controlling Cold Atoms using Nanofabricated Surfaces: Atom Chips*, *Phys. Rev. Lett.* **84**, 4749 (2002).
- [133] J. Fortágh and C. Zimmermann, *Bose-Einstein-Kondensate in magnetischen Mikrofallen*, *Phys. J.* **2**, 39 (2003).
- [134] R. Folman, P. Krüger, J. Schmiedmayer, J. Denschlage, and C. Henkel, *Microscopic atom optics: from wires to an atom chip*, *Adv. At. Mol. Opt. Phys.* **48**, 263 (2003).
- [135] M. B. d'Arcy, *Quantum chaos in atom optics*, Ph.D. thesis, University of Oxford, Oxford (2002).
- [136] G. P. Berman and G. M. Zaslavsky, *Condition of stochasticity in quantum nonlinear systems*, *Physica A* **91**, 450 (1978).
- [137] I. C. Percival, *Regular and irregular spectra*, *J. Phys. B* **6**, L229 (1973).
- [138] A. Peres, *Stability of quantum motion in chaotic and regular systems*, *Phys. Rev. A* **30**, 1610 (1984).
- [139] A. Peres, *Quantum Theory: Concepts and Methods*, Vol. 57 of *Fundamental Theories in Physics* (Kluwer Academic Publishers, Dordrecht, 1993).
- [140] R. Schack and C. M. Caves, *Hypersensitivity to Perturbations in The Quantum Baker's Map*, *Phys. Rev. Lett.* **71**, 525 (1993).
- [141] T. Prosen and M. Žnidarič, *Stability of quantum motion and correlation decay*, *J. Phys. A* **35**, 1455 (2002).
- [142] S. Schlunk, M. B. d'Arcy, S. A. Gardiner, D. Cassettari, R. M. Godun, and G. S. Summy, *Signatures of quantum stability in a classically chaotic system*, *Phys. Rev. Lett.* **90**, 054101 (2003).
- [143] M. B. d'Arcy, R. M. Godun, D. Cassettari, and G. S. Summy, *Accelerator-mode-based technique for studying quantum chaos*, *Phys. Rev. A* **67**, 023605 (2003).

- [144] S. Fishman, I. Guarneri, and L. Rebuzzini, *Stable Quantum Resonances in Atom Optics*, Phys. Rev. Lett. **89**, 084101 (2002).
- [145] S. Fishman, I. Guarneri, and L. Rebuzzini, *A Theory for Quantum Accelerator Modes in Atom Optics*, J. Stat. Phys. **110**, 911 (2003).
- [146] M. G. Floquet, *Équations différentielles linéaires à coefficients périodiques*, Ann. École Norm. Sup. **12**, 47 (1883).
- [147] J. H. Shirley, *Solution of the Schrödinger Equation with a Hamiltonian Periodic in Time*, Phys. Rev. **138**, B979 (1965).
- [148] Y. B. Zel'dovich, *The quasienergy of a quantum-mechanical system subjected to a periodic action*, Sov. Phys. JETP **24**, 1006 (1967).
- [149] F. H. M. Faisal, *Theory of multiphoton processes, Physics of atoms and molecules* (Plenum Press, New York, 1987).
- [150] S. Graffi, V. Grecchi, and H. J. Silverstone, *Resonances and convergence of perturbation theory for N -body atomic systems in external AC-electric field*, Ann. Inst. Henri Poincaré **42**, 215 (1985).
- [151] H. L. Cycon, R. G. Froese, W. Kirsch, and B. Simon, *Schrödinger Operators: With Application to Quantum Mechanics & Global Geometry* (Springer-Verlag, New York, 1987).
- [152] N. L. Salzman, *Quantum mechanics of systems periodic in time*, Phys. Rev. A **10**, 461 (1974).
- [153] J. M. Ziman, *Principles of the Theory of Solids* (Cambridge Univ. Press, Cambridge, 1964).
- [154] N. W. Ashcroft and N. D. Mermin, *Solid State Physics* (Saunders College Publishing, Fort Worth, 1976), college Edition.
- [155] J. J. Sakurai, *Modern Quantum Mechanics* (Addison Wesley, Reading, 1994), edited by S. F. Tuan.
- [156] B. V. Chirikov, *A universal instability of many-dimensional oscillator systems*, Phys. Rep. **52**, 263 (1979).
- [157] M. Abramowitz and I. A. Stegun, *Handbook of mathematical functions* (Dover, New York, 1972).
- [158] G. Casati and I. Guarneri, *Non-Resonant Behaviour in Quantum Dynamics*, Commun. Math. Phys. **95**, 121 (1984).
- [159] M. B. d'Arcy, R. M. Godun, G. S. Summy, I. Guarneri, S. Wimberger, S. Fishman, and A. Buchleitner, *Decoherence as a probe of coherent quantum dynamics*, 2003, phys. Rev. E, in press.
- [160] S. Wimberger, I. Guarneri, and S. Fishman, *Quantum resonances and decoherence for δ -kicked atoms*, Nonlinearity **16**, 1381 (2003).

- [161] F. M. Izrailev, *Limiting Quasienergy Statistics for Simple Quantum Systems*, Phys. Rev. Lett. **56**, 541 (1986).
- [162] G. Casati, I. Guarneri, and G. Maspero, *Fractal Survival Probability Fluctuations*, Phys. Rev. Lett. **84**, 63 (2000).
- [163] G. Benenti, G. Casati, I. Guarneri, and M. Terraneo, *Quantum Fractal Fluctuations*, Phys. Rev. Lett. **87**, 014101 (2001).
- [164] M. Terraneo, S. Wimberger, and I. Guarneri, *Fractal fluctuations in 2D maps and tight-binding models*, unpublished.
- [165] S. Chu, *Laser Manipulation of Atoms and Particles*, Science **253**, 861 (1991).
- [166] W. H. Oskay, D. A. Steck, and M. G. Raizen, *Timing noise effects on dynamical localization*, Chaos, Solitons & Fractals **16**, 409 (2003).
- [167] R. W. Boyd, *Nonlinear optics* (Academic Press, San Diego, 1992).
- [168] J. C. Robinson, C. Bharucha, F. L. Moore, R. Jahnke, G. A. Georgakis, Q. Niu, and M. G. Raizen, *Study of Quantum Dynamics in the Transition from Classical Stability to Chaos*, Phys. Rev. Lett. **74**, 3963 (1995).
- [169] C. F. Bharucha, J. C. Robinson, F. L. Moore, B. Sundaram, Q. Niu, and M. G. Raizen, *Dynamical localization of ultracold sodium atoms*, Phys. Rev. E **60**, 3881 (1999).
- [170] R. Graham, M. Schlautmann, and P. Zoller, *Dynamical localization of atomic-beam deflection by a modulated standing light wave*, Phys. Rev. A **45**, R15 (1992).
- [171] D. A. Steck, *Quantum Chaos, Transport, and Decoherence in Atom Optics*, Ph.D. thesis, University of Texas, Austin (2001).
- [172] P. Meystre and M. Sargent III, *Elements of Quantum Optics* (Springer-Verlag, Berlin, 1991).
- [173] W. H. Oskay, *Atom Optics Experiments in Quantum Chaos*, Ph.D. thesis, University of Texas, Austin (2001).
- [174] B. G. Klappauf, W. H. Oskay, D. A. Steck, and M. G. Raizen, *Quantum chaos with cesium atoms: Pushing the boundaries*, Physica D **131**, 78 (1999).
- [175] R. Blümel, S. Fishman, and U. Smilansky, *Excitation of molecular rotation by periodic microwave pulses. A testing ground for Anderson localization*, J. Chem. Phys. **84**, 2604 (1986).
- [176] A. C. Doherty, K. Vant, G. H. Ball, N. Christensen, and R. Leonhardt, *Momentum distributions for the quantum δ -kicked rotor with decoherence*, J. Opt. B **2**, 605 (2000).

- [177] V. I. Arnold, *Mathematical Methods of Classical Mechanics*, Vol. 60 of *Graduate Texts in Mathematics* (Springer-Verlag, Berlin, 1989).
- [178] J. C. Robinson, *Atom optics: a new testing ground for quantum chaos*, Ph.D. thesis, University of Texas, Austin (1995).
- [179] M. Arndt, M. B. Dahan, D. Guéry-Odelin, M. W. Reynolds, and J. Dalibard, *Observation of a Zero-Energy Resonance in Cs-Cs Collisions*, *Phys. Rev. Lett.* **79**, 625 (1997).
- [180] D. A. Steck, V. Milner, W. H. Oskay, and M. G. Raizen, *Quantitative study of amplitude noise effects on dynamical localization*, *Phys. Rev. E* **62**, 3461 (2000).
- [181] S. Brouard and J. Plata, *Quantum δ -kicked rotor: the effect of amplitude noise on the quantum resonances*, *J. Phys. A* **36**, 3745 (2003).
- [182] M. E. Williams, M. P. Sadgrove, A. J. Daley, R. N. Gray, S. M. Tan, A. S. Parkins, R. Leonhardt, and N. Christensen, *Measurement of Diffusion Resonances for the Atom Optics Quantum Kicked Rotor*, preprint physics/0208090, 2002.
- [183] B. G. Klappauf, W. H. Oskay, D. A. Steck, and M. G. Raizen, *Observation of Noise and Dissipation Effects on Dynamical Localization*, *Phys. Rev. Lett.* **81**, 1203 (1998).
- [184] H. Ammann, R. Gray, I. Shvarchuck, and N. Christensen, *Quantum Delta-Kicked Rotor: Experimental Observation of Decoherence*, *Phys. Rev. Lett.* **80**, 4111 (1998).
- [185] A. Buchleitner, B. Grémaud, and D. Delande, *Wavefunctions of atomic resonances*, *J. Phys. B.* **27**, 2663 (1994).
- [186] M. Gavrilina, in *Collision Theory for Atoms and Molecules*, Vol. 196 of *NATO ASI Series B*, edited by F. A. Gianturco (Plenum Press, New York, 1989), p. 139.
- [187] E. Cormier and P. Lambropoulos, *Optimal gauge and gauge invariance in non-perturbative time-dependent calculation of above-threshold ionization*, *J. Phys. B* **29**, 1667 (1996).
- [188] R. Shakeshaft, *Multiphoton ionization of an atom; the choice of gauge*, *Z. Phys. D* **8**, 47 (1988).
- [189] Y. Imry, in *Physique quantique mésoscopique*, Vol. Session **LXI** of *Les Houches Lectures, 1994*, edited by E. Akkermans, G. Montambaux, J.-L. Pichard, and J. Zinn-Justin (North-Holland, Amsterdam, 1995), p. 181.
- [190] K. Yajima, *Resonances for the AC-Stark Effect*, *Commun. Math. Phys.* **87**, 331 (1982).

- [191] E. Baslev and J. M. Combes, *Spectral Properties of Many-Body Schrödinger Operators with Dilatation-analytic Interactions*, Commun. Math. Phys. **22**, 280 (1971).
- [192] B. Simon, *Resonances in n -body quantum systems with dilatation analytic potentials and the foundations of time-dependent perturbation theory*, Ann. Math. **97**, 247 (1973).
- [193] A. Maquet, S.-I. Chu, and W. Reinhardt, *Stark ionization in dc and ac fields: An L^2 complex-coordinate approach*, Phys. Rev. A **27**, 2946 (1983).
- [194] V. I. Kukulin, V. M. Krasnopol'sky, and J. Horáček, *Theory of Resonances* (Kluwer Academic, Dordrecht, 1989).
- [195] P. D. Hislop and I. M. Sigal, *Introduction to spectral theory*, Vol. 113 of *Applied mathematical sciences* (Springer-Verlag, New York, 1996).
- [196] E. Cassirer, *Determinismus und Indeterminismus in der modernen Physik - Historische und systematische Studien zum Kausalproblem*, in: *Zur modernen Physik* (Wissenschaftliche Buchgesellschaft Darmstadt, Darmstadt, 1994).
- [197] M. Terraneo and I. Guarneri, *Distribution of resonance widths in localized tight-binding models*, Eur. Phys. J. B **18**, 303 (2000).
- [198] N. G. van Kampen, *Stochastic processes in physics and chemistry* (North Holland, Amsterdam, 1992).
- [199] G. Casati, G. Maspero, and D. L. Shepelyansky, *Quantum Poincaré Recurrences*, Phys. Rev. Lett. **82**, 524 (1999).
- [200] M. Titov and Y. V. Fyodorov, *Time-delay correlations and resonances in one-dimensional disordered systems*, Phys. Rev. B **61**, R2444 (2000).
- [201] F. A. Pinheiro, M. Rusek, A. Orłowski, and B. A. van Tiggelen, *Probing Anderson localization of light via decay rate statistics*, 2003, preprint: cond-mat/0307428.
- [202] R. Ketzmerick, L. Hufnagel, F. Steinbach, and M. Weiss, *New Class of Eigenstates in Generic Hamiltonian Systems*, Phys. Rev. Lett. **85**, 1214 (2000).
- [203] G. P. Berman and G. M. Zaslavsky, *Theory of quantum nonlinear resonance*, Phys. Lett. A **61**, 295 (1977).
- [204] S. MacDonald and A. Kaufman, *Spectrum and Eigenfunctions for a Hamiltonian with Stochastic Trajectories*, Phys. Rev. Lett. **42**, 1189 (1979).
- [205] G. Radons and R. E. Prange, *Wave Functions at the Critical Kolmogorov-Arnol'd-Moser Surface*, Phys. Rev. Lett. **61**, 1691 (1988).

- [206] G. Casati, I. Guarneri, and D. L. Shepelyansky, *Classical chaos, quantum localization and fluctuations: A unified view*, Physica A **163**, 205 (1990).
- [207] J. Leopold and D. Richards, *On the quantum Kepler map*, J. Phys. B **23**, 2911 (1990).
- [208] S. Wimberger, *Der Leitwert von Atomen*, Master's thesis, Ludwig-Maximilians-Universität, Munich (2000).
- [209] J. Zakrzewski, D. Delande, and A. Buchleitner, *Nonspreading Electronic Wave Packets and Conductance Fluctuations*, Phys. Rev. Lett. **75**, 4015 (1995).
- [210] J. Zakrzewski, D. Delande, and A. Buchleitner, *Ionization via chaos assisted tunneling*, Phys. Rev. E **57**, 1458 (1998).
- [211] D. F. Walls and G. J. Milburn, *Quantum optics* (Springer, Berlin, 1995).
- [212] D. Delande, *Atomes de Rydberg en champs statiques intenses*, Thèse de Doctorate d'état, Université Pierre et Marie Curie, Paris (1988).
- [213] W. A. Lin and L. E. Ballentine, *Quantum tunneling and chaos in a driven anharmonic oscillator*, Phys. Rev. Lett. **65**, 2927 (1990).
- [214] O. Bohigas, S. Tomsovic, and D. Ullmo, *Manifestation of classical phase space structure in quantum mechanics*, Phys. Rep. **223**, 43 (1993).
- [215] O. Bohigas, D. Boosé, R. E. de Carvalho, and V. Marvulle, *Quantum tunneling and chaotic dynamics*, Nucl. Phys. A **560**, 197 (1993).
- [216] S. Tomsovic and D. Ullmo, *Chaos-assisted tunneling*, Phys. Rev. E **50**, 145 (1994).
- [217] O. Brodier, P. Schlagheck, and D. Ullmo, *Resonance-assisted tunneling in near-integrable systems*, Phys. Rev. Lett. **87**, 064101 (2001).
- [218] L. D. Landau and E. M. Lifschitz, *Lehrbuch der theoretischen Physik* (Akademie-Verlag, Berlin, 1979), Vol. III, Quantenmechanik.
- [219] Y.-C. Lai, C. Grebogi, R. Bümel, and M. Ding, *Algebraic decay and phase-space metamorphoses in microwave ionization of hydrogen Rydberg atoms*, Phys. Rev. A **45**, 8284 (1992).
- [220] F.-M. Dittes, *The decay of quantum systems with a small number of open channels*, Phys. Rep. **339**, 216 (2000).
- [221] A. Ossipov, M. Weiss, T. Kottos, and T. Geisel, *Quantum mechanical relaxation of quasiperiodic systems*, Phys. Rev. B **64**, 224210 (2001).
- [222] M. Weiss, *Quantenmechanik zwischen Regularität und Chaos: Vom gemischten Phasenraum zu ungeordneten Systemen*, Ph.D. thesis, Universität Göttingen, Göttingen (2000).

- [223] W. H. Press, S. A. Teulosky, W. T. Vetterling, and B. P. Flannery, *Numerical Recipes in FORTRAN: the art of scientific computing* (Cambridge Univ. Press, Cambridge, 1994).
- [224] C. F. F. Karney, *Long-time correlations in the stochastic regime*, Physica D **8**, 360 (1983).
- [225] R. S. MacKay, J. D. Meiss, and I. C. Percival, *Stochasticity and Transport in Hamiltonian Systems*, Phys. Rev. Lett. **52**, 697 (1984).
- [226] R. S. MacKay, J. D. Meiss, and I. C. Percival, *Transport in Hamiltonian systems*, Physica D **13**, 55 (1984).
- [227] B. V. Chirikov and D. L. Shepelyansky, *Correlation properties of dynamical chaos in Hamiltonian systems*, Naukova Dumka **2**, 420 (1984), English Translation Princeton University Report No. PPPL-TRANS-133, 1983; Physica D **13**, 395 (1984).
- [228] J. D. Meiss and E. Ott, *Markov-Tree Model of Intrinsic Transport in Hamiltonian Systems*, Phys. Rev. Lett. **55**, 2741 (1985).
- [229] G. Zumofen and J. Klafter, *Random Walks in the Standard Map*, Europhys. Lett. **25**, 565 (1994).
- [230] Y.-C. Lai, R. Bümel, E. Ott, and C. Grebogi, *Quantum Manifestation of Chaotic Scattering*, Phys. Rev. Lett. **24**, 3491 (1992).
- [231] B. V. Chirikov and D. L. Shepelyansky, *Asymptotic Statistics of Poincaré Recurrences in Hamiltonian Systems with Divided Phase Space*, Phys. Rev. Lett. **82**, 528 (1999).
- [232] M. Weiss, L. Hufnagel, and R. Ketzmerick, *Do Chaotic Trajectories Care About Self-Similarity?*, preprint, nlin.CD/0106021, 2001.
- [233] M. Weiss, L. Hufnagel, and R. Ketzmerick, *Universal Power-Law Decay in Hamiltonian Systems?*, Phys. Rev. Lett. **89**, 239401 (2002), comment.
- [234] M. Weiss, L. Hufnagel, and R. Ketzmerick, *Can simple renormalization theories describe the trapping of chaotic trajectories in mixed systems?*, Phys. Rev. E **67**, 046209 (2003).
- [235] A. Buchleitner, D. Delande, and J. Zakrzewski, in *Multiphoton Processes 1996*, No. 154 in *Inst. Phys. Conf. Ser.*, edited by P. Lambropoulos and H. Walther (IOP Publishing Ltd, Bristol, 1997), p. 19.
- [236] E. Persson, I. Rotter, H.-J. Stöckmann, and M. Barth, *Observation of Resonance Trapping in an Open Microwave Cavity*, Phys. Rev. Lett. **85**, 2478 (2000).
- [237] W. Lu, M. Rose, K. Pance, and S. Sridhar, *Quantum Resonances and Decay of a Chaotic Fractal Repeller Observed Using Microwaves*, Phys. Rev. Lett. **82**, 5233 (1999).

- [238] Y. Zhang, M. Cioccia, L.-W. He, C. E. Burkhardt, and J. J. Leventhal, *Floquet spectroscopy of hydrogen states: Classical and quantal description*, Phys. Rev. A **50**, 4608 (1994).
- [239] J. W. Pang, D. Neuhauser, and N. Moiseyev, *Photoabsorption probability for a system governed by a time-dependent Hamiltonian through the t, t' formalism*, J. Chem. Phys. **106**, 6839 (1997).
- [240] A. Buchleitner and D. Delande, *Secular motion of three-dimensional Rydberg states in a microwave field*, Phys. Rev. A **55**, R1585 (1997).
- [241] A. Buchleitner, *Transport in periodisch getriebenen Rydbergsystemen*, Habilitationsschrift, Ludwig-Maximilians-Universität, Munich (1998).
- [242] Y. Imry, *Active Transmission Channels and Universal Conductance Fluctuations*, Europhys. Lett. **1**, 249 (1986).
- [243] J.-L. Pichard, *The one-dimensional Anderson model: scaling and resonances revisited*, J. Phys. C **19**, 1519 (1986).
- [244] J.-L. Pichard, N. Zanon, Y. Imry, and A. D. Stone, *Theory of random multiplicative transfer matrices and its implications for quantum transport*, J. Phys. (Paris) **51**, 587 (1990).
- [245] L. Sirko, M. Arndt, P. M. Koch, and H. Walther, *Microwave ionization of Rb Rydberg atoms: Frequency dependence*, Phys. Rev. A **49**, 3831 (1994).
- [246] L. Sirko, A. Buchleitner, and H. Walther, *Rabi-nutations of four- and six-photon transitions between Rydberg states*, Opt. Commun. **78**, 403 (1990).
- [247] R. Blümel and U. Smilansky, *Classical irregular scattering and its quantum-mechanical implications*, Phys. Rev. Lett. **60**, 477 (1988).
- [248] H. Hegger, B. Huckestein, K. Hecker, M. Janssen, A. Freimuth, G. Reckziegel, and R. Tuzinski, *Fractal Conductance Fluctuations in Gold Nanowires*, Phys. Rev. Lett. **77**, 3885 (1996).
- [249] A. P. Micolich, R. P. Taylor, R. Newbury, J. P. Bird, R. Wirtz, D. P. Dettmann, Y. Aoyagi, and T. Sugano, *Geometry-induced fractal behaviour in a semiconductor billiard*, J. Phys. Condens. Matter **10**, 1339 (1998).
- [250] E. Louis and J. A. Vergés, *Self-similar magnetoconductance fluctuations in quantum dots*, Phys. Rev. B **61**, 13014 (2000).
- [251] R. Ketzmerick, *Fractal conductance fluctuations in generic chaotic cavities*, Phys. Rev. B **54**, 10841 (1996).
- [252] A. S. Sachrajda, R. Ketzmerick, C. Gould, Y. Feng, P. J. Kelly, A. Delage, and Z. Wasilewski, *Fractal Conductance Fluctuations in a Soft-Wall Stadium and a Sinai Billiard*, Phys. Rev. Lett. **80**, 1948 (1998).
- [253] I. Guarneri and M. Terraneo, *Fractal fluctuations in quantum integrable scattering*, Phys. Rev. E **65**, 015203(R) (2002).

- [254] D. L. Shepelyansky, *Dynamical stochasticity in nonlinear quantum systems*, *Theor. Mat. Fiz.* **49**, 117 (1981).
- [255] B. V. Chirikov and D. L. Shepelyansky, *Correlation properties of dynamical chaos in Hamiltonian systems*, *Physica D* **13**, 395 (1984).
- [256] D. L. Shepelyansky, *Localization of diffusive excitation in multi-level systems*, *Physica D* **28**, 103 (1987).
- [257] S. Gradshteyn and I. M. Ryzhik, *Table of integrals, series, and products* (Academic Press, New York, 1994).
- [258] P. M. Morse and H. Feshbach, *Methods of theoretical physics*, Vol. I of *International series in pure and applied physics* (McGraw-Hill, New York, 1953).
- [259] W. Feller, *An introduction to probability theory and its applications* (Wiley, New York, 1971), Vol. II.
- [260] M. B. d'Arcy and G. S. Summy, private communication.
- [261] H.-P. Breuer and F. Petruccione, *The theory of open quantum systems* (Oxford Univ. Press, Oxford, 2002).
- [262] P. Goetsch and R. Graham, *Decoherence by spontaneous emission in atomic-momentum transfer experiments*, *Phys. Rev. A* **54**, 5345 (1996).
- [263] R. Graham and S. Miyazaki, *Dynamical localization of atomic de Broglie waves: The influence of spontaneous emission*, *Phys. Rev. A* **53**, 2683 (1996).
- [264] A. R. Kolovsky, A. V. Ponomarev, and H. J. Korsch, *Damped Bloch oscillations of cold atoms in optical lattices*, *Phys. Rev. A* **66**, 053405 (2002).
- [265] I. Guarneri, *Energy growth in a randomly kicked quantum rotor*, *Lett. Nuovo Cim.* **40**, 171 (1984).
- [266] C. Cohen-Tannoudji, J. Dupont-Roc, and G. Grynberg, *Atom-Photon Interactions, Basic Processes and Applications* (John Wiley & Sons, New York, 1992).
- [267] Y. G. Sinai, *Probability theory, Springer textbook* (Springer-Verlag, Berlin, 1992).
- [268] I. N. Bronstejn and K. A. Semendjaev, *Handbook of mathematics* (Springer-Verlag, Berlin, 1998).
- [269] L. Mandel and E. Wolf, *Optical Coherence and Quantum Optics* (Cambridge Univ. Press, Cambridge, 1997).
- [270] M. Reed and B. Simon, *Functional analysis*, Vol. I of *Methods of modern mathematical physics* (Academic Press, San Diego, 1980).

- [271] V. V. Sokolov, O. V. Zhirov, D. Alonso, and G. Casati, *Quantum Resonances of the Kicked Rotor and the $SU(q)$ Group*, Phys. Rev. Lett. **84**, 3566 (2000).
- [272] V. V. Sokolov, O. V. Zhirov, D. Alonso, and G. Casati, *Quantum Resonances and regularity islands in quantum maps*, Phys. Rev. E **61**, 5057 (2000).
- [273] P. Szriftgiser, J. Ringot, D. Delande, and J. C. Garreau, *Observation of Sub-Fourier Resonances in a Quantum-Chaotic System*, Phys. Rev. Lett. **89**, 224101 (2002).
- [274] I. Dana and S. Fishman, *Diffusion in the standard map*, Physica D **17**, 63 (1985).
- [275] D. R. Grempel, S. Fishman, and R. E. Prange, *Constant Scaling at Stochastic Transitions of Dynamical Systems*, Phys. Rev. Lett. **53**, 1212 (1984).
- [276] S. Fishman, D. R. Grempel, and R. E. Prange, *The Temporal Crossover from Classical to Quantal Behavior Near Dynamical Critical Points*, Phys. Rev. A **36**, 289 (1987).
- [277] E. Ott, T. M. Antonsen, and J. D. Hanson, *Effect of Noise on Time-Dependent Quantum Chaos*, Phys. Rev. Lett. **53**, 2187 (1984).
- [278] R. Schack and C. M. Caves, *Information-theoretic characterization of quantum chaos*, Phys. Rev. E **53**, 3257 (1996).
- [279] P. Jacquod, P. G. Silvestrov, and C. W. J. Beenakker, *Golden rule decay Lyapunov decay of the quantum Loschmidt echo*, Phys. Rev. E **64**, 055203(R) (2001).
- [280] N. R. Cerruti and S. Tomsovic, *Sensitivity of Wave Field Evolution and Manifold Stability in Chaotic Systems*, Phys. Rev. Lett. **88**, 054103 (2002).
- [281] G. Benenti and G. Casati, *Quantum-classical correspondence in perturbed chaotic systems*, Phys. Rev. E **65**, 066205 (2002).
- [282] D. A. Wisniacki and D. Cohen, *Quantum irreversibility, perturbation independent decay, and the parametric theory of the local density of states*, Phys. Rev. E **66**, 046209 (2002).
- [283] J. Vanicek and E. J. Heller, *Semiclassical evaluation of fidelity in the Fermi-golden-rule and Lyapunov regimes*, 2003, preprint: quant-ph/0302192.
- [284] P. Jacquod, I. Adagideli, and C. W. J. Beenakker, *Anomalous power law of quantum reversibility for classically regular dynamics*, Europhys. Lett. **61**, 729 (2003).

- [285] M. A. Nielsen and I. L. Chuang, *Quantum computation and quantum information* (Cambridge Univ. Press, Cambridge, 2000).
- [286] S. A. Gardiner, J. I. Cirac, and P. Zoller, *Quantum Chaos in an Ion Trap: The Delta-Kicked Harmonic Oscillator*, Phys. Rev. Lett. **79**, 4790 (1997).
- [287] S. A. Gardiner, J. I. Cirac, and P. Zoller, *Erratum: Quantum Chaos in an Ion Trap: The Delta-Kicked Harmonic Oscillator [Phys. Rev. Lett. 79, 4790 (1997)]*, Phys. Rev. Lett. **80**, 2968 (1998).
- [288] S. Schlunk, M. B. d'Arcy, S. A. Gardiner, and G. S. Summy, *Experimental Observation of High-Order Quantum Accelerator Modes*, Phys. Rev. Lett. **90**, 124102 (2003).
- [289] N. F. Ramsey, *Molecular beams* (Oxford Univ. Press, Oxford, 1986).
- [290] M. K. Oberthaler, R. M. Godun, M. B. d'Arcy, G. S. Summy, and K. Burnett, *Observation of Quantum Accelerator Modes*, Phys. Rev. Lett. **83**, 4447 (1999).
- [291] R. M. Godun, M. B. d'Arcy, M. K. Oberthaler, G. S. Summy, and K. Burnett, *Quantum accelerator modes: A tool for atom optics*, Phys. Rev. A **62**, 013411 (2000).
- [292] J. M. Raimond, M. Brune, and S. Haroche, *Colloquium: Manipulating quantum entanglement with atoms and photons in a cavity*, Rev. Mod. Phys. **73**, 565 (2001).
- [293] N. Friedman, A. Kaplan, and N. Davidson, *Dark optical traps for cold atoms*, Adv. At. Mol. Opt. Phys. **48**, 99 (2003).
- [294] A. R. R. de Carvalho, *Caos, descoerência, proteção de estados e a transição quântico-clássico para íons aprisionados*, Universidade Federal do Rio de Janeiro, Rio de Janeiro (2002).
- [295] L. Deng, E. W. Hagley, J. Denschlag, J. E. Simsarian, M. Edwards, C. W. Clark, K. Helmerson, S. L. Rolston, and W. D. Phillips, *Temporal, Matter-Wave-Dispersion Talbot Effect*, Phys. Rev. Lett. **83**, 5407 (1999).
- [296] M. J. Davis and E. J. Heller, *Quantum dynamical tunneling in bound states*, J. Chem. Phys. **75**, 246 (1981).
- [297] D. A. Steck, W. H. Oskay, and M. G. Raizen, *Observation of Chaos-Assisted Tunneling Between Islands of Stability*, Science **293**, 274 (2001).
- [298] W. K. Hensinger, H. Häffner, A. Browaeys, N. R. Heckenberg, K. Helmerson, C. McKenzie, G. J. Milburn, W. D. Phillips, S. L. Rolston, H. Rubinsztein-Dunlop, and B. Urošević, *Dynamical tunnelling of ultracold atoms*, Nature **412**, 52 (2001).
- [299] A. Mouchet and D. Delande, *Signatures of chaotic tunneling*, Phys. Rev. E **67**, 046216 (2003).

- [300] C. Dembowski, H.-D. Gräf, A. Heine, R. Hofferbert, H. Rehfeld, and A. Richter, *First experimental evidence for chaos-assisted tunneling in a microwave annular billiard*, Phys. Rev. Lett. **84**, 867 (2000).
- [301] A. Mouchet, C. Miniatura, B. Grémaud, and D. Delande, *Chaos-assisted tunneling with cold atoms*, Phys. Rev. E **64**, 016221 (2001).
- [302] K. Hornberger, *Strahlungszzerfall nichtdispergierender Wellenpakete*, Master's thesis, Ludwig-Maximilians-Universität, Munich (1997).
- [303] K. Hornberger and A. Buchleitner, *Radiative decay of nondispersive wave packets*, Europhys. Lett. **41**, 383 (1998).
- [304] R. R. Jones, D. You, and P. H. Bucksbaum, *Ionization of Rydberg atoms by subpicosecond half-cycle electromagnetic pulses*, Phys. Rev. Lett. **70**, 1236 (1993).
- [305] M. T. Frey, F. B. Dunning, C. O. Reinhold, and J. Burgdörfer, *Ionization of very-high- n Rydberg atoms by half-cycle pulses in the short-pulse regime*, Phys. Rev. A **53**, R2929 (1996).
- [306] M. Klews and W. Schweizer, *Three-dimensional kicked hydrogen atom*, Phys. Rev. A **64**, 053403 (2001).
- [307] E. Persson, S. Yoshida, X.-M. Tong, C. O. Reinhold, and J. Burgdörfer, *Quantum localization in the high-frequency limit*, Phys. Rev. A **66**, 043407 (2002).
- [308] E. Persson, S. Yoshida, X.-M. Tong, C. O. Reinhold, and J. Burgdörfer, *Quantum localization in the three-dimensional kicked Rydberg atom*, preprint, 2003.
- [309] E. Persson, private communication.
- [310] P. Schlagheck, *Das Drei-Körper-Coloumbproblem unter periodischem Antrieb*, Ph.D. thesis, Technische Universität München, München (1999).
- [311] P. Schlagheck and A. Buchleitner, *Algebraic decay of the survival probability in chaotic helium*, Phys. Rev. A **64**, 024701 (2001).
- [312] R. J. Serfling, *Contributions to Central Limit Theory for dependent variables*, Ann. Math. Stat. **39**, 1158 (1968).

Acknowledgements

This thesis in the frame of a **binational dissertation** would not have been accomplished without the support, advice, and help of many people whom I am extremely grateful to:

many thanks to Andreas Buchleitner who spent a lot of his precious time on bureaucratic issues, making the binational doctorate possible. Seine nichtendende Geduld mit allen Problemchen gab mir die nötige Stütze in mancher komplexen Situation.

Italo Guarneri for accepting the offer of the first binational doctorate programme with the Università degli Studi dell' Insubria. His advice on physical problems in general as well as on detailed questions was often given with outstanding humour. La ringrazio molto!

Herrn Dr. Herbert Stöhr gebührt besonderer Dank für sein Engagement, welches die vorliegende binationale Promotion an der Fakultät für Physik der Ludwig-Maximilians-Universität München möglich machte.

professore Giulio Casati and his group at the International Centre for the Study of Dynamical Systems in Como. Many bureaucratic issues could be solved by the ingenious efforts of the professori Giorgio Mantica and Roberto Artuso. Mille, mille grazie!

many thanks also to my collaborator Prof. Shmuel Fishman. His ideas, accompanied by continuously imposed pressure of exactness, led to fruitful results.

Dr. Andreas Krug for computing 3D data for the driven hydrogen problem, and his very useful visit in Como. Wir vermissen unseren Rechenmeister!

dott. Marcello Terraneo for the collaboration on fluctuations, and for many advises what concerns “quantum maps”.

Dr. Gregor Veble whose help with a physicist's everyday-life problems, his cooking skills, together with Mojca's charm made my life pleasant in Como.

Dr. Gil Summy, Dr. Michael d'Arcy for their courtesy to use their experimental data in this thesis as well as for the generous invitation to Oxford – which, actually, I had missed a lot. Our discussions fostered the work presented in this thesis. Many thanks also to Dr. Rachel Godun, Dr. Simon Gardiner, Frau Dipl.-Phys. Sophie Schlunk, and the “alumnus” at the Oxford quantum-chaos experiments, Herrn Prof. Dr. Markus Oberthaler.

dott. Giuliano Benenti for discussions on “fidelity”.

den Mitgliedern und Ehemaligen meiner Dresdner Arbeitsgruppe: den Herren Peter Schlagheck, Klaus Hornberger, Cord Müller, sowie den Herren Thomas Wellens, Javier Madroño, Florian Minter. Besondern Dank den lehrreichen Diskussion mit Herrn Boris Fine, Herrn André R. R. Carvalho und Herrn Vyacheslav Shatokhin.

Dr. Christian Miniatura and Prof. Ken Taylor for discussions on spontaneous emission processes and scattering theory.

dott. Fabrizio Lillo e professore Rosario Mantegna per l'ospitalità a Palermo.

ai membri del gruppo "Optical Nonlinear Processes", Dr. Ottavia Jedrkiewicz, Dr. Josè Trull e professore Paolo Di Trapani per alcune discussioni a Como.

ringrazio le nostre segretarie a Como per tutto l'aiuto: Barbara Arcari, Roberta Meroni, Lorenza Paolucci e Barbara Spanò. In particolare, ringrazio Alessandra Parassole per essere la mia "mamma" italiana, e Silvia Ceccarelli per le gite in Questura. Mille grazie anche ad Annalisa Bardelli per tutti i libri che mi ha aiutato a trovare.

vielen herzlichen Dank an Frau Claudia Lantsch, Frau Gabriele Makolies und Frau Ilona Auguszt für die Meisterung organisatorischer Probleme in Dresden. Unserer Bibliothekarin Frau Heidi Näther für die vielen Buch- und Artikelbestellungen.

ai miei amici, Damiano Monticelli, Giampaolo Cristadoro, Gloria Tabacchi, Alice Barale, e Franz Josef Kaiser. Mille grazie anche a Daniela Fanetti per le corse vicino alla nostra Via Pannilani.

my friends, Mario Brandhorst & Kelley Wilder, Bettina Hartz, Stephanie Hutzler, Chien-Nan Liu, Lieselot Vandevenne, and Simone Zerer for their visits in Como.

Ivo Häring and Nilüfer Baba for many stimuli beyond the ivory tower of physics. The "Finite Systems Group", and the football teams of the MPI-PKS and the MPI-CPFS for the international atmosphere in Dresden.

e mille baci ad Andreana che mi fa piacere l'Italia come nessun altro.

Alles Vergängliche
ist nur ein Gleichnis;
das Unzulängliche
Hier wirds Ereignis;
Das Unbeschreibliche,
Hier ist es getan,
Das Ewig-Weibliche
Zieht uns hinan.

J. v. Goethe, Faust, 2. Teil

Lebenslauf

Name Sandro Marcel Wimberger
Geburtsdatum/ort 22. Oktober 1974 in Passau
Staatsangehörigkeit deutsch
Adresse Im Täental 28
D-94051 Hauzenberg

Schulbildung

1981 - 1985 Grundsschule Hauzenberg
1985 - 1994 Gymnasium Leopoldinum Passau
(humanistischer Zweig)
1994 **Abitur** (Note: 1.0)

Studium der Physik

1994 - 2000 Ludwig-Maximilians-Universität München
1997 - 1998 Visiting student an der University of Oxford (England)
1999 - 2000 Visiting student am Weizmann Institute of Science
(Israel)
14. November 2000 **Physik Diplom** (mit Auszeichnung)
Diplomarbeit: „Der Leitwert von Atomen“,
Betreuer: PD Dr. Andreas Buchleitner,
angefertigt am Max-Planck-Institut für
Physik komplexer Systeme, Dresden

Binationale Promotion in Physik

2000 - 2003 an der Fakultät für Physik der LMU München
und an der Università degli Studi dell' Insubria
Betreuer:
PD Dr. Andreas Buchleitner (München/Dresden)
und Prof. Italo Guarneri (Como)

Stipendien

1994 - 2000 Stipendium nach dem Bayerischen
Begabtenförderungsgesetz
1997 - 2000 Studienstiftung des deutschen Volkes
2001 - 2003 Contratto di Collaborazione des
Istituto Nazionale per la Fisica della Materia (Italien)

München, den 17. Oktober 2003